DOCTOR OF PHILOSOPHY

Improved TIPS-Pentacene-Based Organic Thin Film Transistors and Their applications; Memory Transistor and Gas Sensing

Al-Shawi, Amjad Jassim Mohammed

Award date:
2021

Awarding institution:
Bangor University

PRIFYSGOL
BANGOR
UNIVERSITY

Improved TIPS-Pentacene-Based Organic Thin Film Transistors and Their Applications; Memory Transistor and Gas Sensing.

By

Amjad Jassim Al-Shawi

A thesis submitted in partial fulfillment for the

degree of Doctor of Philosophy

in the

College of Environmental Science and Engineering

School of Computer Science and Electronic Engineering

April 2021

Declaration and Consent

Details of the Work

I hereby agree to deposit the following item in the digital repository maintained by Bangor University and/or in any other repository authorized for use by Bangor University.

Author Name**: Amjad Jassem Al-Shawi**

Title: **Improved TIPS-Pentacene-Based Organic Thin Film Transistors and their application;Memory Transistor And Gas Sensing.**

Supervisor/Department: **Dr. Mohammed Mabrook / Electronic Engineering**

Qualification/Degree obtained: **PhD**

This item is a product of my own research endeavors and is covered by the agreement below in which the item is referred to as "the Work". It is identical in content to that deposited in the Library, subject to point 2 below.

Non-exclusive Rights

Rights granted to the digital repository through this agreement are entirely nonexclusive. I am free to publish the Work in its present version or future versions elsewhere.

I agree that Bangor University may electronically store, copy or translate the Work to any approved medium or format for the purpose of future preservation and accessibility. Bangor University is not under any obligation to reproduce or display the Work in the same formats or resolutions in which it was originally deposited.

Bangor University Digital Repository

I understand that work deposited in the digital repository will be accessible to a wide variety of people and institutions, including automated agents and search engines via the World Wide Web.

I understand that once the Work is deposited, the item and its metadata may be incorporated into public access catalogues or services, national databases of electronic theses and dissertations such as the British Library's EThOS or any service provided by the National Library of Wales.

I understand that the Work may be made available via the National Library of Wales Online Electronic Theses Service under the declared terms and conditions of use

(http://www.llgc.org.uk/index.phpid=4676). I agree that as part of this service the National Library of Wales may electronically store, copy or convert the Work to any approved medium or format for the purpose of future preservation and accessibility. The National Library of Wales is not under any obligation to reproduce or display the Work in the same formats or resolutions in which it was originally deposited.

Statement 1:

This thesis is the result of my own investigations, except the preparation of PAMAM dendrimers materials were performed in collaboration with the School of chemistry, Bangor University, UK.

Signed …… (candidate) Date ……

Statement 2:

I agree to submit my thesis (the Work) electronically via Bangor University's e-submission system, however I opt-out of the electronic deposit to the Bangor University (BU) Institutional Digital Repository, the British Library ETHOS system, and/or in any other repository authorized for use by Bangor University, due to lack of permissions for use of third party material.

In addition to the above I also agree to the following:

That I am the author or have the authority of the author(s) to make this agreement and do hereby give Bangor University the right to make available the Work in the way described above.

That the electronic copy of the Work deposited in the digital repository and covered by this agreement, is identical in content to the paper copy of the Work deposited in the Bangor University Library, subject to point 4 below.

That I have exercised reasonable care to ensure that the Work is original and, to the best of my knowledge, does not breach any laws – including those relating to defamation, libel and copyright.

That I have, in instances where the intellectual property of other authors or copyright holders is included in the Work, and where appropriate, gained explicit permission for the inclusion

of that material in the Work, and in the electronic form of the Work as accessed through the open access digital

Repository, or that I have identified and removed that material for which adequate and appropriate permission has not been obtained and which will be inaccessible via the digital repository.

That Bangor University does not hold any obligation to take legal action on behalf of the Depositor, or other rights holders, in the event of a breach of intellectual property rights, or any other right, in the material deposited.

That I will indemnify and keep indemnified Bangor University and the National Library of Wales from and against any loss, liability, claim or damage, including without limitation any related legal fees and court costs (on a full indemnity bases), related to any breach by myself of any term of this agreement.

Signature: …… Date: …….....

Contents

Abstract

Organic thin film devices based on 6,13-bis (tri-isopropyl silylethynyl) pentacene (TIPS-pentacene) semiconductors were fabricated using off-centre spin-coating (OCSC) technique for depositing the organic insulating layers. Using this technique in our work produced stable transistors with high mobility and low operating voltage which can be realised from the improvement of insulator/semiconductor interface. All the devices were fabricated using organic gate insulators; poly(methyl methacrylate) (PMMA) and poly(vinyl alcohol) (PVA) after having been cross-linked with 1,6-bis (trichlorosilyl) hexane (C6-Si) (10µl/1ml) and **ammonium dichromate, 0.8 wt.%, respectively.** In the first part of this work, surface morphology study was carried out for the two insulating layers to find the optimal parameters. It was found that the OCSC method produces large and uniform grains leading to negligible hysteresis and leakage current organic thin film transistors (OTFTs) devices. Relatively high mobility of about 1.42 $cm^2\ V^{-1}\ s^{-1}$, on/off ratio 7.5×10^5 and low threshold voltage of -2 V were achieved for the PMMA-based OTFTs, while values of 1.22 $cm^2\ V^{-1}\ s^{-1}$, 8.6×10^4 and -2 V were recorded for mobility, on/off ratio and threshold voltage for the PVA-based OTFTs, respectively. Also, the environmental effect on the OTFTs was investigated during this work. For reliability tests, the effect of bias stress on the devices in term of threshold voltage shift ΔVT was investigated by applying various bias stress at different time. The tests showed negligible hysteresis when applying a forward and reverse stress voltage with a fixed shape of transfer characteristics.

In the second part of this study, organic thin film memory transistors (OTFMTs) were fabricated and characterised using graphene oxide (GO) as a floating gate inserted between two insulating layers for both types of devices, PMMA and PVA-based OTFTs. The hysteresis obtained in these devices is an evidence for the memory behaviour and charge storage in these devices. A memory window of 38 V and 29 V were achieved for the PMMA and PVA- based OTFMT, respectively.

The last part of this study is to investigate OTFTs devices as gas sensors. In this investigation, the OTFTs from part one of this study were used to detect alcohol vapour (ethanol and methanol) with parts per million (ppm) concentrations. A sensing system was designed and set up for this purpose. The device's sensing was indicated from the change in the output characteristics parameters while the devices are exposed to alcohol vapour. Different parameters of sensitivity have been used such as the change in the mobility(µ), drain-source current (I_{DS}) and threshold voltage shift (ΔV_{GS}). High sensitivity was achieved for PMMA-based OTFTs for detection of ethanol vapour; (6.6% ppm^{-1} depending on the change in the saturation current, 17.2% ppm^{-1} for the change in the threshold voltage shift and -0.0574 $(cm^2\ V^{-1}s^{-1}).ppm^{-1}$ depending on the mobility with a short response and recovery time of 54 s and 36 s respectively.

Dedicated To My Beloved Parents, My Lovely Wife, My Beautiful Daughters Raniah, Zahraa and wonderful Noor and to My Little Son Mustafa.

Acknowledgments

All praises go to Allah for his blessing and reconcile me in completing this thesis. Firstly, I would like to thank my supervisor Dr. Mohammed Mabrook for the help he granted me throughout this thesis with his knowledge and clear guidance. I greatly appreciate the encourgment and advice given by Dr. Paul Sayers, Dr. Maysoon Ahmed and Fahad Almutairi . Also Ben Assinder and Iwan Jones for their technician support during my research. I am forever grateful. I am also very much thankful to the Higher Education in Iraq for the provision of a studentship and to Iraqi cultural attaché in UK for help and support. And of course, the most important acknowledgment goes to my family, my father, and mother. Especially my lovely daughter Noor for giving the most support. My children, Raniah, Zahraa and little prince Mustafa. And finally a special thanks to my wife for all her assistance. Many thanks to everyone in electronic engineering school who has given me support and encouragement throughout this research, without them I could have never done this.

Chapter 1

Introduction

1.1 Introduction

In the last four decades, inorganic semiconductors such as gallium arsenide and silicon, metals such as copper and aluminium and dioxide insulators have been the main base materials for the fabrication of electronic devices. However, many investigations have been performed using organic materials, in particular semiconductors to fabricate electronic devices. Organic semiconductor electronic devices are important due to their low-cost and fast fabrication, flexibility, and lightweight [1].The key element in microelectronics is transistor. Therefore, significant research has been done to improve performance of organic thin-film transistors for future electronics [2-5]. The market demand for high-performance organic electronics has also increased because of the new emerging applications. It is now estimated that the market for flexible electronics will reach $300 billion by 2028, with growth from $29.28 billion in 2017 to over $63 billion in 2023 [6]. In the last few years, organic materials have become widely used in electronic devices and circuits providing lightweight and flexible electronics. Also, organic materials can be processed at low-temperature, low-cost manufacturing and solution deposited to be used for large-area coverage electronics. Figure 1.1 illustrates the cost versus performance diagram of organic semiconductor technology compared to silicon technology. It is clear from Figure 1.1 that some organic semiconductor devices have similar performance as the solid state-based devices but with lower fabrication cost (The shadow area in Figure 1.1).

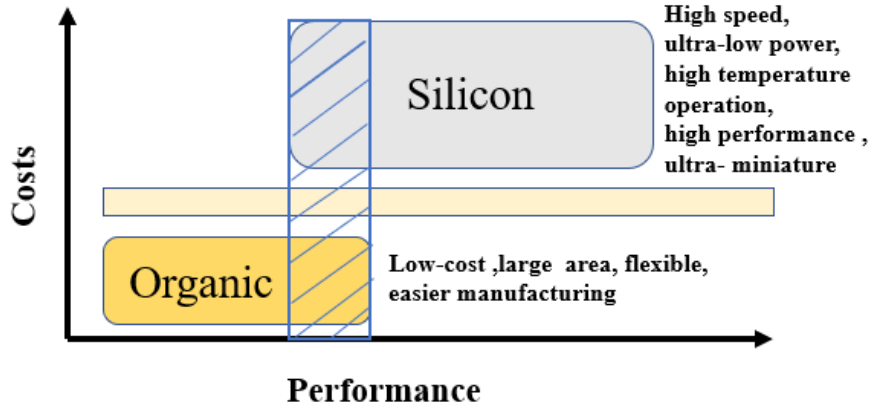

Figure 1. 1: *Illustration of performance versus cost for organic semiconductor and silicon technologies*

Different devices built using organic materials have attracted researchers attention such as organic thin-film transistors (OTFTs) [7,8], organic memory devices [9], organic solar cells [10], sensors [11], and organic light-emitting diodes (OLEDs) [12]. Also, electronic materials have become more attractive for display applications such as televisions and mobile phones. Figure 1.2 shows the current market size of the printed, organic and flexible electronics industry for the year 2019 [13].

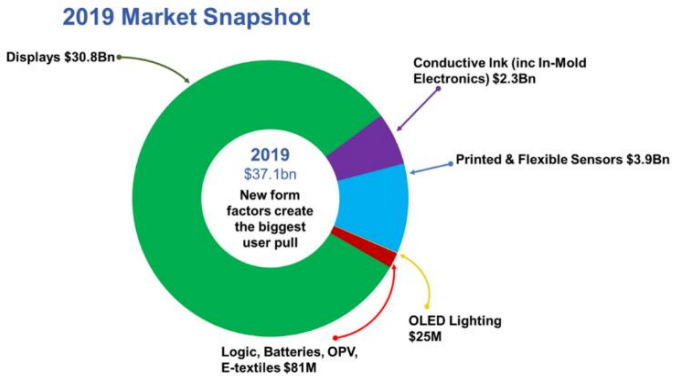

Figure 1.2: *Current market size of the organic and flexible electronics industry [8].*

1.2 Historical background

Organic electronics is a subdivision of modern electronics, and it deals with organic materials, such as polymers or small molecules. The discovery of the electrical conductivity in organic materials can be traced to 1862 when Henry Letheby obtained a partly conductive material using anodic oxidation of aniline in sulfuric acid. In history, the beginning of organic electronics has started with the identification of organic semiconductors in the late 1940s [14]. Literature shows that the research in the electrical behaviour of organic materials was carried out in the 1960s [15], while in the early 1970s [14] photoconductive organic materials were found, and in this decade, the conductive polymers were discovered. Later in the 1980s, [16] photo-emissive polymers created a new wave in the field of organic electronics. The discovery of electrically conductive polymers considerably changed our views on polymer materials and shaped the basis of future organic electronics. Heeger, MacDiarmid, and Shirakawa discovered in the 1970s that the polymer polyacetylene, after certain modifications, can be made conductive. Where doped polyacetylene can be used to form a new group of conducting polymers, and the electrical conductivity of the material can be systematically tuned over a range of magnitudes [17]. Alan J. Heeger, Alan G.

MacDiarmid, and Hideki Shirakawa were awarded the Nobel Prize (in the year 2000) in chemistry for their discovery of highly-conductive organic polymers (iodine-doped polyacetylene) [17]. Later, the performance of organic electronic devices has continuously improved; the power conversion efficiencies of organic photovoltaic cells (OPVCs) have reached over 5 % [18]. Figure 1.3. shows the timeline performance of carrier mobility in organic field-effect transistor (OTFs) started from 1986 with mobility of 10^{-5} cm^2 V^{-1} s^{-1} reported from poly-thiophene up to 20 cm^2 V^{-1} s^{-1} [19-21].

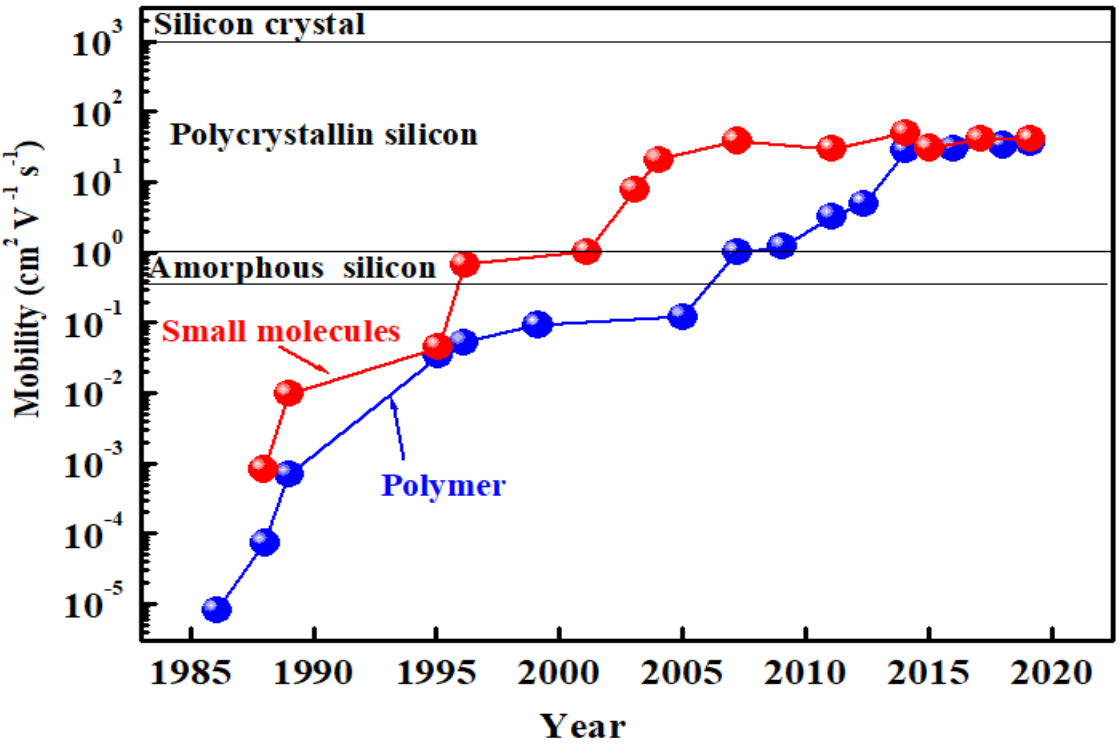

Figure 1. 3: *Timelines performance of carrer mobility in organic field-effect transistor OTFTs*

1.3 Organic electronics applications

Organic electronics have attracted remarkable attention over the last several decades as a potential candidate for low-cost, lightweight, flexible, semi-transparent, and customisable solution for a large variety of applications not well suited to traditional inorganic technologies. The most researched device applications have been organic photovoltaics (OPVs), organic light-emitting diodes (OLEDs) and organic field-effect transistors (OFETs). Figure 1.4 shows some application areas of organic electronics technology. The major applications of organic electronics are sensors, active-matrix (AM), flat panel displays (FPDs), organic light-emitting diodes, low-end smart cards, electronic ink, flexible

electronics and electronic identification tags. Sensors based on organic electronics are widely used and studded for home safety, medical purpose and environmental monitoring [22]. Herein, we will review some of these applications of organic electronics.

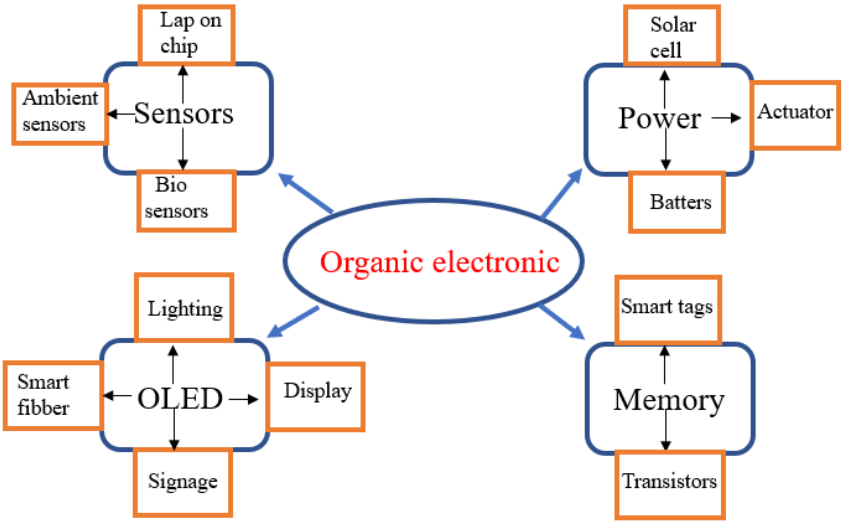

***Figure 1. 4**: Typical applications of organic electronics*

Nowadays, thin-film transistors (TFTs) play an important role in the field of electronic devices technology. TFTs are the backplanes of most displays such as LCDs and OLED. However, OTFTs have several advantages such as low-cost of manufacturing, large area coverage, flexibility and low-power operation. Therefore, OTFTs are promised to be a candidate for new emerging backplanes applications. For instance, it is impossible to fabricate AM LCDs based on hydrogenated amorphous silicon TFTs on a plastic substrate because of the high temperature required (> 300 ^{o}C). Whereas, organic materials easy to be fabricated and deposited on a flexible substrate at a low temperature. The early Active Matrix (AM) display based on organic semiconductors was reported in 2000 [23] while Rogers et al. in 2001 [24] have demonstrated electrophoretic flexible display based on OTFTs. Hong et al. in 2005 [25] produced a high-resolution AM LCDs based on OTFT. Organic electronics technology can be used to develop low-cost circuits for applications like card games, electronic ticket, and product packaging as well as organic sensors. Hence, the integrated radio frequency identification (RFID) tag which is required 13.56 MHz (high-frequency, HF) to be operated and can provide the operating power to the tags via inductive coupling for example; ticket, smart card passport, library labels and many applications will be a promising candidate for organic electronics. The organic RFID tags are made from

plastic make them more flexible and thinner than silicon-based tags. Furthermore, organic RFID tags can be produced from solution process providing low-cost fabrication to compute with bar code tags. Baude et al. in 2003 [26] used vacuum deposition technique to demonstrate pentacene-based RFID circuits. In 2005, Subramanian et al [27] provided an organic RFID tag using novel pentacene and oligothiophene precursors. Blache et al. [28] in 2009 demonstrated 4-bit transponder based on organic complementary metal-oxide-semiconductor (CMOS) and working at a frequency of 13.56 MHz.

Another application of organic material is memory devices. There is more interest from researchers to develop and improve memories using organic materials due to there properties such as low-cost fabrication, high density, high speed and nonvolatility. There are many types of organic memory devices, for instance, organic thin-film memory transistors (OTFMTs) [29-33], charge storage in metal-insulator-semiconductor (MIS) [34] and bi-stable switching memory devices [35], which have been wildly fabricated and tested by researchers.

In the past few decades, gas sensors have been extremely important in many applications. The most applications of gas sensors are monitoring automotive exhaust gases [36], controlling the air quality and concentration of some gases in the air [37]. Therefore, organic semiconductor materials have been used for manufacturing of high sensitivity sensors [38]. There are many advantages of using organic materials to produce sensors such as fabrication with low-cost processes on flexible plastic substrates with large-area coverage at room temperature, flexibility and lightweight.

This thesis focuses on the improvement of TIPS-pentacene-based organic TFTs and their applications such as organic thin-film memory transistors (OTFMTs) and organic transistor-based gas sensors.

1.4 Memory devices

Memory devices are used to store information or data that can be recovered later. There are two main classifications of memory devices: volatile and non-volatile memories. The information stored in the volatile memory devices is lost as soon as the power supply is turned off and requires persistent power to maintain working. Volatile memory devices can be classified into two types: Static Random-Access Memory (SRAM) and Dynamic Random-Access Memory (DRAM). SRAM is a type of random-access memory (RAM) which can store each bit using latching circuitry (flip-flop) and the data is lost when the

power is removed (volatile memory). Whereas DRAM is classified as a random-access semiconductor memory and is able to reserve every bit piece of data in a memory cell. Therefore, the difference between them is the lifetime. The memory cell is made up of a miniature capacitor and a transistor. Each one of them is generally based on metal-oxide-semiconductor (MOS) technology. Charged or discharged are the only options a capacitor can be to portray two values of a bit (standardly called 0 and 1). SRAM is used for CPU cache memory because it is faster than DRAM which is used as the main memory for a computer.

There are four types of non-volatile memory devices (NVMs) which can keep the stored data even when the power supply is turned off: Ferroelectric Random Access Memory (FeRAM), Flash memory, Phase-Change Memory (PCM) and Magnetic Random Access Memory (MRAM). Figure 1.5 shows the categories of memory devices technologies.

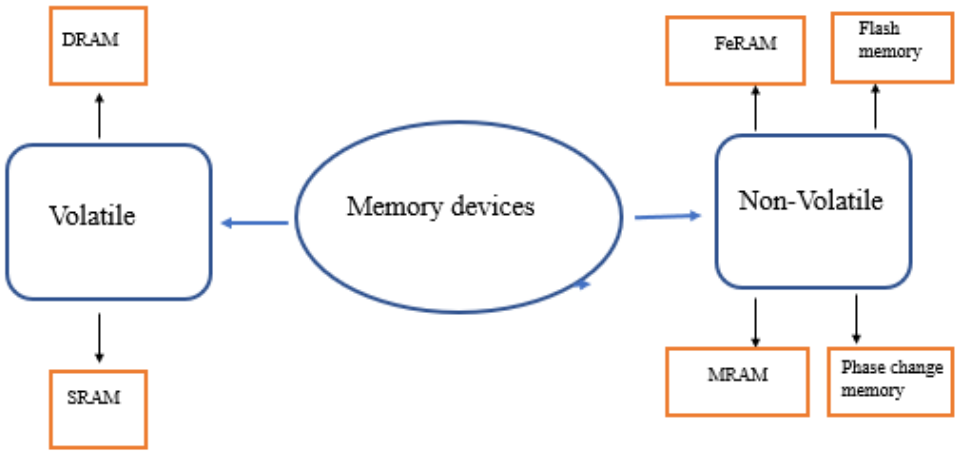

Figure 1. 5: *A classification of memory devices technologies*

Ferroelectric RAM has a similar structure of DRAM but instead of the dielectric layer, a ferroelectric layer is installed to obtain non-volatility. FeRAM is the same as flash memory in functionality and it is one of the non-volatile random-access memory alternative technologies. Ferroelectric RAM as a switch and storage was published in 1952 by Dudley Allen Buck [39]. Two types of FeRAM devices are found, capacitor-type and ferroelectric field-effect transistor (FeFET). Capacitor-type is similar to DRAM, the main difference between them is using ferroelectric thin film as a gate in capacitor-type to store data whereas, for DRAM the data can be stored in a dielectric layer while FeFET is a device of

a single element with a ferroelectric thin film layer as a gate dielectric in its structure [40]. Flash memory is a non-volatile memory device which is used to store and transfer the data information between digital devices. It can be electronically programmed and erased easily. It is usually used in USB flash devices, digital camera, MP3 players and other solid-state drives. One of the most used non-volatile memory is flash memory where a floating gate can be used to store data and the change in threshold voltage illustrate the memory state. FeRAMs memory devices have low power usage, high read/write endurance cycles and fast write performance which make them more demand than flash memory.

Another type of non-volatile random-access memory called Magnetoresistive Random-Access Memory (MRAM) which is developed in 1980 and it was supposed to be dominant memory where the data can be stored in magnetic domains [41]. Unlike SRAM and DRAM that utilize electric charges to store data, MRAM (magnetoresistive RAM or magnetic RAM) utilizes magnetic charges instead, which makes it a type of non-volatile RAM. MRAM is beneficial because it can still maintain data even when the power is switched off. The rule of MRAM technology is for the data to not be stored as electric charge or current flow, but instead as magnetic storage elements in micro-size cells. MRAM uses electron spin to store data, as well as a magnetic tunnel junction and a transistor to perform.

The fourth type of non-volatile RAM is Phase change memory where data is stored by changing the used material's state signifying, on a micro-scale, it reciprocates amongst crystalline and amorphous. A cell of Phase Change Memory (PCM) is formed of one resistor and a bipolar junction transistor. In this non-volatile memory technology, recorded data is in accordance with the utilization of convertible phase change in materials. PCM materials alter state rapidly reciprocating between an amorphous and crystalline phase if appropriate heat pulses are implemented [42]. PCM is presumed to be an auspicious rising non-volatile memory. It has already been used in DVDs, CD-ROMS and other similar optical information technologies

1.4.1 Floating gate memory device

In general, flash memory technology is constructed on a floating gate concept. This type of memory operates on the principle of charging nanoparticles, nanowires, or nanocrystals which are integrated into the insulating layer of a MOS capacitor or TFT [43-45]. A floating gate memory has a field-effect transistor or metal insulator semiconductor (MIS) structure

with two gates, in addition to the control gate; it has a floating gate embedded in the gate dielectric. A floating-gate memory cell is a MOS transistor with a gate surrounded by dielectrics. The floating-gate (FG) is electrically governed by a capacitive-coupled control-gate (CG). Electrically isolated FG acts as a storage electrode for the cell device. Charges injected into the FG can be stored as a data and describes the memory state by altering the transistor's threshold voltage.

MIS capacitors provide the basis for numerous types of electronic devices from thin-film transistors to charge-coupled devices and memory devices. The straightforwardness of the MIS structure has made it a strong device extensively used for the analysis of the interfaces and electrical properties of MIS-based systems. This is similar to metal oxide semiconductor (MOS) capacitors used as analytical tools for the improvement and understanding of silicon-based devices. Understanding the theory and physics of MIS capacitors was used to improve the inorganic-based devices. Organic MIS structures are explained by their capacitance-voltage (C-V) characteristics which exhibit three distinct regions: accumulation, depletion and deep depletion (inversion in inorganic MOS). Memory devices based on MIS structures comprise of charge traps added inside the insulator of the structure, the charge traps behave as the floating gate. Adding the floating gate results in a clear modification in the C-V characteristics and hysteresis in the double-sweep C-V curve. The hysteresis leads to the two stable capacitance states which may be controlled and read by an external bias and thus exhibiting the anticipated memory performance.

As for organic thin-film memory transistors (OTFMs), when a large enough program voltage is applied between the control gate and the source contact, an electronic charge can be brought onto the floating gate by quantum tunnelling or thermal emission [43]. Charging the floating gate changes the transistor's threshold voltage, as the charge on the floating gate partly screens the electric field between the control gate and the semiconductor. The threshold voltage shift can be sensed by measuring the drain current at a certain gate-source voltage. As the floating gate is totally isolated by the dielectric layer, charges stored on the floating gate remain there without the need for any applied voltage (non-volatile memory). To delete the memory, a voltage of opposite polarity should be applied to discharge the floating gate [43].

1.5 Gas sensing

One of the essential elements of modern organic electronics is organic field-effect transistors (OFETs) which can be used as gas sensors. The main defining factor for the increase in new legislations and motivation has been global warming and pollution levels in the atmosphere (for both urban and rural areas) as well as health problems related with atmospheric pollution. Because of the intense necessity of technology (such as smartphones, iPad, tablets, and laptops) from the public in modern-day, the industry advanced powerfully and rapidly. The actions involved with these industries and technologies require chemical activities that entail chemical reactions. Material waste in the gaseous state is the most common outcome of these chemical reactions and serval of these gases may be highly flammable plus dangerous to both human health and the environment. In the past two decades, global warming has been getting notices as an environmental issue with greenhouse gases being released into the atmosphere as the main cause. As mentioned above, industrial activity plays a big part in releasing those toxic and harmful gases. The gases pile up in the atmospheric structure which induces global warming. This sparked fields such as science and engineering to research and develop in this issue. The recent industrialisation has set human living standards positively to a very high level in the last several decades. Though it also brought negative effects such as gases that are hazardous for the environment and public health [46]. So gas sensors have been created for the inspection and sense of a few gases like oxygen (for breathable atmospheres [47] and combustion processes, such as boilers and internal combustion engines) [48], hydrocarbons (in oil fields), plus other gases frequently used in medical applications or manufacturing of chemicals. In vehicles, hydrocarbons gases are used as fuels. However, they are very flammable and can cause an explosion or fire so for safety they should be used up to the legalised level. Other things that need monitoring to protect workers in industrial sectors are loathsome odours, toxic gases, and volatile organic compounds. It is significant for the gas sensors to be miniature and low-cost so it can be provided for a variety of uses [49]. Small and cheap gas sensors are increasingly demanded in important places such as medical diagnostics, food quality control, indoor and outdoor air quality monitoring. Some diseases can also be identified from exhaled breath being analysed for trace gases [50]. Being able to read and record signals smoothly through low-end supporting electronics is an advantage which can be achieved by using electronic sensors in these applications. Because of their low-temperature deposition, customizable surface and their low-cost fabrication process

compared to inorganic counterparts, organic transistors have risen as remarkable semiconductor technology and widely used for OTFTs-based sensors [51]. In this study, TIPS-pentacene-based OTFTs (explained in chapter 4) is tested as a gas sensor for alcohol (ethanol and methanol) using a gas sensing system. The test is applied for two types of organic transistors (cPMMA-based and cPVA-based OTFTs).

1.6 Importance of the study and aim

Organic electronics are widely used in electronic devices due to their flexibility, low cost-fabrication and lightweight with nano sizes. Therefore, this study aimed to fabricate and improve TIPS-pentacene-based OTFTs using the off-centre spin-coating method for depositing two types of insulators (cPMMA and cPVA) to improve the interface between semiconductor and insulating layers. Memory transistors have been very demanded during the last few decades. Hence, part of this study aimed to employ OTFTs as memory transistors by adding graphene oxide as a floating gate (embedded in the insulating layer) applied for two types of transistors (cPMMA-based and cPVA-based OTFTs). Since ethanol and methanol are of the most commonly used alcohol in chemical industries and scientific labs, detecting their vapours in the atmosphere is a matter of importance and this is taken in account in this work to test OTFTs devices as gas sensors for ethanol and methanol.

This project is divided into seven main objectives:

1. Fabrication of organic thin-film transistor OTFTs using the off-centre spin-coating method for depositing the insulating layers to improve the insulator-semiconductor interface.
2. Study the surface morphology of deposited materials.
3. Study and analysis of the electric characteristics of the deposited layers.
4. Fabrication of organic thin-film memory transistors OTFMTs following the same procedure for OTFT with inserting graphene oxide (GO) layer as the floating gate.
5. Study and analysis of the electric characteristics of the OTFMTs.
6. Test the OTFTs as a gas sensor for alcohol (ethanol and methanol).
7. Study and analysis of the electric characteristics of the OTFT as a gas sensor.

1.7 Structure of this Thesis

This thesis focuses on the development of organic TFTs and their applications such as organic thin-film memory transistors OTFMTs devices and gas sensor devices.

The structure of this thesis is as follows:

Chapter 1 illustrates a general introduction to organic electronics. Historical background of organic electronics as well as their applications such as OTFMTs and gas sensing are briefly reviewed. **Chapter 2** provides a principal theory of organic semiconductors and dielectric materials. Also, the charge transport in the organic semiconductor is explained. Organic thin-film transistors (OTFTs), organic thin-film memory transistors (OTFMTs) as well as gas sensing operation principles and electrical characterisation are illustrated in this chapter. **Chapter 3** demonstrates the experimental methods, setups used for manufacturing and characterisation of organic TFTs, organic TFMTs and gas sensing. Also, displays the materials used in this work. **Chapter 4** is the first experimental part which focuses on the fabrication and characterisation of organic thin-film transistors. The main aspect in this chapter is improving the charge transport through MSI in OTFT, where the off-centre spin-coating technique is used to deposit two types of insulator layers (cPVA and cPMMA) in order to improve the insulator-semiconductor interface. TIPS-pentacene semiconductor, aluminium and gold are employed as the active layer, gate electrode and drain-source connectors respectively to fabricate two types of OTFTs (cPMMA-based and cPVA-based OTFTs). The surface morphology of the insulators and semiconductors are studied in this chapter to provide the optimal deposition parameters and high carrier mobility. **Chapter 5** demonstrates one of the OTFT's applications which is organic thin-film memory transistor. Where the same structure of OTFT in chapter 4 are used in addition to graphene oxide GO layer being embedded in the insulator layer to provide two types of memory transistors (cPMMA-based and cPVA-based organic memory transistors). Also, the electric characteristics were studied. **Chapter 6** presents the second application of OTFTs, which is OTFTs-based gas sensors. In this chapter, the design and setup of the gas sensing system are illustrated to test OTFTs devices which were fabricated in chapter 4 as a gas detector for two types of alcohol (ethanol and methanol). The electric characterisation of OTFT-based gas sensors is studied in this chapter as well. **Chapter 7** summarises the main results from the thesis and discusses possible directions for further work.

1.8 References

[1] A. C. Arias, J. D. MacKenzie, I. McCulloch, J. Rivnay, and A. Salleo, "Materials and applications for large area electronics: Solution-based approaches," *Chem. Rev.*, vol. 110, no. 1, pp. 3–24, 2010, doi: 10.1021/cr900150b.

[2] Y. Sun, Y. Ma, Y. Liu, Y. Lin, Z. Wang, Y. Wang, C. Di, K. Xiao, X. Chen, W. Qiu, B. Zhang, G. Yu, W. Hu, and D. Zhu, "High-performance and stable organic thin-film transistors based on fused thiophenes," *Adv. Funct. Mater.*, vol. 16, no. 3, pp. 426–432, 2006, doi: 10.1002/adfm.200500547..

[3] P. Liu, Y. Wu, Y. Li, B. S. Ong, and S. Zhu, "Enabling gate dielectric design for all solution-processed, high-performance, flexible organic thin-film transistors," *J. Am. Chem. Soc.*, vol. 128, no. 14, pp. 4554–4555, 2006, doi: 10.1021/ja060620l.

[4] K. Fukuda, Y. Takeda, Y. Yoshimura, R. Shiwaku, L. T. Tran, T. Sekine, M. Mizukami, D. Kumaki, and S. Tokito, "Fully-printed high-performance organic thin-film transistors and circuitry on one-micron-thick polymer films," *Nat. Commun.*, vol. 5, no. May, pp. 5–12, 2014, doi: 10.1038/ncomms5147.

[5] A. Petritz, A. Wolfberger, A. Fian, J. R. Krenn, T. Griesser, and B. Stadlober, "High performance p-type organic thin film transistors with an intrinsically photopatternable, ultrathin polymer dielectric layer," *Org. Electron.*, vol. 14, no. 11, pp. 3070–3082, 2013, doi: 10.1016/j.orgel.2013.07.014.

[6] S. Gupta, W. T. Navaraj, L. Lorenzelli, and R. Dahiya, "Ultra-thin chips for high-performance flexible electronics," *npj Flex. Electron.*, no. January, 2018, doi: 10.1038/s41528-018-0021-5.

[7] J. Zhou, Y. Hao, X. Yu, N. Zhou, and H. Lin, "High-performance and operationally stable organic thin-film transistors using bi-buffer layers with low-cost electrodes," *J. Phys. D. Appl. Phys.*, vol. 46, no. 38, 2013, doi: 10.1088/0022-3727/46/38/385104.

[8] S. D. Ogier, H. Matsui, L. Feng, M. Simms, M. Mashayekhi, J. Carrabina, L. Terés, and S. Tokito, 'Uniform, high performance, solution processed organic thin-film transistors integrated in 1 MHz frequency ring oscillators', *Org. Electron.*, vol. 54, no. December 2017, pp. 40–47, 2018, doi: 10.1016/j.orgel.2017.12.005.

[9] S. Nam, Y. G. Ko, S. G. Hahm, S. Park, J. Seo, H. Lee, H. Kim, M. Ree, and Y. Kim, "Organic nonvolatile memory transistors with self-doped polymer energy well

structures," *NPG Asia Mater.*, vol. 5, no. 1, pp. e33-6, 2013, doi: 10.1038/am.2012.62.

[10] J. R. O'Dea, L. M. Brown, N. Hoepker, J. A. Marohn, and S. Sadewasser, "Scanning probe microscopy of solar cells: From inorganic thin films to organic photovoltaics," *MRS Bull.*, vol. 37, no. 7, pp. 642–650, 2012, doi: 10.1557/mrs.2012.143.

[11] S. J. Fakher, "Advanced Study of Pentacene-Based Organic Memory Structures," no. January, 2014.

[12] H. Uoyama, K. Goushi, K. Shizu, H. Nomura, and C. Adachi, "Highly efficient organic light-emitting diodes from delayed fluorescence," *Nature*, vol. 492, no. 7428, pp. 234–238, 2012, doi: 10.1038/nature11687.

[13] S. Only, "Printed , Organic and Flexible Electronics 2020-2030 : Forecasts , Technologies , Markets IDTechEx provides clarity on emerging technologies Reports | Subscriptions | Consulting | Events | Journals | Webinars," 2020.

[14] H. Klauk, *Organic Electronics II: More Materials and Applications*. 2012.

[15] J. M. Shaw and P. F. Seidler, "Organic electronics: Introduction," *IBM J. Res. Dev.*, vol. 45, no. 1, pp. 3–8, 2001, doi: 10.1147/rd.451.0003.

[16] B. G. Horowitz, "Organic Field-Effect Transistors," no. 5, pp. 365–377, 1998.

[17] M. Audenaert, G. Gusman, and R. Deltour, "Electrical conductivity of I2-doped polyacetylene," *Phys. Rev. B*, vol. 24, no. 12, pp. 7380–7382, 1981, doi: 10.1103/PhysRevB.24.7380.

[18] S. R. Forrest, "The Limits to Organic Photovoltaic Cell Efficiency," *MRS Bull.*, vol. 30, pp. 28–32, 2011., 2011.

[19] A. Tsumura, H. Koezuka, and T. Ando, "Macromolecular electronic device: Field-effect transistor with a polythiophene thin film," *Appl. Phys. Lett.*, vol. 49, no. 18, pp. 1210–1212, 1986, doi: 10.1063/1.97417.

[20] Y. Yao, H. Dong, F. Liu, T. P. Russell, and W. Hu, "Approaching Intra- and Interchain Charge Transport of Conjugated Polymers Facilely by Topochemical Polymerized Single Crystals," *Adv. Mater.*, vol. 29, no. 29, pp. 1–6, 2017, doi: 10.1002/adma.201701251.

[21] Y. Sui, Y. Deng, T. Du, Y. Shi, and Y. Geng, "Design strategies of n-type conjugated

polymers for organic thin-film transistors," *Mater. Chem. Front.*, vol. 3, no. 10, pp. 1932–1951, 2019, doi: 10.1039/c9qm00382g.

[22] G. G. Malliaras, "Organic Semiconductors in Sensor Applications," *Org. Semicond. Sens. Appl.*, 2008, doi: 10.1007/978-3-540-76314-7.

[23] C. D. Sheraw, L. Zhou, J. R. Huang, D. J. Gundlach, T. N. Jackson, M. G. Kane, I. G. Hill, M. S. Hammond, J. Campi, B. K. Greening, J. Francl, and J. West, "Organic thin-film transistor-driven polymer-dispersed liquid crystal displays on flexible polymeric substrates," *Appl. Phys. Lett.*, vol. 80, no. 6, pp. 1088–1090, 2002, doi: 10.1063/1.1448659.

[24] J. A. Rogers, Z. Bao, K. Baldwin, A. Dodabalapur, B. Crone, V. R. Raju, V. Kuck, H. Katz, K. Amundson, J. Ewing, and P. Drzaic, "Paper-like electronic displays: Large-area rubber-stamped plastic sheets of electronics and microencapsulated electrophoretic inks," *Proc. Natl. Acad. Sci. U. S. A.*, vol. 98, no. 9, pp. 4835–4840, 2001, doi: 10.1073/pnas.091588098.

[25] E. J. J. and L. S. P. M. P. Hong, B. S. Kim, Y. U. Lee, K. K. Song, J. H. Oh, J. H. Kim, T. Y. Choi, M. S. Ryu, K. Chung, S. Y. Lee, B. W. Koo, J. H. Shin, "Recent progress in large sized & high performance organic TFT array,"," *Soc. Inf. Disp. Symp. Dig.*, vol. 36, no. 23–26, 2005.

[26] P. F. Baude, D. A. Ender, M. A. Haase, T. W. Kelley, D. V. Muyres, and S. D. Theiss, "Pentacene-based radio-frequency identification circuitry," *Appl. Phys. Lett.*, vol. 82, no. 22, pp. 3964–3966, 2003, doi: 10.1063/1.1579554.

[27] and S. V. V. Subramanian, J. Frechet, P. Chang, D. C. Huang, J. Lee, S. Molesa, A. Murphy, D. Redinger, "Progress towards development of all-printed RFID tags: Materials, Processes, and Devices," *Proc. IEEE*, vol. 93, no. 1330–38, 2005.

[28] J. K. and W. F. R. Blache, "Organic CMOS circuits for RFID applications," *ISSCC Dig. Tech. Pap.*, vol. 208–209.

[29] A. Rani, J. M. Song, M. Jung Lee, and J. S. Lee, "Reduced graphene oxide based flexible organic charge trap memory devices," *Appl. Phys. Lett.*, vol. 101, no. 23, 2012, doi: 10.1063/1.4769990.

[30] Y. H. Chou, H. C. Chang, C. L. Liu, and W. C. Chen, "Polymeric charge storage electrets for non-volatile organic field effect transistor memory devices," *Polym.*

Chem., vol. 6, no. 3, pp. 341–352, 2015, doi: 10.1039/c4py01213e.

[31] C. Lee, J. Seo, H. Kim, D. I. Song, and Y. Kim, "Stable low-voltage organic memory transistors with poly(vinyl alcohol) layers stabilized by vinyl silicon oxide interlayers," *Org. Electron.*, vol. 34, pp. 223–228, 2016, doi: 10.1016/j.orgel.2016.03.039.

[32] H. C. Chang, C. L. Liu, and W. C. Chen, "Nonvolatile organic thin film transistor memory devices based on hybrid nanocomposites of semiconducting polymers: Gold nanoparticles," *ACS Appl. Mater. Interfaces*, vol. 5, no. 24, pp. 13180–13187, 2013, doi: 10.1021/am404187r.

[33] Y. Park, K. J. Baeg, and C. Kim, "Solution-Processed Nonvolatile Organic Transistor Memory Based on Semiconductor Blends," *ACS Appl. Mater. Interfaces*, vol. 11, no. 8, pp. 8327–8336, 2019, doi: 10.1021/acsami.8b20571.

[34] M. F. Mabrook, Y. Yun, C. Pearson, D. A. Zeze, and M. C. Petty, "Charge storage in pentacene/polymethyimethacrylate memory devices," *IEEE Electron Device Lett.*, vol. 30, no. 6, pp. 632–634, 2009, doi: 10.1109/LED.2009.2018128.

[35] G. Liu, X. Zhuang, Y. Chen, B. Zhang, J. Zhu, C. X. Zhu, K. G. Neoh, and E. T. Kang, "Bistable electrical switching and electronic memory effect in a solution-processable graphene oxide-donor polymer complex," *Appl. Phys. Lett.*, vol. 95, no. 25, pp. 2007–2010, 2009, doi: 10.1063/1.3276556.

[36] J. Riegel, H. Neumann, and H. M. Wiedenmann, "Exhaust gas sensors for automotive emission control," *Solid State Ionics*, vol. 152–153, pp. 783–800, 2002, doi: 10.1016/S0167-2738(02)00329-6.

[37] R. Piedrahita, Y. Xiang, N. Masson, J. Ortega, A. Collier, Y. Jiang, K. Li, R. P. Dick, Q. Lv, M. Hannigan, and L. Shang, "The next generation of low-cost personal air quality sensors for quantitative exposure monitoring," *Atmos. Meas. Tech.*, vol. 7, no. 10, pp. 3325–3336, 2014, doi: 10.5194/amt-7-3325-2014.

[38] and J. T. T. Hasegawa," *Org. field-effect transistors using single Cryst".*, vol. 10, pp. 024314–1–024314–16, 2009.

[39] D.A. Buck "Ferroelectrics for Digital Information Storage and Switching". MASSACHUSETTS INST OF TECH CAMBRIDGE DIGITAL COMPUTER LAB;

1952 Jun 5.

[40] D. J. Jung, “Highly Manufacturable 1T1C 4Mb FRAM with Novel Sensing Scheme,” *IEDM*, pp. 79–282, 1999.

[41] J. Åkerman, “Toward a universal memory,” *Science (80-.).*, vol. 308, no. 5721, pp. 508–510, 2005, doi: 10.1126/science.1110549.

[42] S. Lai and T. Lowrey, “OUM-a 180 nm nonvolatile memory cell element technology for stand alone and embedded applications,” *Tech. Dig. Electron Devices Meet.*, pp. 803–806, 2001, doi: 10.1109/IEDM.2001.979636.

[43] S. Astrophysique, C. E. A. Saclay, G. Yvette, I.- Trieste, S. Padova, and I.- Padova, “10,11,7,” vol. 326, no. December, pp. 1516–1520, 2009.

[44] M. F. Mabrook, Y. Yun, C. Pearson, D. A. Zeze, and M. C. Petty, “A pentacene-based organic thin film memory transistor,” *Appl. Phys. Lett.*, vol. 94, no. 17, pp. 92–95, 2009, doi: 10.1063/1.3126021.

[45] J. Han, W. Wang, J. Ying, and W. Xie, “Ambipolar organic thin-film transistor-based nano-floating-gate nonvolatile memory,” *Appl. Phys. Lett.*, vol. 104, no. 1, 2014, doi: 10.1063/1.4860990.

[46] P. R. Shakya, P. Shrestha, C. S. Tamrakar, and P. K. Bhattarai, “Studies on potential emission of hazardous gases due to uncontrolled open-air burning of waste vehicle tyres and their possible impacts on the environment,” *Atmos. Environ.*, vol. 42, no. 26, pp. 6555–6559, 2008, doi: 10.1016/j.atmosenv.2008.04.013.

[47] K. Wetchakun, T. Samerjai, N. Tamaekong, C. Liewhiran, C. Siriwong, V. Kruefu, A. Wisitsoraat, A. Tuantranont, and S. Phanichphant, “Semiconducting metal oxides as sensors for environmentally hazardous gases,” *Sensors Actuators, B Chem.*, vol. 160, no. 1, pp. 580–591, 2011, doi: 10.1016/j.snb.2011.08.032.

[48] S. Candel and N. Docquier, “Combustion control and sensors: a review,” *Prog. Energy Combust. Sci.*, vol. 28, pp. 107–150, 2002.

[49] R. Baron and J. Saffell, “Amperometric Gas Sensors as a Low Cost Emerging Technology Platform for Air Quality Monitoring Applications: A Review,” *ACS Sensors*, vol. 2, no. 11, pp. 1553–1566, 2017, doi: 10.1021/acssensors.7b00620.

[50] A. Amann, W. Miekisch, J. Schubert, B. Buszewski, T. Ligor, T. Jezierski, J. Pleil, and T. Risby, "Analysis of exhaled breath for disease detection," *Annu. Rev. Anal. Chem.*, vol. 7, pp. 455–482, 2014, doi: 10.1146/annurev-anchem-071213-020043.

[51] J. Chang, Z. Lin, C. Zhang, and Y. Hao, "Organic Field-Effect Transistor: Device Physics, Materials, and Process," *Differ. Types Field-Effect Transistors - Theory Appl.*, 2017, doi: 10.5772/intechopen.68215.

Chapter 2

Devices Theory of Organic Electronics

This chapter reports on the background theory of organic semiconductor devices. Firstly, the basic properties of organic semiconductors are reviewed and followed by a discussion of their charge transport properties. Further, the small molecular organic semiconductors theory is also detailed. Device fabrication and characterisations are also discussed in this chapter.

2.1 Introduction

The research concentrated on organic electronics has expeditiously advanced in the last three decades reaching industrial progress and increasing applications. The research on organic electronics comprised electronic engineering, material science, applied physics and industrial chemistry plus further areas. Pentacene-based organic devices have the ability to be used in various applications such as integrated circuits (IC), flexible displays and organic displays due to their lightweight, low-cost manufacture, large-area coverage, and higher integration density. These are the main reasons why they have been firmly improved and developed.

In this chapter, electric characterisation and fundamental concepts concerning organic thin-film transistors (OTFTs) and their applications such as organic thin-film memory transistors (OTFMTs) and gas sensing have been reviewed to give the base for the discussion about the results provided in Chapters 4, 5, and 6. In sections 2.2 - 2.4, an overview of the principal elements of organic devices, semiconductors and insulators, are presented as well as a short review of the charge transport mechanisms in organic semiconductors and metal-semiconductor interface. Whereas in section 2.5, the doping density is explained. Then thin film transistor structure is illustrated in section 2.6. After that, the principles behind the work of memory devices are addressed in section 2.7 with floating gate memory devices being an important focus. Lastly, section 2.8 clarifies the application of OTFTs as gas sensors in details.

2.2 Organic semiconductors

Organic semiconductor materials have attracted the focus of industrial and academic researchers in recent decades because of the wide variety of applications for these materials. Various organic semiconductors have been used as an active layer in organic thin-film transistor devices (OTFTs) [1-3], organic light-emitting diodes devices (OLEDs) [4,5], organic memories devices [6,7], organic photovoltaic devices (OPVs) [8,9] and organic sensors [10-12]. The thermal evaporation method can be used for depositing most of these materials including molecular crystals, and other materials such as conductive polymers which are deposited by spin-coating and inkjet printing methods. Polymeric semiconductor materials have been widely used in electronic devices due to their outstanding properties, for instance, high solubility in various solvents and low-temperature fabrication which make these materials more suitable for large area deposition processes such as spray coating and printing. On the other hand, insoluble small-molecule semiconductor materials are the majority and often are deposited through a vacuum process. The most frequently used small-molecule organic semiconductor is pentacene. Pentacene, however, experiences instability due to oxidation once exposed to humidity and/or oxygen. This makes the carrier mobility decreases, reducing the lifetime of the organic devices. Therefore, TIPS-pentacene which is one of the pentacene derivatives is used to reduce the oxidation effect [13]. Figure 2.1 (a) and (b) shows the molecular structure of pentacene and TIPS-pentacene, respectively.

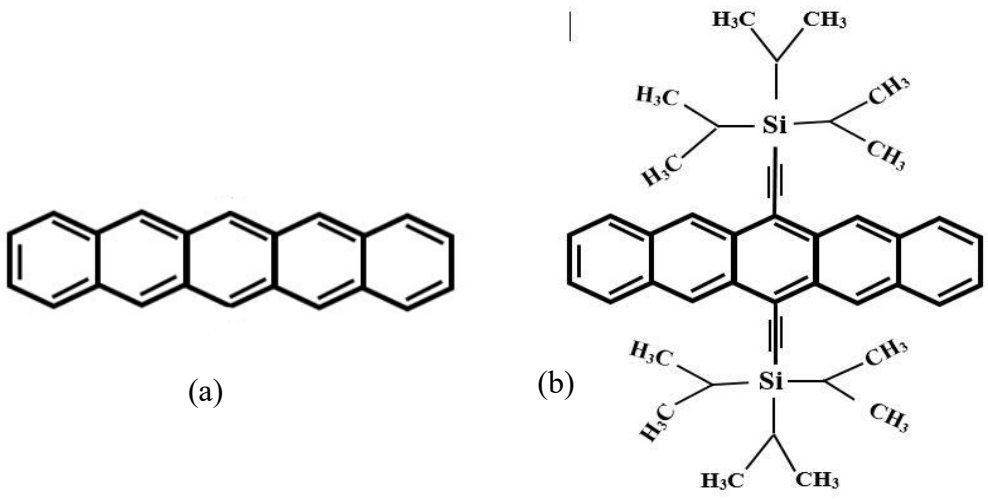

Figure 2. 1: *Molecular structure of (a) Pentacene (b) TIPS-Pentacene*

Small-molecule organic semiconductors are different from inorganic semiconductors, which are usually undoped (intrinsic semiconductors). Thus, the idea of p-type or n-type organic semiconductors relies on Highest Occupied Molecular Orbital (HOMO) and Lowest Unoccupied Molecular Orbital (LUMO) levels instead of the possibility of a doping process. The holes are more readily injected than electrons in p-type semiconductors, while it's the reverse for n-type semiconductors. A determining feature of p-type semiconductors is that their holes typically have greater mobility than electrons [14].

2.2.1 Charge transport in organic semiconductors

Organic semiconductors are conjugated carbon-based materials with electrical conductivity located in between the conductivity of insulators and metals. Conjugated molecules have a network of p-orbitals with delocalized electrons as well as alternating single and double bonds [15]. Crystalline structures can be formed from the small molecule semiconductor which can improve the charge carrier transport. On the other hand, conjugated polymers are usually semicrystalline with amorphous regions which restrict their charge transport property. Weak intermolecular van der Waals forces bond organic molecules and influence their thermodynamic, electrical, and mechanical properties [16], which are contrary to the inorganic molecules with strong covalent bonds.

Semiconductors and small molecules are structured of hydrocarbon molecules with a carbon atom as a backbone. The carbon atoms have six electrons which are located in the electron configuration of $1s^2\ 2s^2\ 2p^2$. The first orbital *1s* contains the electrons with lower potential energy and closest to the nucleus. Whereas, the electrons with higher potential energy are placed in the *2s* and *2p* orbitals which are responsible for interaction with other elements to produce different compounds by formatting bonds with other electrons. Holes and free electrons are the main charge carriers that pass between molecules. Organic materials become conjugated when they have sp2 hybridized carbons. In hybridization processes, two bonds types can be formed, sigma ($\boldsymbol{\sigma}$) which are single bonds created between carbon-carbon atoms and carbon-hydrogen atoms (localised electrons). While weakly couples Pi (π) bonds dominated the dislocated electrons. Figure 2.2 (a) illustrates the creation of sp^2 hybrid orbitals, while Figure 2.2 (b) shows an example of π -conjugated electron system structure in ethylene. $\boldsymbol{\sigma}$ bonds formatted the molecules' backbone with a potential energy of (> 10 eV) which is stronger than π bonds (< 4 eV) [17].

In organic semiconductors, there are two potential energy levels, the highest bonding energy level which is called Highest Occupied Molecular Orbital (HOMO) and the lowest anti-bonding level Lowest Unoccupied Molecular Orbital (LUMO). These (HOMO) and (LUMO) energy levels are similar to the highest energy level in valence band (E_V) and the lowest energy level in conduction band (E_C) in inorganic semiconductors, respectively [18].

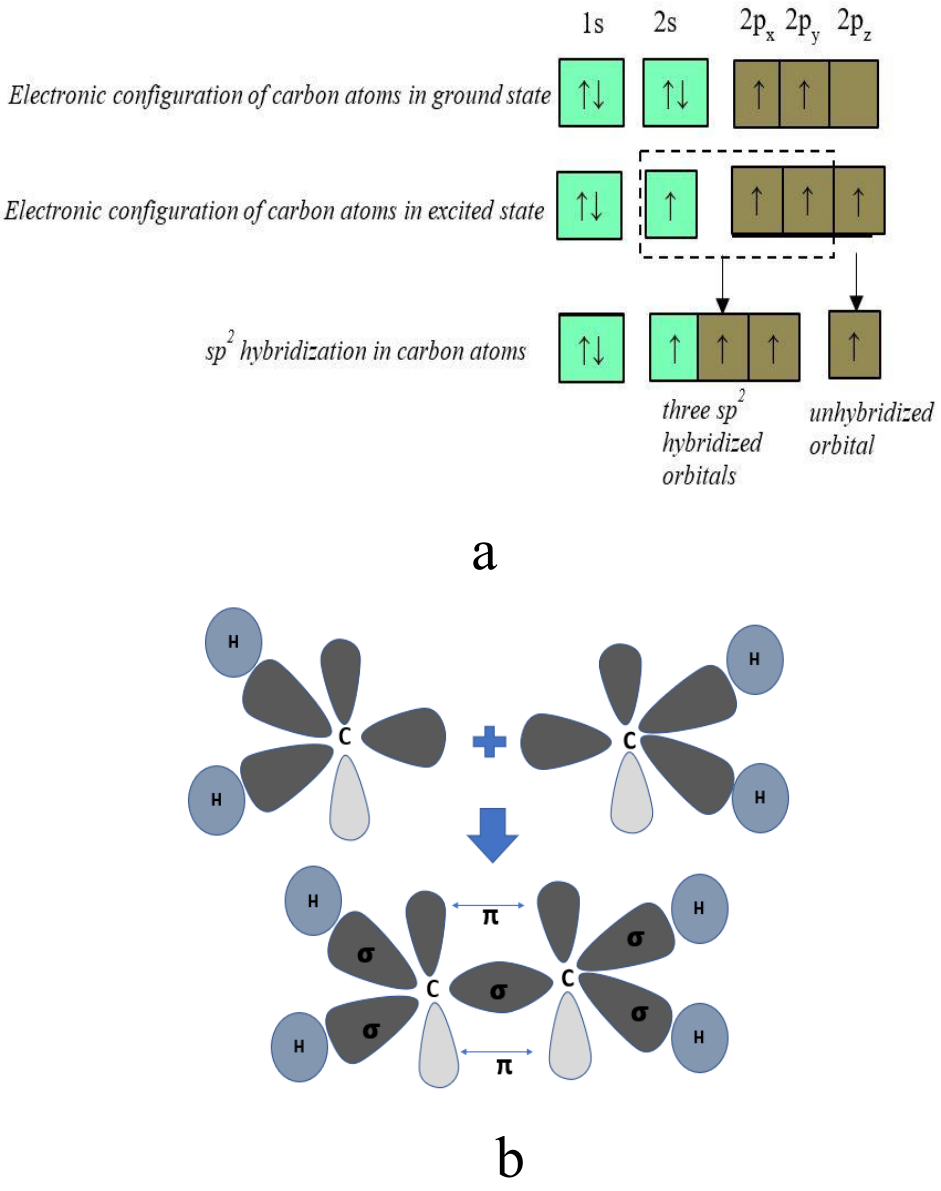

Figure 2. 2: *(a) Illustrates the electronic configuration of sp^2 hybridization. (b) The structure of conjugated π-electron as an example for ethylene.*

Because σ bonds nonreactive, they have a weak effect on the optoelectronic properties and a strong one on the molecular structure. The energy gap plays a significant role in organic semiconductors properties. Therefore, molecular orbitals are used to explain the energy gap properties [16].

For the interaction of two atomic orbitals, two new molecular orbitals will be formed; bonding orbital and antibonding orbital (stated with "*"). Bonding orbitals can be produced from the in-phase combination of two similar atomic orbitals, while antibonding orbitals are developed from the out-of-phase combination.

Bonding orbitals occupied with electrons while antibonding is empty making the molecular orbitals more stable. Antibonding orbitals π* represent the lowest unoccupied molecular orbitals (LUMO), while the highest occupied molecular orbitals (HOMO) are represented by π bonding orbitals. The orbitals of molecules can be limited by the HOMO-LUMO orbitals. The energy gap of the molecules is the main difference between HOMO and LUMO [18].

Similar to inorganic semiconductors, the conductivity of an intrinsic semiconductor can be altered by doping. Doping an organic semiconductor with an electron donor or acceptor will respectively produce an *n*-type or *p*-type semiconductor. An electron-transporting semiconductor (majority electrons) falls within the *n*-type category and a hole-transporting one (majority holes) belongs to the *p*-type group. Current organic semiconductor devices, however, are generally based on the intrinsic materials and one of the key reasons for this is the stability challenges associated with doping. Typically, device instability materializes as a result of diffusion of dopant ions or very small molecules. The diffusion of these small dopant molecules could cause malfunction of organic electronics devices. To realize device stability, the use of larger aromatic molecules (i.e. ones with strong π-electron donors or acceptors) are better choices for doping [17]. Akin to inorganic semiconductor doping, establishing mobile majority charge carriers involves introducing impurities (electron donors or acceptors) into the material. Dopants either accept electrons from the HOMO to create holes (*p*-type doping) or donate electrons to the LUMO energy levels to increase the electrons (*n*-type doping) [18-20].

The degree ordering of the chain is more important and the charge transporting in the solid state critically depends on it. Also, structural defects and chemical density affect charge transport properties [19-21]. This dependence can be recognised in the experimental characterisation of the organic thin-film transistor as the result of transport properties vary with the quality of the sample.

Shows in Figure 2.3 the molecular orbital with electronic order for the ground state (S_0), first excited state (S_1), and first triplet excited state (T_1). It shows that there are two electrons with an antiparallel spin which saturates the HOMO of the molecule in the ground state. Nevertheless, the LUMO band remains vacant until a state of agitation arises. To stimulate conduction in organic materials, an extra electron must be introduced to the LUMO band or an electron removed from the HOMO band [22]. When the excitation process occurs, an electron moves from the HOMO to the LUMO, where the additional or missing electron in the anti-bonding or bonding orbital, respectively, are compatible with the nature of the excited state. The injection or extraction at electrodes is one of the main processes to achieve conduction in such materials. In such materials due to the weak intermolecular bonds, delocalisation of charges is limited to few close molecules causing low charge mobility [10]. Under the effect of electric field or application of temperature, the carriers (electrons or holes) are moved in the case of the availability of similar energy levels [23].

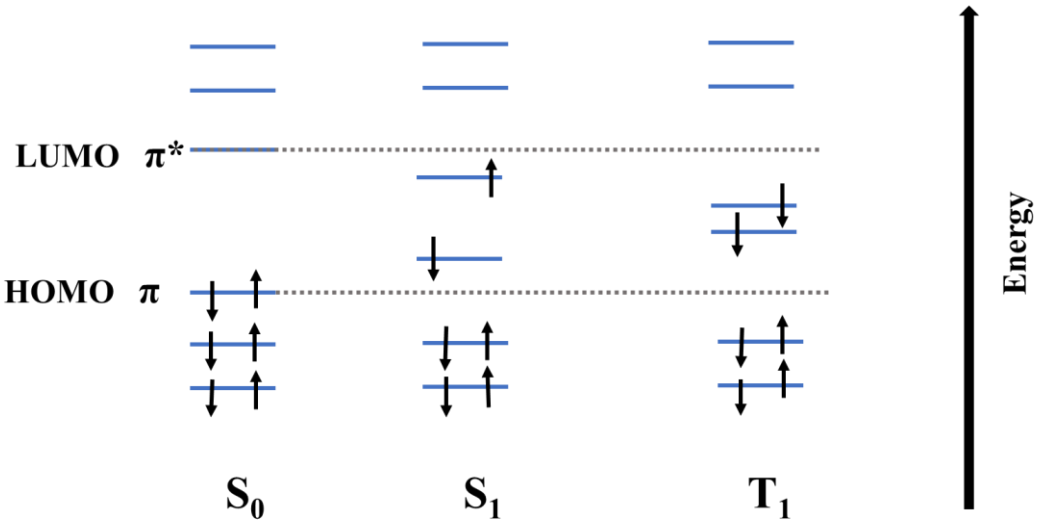

Figure 2. 3: *Molecular orbitals with electronic order for the ground state (S_0), first excited state (S_1), and first triplet excited state (T_1) in organic semiconductors.*

The doping in conventional semiconductors such as (Si) with a few parts per million of donor or acceptor impurities produces localised energy states in the bandgap close to the conduction and valence bands. Because of the low purity of organic materials, this kind of doping is not practical in organic semiconductors. Consequently, p-type organic semiconductors have energy alignment with the electrode and this results in better injection of the hole, whereas n-type semiconductors have a better alignment for the injection of electrons.

2.2.2 Polymeric and small molecular organic semiconductors.

Polymer and small-molecule semiconductors have an advantage in electronic organic because of their electrical and optical proprieties and low-cost fabrication with the capability of modified their polycrystalline films to improve charge transport [24,25]. In spite of discovering new organic materials, the development of these materials is an important role to improve charge transport properties, electronic structure and charge-charge interaction [26]. Depends on the molecular weight, organic semiconductors can be classified into two groups heterocyclic polymers which are of molecular weight more than 1000 and conjugated polycyclic compound with less than 1000 molecular weight [27]. Polymers can form with a large area thin film make them suitable materials for semiconductors. Nevertheless, they have poor solubility in organic solvents. Therefore, researchers use small molecules as semiconductors. The advantage of small molecules is the ability to modify the molecular parameters leads to enhance charge transport.

Unceasing efforts have been made to improve charge transport mechanisms and achieve higher carrier mobilities in polymers and organic small molecules. Within the backbone of polymers, torsion gives rise to disorder. As a result of such a disorder, the hopping mechanism is primarily responsible for charge transport, under which the applied voltage causes a charge carrier to jump, or more specifically ‘hop’ from one discrete level of energy to another. Figure 2.4 illustrate the electron transport via hopping between different energy levels. However, it remains uncertain as to what mechanism dominantly controls charge transport in small molecules. The disorder grade of energy levels tends to incline towards lower value, giving a vague image of any transport mechanism or possibly opening gates for another one.

2.3 Gate Dielectrics

In organic electronic devices such as the OTFTs, the boundary between the gate dielectric and the active layer acts as an important player by possessing the control of charge carriers flowing through it. This particularly active function of the interface has essentially resulted in the growing interest in improving dielectric materials as key principles when developing organic electronic devices. In a gate dielectric, important aspects such as the permittivity constant and the thickness of its film are indirectly responsible for determining the operating voltage of the device. Charge movement in organic thin film transistors is heavily stimulated by the mechanical and chemical properties of the insulator-semiconductor interface, which is regulated by another significant aspect known as the dielectric film roughness. The "decision-taking" activity is also influenced by additional important elements such as the process and groundwork of the insulating layer and the deposition process, besides the above mentioned factors. The classification of insulating materials can be under; inorganic, organic, multilayer, nanocomposite, and ultra-thin self-assembled monolayers (SAMs) materials. However, the focus of this study is on organic(polymeric) materials.

Inorganic materials such as tantalum oxide (Ta_2O_5) and titanium dioxide (TiO_2) are chosen as excellent examples of materials of high dielectric constants. Additionally, silicon dioxide (SiO_2) acts as an exceptional dielectric layer as a result of its thermodynamic stability and huge bandgap, besides the high dielectric constant value [28] Highly valuable qualities of short-chain length and dense packaging present in self-assembled monolayer (SAM) dielectric films has enabled them to be considered amongst the good dielectrics for organic electronics such as low-voltage OTFT [29]. These SAM dielectric films are otherwise usually used as surface treatments. It is possible to make crucial modifications to the surface of dielectric materials. The addition of a layer of multilayers insulating films makes it possible to improve the development of crystalline gains of a semiconductor as well as the roughness of its surface. These materials represent a category of dielectric layers comprising of organic or inorganic insulating materials. Namely, octadecyl-trimethoxysilane (OTMS) on zirconium oxide dielectrics, octadecyl-trichlorosilane (OTS) on silicon oxide, and alkyl phosphonic acid monolayers on alumina are excellent examples of such additives [30-32]. Also, the important objective of improving the field-effect mobility of OTFTs can be achieved by the addition of polymers such as polystyrene on the oxide layer [32,33].

An important highlight of the permittivity of organic insulators is that their frequency is dependent. However, it is not an unachievable task to alter this permittivity. The production of dielectric materials through the blending of ceramic and polymeric materials, such as nanocomposites, are capable of doing so. Studies and investigations in a number of recent decades have been widely focusing on inorganic dielectric materials, some of which are mentioned below along with their important characteristics:

2.3.1 Polymer dielectrics

Organic materials possessing the qualities of dielectric importance can be majorly classified as polymers. With the help of techniques such as spin-coating, inkjet printing or dip coating, it is possible to synthesise polymers. Initially, the first common polymers administered as insulating layers in organic electronics were poly(methyl methacrylate) (PMMA) and polystyrene (PS). The production of organic devices is also done using polymer dielectric materials such as poly(vinyl phenol) (PVP) and poly(vinyl alcohol) (PVA). Where they have superior insulating characteristics with neglected leakage currents. Furthermore, the cross-linking technique using some of the agents such as [1,6-bis (trichloro silyl) hexane (C6-Si) with PMMA or ammonium dichromate with PVA, will help improve the strength of these insulators and achieve the desired thermal stability, surface hardness and solvent resistance [34]. On the other hand, a number of reports have remarked research highlighting the enhanced characteristics of low leakage currents, insolubility and high capacitance in OTFTS with siloxane cross-linked ultra-thin polymeric films [35-38]]. Dielectric materials, in general, have low capacitance, so organic transistors based on them must run at relatively high voltages [39]. Table 2.1 illustrate the dielectric constant for most used organic and inorganic materials in electronic devices [40].

Table 2. 1: *Dielectric constant for some organic and inorganic materials.*

Organic Materials(Polymeric)	Dielectric constant	Inorganic Materials	Dielectric constant
PS (Polystyrene)	2.6, 2.4	SiO_2 (silicon dioxide)	3.5-4.5, 3.9
P4VP (poly (4-vinyl phenol)	2.6, 2.4	Si_3N_4 (silicon nitride)	6.2
PI (polyimide)	2.6	Al_2O_3 (aluminium oxide)	8.5-9
PMMA (polymethyl methacrylate)	3.6, 2.65-3.9, 3.3	MgO (magnesium oxide)	9.8
PVP (polyvinyl phenol)	3.8	ZrO_2 (zirconium oxide)	25, 17.5
PVC (polyvinyl chloride)	4.6	Ta_2O_3(tantalum pentoxide)	26
PVA (polyvinyl alcohol)	7.8	TiO_2	80

2.4 Metal-semiconductor interface

In metal-semiconductor contacts, there has been an assumption of low resistance. Such is the case of two connected metals. An Ohmic contact can be synthesised by assigning the value of Fermi energy level of a p-type semiconductor, to be less than or equal to the work function of the metal ($\varnothing_m$), as shown in figure 2.4 below which illustrate the energy band for metal and semiconductor before and after contact. It is important to note the location of the Fermi level, which is near the valence band (*E*v).

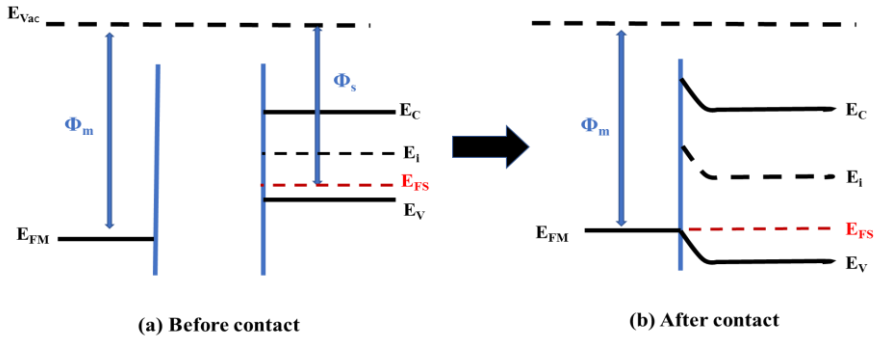

Figure 2. 4: *Energy band diagram of a p-type semiconductor (work function (Øs)) and a metal (work function ($\varnothing_m$)), (a) before contact and (b) directly after contact.*

The contact, whether Ohmic or rectifying, is identified on the basis of the Fermi energy level of the semiconductor (E_{FS}) and $\emptyset_m$. It is the characteristics of the interface between metal and semiconductor that the nature of this contact is depended upon. On the contrary, the Fermi level of n-type semiconductors must be higher than ∅m [41].

It can be seen that the two materials are brought into contact resulting in thermal equilibrium. A modest downward band bending in the semiconductor band structure aligned the Fermi levels. It also depicts the electrons increasing the number of holes in the interface as they travel into the metal from the semiconductor, while the electrons in the metal are capable of moving into empty states in the semiconductors [42].

2.5 Doping density

In organic semiconducting materials, the function of doping density is to primarily represent the number of free majority charge carriers that exist in semiconductor bulk. The Mott-Schottky analysis from the slope inverse of $1/Cm^2$ versus gate voltage, V_G, in the depletion region, can be performed to determine the doping density $(Na(w))$ as follows [43];

$$N_a(w) = -2[q\varepsilon_s \frac{d}{dV_G}(\frac{1}{C_m})^2]^{-1} \quad (2.1)$$

Herein, the depletion layer width is given by w.

The uniform distribution of dopants gives a straight line with a slope proportional to doping density. To consider dopants as acceptors, the slope of the plot must be positive. To consider dopants as donors, the slope of the plot must be negative.

2.6 Organic thin film transistor (OTFT) devices

The concept of thin film transistors began in the latter half of the 20th century. The successful development of the first TFT, by Le Comber, known as Si:H TFT, took place in 1979 after drawing inspiration from the first concept reported by Weimer in 1962 [44,45]. Since then, research and investigations have been continuously undertaken on organic thin film transistors (OTFTs), which have largely occupied multiple areas of electronic applications [46-49]. The formation of a channel in metal-oxide-semiconductor-field-effect-transistor (MOSFET) as a result of inversion of charge carriers close to the insulator-semiconductor

interface is the key highlight to differentiate it from OTFTs. The off-state and on-state, otherwise known as high channel resistance and low channel resistance respectively, occurs as a result of the application of voltage to the gate electrode. For a p-type semiconductor-based FETs, the depletion mode is activated when a positive voltage is applied leading to the depletion layer of charge carriers, resulting in an off-state. On the other hand, accumulation mode is activated when a negative voltage is applied leading to a large concentration of charge carriers, resulting in an on-state.

2.6.1 Device structures of OTFTs

Organic thin film transistors (OTFTs) can be structured or configured in four different ways. The first two methods involve assembling the gate at the bottom. Among them, the first technique is bottom-gate, bottom-contact (B-G, B-C) where the source and drain adjacent to the semiconductor layer, which is situated at the top place as shown in Figure 2.5 (a). The second way is bottom-gate, top-contact (B-G, T-C) herein, the source and drain above the semiconductor layer, Figure 2.5 (b). In the next two techniques of configuring OTFTs, the gate is situated at the top. Amongst these, the source and drain are located adjacent to the semiconductor, top-gate, bottom-contact (T-G, B-C) as in Figure 2.5 (c). Lastly, the semiconductor is at the bottom and the source and drain are above it, adjacent to the gate dielectric, top-gate, top-contact (T-G, T-C), as shown in Figure 2.5 (d).

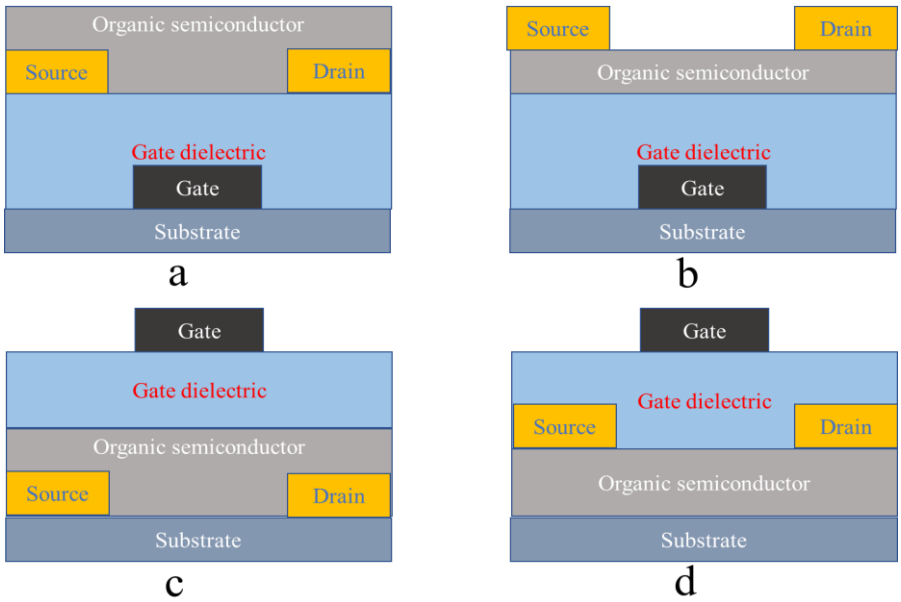

Figure 2. 5: *The four schematic diagrams configurations of OTFTs with (a) bottom-gate, bottom contact (BG-BC), (b) bottom-gate, top contact (BG-TC), (c) top-gate, bottom-contact (TG-BC) and (d) top-gate, top-contact (TG-TC).*

In between the semiconductor and the gate electrode, a dielectric layer must be present so as to separate them from each other. Also, factors such as the order of electrode and source-drain electrodes, their location at the top or bottom, and the presence of semiconductors and dielectric layers between them are possible aspects upon which the structural architecture of OTFTs depend upon. It is essential for charge carriers to be able to inject and retrieve between the source/drain electrodes and the semiconductor. Hence, it is required for the nature of the contact present to be Ohmic.

It is assumingly understandable that each of the structural architectures of OTFTs has its own benefits and downsides. For OTFTs having gate electrodes as the top layer, it is comparatively difficult to deposit the dielectric layer on the semiconductor in OTFT which has top layer gate electrode and bottom layer contact configuration. However, the advantage of the dielectric layer in this arrangement is that it performs an additional function of offering a passivation layer for the semiconductor, besides acting as a gate insulator. On the other hand, for OTFTs having an arrangement with the bottom layer as a gate electrode, the semiconductor occupies the top layer allowing the source and drain electrodes to be patterned through photolithographic methods. However, due to lower contact resistance, the OTFTs with top contact layer have a higher performance rate than OTFTs having bottom contact layer. The lower contact resistance mentioned here arises as a result of the increment in the contact area between the semiconductor and metal.

This study mainly focuses on the OTFTs with bottom-gate layer and top-contact layers arrangement. Basically, OTFTs with such structural architecture mainly operate through three-terminal devices; the gate, source, and drain. Firstly, the deposition of the gate electrode onto the substrate takes place. The next step involves separating the gate from the semiconductor, which is achieved using a dielectric layer. Lastly, the source and drain contacts are deposited on the semiconductor. Furthermore, a channel, or an uncovered semiconductor distance, separates drain and source from each other. These structural configurations are similar to the MIS capacitor as shown in Figure 2.6. For effective functioning, a direct current (DC) voltage is applied to the gate electrode. This results in a successful achievement of the control process for the flow of current when applying a gate-source voltage (V_{GS}) higher than a threshold voltage (V_T) to create the channel between source and drain contacts.

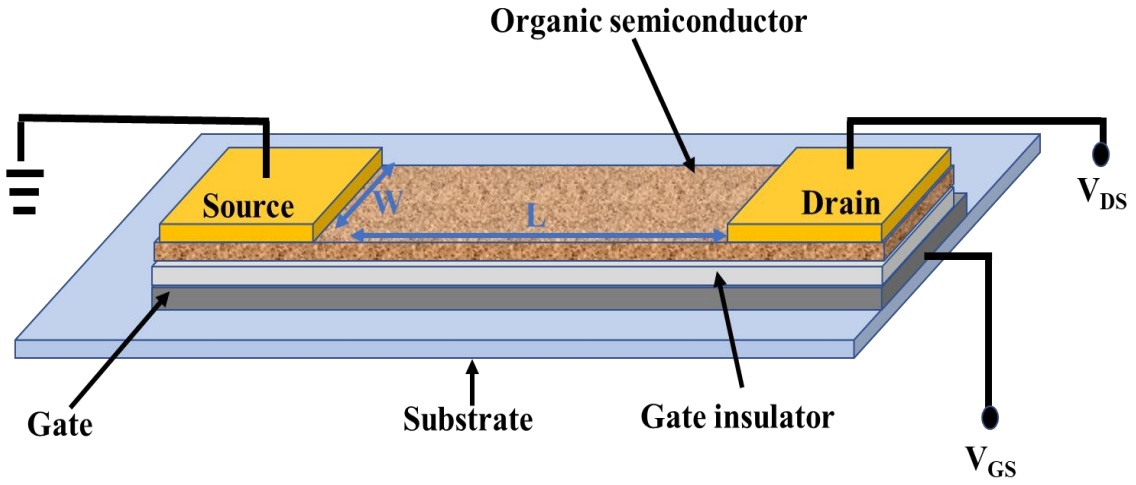

Figure 2.6: *Schematic structure of the bottom-gate, top-contact organic thin-film transistor OTFT.*

2.6.2 Electrical characteristics of OTFTs

In this study, organic thin film transistors are constructed based on p-type semiconductors. To control the conductivity of the transistor channel, the application of a negative gate-source voltage (V_{GS}) results in the accumulation of holes. The curves of drain-source current (I_{DS}) versus drain-source voltage (V_{DS}) occurrence takes place through this moderation of the accumulation layer. The output characteristics of a p-type transistor can be stated for different applied values of gate-source voltage (V_{GS}), the values of the drain-source current (I_{DS}) change as a function of the applied drain-source voltage (V_{DS}). At low V_{DS} ($V_{DS} < V_{GS}$), I_{DS} initially increases proportionally with V_{DS}, to help the device operate in the linear region as shown in Figure 2.7. In other words, this can be described as $I_{DS(lin)}$ related to the V_{DS} (as in equation 2.2 [50].

$$I_{DS(lin)} = \frac{WC_i}{L} \mu \left[V_{GS} - V_T - \frac{V_{DS}}{2}\right] V_{DS} \quad (2.2)$$

The operation in the saturation region, $V_{DS} \geq (V_{GS} - V_T)$

$$I_{DS(lin)} = \frac{WC_i}{L} \mu [V_{GS} - V_T] V_{DS} \quad (2.3)$$

Here, C_i = insulator capacitance per unit area, μ = field-effect mobility and V_T = threshold voltage which in definition can be stated as 'the value of the gate-source voltage that required for the transistor to be switched on' [51]. The presence of dopants or traps can effectively change the ideal value of threshold voltage, which is otherwise equal to zero in any ideal transistor.

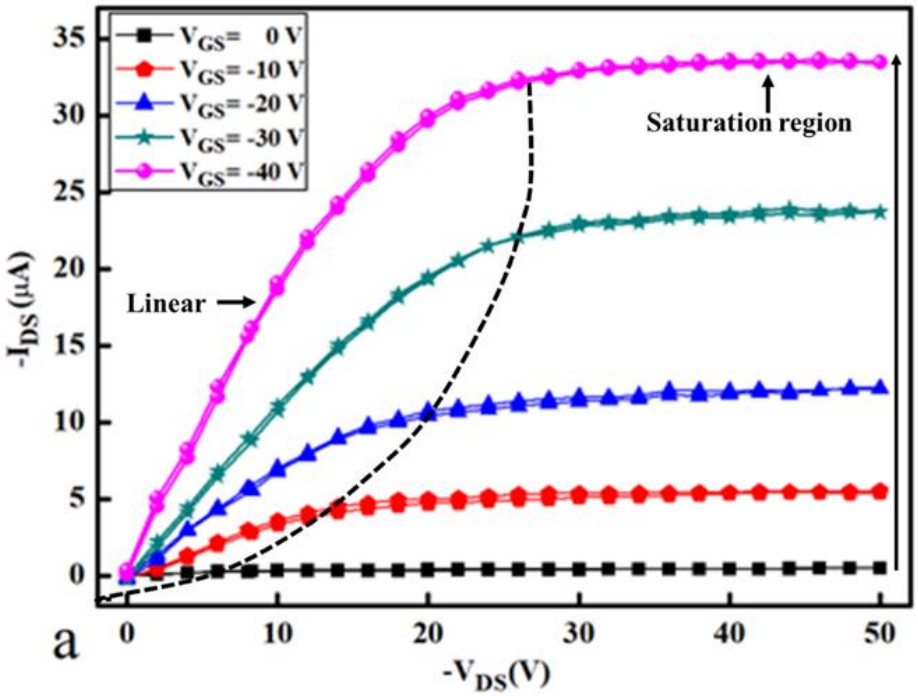

Figure 2. 7: *Output chractristics of a usual p-type-based OTFT, The black dashed line shows the channel pinch-off for OTFT.*

For a drain-source voltage V_{DS} value greater than (gate-source voltage V_{GS} - threshold voltage V_T), i.e. ($V_{DS} > V_{GS} - V_T$), the drain-source current saturates to 'pinch-off' the conductive channel. Here, it is important to note that I_{DS} do not depend on V_{DS}. This whole activity takes place in the saturated region, wherein, the saturated drain-source current, $I_{DS}(sat)$, can be given by [50];

$$I_{DS(sat)} = \frac{WC_i}{2L}\mu(V_{GS} - V_T)^2 \qquad (2.4)$$

In the saturated regime, μ_{lin}, the field-effect mobility can be estimated by rewriting equation 2.3 as;

$$\frac{\sqrt{I_{DS}}}{V_{GS}-V_T} = \sqrt{\left(\frac{WC_i\mu_{sat}}{2L}\right)} \tag{2.5}$$

The transfer characteristics can be known from the plot slope of $(I_{DS(sat)})^{1/2}$ versus gate-source voltage $V_{GS.}$ (represented by the black curve in figure 2.8). The figure below represents a plot in which the intercept on the voltage axis can be seen, which helps determine the threshold voltage. Moreover, the on/off current ratio (ratio between off-current and on-current) can be evaluated from the plot of $I_{DS}(sat)$ on a logarithmic scale versus V_{GS} (blue curve). This also denotes the switching performance of TFT. Lastly, the speed of I_{DS} ramping up with the increasing source-drain voltage can be identified from the remaining parameter, the subthreshold slope values (red colour in Figure 2.8). Also, the transfer curve in Figure 2.8 shows two ways of applied V_{GS} voltage (from -10 V to 50 V then back to -10V) with negligible or without hysteresis.

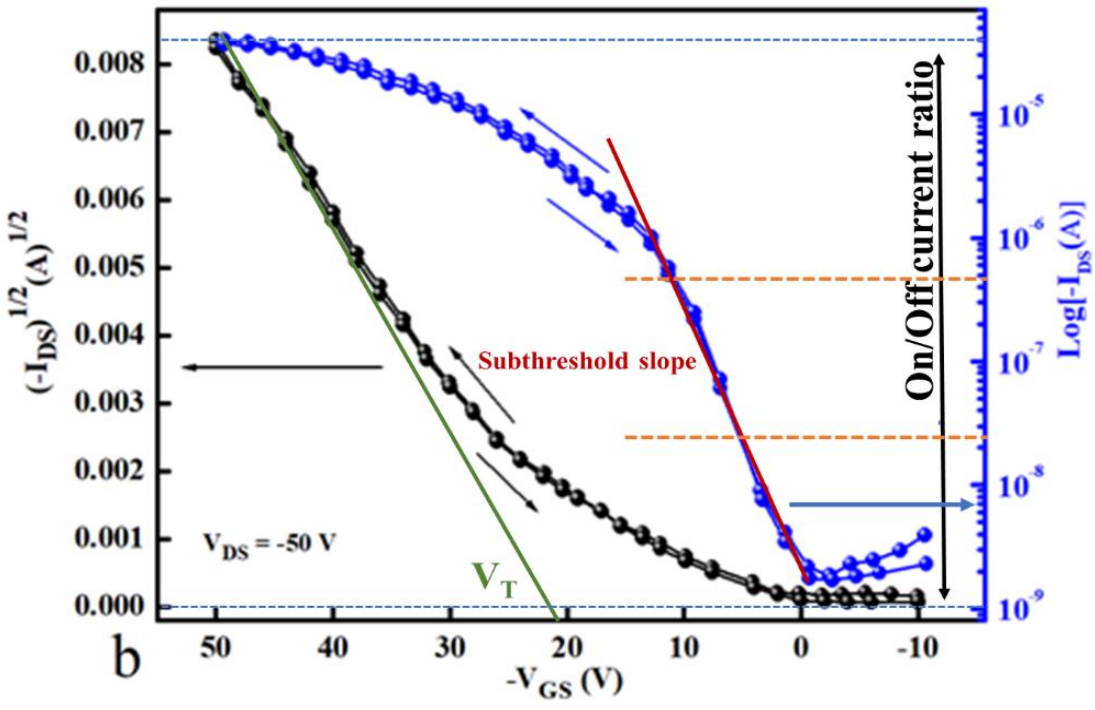

Figure 2. 8: *A typical p-type semiconductor based OTFT's transfer characteristics in the in the form of $I_{DS}^{1/2}$ (the black left axis) and I_{DS} on a logarithmic scale (the blue right axis) versus applied gate viltage V_{GS}.*

2.7 Organic non-volatile memory devices

The future of low-cost electronics has been mainly driven by organic non-volatile memory devices (ONVM). The ONVM device has also helped in reducing electronics to the least possible weight and increasing their flexibility [52-54]. The NVM can be categorised under a) floating gate memory, in which the addition of a thin layer of nanoparticles within the device insulator differentiates them from conventional devices such as MIS and TFTs, and b) charge-trapping, in which the metal gate and original dielectric have an extra memory stack between them. Integrated devices such as inductors, resistors, capacitors and transistors can be recognised under the second category.

The characteristic features mentioned can be achieved through ONVM devices based on OMIS and OTFT structures with a floating gate as these have the ability to integrate data processing and store a large amount of data. Specific features such as high switching speed, long retention time and large memory window were observed in nano-floating gate memories which are designed on the basis of transistor structure [55-62]. The following overviews on ONVM give us a better understanding and clarification, specifically focusing on floating gate memories devised on the basis of MIS capacitor and TFT structures.

2.7.1 Floating gate memories

ONVM devices based on OTFTs are capable of reading while keeping their memory state intact i.e. “non-destructive read-out”, which has made them especially attractive in the field of organic electronics. Also, it is possible to fabricate them in any integrated circuit or the same production line as OTFTs. The passive crossbar array of memory elements mostly possess the issue of sneak current (a very weak electric current that doesn’t damage the device immediately, but will burn out the device over time) , but the integration of ONVM devices with OTFTs settles this issue [63,71]. Several other extraordinary features of floating gate memories have resulted in manufacturing more than 90% of NVM production based on the floating gate principle [70]. The structural configuration in these devices is not very different from modified MIS and TFTs, wherein the internal gate acts as a semi-permanent charge storage unit, also known as ‘floating gate’. The basic structural assembly of non-volatile floating gate memory is based on the following two structures: a) thin-film transistor, and b) metal-insulator-semiconductor (MIS). For floating gate memory based on the first category (TFT), the insulating layer completely surrounds the metal layer, in which

the charges are stored. The transistor channel responsibly injects the charges into the floating gate causing the threshold voltage, V_T, to change, as a result of the application of sufficient voltage V_G. The charges stored in the floating gate can be discharged by applying reverse polarity [63]. Figure 2.9 illustrate the schematic structure of an organic thin film memory transistor (OTFMT) device based on a floating gate inserted between two insulating layers.

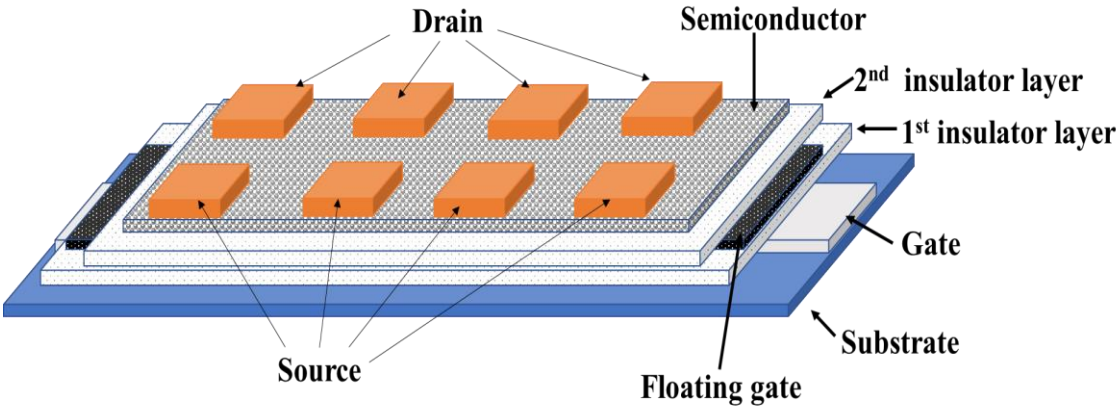

Figure 2. 9: *A schematic structure of OTFMT based on a floating gate.*

The latter half of the twentieth century witnessed the introduction of the first-ever nonvolatile floating gate memory device [72]. It was in the year 1967 when Kahng and Sze introduced the device, based on an n-type semiconductor of metal oxide semiconductor field-effect transistor (MOSFET) [72]. It can be seen that two insulators: insulator 1 (I_1) and 2 ($I2$), I_1 with a thickness of d_1 separating the floating metal gate (FG) from the semiconductor and I_2 with a thickness of d_2 between the FG and the external metal gate (G). Both insulators develop an electric field, E, after the external gate experiences a positive gate voltage, i.e. $V_G > 0$. This allows the device to activate accumulation mode, in which the electrons flow through I_1 into the FG. This occurs as a result of the conduction band of the semiconductor bending downwards as shown in Figure 2.10 which illustrates the energy band of a memory device based on a floating gate when applying different gate voltages V_{GS}; $0\ V > V_{GS}$, $V_{GS} = 0\ V$ and $V_{GS} < 0\ V$. In general, the current through the insulators is highly dependent on the electric field, and Fowler-Nordheim tunnelling is more likely to expertise it, by applying Gauss's law [73].

$$\varepsilon_1 E_1 = \varepsilon_2 E_2 + \mathrm{Q} \tag{2.6}$$

and

$$V_G = V_1 + V_2 = d_1E_2 + d_2E_2 \tag{2.7}$$

ε_1 = absolute permittivity of insulator 1 = $\varepsilon_0\ \varepsilon_{r1,}$ (where ε_0 is the permittivity of free space (a vacuum), which has a value of 8.85×10^{-12} Fm^{-1}, and $\varepsilon_{r1,}$ is the relative permittivity of insulator 1, more usually called the 'dielectric constant')

ε_2 = absolute permittivity of insulator 2 = $\varepsilon_0\ \varepsilon_{r2,}$ (ε_{r2} is the relative permittivity of insulator 2)

Q = stored charge in the floating gate (write step).

V_1 = voltage across insulator 1

V_2 = voltage across insulator 2

By solving the above equations (2.6 and 2.7), the electric field across insulators, e.g. E_1 in I_1, can be given by:

$$E_1 = \frac{V_G}{d_1+d_2\left(\frac{\varepsilon_1}{\varepsilon_2}\right)} + \frac{Q}{\varepsilon_1+\varepsilon_2\left(\frac{d_1}{d_2}\right)} \tag{2.8}$$

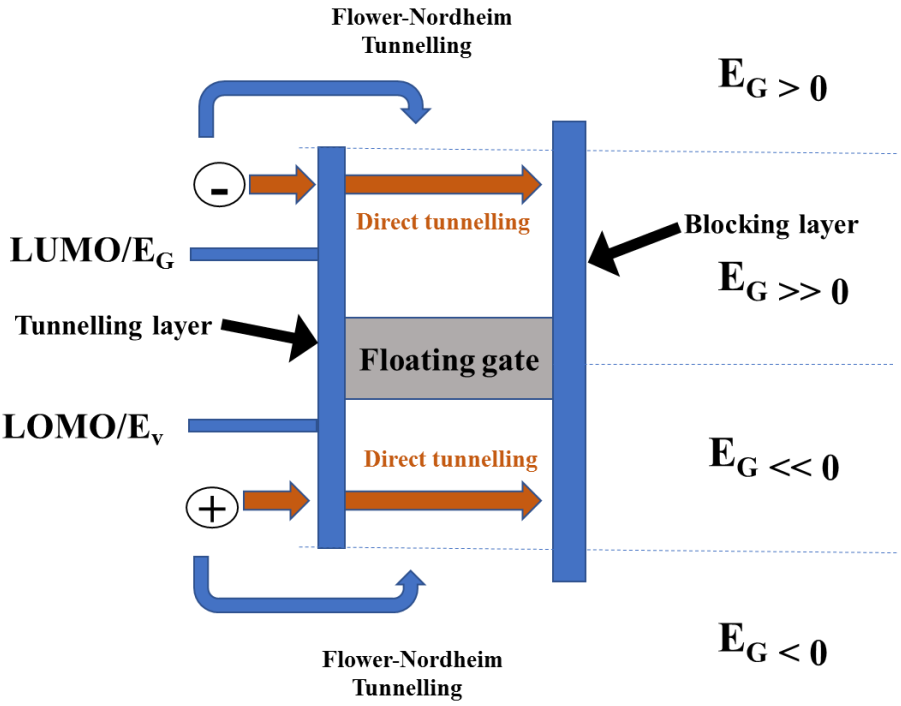

Figure 2. 10: *Schematic of energy band structure for a memory device based on a flating gate during appling different values of gate voltage V_G; $0 > V_G$, $V_G = 0$ and $V_G < 0$*

For the whole time of currents in two insulators are different, and continuous variation of charge of floating gate with time, with the application process of V_{GS} pending, we can have [70],

$$Q(t) = \int_0^t [J_1(E_1) - J_2(E_2)]dt \tag{2.9}$$

$Q(t)$ = the stored charge as a function of time t

J_1 = the current densities in insulator 1

J_2 = the current densities in insulator 2

Further, if the Fowler–Nordheim tunnelling represents the transfer of charge through the insulator, the J can be given as:

$$J = C_1 E^2 \exp\left(-\frac{E_0}{E}\right) \tag{2.10}$$

Here, C_1 and E_0 are constants.

The stored charge Q can be calculated from this point onwards using the current density. Assuming that $d_2 >> d_1$, when the external voltage V_{GS}, is removed after time t, there occurs a shift in the threshold voltage by an amount ΔV_T which is caused by Q and can be given as [70];

$$\Delta V_T = -\frac{d_2 Q}{\varepsilon_2} \tag{2.11}$$

The electrons stored in the floating gate are discharged due to the effective functioning of the erase step, which occurs as a result of applying a negative V_{GS} ($V_{GS} < 0$). It is possible to leave the floating gate completely free of electrons and with a positive charge by applying enough negative V_{GS}.

2.7.2 Characterisation of floating gate memory devices

2.7.2.1 Write/Erase processes

The conductivity of the device, if possibly changed in a non-destructive method, has the ability to enable memory cells to store information so as to keep it autonomous from external conditions and keep its states changeable (from “programmed, 0” to “erased, 1”). Such quality of the memory cells, in other words, can be expressed as, the amount of stored or removed charges in or from the floating gate, respectively, determines the magnitude of change in threshold voltage, V_T, from a high to low state [70]. This particular mechanism occurs for floating gate memories based on n-type channel semiconductors, whereas in the p-type channel, the functioning mechanism is vice-versa.

The plot of the drain-source current (I_{DS}) versus gate-source voltage (V_{GS}) at a constant drain-source voltage (V_{DS}) simplifies the understanding of write and erase processes for a floating gate memory device, shown in Figure 2.11 (a) for a p-type and (b) for n-type semiconductor channel respectively [63].

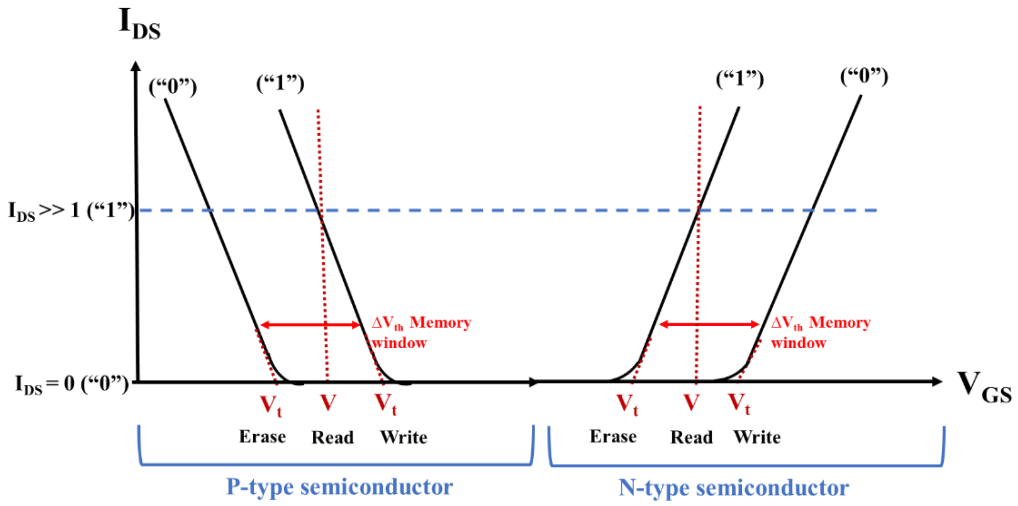

Figure 2. 11: *The operation of write and erase of memory device based on a floting gate for (a) p-type and (b) n-type semiconductor channel.*

It can be clearly seen in the figure that there is a shifting in threshold voltage, V_T, from the initial device state to the charged floating gate state. As a result of the shift, a memory window is created signifying the capability of memory devices to the storage of charges. The logic data "1" for write and "0" for erase of the p-type channel floating gate memory is represented by two diverse current states: a high current ($I_{DS} >> 1$) and a low current ($I_{DS} = 0$), respectively. If the floating gate memory is based on an n-type channel, the mechanism is reversed. When the values of programmed and erased V_T possess the value of applied voltage V_G between them, the "read" process proceeds without ignoring to value the flow of current within the device.

2.7.2.2 Retention properties

Measurement of estimation of time taken to unload the floating gates' information gives retention. The shift in the threshold voltage of memory cell, as a result of charge loss, is dependent on the equation below [107]

$$dQ_{FG} = C_{FG}\, dV_T \tag{2.12}$$

Here,

dQ_{FG} = charge loss of floating gate

C_{FG} = capacitance of floating gate

dV_T = the floating gate threshold voltage shift

Regarding retention, it can also be concluded that it is a time value save by a non-volatile memory cell, irrespective of the power of the floating gate. It is possible that the gate defects and mobile ions cause a leakage of stored charges in the floating gate. The leakage may happen through the insulator or the external gate [74]. Several mechanisms such as thermionic emission, electron de-trapping, or contamination can lead to the loss of charges [74-76]. On the contrary, factors such as dielectric materials and gate quality are very much capable of improving the retention features of memory cells [76].

2.8 Gas sensing

The behaviour of a gas sensor is labelled by the response factor (R) of a TFT parameter; current mobility (μ), threshold voltage (V_T) and on/off current ratio ($I_{ON/off}$) at particular bias voltage (V_{GS}) as:

$$R = \frac{\Delta X}{X_o} \tag{2.13}$$

Where ΔX is the distinction between the parameter derived at a particular gaseous analyte concentration (C) and its amount at a reference gas (e.g. an inert gas or atmospheric air, where C = 0 ppm). In contrast, Sensitivity (S), is characterised as:

$$S = \frac{dR}{dC} \tag{2.14}$$

The approximation of this gas sensing parameter (S) is generally obtained by the slope from a linear fit of the R versus C plot within a particular concentration interval. Furthermore, the limit of detection (LOD) can be estimated from the intercept of that line with the concentration axis with a zero response. There are two more parameters linked to timing since the sensor response doesn't befall instantly. For ΔX to differ from 10% to 90% of its value, the interval needed is the onset time (t_{set}). Calculating the reset time (t_{reset}) is the same way, only that X differs from its value at a particular C to its value at the reference atmosphere.

Organic semiconductors are sensitive to the chemicals in the environment, which is dependent on the type and concentration of the chemical analyte. As for the gas sensing motives, a usual mechanism of detection states that the chosen analyte molecule may act on the charge carriers within the semiconductor sensing layer by either impurities (generating electrons or holes) or traps. Since most of the semiconductors act as a p-type, the nearby electron-donating molecules affect and reduce the charge carrier density, which is increasing the sensing layer resistivity. However, electron-withdrawing molecules led to decreasing of the sensing layer resistivity by increasing the charge density. Otherwise, the sensing layer may be only polarized by the analyte molecule and can be detected by a capacitive current. Therefore, the incidence of each mechanism depends on the operation conditions, such as temperature and voltage bias. Whereas, analyte adsorption and charge carrier are exceedingly dependent on these parameters.

To produce any gas vapour, there is a need for inert gas as a gas carrier such as nitrogen. To produce alcohol vapour, a flow rate (F_1 ml.min^{-1}) of nitrogen is passing over a vial contain alcohol solvent at room temperature ($23\ ^0C \pm 1\ ^0C$) and under atmospheric pressure as shown in Figure 2.12. Then the concentration of alcohol vapour C_1 can be calculated using equation (3.3) [77].

$$C_1 = \frac{P\,\rho}{F_1} \tag{2.15}$$

Herein,

P is the permeation rate,

ρ is the reciprocal vapour density of alcohol,

and F_1 is the nitrogen gas flow rate.

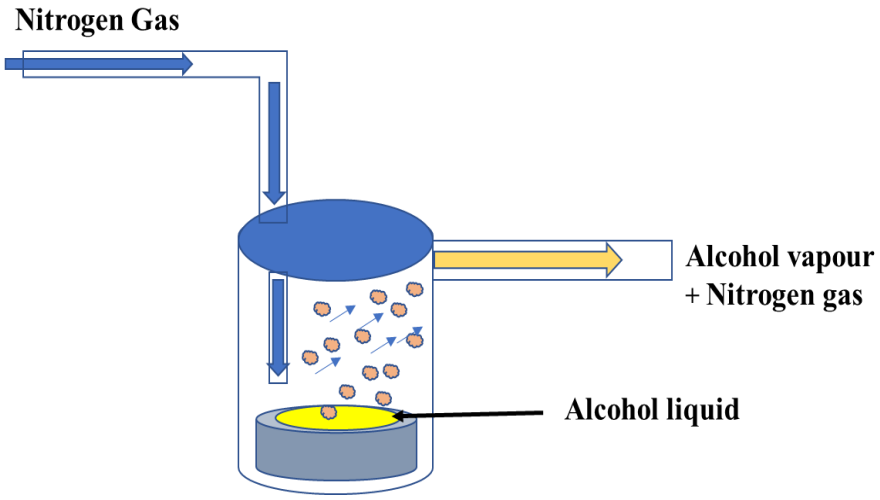

Figure 2. 12: *Schematic diagram shows producing alcohol vapour with a nitrogen currier gas.*

For different alcohol vapour concentration, another nitrogen streaming of a flow rate F_2 can be mix with the original alcohol vapour which is working as a diluting gas and the final alcohol concentration can be determined using equation (2.16);

$$C = C_1 \frac{F_1}{F_1 + F_2} \tag{2.16}$$

Where C is the alcohol vapour concentration under the test, F_2 is the flow rate of the dilution stream. (*More details for the gas sensing system in section 3.5.4, chapter 3*)

2.9 References

[1] X. Peng, G. Horowitz, D. Fichou, and F. Garnier, “All organic thin film transistors made of alphasexithienyl semiconducting and various polymeric insulating layers,” vol. 2013, no. 1990, pp. 17–20, 2013, doi: 10.1063/1.103994

[2] Y. Yuan, G. Giri, A. L. Ayzner, A. P. Zoombelt, S. C. B. Mannsfeld, J. Chen, D. Nordlund, M. F. Toney, J. Huang, and Z. Bao, “Ultra-high mobility transparent organic thin film transistors grown by an off-centre spin- coating method Ultra-high mobility transparent organic thin film transistors grown by an off-centre spin-coating method,” *Nat. Commun.*, vol. 5, no. January, pp. 1–9, 2014.

[3] A. Shih, “Flexible and Solution-Processed Organic Thin Film Transistors for High Voltage Applications,” no. 2008, 2018.

[4] C. T. Chen, “Evolution of red organic light-emitting diodes: Materials and devices,” *Chem. Mater.*, vol. 16, no. 23, pp. 4389–4400, 2004, doi: 10.1021/cm049679m.

[5] Y. Karzazi, “Organic light emitting diodes: Devices and applications,” *J. Mater. Environ. Sci.*, vol. 5, no. 1, pp. 1–12, 2014.

[6] M. F. Mabrook, Y. Yun, C. Pearson, D. A. Zeze, and M. C. Petty, “Charge storage in pentacene/polymethyimethacrylate memory devices,” *IEEE Electron Device Lett.*, vol. 30, no. 6, pp. 632–634, 2009, doi: 10.1109/LED.2009.2018128.

[7] Y. Park, K. J. Baeg, and C. Kim, “Solution-Processed Nonvolatile Organic Transistor Memory Based on Semiconductor Blends,” *ACS Appl. Mater. Interfaces*, vol. 11, no. 8, pp. 8327–8336, 2019, doi: 10.1021/acsami.8b20571.

[8] J. Hou and X. Guo, “Active Layer Materials for Organic Solar Cells,” *Green Energy Technol.*, vol. 128, no. November, pp. 17–42, 2013, doi: 10.1007/978-1-4471-4823-4_2.

[9] S. Sumaiya, K. Kardel, and A. El-Shahat, “Organic Solar Cell by Inkjet Printing—An Overview,” *Technologies*, vol. 5, no. 4, p. 53, 2017, doi: 10.3390/technologies5030053.

[10] K. Wetchakun, T. Samerjai, N. Tamaekong, C. Liewhiran, C. Siriwong, V. Kruefu, A. Wisitsoraat, A. Tuantranont, and S. Phanichphant, “Semiconducting metal oxides as sensors for environmentally hazardous gases,” *Sensors Actuators, B Chem.*, vol. 160, no. 1, pp. 580–591, 2011.

[11] Y. Chen, X. Kong, G. Lu, D. Qi, Y. Wu, X. Li, M. Bouvet, D. Sun, and J. Jiang, "The lower rather than higher density charge carrier determines the NH 3 -sensing nature and sensitivity of ambipolar organic semiconductors," *Mater. Chem. Front.*, vol. 2, no. 5, pp. 1009–1016, 2018.

[12] S. Yuvaraja, A. Nawaz, Q. Liu, D. Dubal, S. G. Surya, K. N. Salama, and P. Sonar, "Organic field-effect transistor-based flexible sensors," *Chem. Soc. Rev.*, vol. 49, no. 11, pp. 3423–3460, 2020.

[13] O. L. Griffith, J. E. Anthony, A. G. Jones, Y. Shu, and D. L. Lichtenberger, "Substituent effects on the electronic characteristics of pentacene derivatives for organic electronic devices: Dioxolane-substituted pentacene derivatives with triisopropylsilylethynyl functional groups," *J. Am. Chem. Soc.*, vol. 134, no. 34, pp. 14185–14194, 2012, doi: 10.1021/ja3056672.

[14] W. Brütting and C. Adachi, *Physics of Organic Semiconductors: Second Edition*. 2013.

[15] F. Cacialli, "Organic semiconductors for the new millennium," *Philos. Trans. R. Soc. A Math. Phys. Eng. Sci.*, vol. 358, no. 1765, pp. 173–192, 2000, doi: 10.1098/rsta.2000.0526.

[16] J. Cornil, S. Verlaak, N. Martinelli, A. Mityashin, Y. Olivier, T. Van Regemorter, G. D'Avino, L. Muccioli, C. Zannoni, F. Castet, D. Beljonne, and P. Heremans, "Exploring the energy landscape of the charge transport levels in organic semiconductors at the molecular scale," *Acc. Chem. Res.*, vol. 46, no. 2, pp. 434–443, 2013.

[17] R. Jaiswal, M. Menon, "Polymer electronic materials: a review of charge transport," Polymer International, vol. 55, pp. 1371–1384, 2006..

[18] M. E. SantosMiranda, C. Marcolla, C. A. Rodriguez, H. M. Wilhelm, M. R. Sierakowski, T. M. BelleBresolin, and R. Alves de Freitas, "I . The role of N-carboxymethylation of chitosan in the thermal stability and dynamic," *Polym Int*, vol. 55, no. December 2005, pp. 961–969, 2006.

[19] D. Fichou, "Structural order in conjugated oligothiophenes and its implications on opto-electronic devices," *J. Mater. Chem.*, vol. 10, no. 3, pp. 571–588, 2000, doi:

10.1039/a908312j.

[20] J. G. Laquindanum, H. E. Katz, A. J. Lovinger, and A. Dodabalapur, "Morphological Origin of High Mobility in Pentacene Thin-Film Transistors," *Chem. Mater.*, vol. 8, no. 11, pp. 2542–2544, 1996, doi: 10.1021/cm9603664.

[21] D. J. Gundlach, Y. Y. Lin, T. N. Jackson, S. F. Nelson, and D. G. Schlom, "Pentacene organic thin-film transistors - Molecular ordering and mobility," *IEEE Electron Device Lett.*, vol. 18, no. 3, pp. 87–89, 1997, doi: 10.1109/55.556089.

[22] H. K. A. Bassler, "Charge transport in organic semiconductors," *Top. Curr. Chem.*, vol. 312, pp. 1–66, 2011.

[23] S. M. Sze, "Semiconductor Devices: Physics and Technology," *John Wiley Sons*, 1985.

[24] J. E. Coughlin, Z. B. Henson, G. C. Welch, and G. C. Bazan, "Design and synthesis of molecular donors for solution-processed high-efficiency organic solar cells," *Acc. Chem. Res.*, vol. 47, no. 1, pp. 257–270, 2014, doi: 10.1021/ar400136b.

[25] H. S. Nalwa, "Handbook of Organic Conductive Molecules and Polymers, Charge-Transfer Salts, Fullerenes and Photoconductors." p. 828, 1997.

[26] C. Wang, H. Dong, W. Hu, Y. Liu, and D. Zhu, "Semiconducting π-conjugated systems in field-effect transistors: A material odyssey of organic electronics," *Chem. Rev.*, vol. 112, no. 4, pp. 2208–2267, 2012, doi: 10.1021/cr100380z.

[27] H. E. Katz, Z. Bao, and S. L. Gilat, "Synthetic chemistry for ultrapure, processable, and high-mobility organic transistor semiconductors," *Acc. Chem. Res.*, vol. 34, no. 5, pp. 359–369, 2001, doi: 10.1021/ar990114j.

[28] Z. Bao, and J. Locklin, Organic Field-Effect Transistors. CRC Press, Boca Raton, 2007.

[29] M. A. Hussein, "Role of Cross-Linking Process on the Performance of PMMA," *Int. J. Biosens. Bioelectron.*, vol. 3, no. 3, pp. 279–284, 2018, doi: 10.15406/ijbsbe.2017.03.00065.

[30] B. Kumar, B. K. Kaushik, and Y. S. Negi, "Perspectives and challenges for organic thin film transistors: Materials, devices, processes and applications," *J. Mater. Sci. Mater. Electron.*, vol. 25, no. 1, pp. 1–30, 2014, doi: 10.1007/s10854-013-1550-2.

[31] J. Namieśnik, "Generation of standard gaseous mixtures," *J. Chromatogr. A*, vol.

300, no. C, pp. 79–108, 1984, doi: 10.1016/S0021-9673(01)87581-6.

[32] T. W. Kelley, L. D. Boardman, T. D. Dunbar, D. V. Muyres, M. J. Pellerite, and T. P. Smith, "High-Performance OTFTs Using Surface-Modified Alumina Dielectrics," J. Phys. Chem. B, vol. 107, pp. 5877–5881, 2003.

[33] Y. -Y. Lin, D. J. Gundlach, S. F. Nelson, and T. N. Jackson, "Stacked Pentacene Layer Organic Thin-film Transistors with Improved Characteristics," *IEEE Electron Device Lett*., Vol. 18, No. 12, pp. 606–608, 1997.

[34] J. -M. Kim, J. -W. Lee, J. -K. Kim, B. -K. Ju, J. -S. Kim, Y. -H. Lee, and M. -H. Oh, "An organic thin-film transistor of high mobility by dielectric surface modification with organic molecule," *Appl. Phys. Lett*., vol. 85, pp. 6368–6370, 2004.

[35] L. A. Majewski, R. Schroeder, and M. Grell, "One Volt Organic Transistor," *Adv. Mater*., vol. 17, pp. 192–194, 2005.

[36] S. E. Fritz, T. W. Kelley, and C. D. Frisbie, "Effect of Dielectric Roughness on Performance of Pentacene TFTs and Restoration of Performance with a Polymeric Smoothing Layer," *J. Phys. Chem. B*, vol. 109, pp. 10574–10577, 2005.

[37] F. -C. Chen, C. -W. Chu, J. He, Y. Yang, and J. -L. Lin, "Organic thin-film transistors with nanocomposite dielectric gate insulator," *Appl. Phys. Lett*., vol. 85, pp. 3295–3297, 2004.

[38] A. Facchetti, M. -H. Yoon, and T. J. Marks, "Gate Dielectrics for Organic Field-Effect Transistors: New Opportunities for Organic Electronics," *Adv. Mater*., vol. 17, pp. 1705–1725, 2005.

[39] M. -H. Yoon, H. Yan, A. Facchetti, and T. J. Marks, "Low-Voltage Organic Field-Effect Transistors and Inverters Enabled by Ultrathin Cross-Linked Polymers as Gate Dielectrics," *J. Am. Chem. Soc*., vol. 127, pp 10388–10395, 2005.

[40] Y. -Y. Noh, N. Zhao, M. Caironi, and H. Sirringhaus, "Downscaling of self-aligned, all-printed polymer thin film transistors," *Nat. Nanotechnol*., vol. 2, pp. 784–789, 2007.

[41] Y. -Y. Noh, and H. Sirringhaus, "Ultra-thin polymer gate dielectrics for top-gate polymer field-effect transistors," *Org. Electron*., vol. 10, pp. 174–180, 2009.

[42] E. H. Rhoderick, Metal-semiconductor Contact. Oxford University Press, 1978.

[43] Bart Van Zeghbroeck (2007), Principles of semiconductor devices. Electronic resource: htpp://ecee.colorado.edu/~bart/book/. Last access on 2011.

[44] S. M. Sze and K. K. Ng, Physics of semiconductor devices. Wiley-Blackwell, 2007.

[45] E. H. Nicollian and J. R. Brews, MOS Metal Oxide Semiconductor Physics and Technology. New York: Wiley, 1982.

[46] E. J. Meijer, A. V. G. Mangnus, C. M. Hart, D. M. de Leeuw, and T. M. Klapwijk, "Frequency behaviour and the Mott-Schottky analysis in poly(3- hexyl thiophene) metal-insulator-semiconductor diodes," *Appl. Phys. Lett*., vol. 78, pp. 3902–3904, June 2001.

[47] I. Torres, and D. M. Taylor, "Interface states in polymer metal-insulator-semiconductor devices," J. Appl. Phys., vol. 98, 073710–073718, 2005.

[48] S. A. Jenekhe, "Special issue of organic electronics," *Chem. Mater*., vol. 16, pp. 4381–4382, 2004.

[49] C. D. Dimitrakopoulos, and P. R. L. Malenfant, "Organic Thin Film Transistors for Large Area Electronics," *Adv. Mater*., vol. 14, pp. 99–117, 2002.

[50] M. Berggren, D. Nilsson, and N. D. Robinson, "Organic materials for printed electronics," *Nat. Mater*., vol. 6, 3–5, 2007.

[51] G. H. Gelinck, H. E. A. Huitema, E. van Veenendaal, E. Cantatore, L. Schrijnemakers, J. B. P. H. van der Putten, T. C. T. Geuns, M. Beenhakkers, J. B. Giesbers, B. H. Huisman, E. J. Meijer, E. M. Benito, F. J. Touwslager, A. W. Marsman, B. J. E. van Rens, and D. M. de Leeuw, "Flexible active-matrix displays and shift registers based on solution-processed organic transistors," *Nat. Mater*., vol. 3, pp. 106–110, 2004.

[52] P. K. Weimer, "The TFT-a new thin-film transistor," *Proc. IRE.*, vol. 50, pp. 1462–1470, 1962.

[53] P.G. Le Comber, W. E. Spear, and A. Ghaith, "Amorphous-silicon Field-Effect Devices and possible applications," *Electron. Lett.*, vol. 15, pp. 179–182, 1979.

[54] F. Ebisawa, T. Kurokawa, and S. Nara, "Electrical properties of polyacetylene/polysiloxane interface," *J. Appl. Phys.*, vol. 54, pp. 3255–3259, 1983.

[55] K. Kudo, M. Yamashina, T. Moriizumi, "Field Effect Measurement of Organic Dye Films," *Jpn. J. Appl. Phys.*, vol. 23, pp. 130–130, 1984.

[56] A. Tsumura, H. Koezuka, and T. Ando, "Macromolecular electronic device: Field-effect transistor with a polythiophene thin film," *Appl. Phys. Lett.*, vol. 49, pp. 210–212, 1986.

[57] T. Mori, "Molecular materials for organic field-effect transistor," *J. Phys.: Condens. Matter*, vol. 20, pp. 184010-1–184010-13, 2008.

[58] E. J. Meijer, C. Tanase, P. W. M. Blom, E. van Veenendaal, B. -H. Huisman, D. M. de Leeuw, and T. M. Klapwijk, "Switch-on voltage in disordered organic field-effect-transistors," *Appl. Phys. Lett.*, vol. 80, pp. 3838–3840, 2002.

[59] S. R. Forrest, "The path to ubiquitous and low-cost organic electronic appliances on plastic," *Nature*, vol. 428, pp. 911–918, 2004.

[60] T. Sekitani, T. Yokota, U. Zschieschang, H. Klauk, S. Bauer, K. Takeuchi, M. Takamiya, T. Sakurai, and T. Someya, "Organic Nonvolatile Memory Transistors for Flexible Sensor Arrays," *Science*, 326, pp. 1516–1519, 2009.

[61] Y. L. Guo, G. Yu, and Y. Q. Liu, "Functional Organic Field-Effect Transistors," *Adv. Mater.*, vol. 22, pp. 4427–4447, 2010.

[62] P. Heremans, G. H. Gelinck, R. Muller, K. J. Baeg, D. Y. Kim, and Y. Y. Noh, "Polymer and Organic Nonvolatile Memory Devices," *Chem. Mater.*, vol. 23, pp. 341–344, 2011.

[63] W. L. Leong, N. Mathews, B. Tan, S. Vaidyanathan, F. Dotz, and S. Mhaisalkar, "Towards printable organic thin film transistor based flash memory devices," *J. Mater. Chem.*, vol. 21, pp. 5203–5214, 2011.

[64] X. J. She, C. H. Liu, Q. J. Sun, X. Gao, and S. D. Wang, "Morphology control of tunneling dielectric towards high-performance organic field-effect transistor nonvolatile memory," *Org. Electron.*, vol. 13, pp. 1908–1915, 2012.

[65] S. T. Han, Y. Zhou, Z. X. Xu, V. A. L. Roy, and T. F. Hung, "Nanoparticle size dependent threshold voltage shifts in organic memory transistors Nanoparticle size dependent threshold voltage shifts in organic memory transistors," *J. Mater. Chem.*, vol. 21, pp. 14575–14580, 2011.

[66] K. J. Baeg, Y. Y. Noh, H. Sirringhaus, and D. Y. Kim, "Controllable Shifts in Threshold Voltage of Top-Gate Polymer Field-Effect Transistors for Applications in Organic Nano Floating Gate Memory," *Adv. Funct. Mater.*, vol. 20, pp. 224–230, 2010.

[67] Y. M. Kim, S. J. Kim, and J. S. Lee, "Organic-Transistor-Based Nano-Floating-Gate Memory Devices Having Multistack Charge-Trapping Layers," *IEEE Electron Device Lett.*, vol. 31, pp. 503-506, 2010.

[68] W. Wang and D. G. Ma, "Organic floating-gate transistor memory based on the structure of pentacene/nanoparticle-Al/Al2O3," *Appl. Phys. Lett.*, vol. 96, pp. 203304-1–203304-3, 2010.

[69] C. W. Tseng, and Y. T. Tao, "Electric Bistability in Pentacene Film-Based Transistor Embedding Gold Nanoparticles," *J. Am. Chem. Soc.*, vol. 131, pp. 12441–12450, 2009.

[70] P. Pavan, L. Larcher, and A. Marmiroli, Floating gate devices: operation and compact modelling. Boston, U.S.A.: Kluwer Academic Poblishers, 2004.

[71] R. C. G. Naber, K. Asadi, P. W. M. Blom, D. M. de Leeuw, B. de Boer, "Organic Nonvolatile Memory Devices Based on Ferroelectricity," *Adv. Mater.*, vol. 22, pp. 933–945, 2010.

[72] S. -J. Kim, Y. -S. Park, S. -H. Lyu, and J. -S. Lee, "Nonvolatile nano-floating gate memory devices based on pentacene semiconductors and organic tunneling insulator layers," *Appl. Phys. Lett*., vol. 96, pp. 033302-1–033302-3, 2010.

[73] D. Kahng, and S. M. Sze, "A floating-gate and its application to memory devices," *The Bell System Technical Journal*, vol. 46, pp. 1288–1291, 1967.

[74] S. M. Sze, Physics of Semiconductor Devices. 2nd Edition. A Wiley-Interscience, 1981.

[75] R. E. Shiner, Data retention in EPROMs. Proceedings IRPS, 238, 1980.

[76] N. Mielke, New EPROM data-loss mechanisms. Proceedings IRPS, 106, 1983.

[77] J. -S. Lee, "Review Paper: Nano-Floating Gate Memory Devices," *Electronic Materials Letters*, vol. 7, pp. 175–183, 2011.

Chapter 3

Materials and Experimental Techniques

3.1 Introduction

This chapter explains the materials and experimental techniques used during this work. Different materials were used to fabricate organic thin-film transistors (OTFTs) such as metals, insulators, and semiconductors. The experimental technique involves different methods to deposit the metal gate, gate insulator and the semiconductor active layer, for instant thermal evaporation, off-centre spin-coating, and drop-coasting techniques. To minimise device contamination, all fabrication work was performed in class 1000 cleanroom (maximum of 1,000 particles in size of ($\geq$0.5 μm) are permitted per cubic foot of air) .Two types of OTFTs were fabricated in this work depending on the insulating layer (cPMMA-based and cPVA-based OTFTs) using same fabrication technique. Also, these OTFTs were tested as gas sensors using a gas home-built testing system, as explained in section 3. Moreover, organic thin-film memory transistors (OTFMTs) were fabricated using the same procedure for the OTFTs besides inserting graphene oxide as the floating gate.

3.2 Materials

The materials used in this work were purchased from Sigma Aldrich; Poly (methyl methacrylate) (PMMA) (molecular weight 93,000),6,13-bis(triisopropylsilylethynyl) pentacene (TIPS-pentacene), Polyvinyl alcohol (PVA) (molecular weight 89,000-98,000, 99+% hydrolysed), Graphene oxide (GO)(water-based 4%)

3.2.1 TIPS-Pentacene

For the active layer, 6,13-bis (triisopropylsilylethynyl) pentacene (TIPS-pentacene) was employed. Tips-pentacene is produced when a bulky group of tri isopropyl silylethynyl of the pentacene molecular have been replaced at the 6,13-positions in order to give it a solubility [1]. Moreover, the herringbone packing in pentacene will be interrupted by functionalised groups in the TIPS-pentacene core which is cooperating in a face-to-face (π-stacking) orientation. This interreact will improve π-orbital overlap, which enhances and increases carrier mobility [2].

This interreact will improve π-orbital overlap, which enhances and increases carrier mobility [2]. Figure 3.1 represents TIPS-pentacene's chemical structure. Because the functionalised group for TIPS-pentacene is permanent, it will be substituted even after deposition, and this new structure of pentacene will not affect the semiconducting properties of the material. TIPS-pentacene has a high solubility (>100 mg mL^{-1}) in many organic solvents which is more useable and economical than pentacene. TIPS-pentacene crystal has a unique molecule arrangement after deposition, which means the direction of the crystal will decide the resistivity of the semiconductor [3,4].

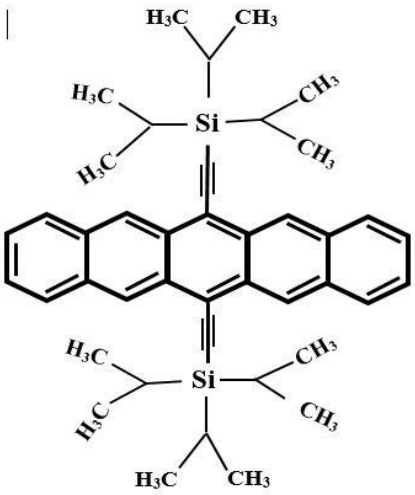

Figure 3.1: *Molecular structures of 6,13-bis(triisopropylsilylethynyl) (TIPS- pentacene).*

3.2.2 Poly (methyl methacrylate) (PMMA)

One of the widely used polymers in electronic devices is poly(methyl methacrylate) (PMMA). PMMA was first used in 1933 as a gate dialectic for several electronic devices by German chemist Otto Röhm [5]. The low dielectric constant and high resistivity (around 3 and 2×10^{15} Ω cm, respectively) made PMMA highly chosen in electronic applications [6,7]. Furthermore, PMMA has a hydrophobic methyl radical, which makes it a moisture inhibitor [8]. PMMA is the synthetic polymer of Methacrylate (MMA), which is polymerised from MMA droplets in water under the influence of free-radical initiators to form solid PMMA. In this work PMMA (Mw = 93,000 porches from Sigma-Aldrich) is employed as the gate dielectric of the OTFTs and OTFMTs devices after being cross-linked. Figure 3.2 shows the molecular structure of PMMA.

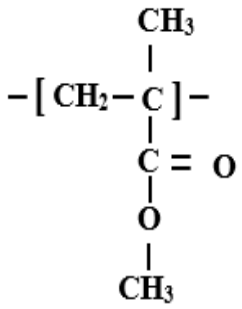

Figure 3. 2: *Molecular structure of Poly(methyl methacrylate) (PMMA)*

3.2.3 Poly (vinyl alcohol) (PVA).

Poly (vinyl alcohol) (PVA) is a flexible, hard, and durable polymer which is mostly studied and applied as an insulating layer in electronic devices. It is widely used in electronics and medical products due to its remarkable properties such as water-solubility, nontoxicity, low-cost, flexible hydrophilic network, high charge storage, considerable dielectric strength, stable thermal and has an oxygen/aroma barrier property [9-12]. PVA was used as the gate dielectric layer for OTFTs in 1990 [13]. The monomers of vinyl alcohol are unstable and rearranging to its tautomeracetaldehyde. Hence, polyvinyl acetate (PVAc) is hydrolysed to form PVA by polymerisation of the monomer, and the hydrolysis is incomplete, which provides different hydrolysis degrees of polymers. The physical proprieties of PVA such as density, crystallinity, water-solubility, film formation and polarisation degree depend on the crystal deposition, moisture, molecular mass and degree of hydrolysis [14]. Figure 3.3 shows the molecular structure of PVA.

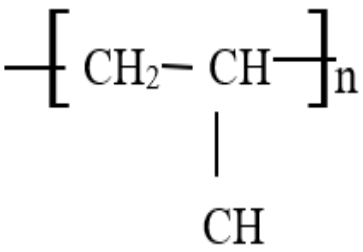

Figure 3. 3: *Molecular structure of polyvinil alcohol (PVA)*

3.2.4 Graphene oxide (GO)

Graphene oxide (GO) is a two-dimensional structured oxygenated material synthesised from graphene by chemical or thermal reduction processes. There are three methods that can be used to synthesise GO; Brodie [15], Staudenmaier [16], or Hummers method [17]. For all these methods, graphite was oxidized to various levels of oxidation to provide GO. Due to the polar oxygen functional group, graphene oxide is hydrophilic, which is contrary to graphene (hydrophobic). Many solvents can exfoliate GO, but it is well exfoliated in water [18]. Desperation graphene oxide platelets can be produced by simple stirring and sonicating GO in a solvent. Figure 3.4 illustrates the chemical structure of graphene oxide [19], which contains sheets of sp^2 hybridized carbon atoms structured in a hexagonal arrangement in addition to a few sp^3 hybridised carbon atoms constructed as epoxide or hydroxyl. Carboxyl and carbonyl groups are produced by the edge areas of these sheets [20]. GO flakes are varied in sizes (from a few nm to mm) [21]. These size variation and the chemical structure tunability made graphene oxide to be attractive material and widely used in different fields of electronics such as composites materials, sensors, clean energy devices and medicine [22].

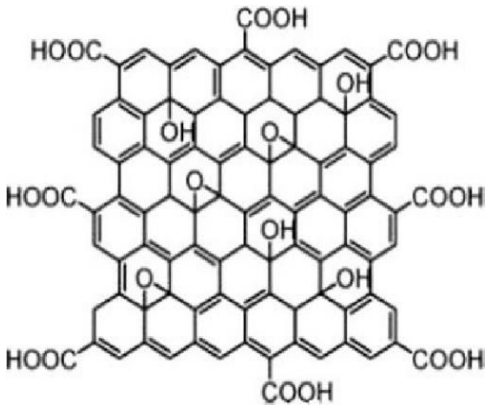

Figure 3. 4: *Molecular structure of graphene oxide consists of carbon, hydrogen and oxygen.[19]*

3.2.5 Gases used for sensing

For the gas sensing test, two types of alcohol formula were used (Ethanol and Methanol) because of their wide use in factories and our life.

3.2.5.1 Ethanol

Ethanol has different names such as alcohol, grain alcohol or ethyl alcohol. It is an organic compound and has a chemical formula of (C_2H_5OH), as shown in Figure 3.5. Ethanol is widely used in the industry as a solvent, and it is an intoxicating material. There are two types of processes to produce alcohol, fermentation and hydration of ethylene. Fermentation is usually used for alcoholic beverages by growing yeast cell to convert carbohydrate to ethanol. Sugar crops like beets and corn are the essential formatted materials to product alcohol. Another way of producing alcohol is hydrating ethylene which can be obtained by passing a mixture of steam and ethylene over an acid catalyst at a high temperature and pressure. Ethanol can be obtained as a dilute solution from both methods. In this study, ethanol solution 99.8% was purchased from Sigma Aldrich to be used in testing OTFT-based sensors.

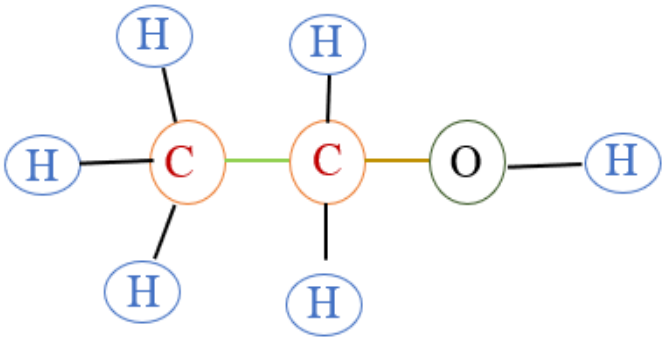

Figure 3. 5: Molecular structure of ethanol

3.2.5.2 Methanol

Methanol is a colourless liquid. It has a boiling point of 64.96 °C, and it can be solidified at -93.9 °C. Methanol burns with a non-luminous flame when mixed with air. It has high miscibility with water and an odour similar to ethyl alcohol. Methanol is also called wood alcohol, or methyl alcohol. It has the chemical formula of (CH_3OH) which is an organic compound with a long series of the alcohol as shown in Figure 3.6. The structure of methanol contains a methyl group (CH_3) connected by a hydroxyl group (OH). Methanol is produced from heating wood in a vacuum (without air) leading to form methanol by breaking some of the carbohydrates. Then it can be condensed to produce methanol vapour. Methanol is a polar organic solvent and is widely used in the industry. However, it is a toxic gas, and it may cause death when inhaled or ingested in a large amount.

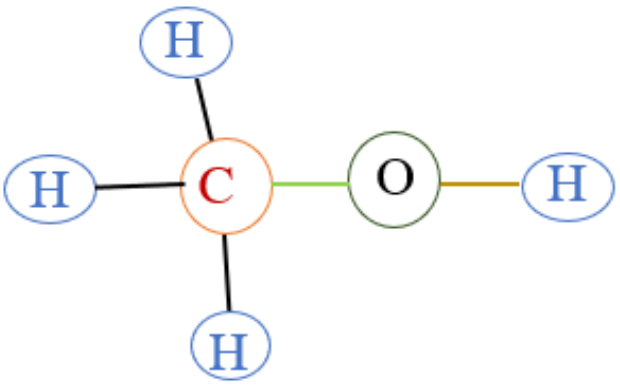

Figure 3. 6: Molecular structure of methanol

3.3 Experimental techniques

In this section, all the experimental techniques used in the fabrication and measurement methods will be explained. Thermal evaporation was used to deposit the metal gate and drain-source connectors while spin-coating was used to deposit the gate insulator and the floating gate thin film layer for the OTFTs and OTFMTs devices. On the other hand, the drop-casting technique was used to deposit the active semiconductor layer. In the section of testing OTFTs devices as gas sensors, the testing gas system employed for this purpose will be explained in detail.

3.3.1 Thermal evaporation of metals

Two metal types were thermally evaporated, aluminium (Al) and gold (Au) for the gate electrode and drain-source connectors, respectively. Figure 3.7 shows the schematic diagram and a real image of the Oerlikon Leybold Vacuum Univex 250 deposition system used during this work. In this deposition technique, the electric energy was applied to heat the metal contained in a small boat to its evaporation points. The evaporated metal then was deposited through a proper shadow mask on a cold substrate fixed by several centimetres on the top of the boat. The evaporation system was set under high vacuum of 5×10^{-6} Torr in order to reduce film impurities and prevent reaction between the metal vapour and the atmosphere. In this system, the evaporation rate and the final deposited layer thickness can be controlled by a quartz crystal sensor (QCS) and a software program [19]. The evaporation rate for Al and gold deposition was set to 1Å/s.

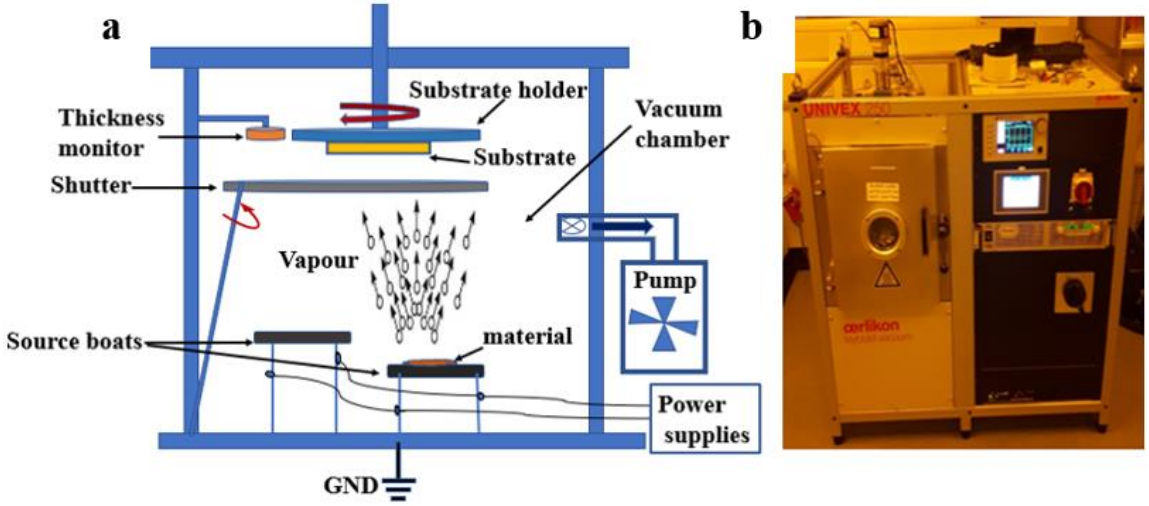

Figure 3. 7: *(a) Schematic digram of thermal evaporator, (b) Real image of thermal evaporator*

3.3.2 Spin-coating

The spin-coating technique has been used to deposit thin film layers for different organic materials such as polymers and semiconductors. This technique can provide a uniform thin film with variable thickness. The spin-coating process uses diluted materials in a solution form. Then the solution will be dispensed on the substrate surface sequentially, which is fixed on the spinner chuck followed by operating the spinner with a specific speed for a fixed time. The layer thickness depends on the deposited material's concentration, spinning speed and duration, surface tension, the viscosity of the solution and drying time. Therefore, the higher spinning speed with a longer time provides a thinner layer [23-25]. Figure 3.8 illustrates the steps of the spin-coating process, while the theoretical model for the spin-coating process is shown in equation 3.1 [23];

$$\mathbf{d} = \sqrt{\frac{n}{4\,\pi\rho\omega^2}}\sqrt{\frac{1}{t}} \tag{3.1}$$

Where d is the thickness of the spun film, η and ρ are the viscosity coefficient and the density of the solution, ω is the angular velocity and t is the spinning time [23]. In this work, the off-centre spin-coating method [26], was used to deposit the insulating layer for the OTFTs and OTFMTs as well as the GO floating gate. This method is similar to the on-centre spin-coating technique, but in this case, the sample was placed on the edge of the spinner holder

about 3-4 cm away from the centre, as shown in Figure 3.8. Using a conventional on-centre spin coating method leads the centrifugal force to act on the grains in multi-directions which results in multiple directions of the crystal alignment and depends on the location of the samples (randomly-aligned domain formations). Whereas, when an off-centre spin-coating method is applied (in which the sample is located a distance away from the centre of the spinner), the grain alignment will be nearly in the same direction of the centrifugal force. Also, in the solution polymer, it was found that a chain pre-aggregation is presented. In this crystal alignment, the chain alignment was found localised at the polymer film surface in addition to the bulk. Spin speed is found to be a parameter to influence the grain size while the overall crystal alignment depends on the distance from the spinner centre [27-29].

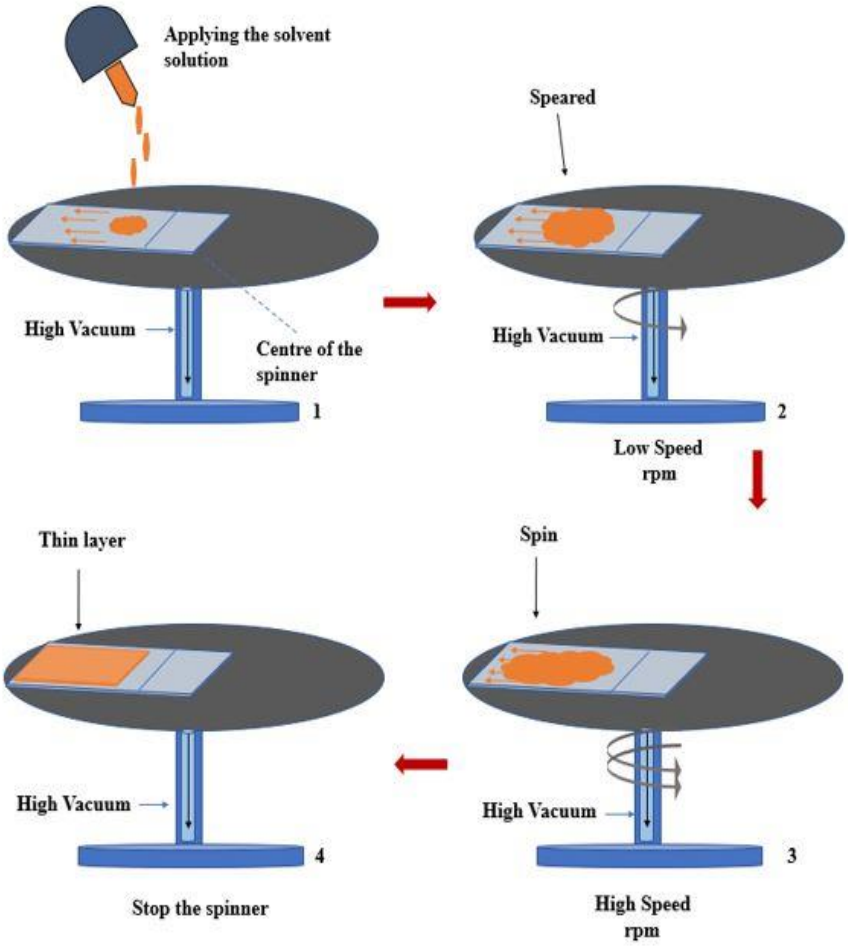

Figure 3. 8: *Steps of the spin-coating method (off-centre technique).*

3.3.3 Drop-casting

Drop-casting is a simple method with less cost used to deposit organic solvents such as semiconductors and polymers, where the solvent will be evaporated to provide a thin film of a single crystal. Figure 3.9 shows the steps of the drop-casting process. The first step of this method is dropping the organic material on the substrate surface via a pipet as shown in Figure 3.9 (a). Secondly, the dropped organic material will be left for a few minutes to evaporate the solvent before placing the substrate on a hot plate for fast evaporation as shown in Figure 3.9 (b). In this work, the sample substrate was put on a 3 mm glass from one side to make an angle of about 7° with the substrate holder to facilitate the orientation of the crystals and making the film thickness uniform on the substrate as shown in Figure 3.9. Evaporating the solvent will lead to initial nucleation followed by crystalline growing of the organic material. The evaporation starts from the interface between the dropped solution material and air [30]. Different conditions can be applied to improve the crystal grain size, coverage and the growth orientation direction. For instance, the solvent evaporation can be controlled by choosing the appropriate solvent having a specific boiling point which is the main factor for controlling nucleation [30]. Also, the dual solvent can be used to reduce the coffee stain effect (when a fluid containing particles evaporates and a dark-coloured edge remains). Using a saturated solvent environment will control the evaporation rate, as well as vibration-assistance, can improve the crystallisation, soluble additives and nucleation [30-32].

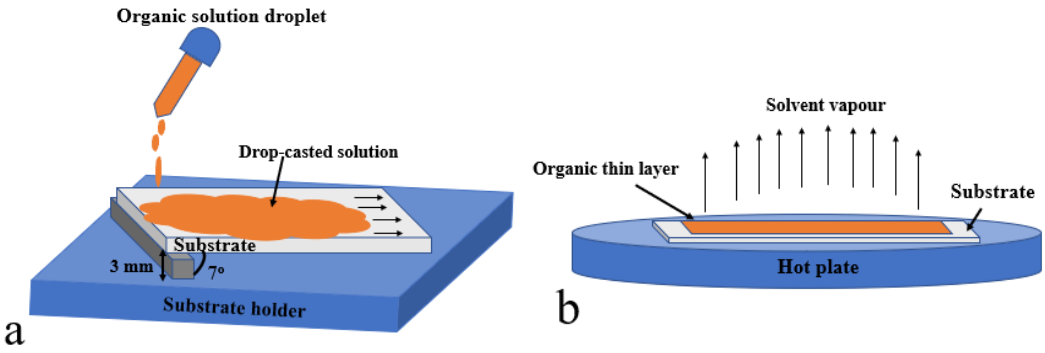

Figure 3. 9: *Drop-casting method for depositing a thin layer of organic semiconductors (a) drops of TIPS- pentacene solution over the substrate (b) getting thin layer by evaporating the solvent on a hot plate .*

In this work, the drop-casting method was used to deposit the active semiconducting layer (TIPS-pentacene) for OTFTs and OTFMTs. Organic semiconductors having strong self-organisation are easy to crystallise using this method. Nevertheless, this method is not appropriate to be used for deposing a thin film with a large area, as the solvent evaporation cannot be uniformly controlled [33]. Even for the inadequate large area coverage and uncontrollable crystal thickness, many deposition processes are built on this method to improve the morphology of the deposited solution. Some of these processes control the evaporation rate [34], where slower evaporation rate results in high crystallisation as the solution will have more time for self-organisation. Therefore, solvent evaporation is significant in the drop-casting evaporation technique. The drop-casting method can save materials and fabrication power, as there is no need for high temperature. Also, slanting the substrate is a process which can help improve the crystal orientation and quality. In this process, the solution droplets will be pinned at the higher end of the substrate and then transferred toward the lower end side [34] as sown in Figure 3.9. Also, the solvent evaporation will be faster on the top end, and crystallisation starts in this region first then moves to the bottom end [35].

3.4 Experimental details

In this section, the experiment will be explained in more detail for each process, starting from preparing the substrate up to finishing the device fabrication.

3.4.1 Preparation of the substrate

For preparing the substrate, one or more sizes of slides can be used depending on the device's base size. These sizes are in millimetre dimension, and one or more devices can be built on each substrate at one time. Dicer tool is needed to cut the substrates into fit sizes, and shadow masks should be ready to be used for the deposition process. In this work, the glass substrate slide was cut in the size of 25×15 mm each. A holder with four slides was used, and four devices can be fabricated in each slide as shown in Figure 3.10 (a, b). Before starting to deposition layers, the substrate was cleaned by hands with hot water to ensure there is no contamination caused during cutting the glass, then dried by streaming nitrogen gas.

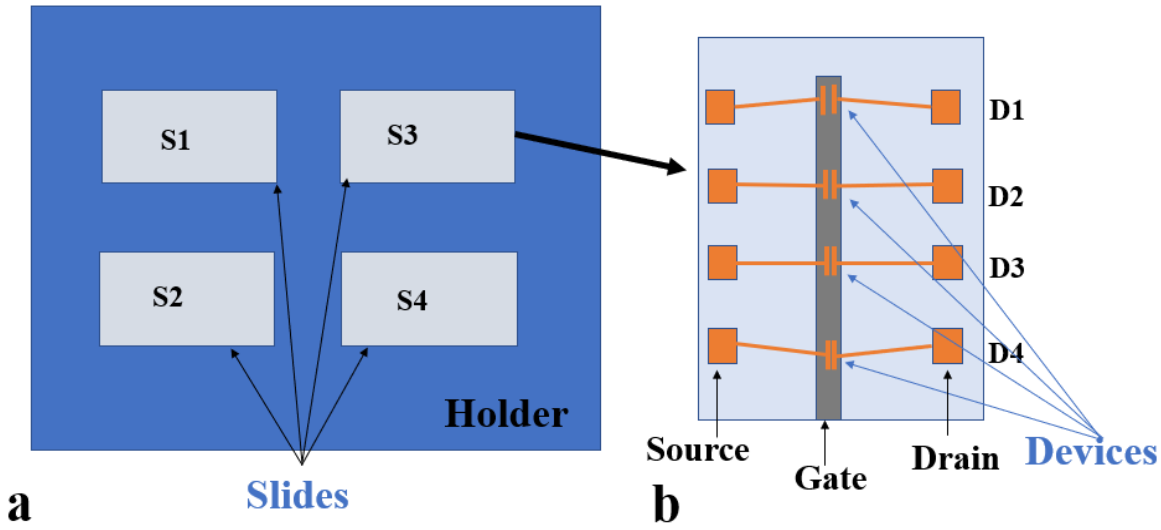

Figure 3. 10: *(a) Four samples on the holder(S1, S2, S3, S4) ,(b) Four devices on the glass sample (D1, D2, D3, D4) as the gold deposited (connectors).*

Furthermore, the slides were rinsed using Decon 90 in De-Ionised water and sonicated in an ultrasonic bath for 10 minutes. After that, acetone, methanol, and 2-propanol were used with the ultrasonic treatment for 5 minutes in each solvent to remove all the impurities on the substrate. The slides were dried after each cleaning process by streaming nitrogen gas. In the end, the substrate is exposed to O_2 in a plasma etcher for 10 minutes to make the slides hydrophilic. Table 3.1 summarises the procedure of cleaning glass substrates before being placed on the substrate holder.

Table 3. 1: *The steps of the cleaning processes*

Step	Number of processes	Cleaning solution	Details
1	1	Decon-90 in DI-water 2%	5 minutes in ultrasonicated at 40 °C
2	3	DI-water	5 minutes in ultrasonicated at 40 °C
3	2	Acetone	5 minutes in ultrasonicated at 40 °C
4	2	Methanol	5 minutes in ultrasonicated at 40 °C
5	2	Isopropanol	minutes in ultrasonicated at 40 °C
6	1	--------	10 minutes in O_2 plasma

3.4.2 Film deposition

3.4.2.1 Deposition of the metal gate

For the metal gate, a thin film of aluminium (Al) was evaporated on the clean glass substrates. An aluminium layer 50-60 nm thick was evaporated on each glass substrate using the thermal evaporation technique, as explained in section 3.3.1. Immediately after finishing the cleaning of the substrate, four glass samples were placed on the substrate holder, as shown in Figure 3.10 (a) then were placed in the evaporator. The evaporation rate was 1Å/s under a vacuum of 5×10^{-6} Tor. After this step, all samples are ready to deposition the insulating layer. Figure 3.11 illustrates the steps of deposition metal gate using a thermal deposition technique, in this work Aluminum (Al) has been used as a gate connector for the OTFTs devices.

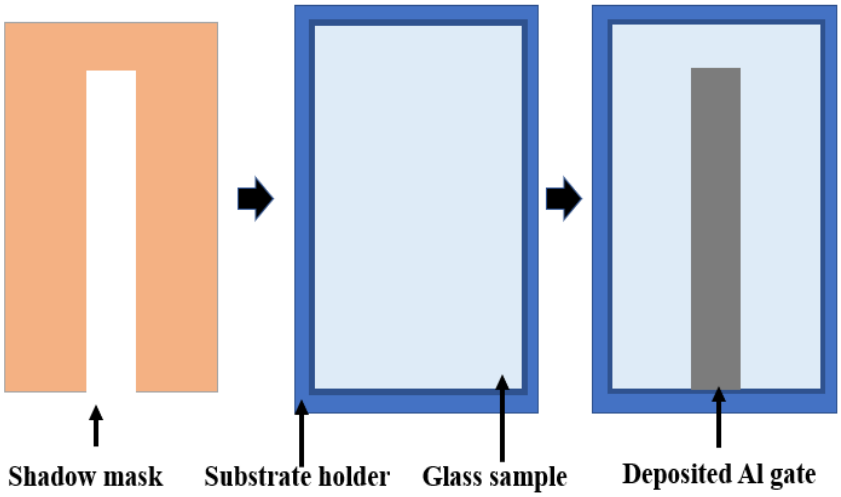

Figure 3. 11: *The steps for depositing Al matel gate through a shadow mask.*

3.4.2.2 Spin-coating the insulating layer

In this section, cross-linked poly(methyl methacrylate) (cPMMA) and cross-linked poly(vinyl alcohol) (cPVA) were deposited as the dielectric layers for the OTFTs. For this purpose, Polymethylmethacrylate (PMMA) 5 wt. % was dissolved in butyl acetate and cross-linked using 1,6-bis (trichlorosilyl) hexane (C6-Si) (10µl/1ml) as the cross-linking agent and filtered using 1µm syringe filter. Whereas, for cross-linking polyvinyl alcohol, PVA 10 wt. % powder was dissolved in deionised water on a stirrer for 48 hours at 70 ^{o}C. Then, the PVA solution was filtered using a 0.45 µm syringe filter. Ammonium dichromate, 0.8 wt. % was added to the PVA solution as the cross-linking agent. Then the solution was placed on a stirrer for 12 hours at a temperature of 65 ^{o}C. After that, the cPVA solution was filtered again using the 0.45 µm syringe filter to remove any accumulating particles. Finally the cPMMA and cPVA solutions were deposited as the insulating layer for the OTFT devices using simple off-centre spin-coating (OCSC) method [26]. The off-centre spin-coating method process is the same as the conventional on-centre method, but in this case the substrate sample is placed on the edge of the spinner about 3-4 cm from the centre as explained in section 3.3.2. EMS spin-coater model 4000 was used in all the spin-coating processes. In this work, the deposition process of cPMMA insulating layer started by applying the solvent solution on the substrate using a disposable glass pipet then immediately the spinner was operated with a low speed (500 rpm for 10 sec) (see steps 1

and 2 Figure 3.8) to spread the solution over the glass substrate. Immediately moving to step 3 (Figure 3.8) by applying a higher spin speed (2000 rpm for 40 sec) to get a uniform thin layer of the insulator, then finishing the process by stopping the spinner as in step 4 (Figure 3.8). To evaporate the solvent from the thin film, all samples were cured on a 120^{o}C heater for 60 minutes. To deposition cPVA thin file, the same process used for the deposition of cPMMA was followed with annealing at 90^{o}C for two hours. Finally, all the samples were exposed to a 0.8 sccm O_2 ozone vacuumed at 3 mbar for 1 min to reduce the moisture and improve the layer surface before they were kept under vacuum for the next step.

3.4.2.3 Deposition the floating gate

In this study, graphene oxide (GO) thin layer was deposited as the floating gate for two types of memory transistors (cPMMA-based and cPVA-based memory transistor). Graphene oxide solution (0.4 mg/ml water dispersion) [purchased from Sigma-Aldrich] was used as the floating gate. Also, to deposit this layer, off-centre spin-coating (OCSC) method was used after dispersing and mixing the solution on the stirrer for 15 minutes. The GO solution was dropped on the substrate using a glass pipet. The spin speed started at 500 rpm for 10 sec to spread the solution over the substrate. Then immediately the speed was increased to 3500 rpm for 20 sec to produce a GO thin layer. Finally, all samples were cured at 80^{o}C for 20 minutes before they were kept under vacuum for the next layer.

3.4.2.4 Deposition of the organic semiconductor

TIPS-Pentacene (6,13-bis(triisopropyl-silylethynyl) pentacene) (2 wt % toluene solution) was chosen as the semiconductor active layer. The TIPS-pentacene solution was deposited using the drop-casting method, as the solution was dropped over the cPMMA (or cPVA) insulating layer. This deposition was performed in a glove box under a nitrogen environment. A special technique was applied for this method by placing the substrate on the holder with a small angle of 7^{o} (3mm high) as shown in Figure 3.9. A glass pipet was used to apply drops of the TIPS-pentacene solution on the substrate then the substrate was left for 10 minutes for the evaporation of the solvent. Finally, the sample was placed on a hot plate at 50^{o}C for 1h to completely remove the solvent from the semiconducting layer before it was kept under a vacuum for 24h to be ready to deposit the gold contacts (drain-source contacts). Atomic Force Microscope (AFM) technique was used to study the surface morphology and estimate the layer thickness, which was found to be in the region of 60-70

nm. Different parameters can affect the device's performance such as the insulator and semiconductor thicknesses, channel length and width plus the fabrication techniques used.

3.4.2.5 Deposition the metal contacts

Gold was used and deposited as source-drain contacts in all the devices. Thermal evaporation method (as explained in section 3.3.1) was used in order to get a thin layer of gold for the drain-source contacts over the semiconducting layer. The evaporation was made through a shadow mask, as shown in Figure 3.10 (b). After placing the shadow mask on the faces of the devices, all devices were placed in the thermal evaporator. The evaporation rate was 1Å/s and was performed under a vacuum of 5×10^{-6} mbar. An optical microscope and profilometer were used to verify the alignment of the gold contacts and estimate the layer thickness, which is found to be 50-60 nm. Immediately, the test and the electrical characterisation measurements were performed for all the devices before storing them under vacuum.

3.5 Characterisation details

This section presents details of all electrical and optical characterisation methods used for OTFTs, memory devices and gas sensor testing.

3.5.1 Atomic Force Microscopy (AFM)

In this work, the digital instrument nasoscope atomic force microscopy (AFM) was used to study the surface morphology for each deposited layer such as the insulator, floating gate and semiconductor active layer. AFM is a technique with a high-resolution scanning probe which can be used to study the morphology surface of materials and gives clear images of the surface smoothing of thin layers. The atomic force microscopy was developed in 1985 by Binnig, Quate and Gerber [36] which facilitates the study of atomic-scale features for a range of materials surfaces. AFM can be used to measure thin film thickness, nanoscale roughness, analyse and study lateral friction forces, van der Waals forces, magnetic forces and repulsive forces [37-40]. AFM images can be obtained by moving (scanning) a sharp probe over the sample surface while analysing the interaction of the tip and the sample. The AFM scanning process can be performed by scanning the sharp probe tip of the microscopic cantilever over and close to the top of the sample surface. Then, the attraction force between the sample and the sharp probe (radius less than 10 nm) with a very short separation distance

(0.2-10 nm) can be measured and recorded while the probe gently touches the top of the sample surface [41].

The attraction force can be described by Hook's low, equation 3.2

$$F = -k.x \tag{3.2}$$

Where F is the attraction force, k is spring constant, and x is the cantilever deflection.

Figure 3.12 shows the main components of an AFM, which are the cantilever, probe, laser, scanner, photodetector and data processor. The force at the interface between the sample surface and the probe will affect how the probe will have interacted with the sample's surface. The probe will be in a contact mode which is when a repulsive force occurs while a non-contact mode will materialise when the probe moves far from the surface during attractive force domination. The distance between the probe tip and the material's surface should be adjusted in order to keep the cantilever deflection a constant. AFM has three imaging modes, the contact mode when the separation between the probe and the surface less than 0.5 nm, while for the separation ranged from 0.5 to 2 nm it is an intermittent contact, and the non-contact mode is when the separation is 10 nm or below. In contact mode, the tip touches the sample surface. Whereas, in a non-contact mode, the tip will be very close to the sample surface without touching. Intermittent mode is similar to the contact mode, but in this case, the cantilever makes intermittent contact with the material's surface in the range of resonant frequency. In this mode, the probe will slightly tap on the surface during the scan, touching the surface when it is swinging bottom. In this mode, the lateral force will be reduced drastically because the contact time is a very short fraction of its oscillation period. The intermittent mode is chosen to investigate the samples with a structure weakly bound to the surface, such as polymers and thin films [42].

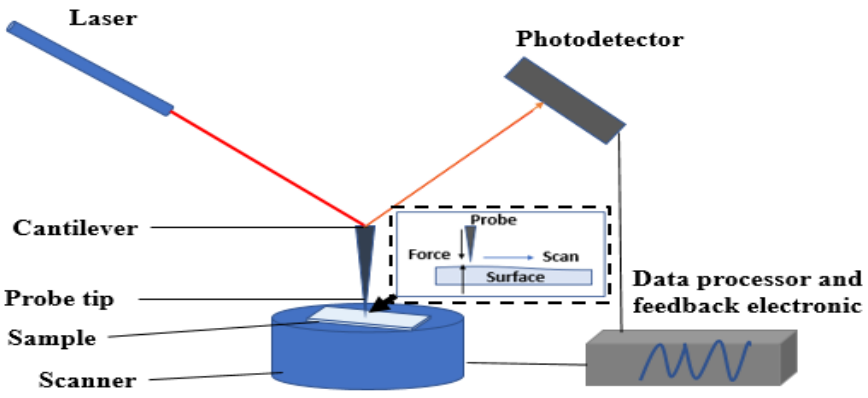

Figure 3. 12 : *Simple princibles of the atomic force microscopy AFM*

3.5.2 Profilometer

In this work, the Dektak XTL profilometer was used to measure all the thin layer's thicknesses. A profilometer is a measuring instrument used to measure and investigate a material's surface, in order to analyse its roughness, flatness, curvature, and critical dimensions which are computed from the surface topography. During the last fifteen years, profilometer is widely used, as well as developed techniques for measuring the surface morphology [43,44]. There are two types of profilometers: contact and non-contact. In most of these devices, the vertical difference between the highest and lowest point of the surface can be measured to find the surface roughness and thin layer thickness as well as uniformity of the thin film. The sample height variation can be measured by either the probe or the sample is being moved. Therefore, the mechanical movement will be converted to an electric signal that can be amplified to give a DC output signal. All profilometers have the same essential components, which are stylus, gearbox, datum, transducer, pickup, sample holder, data acquisition system and control unit. The gearbox drives the pickup, which then moves the stylus over the examined surface at a fixed motion speed. This movement will be changed as the surface varies. All the mechanical movements are transmitted by the transducer to an electric signal. Then, these signals are collected by the data acquisition system after being amplified by the electric amplifier to generate the surface analysis.

3.5.3 Measurements

All the current-voltage (*I*-*V*) characteristics for the OTFTs, OTFMTs devices and gas sensors were performed using a Keithley 2636 source meter at room temperature. Figure 3.13 illustrates the schematic diagram setup of the measurement. For measuring the output characteristics of OTFTs and OTFMTs, a DC voltage was applied to the gate electrode while the drain-source current (I_{DS}) is measured versus the drain-source voltages (V_{DS}) for applying different values of gate voltages. Whereas, the transfers characteristic measurements were performed by applying a fixed drain-source voltage and measuring the drain-source current as a function of different applied gate-source voltages (V_{GS}).

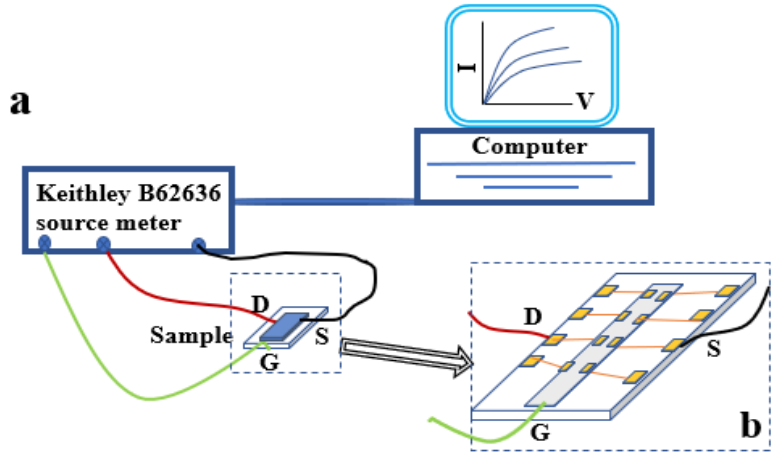

Figure 3. 13: *(a) Schematic diagram of the electric characrisation measurement, (b) The enlarged section of the sample*

3.5.4 Experimental setup for the gas sensing system.

A gas sensing system was built to test and study the capability of the OTFTs as gas sensors. Figure 3.14 shows the schematic diagram of the sensing system for this work. In this study, two types of OTFTs (cPMMA-based and cPVA-based) have been tested as alcohol vapour (ethanol and methanol) detectors. Therefore, the OTFTs devices in chapter 4 were used to perform the sensing behaviour. Alcohol (ethanol and methanol) were prepared and provided in different concentrations. To obtain these concentrations, nitrogen was used as a diluted gas to be mix with a constant concentration of alcohol vapour, producing different concentrations of alcoholic vapour. The second method can be applied by streaming a constant nitrogen gas to be mix with different streaming of alcohol vapour, but the first one is more preferred because alcohol evaporates in certain speeds that are difficult to increase or decrease. As shown in figure 3.14, there are two flowmeters set up in this system (F_1 and F_2). Flowmeter 1 was used to control the nitrogen gas stream flowing over the alcohol (carer gas) which is fixed to a flow rate of 100 ml.min^{-1}, while flowmeter 2 was used for streaming a variable rate of nitrogen gas (100 ml.min^{-1} to 500 ml.min^{-1}) as the dilution gas. Also, the system has two flasks containers, one to hold alcohol liquid to generate alcohol vapour, and the other one is for holding the sample under investigation. The testing was at room temperature. Alcohol vapour for this test was produced with nitrogen as the gas carrier with a flow rate F_1 of 100 ml.min^{-1} passing over a permeation vial containing a quantity of alcohol solvent at room temperature (23 ^0C ±1 ^0C) and under atmospheric pressure. Then the concentration of alcohol vapour C_1 (ppm) was calculated using equation (3.3) [45].

$$C_1 = \frac{P\,\rho}{F_1} \tag{3.3}$$

where P (mg.min^{-1}) is the permeation rate, ρ (ml.mg^{-1}) is the reciprocal vapour density of alcohol and F_1 (ml.min^{-1}) is the nitrogen gas flow rate. To produce different concentrations of alcohol vapour (methanol or ethanol), another nitrogen diluting stream of a flow rate of F_2 was mixed with alcohol vapour to produce alcohol concentrations (1, 2, 4, 6, 7 and 8 *ppm*) using equation (3.4) [45].

$$C = C_1 \frac{F_1}{F_1 + F_2} \tag{3.4}$$

Where C (ppm)is the alcohol vapour concentration under the test, F_2 (ml.min^{-1}) is the flow rate of dilution stream. All measurements were made in atmospheric pressure and room temperature using in-house Bangor gas sensing system and Keithley 2636 source meter, Therefore, the sensing system in this work can control the carer gas (nitrogen) and alcohol vapour through 5 different valves fixed on the streaming tubes and alcohol's concentration was controlled by changing the flow rate in flowmeter 2 while the rate in flowmeter 1 (F_1) remains constant at (100 ml.min^{-1}). Finally, the gas sensing system is connected to Keithly B 2636 as well as a computer in order to measure and record the *I-V* characteristics of the sensor. Because our sensor is OTFT-based, therefore, a gate connector was connected in addition to the drain-source connectors, as shown in Figure 3.14.

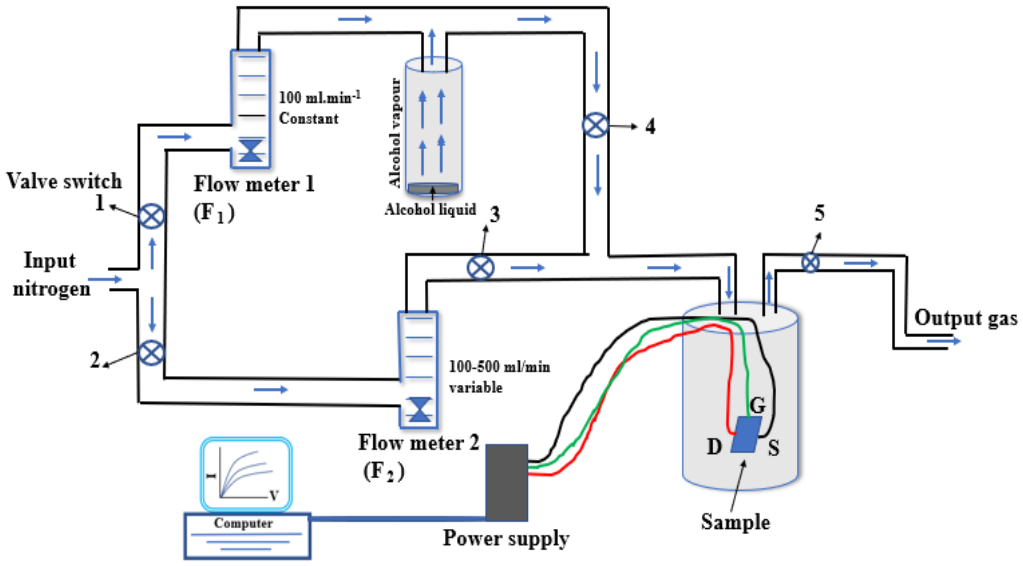

Figure 3. 14: *Schematic diagram of the gas testing system .*

3.6 References

[1] J. Mei, Y. Diao, A. L. Appleton, L. Fang, and Z. Bao, "Integrated materials design of organic semiconductors for field-effect transistors," *J. Am. Chem. Soc.*, vol. 135, no. 18, pp. 6724–6746, 2013.

[2] J. L. Brédas, J. P. Calbert, D. A. Da Silva Filho, and J. Cornil, "Organic semiconductors: A theoretical characterization of the basic parameters governing charge transport," *Proc. Natl. Acad. Sci. U. S. A.*, vol. 99, no. 9, pp. 5804–5809, 2002.

[3] D. A. Kadri, D. A. Karim, M. Seck, K. Diouma, and P. Marcel, "Optimization of 6,13Bis(triisopropylsilylethynyl)pentacene (TIPS-Pentacene) Organic Field Effect Transistor: Annealing Temperature and Solvent Effects," *Mater. Sci. Appl.*, vol. 09, no. 11, pp. 900–912, 2018.

[4] J. E. Anthony, J. S. Brooks, D. L. Eaton, and S. R. Parkin, "Functionalized pentacene: Improved electronic properties from control of solid-state order [20]," *J. Am. Chem. Soc.*, vol. 123, no. 38, pp. 9482–9483, 2001.

[5] M. Kutz, "Handbook of Materials Selection," *John Wiley Sons*, pp. 341–344, 2002.

[6] and G. L. J. Veres, S. Ogier, "Gate Insulators in Organic Field-Effect Transistors," Chem. Mater," *Chem. Mater*, vol. 16, pp. 4543–4547.

[7] and A. Y. G. Horowitz, F. Deloffre, F. Garnier, R. Hajlaoui, M. Hmyene, "All-organic field-effect transistors made of π-conjugated oligomers and polymeric insulators," *Synth. Met.*, pp. 435–438, 1993.

[8] and J. D. L. S. H. Jin, J. S. Yu, C. A. Lee, J. W. Kim, B. G. Park, "Pentacene OTFTs with PVA gate insulators on a flexible substrate," *J. Korean Phys. Soc*, vol. 44, pp. 181–185, 2004.

[9] M. Egginger and R. Schwödiauer, "Analysis of mobile ionic impurities in polyvinylalcohol thin films by thermal discharge current and dielectric impedance spectroscopy," *AIP Adv.*, vol. 2, no. 4, 2012.

[10] I. Saini, A. Sharma, R. Dhiman, S. Aggarwal, S. Ram, and P. K. Sharma, "Grafted SiC nanocrystals: For enhanced optical, electrical and mechanical properties of polyvinyl alcohol," *J. Alloys Compd.*, vol. 714, pp. 172–180, 2017.

[11] E. Marin, J. Rojas, and Y. Ciro, "A review of polyvinyl alcohol derivatives: Promising materials for pharmaceutical and biomedical applications," *African J. Pharm. Pharmacol.*, vol. 8, no. 24, pp. 674–684, 2014.

[12] T. S. Gaaz, A. B. Sulong, M. N. Akhtar, A. A. H. Kadhum, A. B. Mohamad, A. A. Al-Amiery, and D. J. McPhee, "Properties and applications of polyvinyl alcohol, halloysite nanotubes and their nanocomposites," *Molecules*, vol. 20, no. 12, pp. 22833–22847, 2015, doi: 10.3390/molecules201219884.

[13] X. Peng, G. Horowitz, D. Fichou, and F. Garnier, "All-organic thin-film transistors made of alpha-sexithienyl semiconducting and various polymeric insulating layers," *Appl. Phys. Lett.*, vol. 57, no. 19, pp. 2013–2015, 1990.

[14] N. A. Peppas and C. M. Hassan, "Structure and applications of poly (vinyl alcohol) hydrogels produced by conventional crosslinking or by freezing / thawing methods," *Adv. Polym. Sci.*, vol. 153, pp. 37–65, 2000.

[15] B. C. Brodie, "on the Atomic Weight of Graphit," *R. Soc. London*, vol. 149, pp. 423–429, 1858.

[16] L. Staudenmaier, "Method for the preparation of the graphite acid," *Eur. J. Inorg. Chem.*, vol. 31, no. 2, pp. 1481–1487, 1898.

[17] W. S. Hummers and R. E. Offeman, "Preparation of Graphitic Oxide," *J. Am. Chem. Soc.*, vol. 80, no. 6, p. 1339, 1958.

[18] J. I. Paredes, S. Villar-Rodil, A. Martínez-Alonso, and J. M. D. Tascón, "Graphene oxide dispersions in organic solvents," *Langmuir*, vol. 24, no. 19, pp. 10560–10564, 2008.

[19] K. Gerani, H. R. Mortaheb, and B. Mokhtarani, "Enhancement in Performance of Sulfonated PES Cation-Exchange Membrane by Introducing Pristine and Sulfonated Graphene Oxide Nanosheets Synthesized through Hummers and Staudenmaier Methods," *Polym. - Plast. Technol. Eng.*, vol. 56, no. 5, pp. 543–555, 2017.

[20] L. Ravagnan, F. Siviero, C. Lenardi, P. Piseri, E. Barborini, P. Milani, C. S. Casari, A. Li Bassi, and C. E. Bottani, "Cluster-Beam Deposition and in situ Characterization of Carbyne-Rich Carbon Films," *Phys. Rev. Lett.*, vol. 89, no. 28, pp. 1–4, 2002, doi: 10.1103/PhysRevLett.89.285506.

[21] C. Y. Su, Y. Xu, W. Zhang, J. Zhao, X. Tang, C. H. Tsai, and L. J. Li, "Electrical and spectroscopic characterizations of ultra-large reduced graphene oxide monolayers," *Chem. Mater.*, vol. 21, no. 23, pp. 5674–5680, 2009, doi: 10.1021/cm902182y.

[22] F. Perrozzi, S. Prezioso, and L. Ottaviano, "Graphene oxide: From fundamentals to applications," *J. Phys. Condens. Matter*, vol. 27, no. 1, p. 13002, 2015.

[23] I. B. and J. J. Muray, "The Physics of Micro/Nano-Fabrication,"," *Plenum Press. New York*, 1992.

[24] N. Sahu, B. Parija, and S. Panigrahi, "Fundamental understanding and modeling of spin coating process: A review," *Indian J. Phys.*, vol. 83, no. 4, pp. 493–502, 2009.

[25] N.-T. Nguyen, *Fabrication technologies*. 2012.

[26] Y. Yuan, G. Giri, A. L. Ayzner, A. P. Zoombelt, S. C. B. Mannsfeld, J. Chen, D. Nordlund, M. F. Toney, J. Huang, and Z. Bao, "Ultra-high mobility transparent organic thin film transistors grown by an off-centre spin-coating method," *Nat. Commun.*, vol. 5, pp. 1–9, 2014, doi: 10.1038/ncomms4005.

[27] D. Bharti and S. P. Tiwari, "Improved alignment and crystallinity of TIPS-Pentacene thin films by off-center spin coating," *IEEE-NANO 2015 - 15th Int. Conf. Nanotechnol.*, pp. 432–435, 2015.

[28] N. K. Kim, S. Y. Jang, G. Pace, M. Caironi, W. T. Park, D. Khim, J. Kim, D. Y. Kim, and Y. Y. Noh, "High-Performance Organic Field-Effect Transistors with Directionally Aligned Conjugated Polymer Film Deposited from Pre-Aggregated Solution," *Chem. Mater.*, vol. 27, no. 24, pp. 8345–8353, 2015, doi: 10.1021/acs.chemmater.5b03775.

[29] University of Louisville, "Spin Coating Theory," *https://louisville.edu/micronano/files/documents/standard-operating-procedures/SpinCoatingInfo.pdf/view*, no. October, pp. 2–3, 2013.

[30] Z. Bao, A. J. Lovinger, and J. Brown, "New air-stable n-channel organs thin film transistors," *J. Am. Chem. Soc.*, vol. 120, no. 1, pp. 207–208, 1998.

[31] J. A. Lim, W. H. Lee, H. S. Lee, J. H. Lee, Y. D. Park, and K. Cho, "Self-organization of ink-jet-printed triisopropylsilylethynyl pentacene via evaporation-induced flows in a drying droplet," *Adv. Funct. Mater.*, vol. 18, no. 2, pp. 229–234, 2008.

[32] Z. He, J. Chen, J. K. Keum, G. Szulczewski, and D. Li, "Improving performance of TIPS pentacene-based organic thin film transistors with small-molecule additives," *Org. Electron.*, vol. 15, no. 1, pp. 150–155, 2014.

[33] Y. H. Kim, Y. U. Lee, J. I. Han, S. M. Han, and M. K. Han, "Influence of solvent on the film morphology, crystallinity and electrical characteristics of triisopropylsilyl pentacene OTFTs," *J. Electrochem. Soc.*, vol. 154, no. 12, pp. 995–998, 2007.

[34] G. J. Chae, S. H. Jeong, J. H. Baek, B. Walker, C. K. Song, and J. H. Seo, "Improved performance in TIPS-pentacene field effect transistors using solvent additives," *J. Mater. Chem. C*, vol. 1, no. 27, pp. 4216–4221, 2013.

[35] W. H. Lee, D. H. Kim, Y. Jang, J. H. Cho, M. Hwang, Y. D. Park, Y. H. Kim, J. I. Han, and K. Cho, "Solution-processable pentacene microcrystal arrays for high performance organic field-effect transistors," *Appl. Phys. Lett.*, vol. 90, no. 13, pp. 88–91, 2007, doi: 10.1063/1.2717087.

[36] R. Splinter, "Action potential transmission and volume conduction," *Handb. Phys. Med. Biol.*, vol. 56, no. 9, pp. 5-1-5–9, 2010.

[37] R. R. L. De, D. A. C. Albuquerque, T. G. S. Cruz, F. M. Yamaji, and F. L. Leite, "Measurement of the Nanoscale Roughness by Atomic Force Microscopy: Basic Principles and Applications," *At. Force Microsc. - Imaging, Meas. Manip. Surfaces At. Scale*, 2012.

[38] N. Jalili and K. Laxminarayana, "A review of atomic force microscopy imaging systems: Application to molecular metrology and biological sciences," *Mechatronics*, vol. 14, no. 8, pp. 907–945, 2004, doi: 10.1016/j.mechatronics.2004.04.005.

[39] P. Grütter, E. Meyer, H. Heinzelmann, L. Rosenthaler, H. -R. Hidber, and H. -J. Güntherodt, "Application of atomic force microscopy to magnetic materials," *J. Vac. Sci. Technol. A Vacuum, Surfaces, Film.*, vol. 6, no. 2, pp. 279–282, 1988.

[40] C. R. Blanchard, "Atomic Force Microscopy," *Chem. Educ.*, pp. 1–5, 1996.

[41] J. C. Vickerman and I. S. Gilmore, *Surface Analysis - The Principal Techniques: Second Edition*. 2009.

[42] R. R. L. De, D. A. C. Albuquerque, T. G. S. Cruz, F. M. Yamaji, and F. L. Leite, "Measurement of the Nanoscale Roughness by Atomic Force Microscopy: Basic Principles and Applications," *At. Force Microsc. - Imaging, Meas. Manip. Surfaces*

At. Scale, no. June 2014, 2012.

[43] S. H. R. Ali, "Advanced Nanomeasuring Techniques for Surface Characterization," *ISRN Opt.*, vol. 2012, pp. 1–23, 2012, doi: 10.5402/2012/859353.

[44] T. R. Thomas, *Rough Surfaces Second Edition*. 1982.

[45] J. Namieśnik, "Generation of standard gaseous mixtures," *J. Chromatogr. A*, vol. 300, no. C, pp. 79–108, 1984.

Chapter 4

Organic Thin Film Transistors (OTFTs)

4.1 Introduction

Nowadays, TIPS-pentacene-based organic thin film transistors (OTFTs) are gaining significant research interest due to their stability in ambient and solubility in most organic solvents [1-4]. These two properties enable TIPS-pentacene to be deposited from solutions to act as the active layer for OTFTs. Also, it has an anisotropic crystal form with a large bandgap, which enhances performance in organic thin film transistor. In this work, off-center spin-coating technique is used for depositing insulator layer to enhance the performance of the insulator/semiconductor interface. Which is very important to improve current mobility of OTFT. TIPS-pentacene was used as the active layer to fabricate OTFTs. The bottom gate, top contact (BG-TC) configuration has been used in this study [5-7]. For the gate dielectric, cross-linked polymethyl methacrylate (cPMMA) and cross-linked polyvinyl alcohol (cPVA) were chosen because of their good insulating and low leakage current between the gate and the active layer. Gold and aluminium metals were exploited as drain-source contacts and gate, respectively. The channel's length was varied with a fixed channel width, and the fabrication process was buttery butter . For the transistor's characterization measurement; the applied gate and drain-source voltage, channels dimension and insulator thickness were taken into consideration. Also, the devices were investigated during applying a stress voltage to establish the endurance properties of these devices. Three types of stress were used in this investigation; the first one was performed by applying different gate bias stress at a constant time, followed by applied constant gate-bias at different stress time. Finally, constant gate bias was applied at constant stress time with different drain bias stress. This study investigated two different types of transistors with two different gate insulators and the same active layer. All measurements were completed at room temperature with double sweep voltage scan.

4.2 cPMMA-based OTFTs

4.2.1 Device fabrication

In this work, BG-TC fabrication structure was used to fabricate OTFTs devices to reduce the contact resistance [8,9]. For the gate, Al metal was thermally evaporated through a shadow mask on a clean glass substrate as depicted in Figure 4.1(a) and(b). Figure 4.1 (c) is the actual microscopic image shows the drain-source channel with TIPS-pentacene active layer. Polymethylmethacrylate (PMMA) 5 wt. % was dissolved in butyl acetate and cross-linked using [1,6-bis (trichloro silyl) hexane (C6-Si) (10µl/1ml) as the cross-linking agent and filtered using 1µm syringe filter. The cross-linked PMMA (cPMMA) then spin-coated using simple off-center spin-coating (OCSC) method [10] with an initial spin speed of 500 rpm for 10 sec, then 2000 rpm for 40 sec as the gate insulating layer and annealed at 120 C^0 for 60 min. Before drop-casting the semiconductor, the cPMMA layer was exposed to 0.8 sccm O_2 ozone under vacuum (3 mbar) for 1 min to reduce the moisture and improve the layer surface.

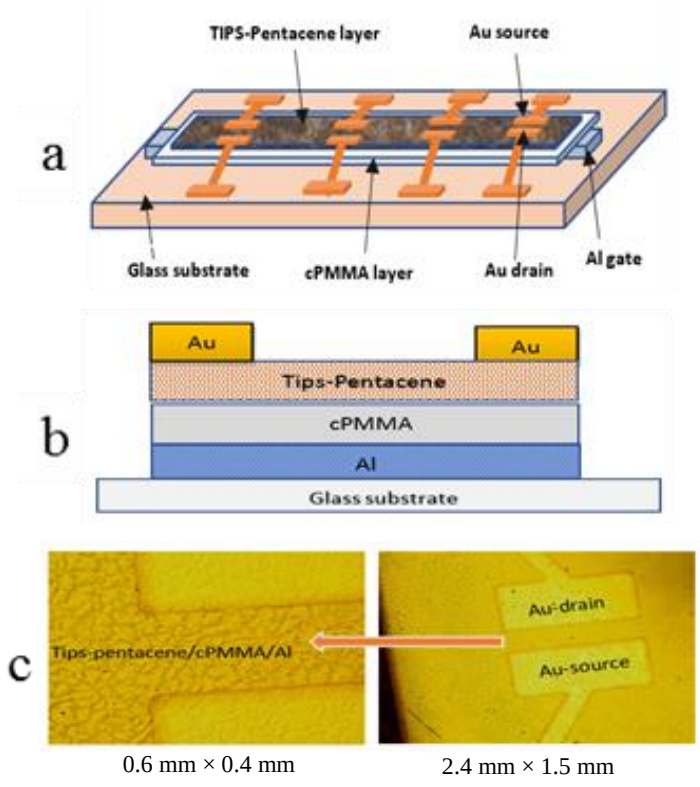

Figure 4. 1: *Schematic diagram of cPMMA-based OTFT structure. (a) slide sample with a top view including all layers. (b) Cross-sectional representation of the device fabrication. (c) Microscopic image of the drain-source channel with the TIPS-pentacene active layer.*

The insulating layer thickness was measured by the profilometer, and it was found to be 330 ±5 nm. For the active layer, (6,13-bis(triisopropyl-silylethynyl) pentacene) TIPS-Pentacene (2 wt % toluene solution) was drop-casted over the cPMMA insulating layer under nitrogen environment in a glove box on a substrate with a small angle of (7^0) as shown in Figure 3.9 in chapter (3). Then all samples were annealed at 50 C° for 1h to remove the solvent from the semiconducting layers toproduce a 60 nm active layer thickness. The devices were left under vacuum for 24 hours before gold was thermally evaporated to create drain-source contacts through a shadow mask with a thickness of 50 nm. Further details explained in the chapter (3), materials and experimental techniques.

4.2.2 Device optimization and surface morphology

In an initial experiment, PMMA was spin-coated using the conventional on-centre spin-coating technique to represent the insulating layer to OTFTs. These devices exhibited high leakage current and a clear hysteresis at the output and transfer *I-V* characteristics with voltage sweep in both directions, as shown in Figure (4.2 (a, b)).

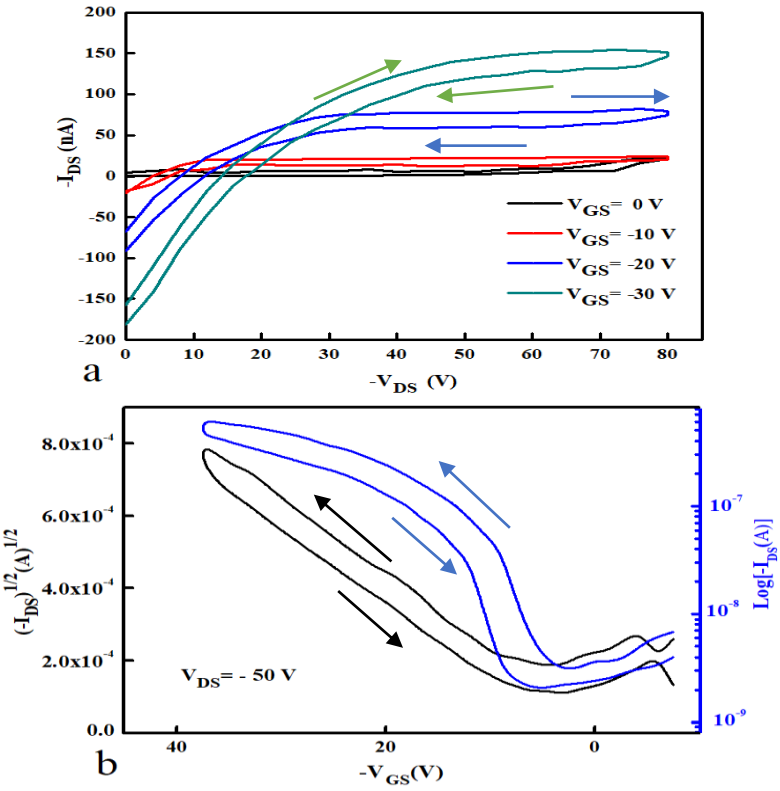

Figure 4. 2: *(a) Output and (b) transfer curves for cPMMA based OTFT (on-center spin-coating method)*

To improve the device's behaviour and avoiding the high leakage current and hysteresis in the PMMA-based OTFT devices, the cPMMA layer was deposited using the off-center spin-coating (OCSC) technique. Using the OCSC technique with its centrifugal force gives high crystalline alignment due to the unidirectional of materials on the substrate as shown in Figure 4.3 To explain these results, a morphology study was also performed for both sets of device's layers. Figure 4.3(a), illustrates the AFM image of the cPMMA insulator layer spin-coated using the on-centre technique,whereas Figure 4.3 (b) represents the AFM image using the off-centre technique to deposit the cPMMA insulator layer. It was found that the roughness of cPMMA layer (using the on-centre technique) and cPMMA (using the off-centre technique) are 5.77 nm and 4.65 respectively. AFM results confirm that the cPMMA layer deposited using the off-centre spin-coating technique has less surface roughness than -cPMMA layer deposited with the on-centre technique. The change in the surface of the insulating layer formed a good interface between the insulating and semiconducting layers [11,12], which gives high mobility, elevated on-off ratio and low threshold voltage in the range of (1.22 -1.42 cm^2 V^{-1} s^{-1}, 6.5 × 10^4 -7.5 ×10^5 and -2 V– (-10 V), respectively.

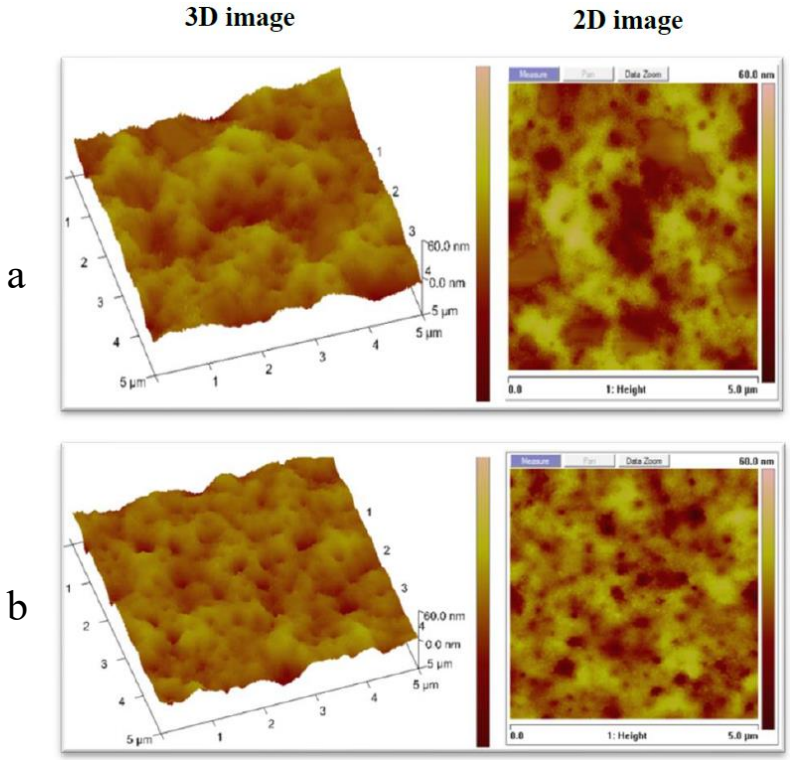

Figure 4. 3: *AFM images of cPMMA thin layer deposited with (a) on-centre spin-coating technique(b) off-centre spin-coating technique.*

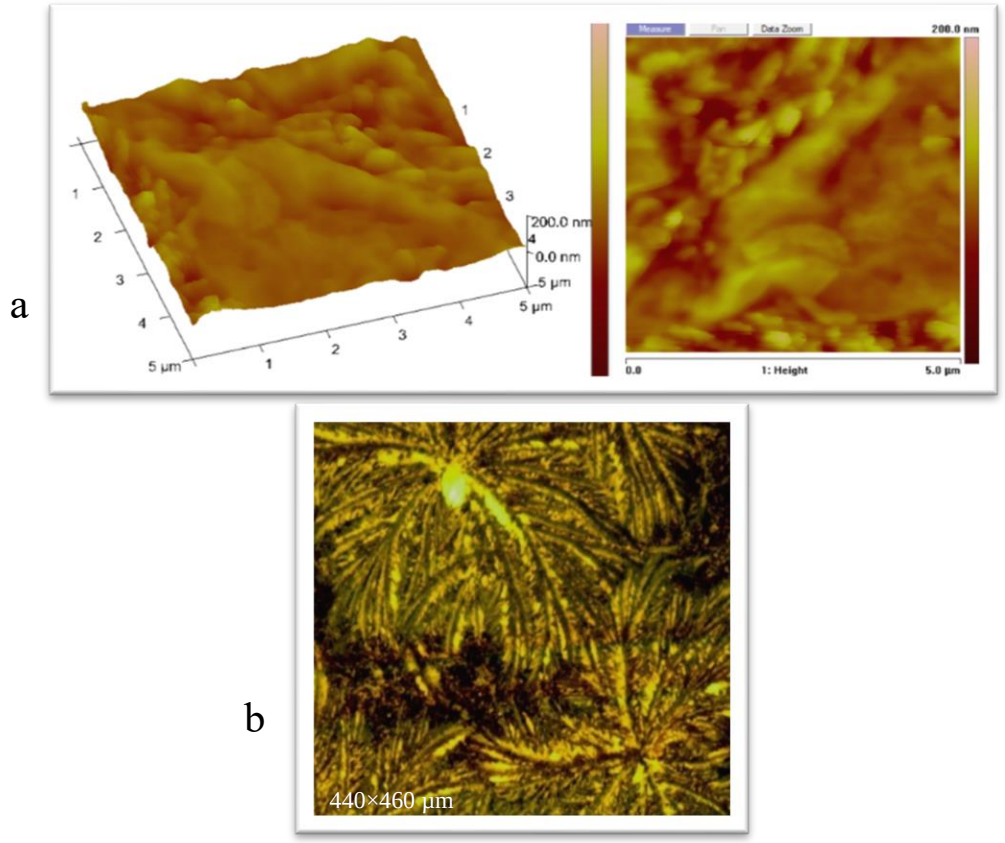

Figure 4. 4: *AFM images for (a) drop-costing Tips- pentacene layer (three dimensions image to the left and two dimensions image to the right). (b) Actual microscopic image of the Tips-pentacene layer drop-costed on cPMMA layer.*

4.2.3 Electrical characterization of OTFTs

Before studying the I-V characteristics of OTFT devices, the fabrication structure should be described. Glass substrates were used in this fabrication with slide dimensions of (25 mm x 15 mm), and each slide contains four devices as shown in Figure 4.1 (a). The four devices have the same channel width (1000 µm) and different channels lengths (50,100,150 and 200 µm). The drain-source electrode contacts were made of gold with an area of (5×10^{-3} cm^2). From the output and transfer plots, electrical parameters can be estimated for the transistor. Double sweep drain-source voltage and gate-source voltage were applied to investigate the current hysteresis in both output and transfer characteristics. Figure 4.5 (a) shows the

relationship between drain-source current (I_{DS}) and drain-source voltage (V_{DS}) from 0 to -50 V with a step of 2 V.

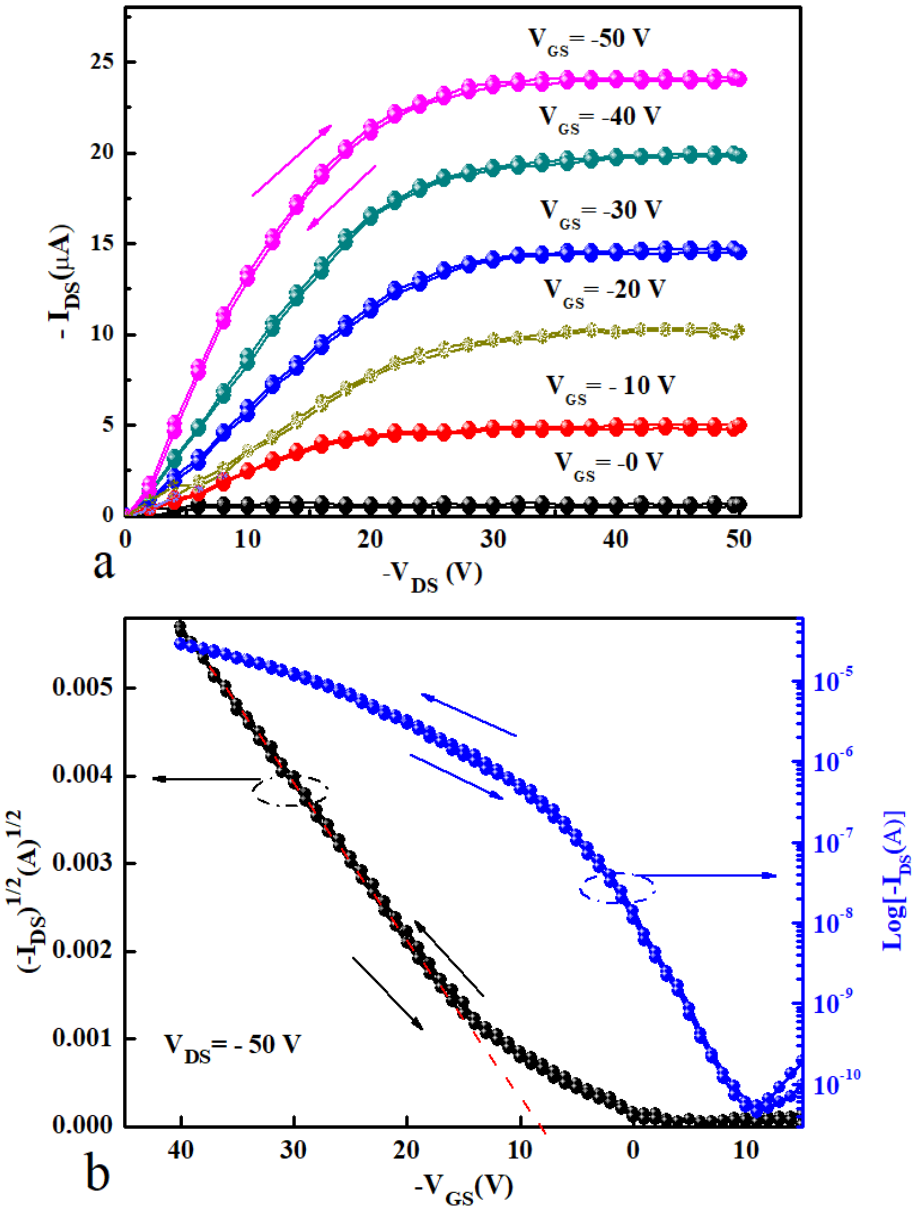

Figure 4. 5: *(a) Output and (b) Transfer characteristics of cPMMA- based OTFT using off-center deposition technique.*

The applied gate voltage was in the range of 0 to -50 V, which is increasing by 10 V each step. The field effect mobility in the saturation region can be estimated from the transfer plot in Figure 4.5 (b) using the mobility equation 4.1 [13,14].

$$I_{DS} = \frac{\mu W C_i}{2L}(V_{GS} - V_T)^2 \quad (4.1)$$

Where V_T is the threshold voltage (the minimum gate-source voltage V_{GS} required to create a drain-source current and turn on the transistor) and C_i is the insulator capacitance per unit area.

From Figure 4.5 (b) the threshold voltage V_T can be estimated by the intercept of the V_{GS} plot versus $(I_{DS})^{1/2}$. For the OTFT device in Figure 4.5, the estimated value for V_T is -8 V and on /Off current ratio is 7.2×10^5. The mobility μ in the saturation region was calculated, and it was found 1.42 $cm^2\ V^{-1}\ s^{-1}$. It is clear that all the devices gave a p-type field effect transistor (FET) behaviour. From Figure 4.5 (a) it can be seen that I_{DS} current increase linearly when the $V_{GS} > V_T$ for a small value of V_{DS}. Furthermore, the saturation region clearly obtained when $V_{DS} \geq V_{GS} - V_T$ and that can be observed from the pinch-off in the channel. The obtained relatively high mobility comes from the good interface between the organic semiconductor and the insulating layer. The output and transfer characteristics show no or negligible hysteresis, which is evidence of the improved surface morphology by using cross-linked insulating layer and ozone treating [15,16].

4.2.4 Repeatability and stability study of cPMMA- based OTFTs

For more investigation, the repeatability of the devices was studied with a similar procedure and fabrication method. In this study, all devices were fabricated and characterised to investigate the repeatability and stability of such devices. Sets of OTFTs were fabricated with the Al/cPMMA/TIPS/Au structure, and then the electrical characteristics were measured to calculate the mobility, threshold voltage, and on/off ratio. Herein, the insulator and semiconductor layers thickness are kept the same for all devices (330 nm and 60 nm respectively). Different channel lengths were used (50,100,150 and 200 μm). Table 4.1 illustrates several fabricated devices with actual measured channels length and their calculated parameters. The average mobility of these sets of devices is (1.35 $cm^2.v^{-1}\ s^{-1}$), and the highest and lowest obtained mobilities were 1.42 and 1.22 $cm^2.v^{-1}\ s^{-1}$, respectively. The attained mobility in this study is higher than the prior research works using TIPS-pentacene as an active layer [5, 9, 17,18]. Because molecular structure and morphology highly depend on the properties of the interface between semiconductor and insulator layer [19]. Therefore, the relatively high mobility can be attributed to the surface treatment and interface morphology, which results in higher carrier mobility due to a good interface

between the semiconductor and insulating layers [20,21] which has obtained from the high aliment and crystalline with a relatively low surface roughness of the deposited insulator layer using the off-centre spin-coating technique as shown in Figure 4.3. Furthermore, the average threshold voltage was found at 6.2 V with a minimum of 2 V and a maximum of 10 V. The average on/off ratio obtained is 3.8×10^5 with a minimum and maximum values of ($6.5. \times 10^4$, 7.5×10^5) respectively.

Table 4. 1: *The electrical parameter for several devices with a different channel length.*

Device	**μ ($cm^2 V^{-1} s^{-1}$)**	**On/off current ratio**	***V_T (V)***	***L (μm)***
D_1(4.3)*	1.42	7.2 x 10^5	-8	100
D_2	1.39	2.0 x 10^5	-10	98
D_3(4.6)*	1.36	1.6 x 10^5	-2	148
D_4(4.8)*	1.40	7.5 x 10^5	-4	145
D_5	1.35	7.0 x 10^5	-5	148
D_6	1.22	6.5. x 10^4	-6	198
D_7	1.36	8. x 10^4	-9	192

(*) refers to the figure's number of each device .

To study the stability, a set of devices were investigated and measured at a different time when they were stored under vacuum between measurements. For example, device (D_3) in Table 4.1 and shown in Figure 4.6 was investigated immediately after fabrication to calculate the electrical parameters. The channel length and width of this device are 148 μm and 1000 μm, respectively. The carrier mobility was found in the region of 1.36 $cm^2 V^{-1}s^{-1}$ with a threshold voltage of - 2 V and an on/off ratio of 1.6×10^5. These measurements were repeated after one month, three months, six months, and twelve months. All devices were kept under vacuum at room temperature (22 ± 1 Cº). Figure 4.7 displays the output (a) and transfer (b) characteristics for the same device (D_3) measured after 12 months. The results show high stability with minimal degradation in the mobility changing from 1.36 to 1.281 $cm^2 V^{-1} s^{-1}$ after 12 months. In addition, the on/off ratio was slightly decreased from 1.6×10^5 to 2.5×10^4. The threshold voltage showed a slight difference between -2 V and -6 V during this period. A negligible hysteresis was observed after storing the device for 12 months as shown in Figures 4.6 and 4.7. Table 4.2 describes the results of these

measurements after one, two, six and twelve months. All the measurements were performed under laboratory conditions at room temperature.

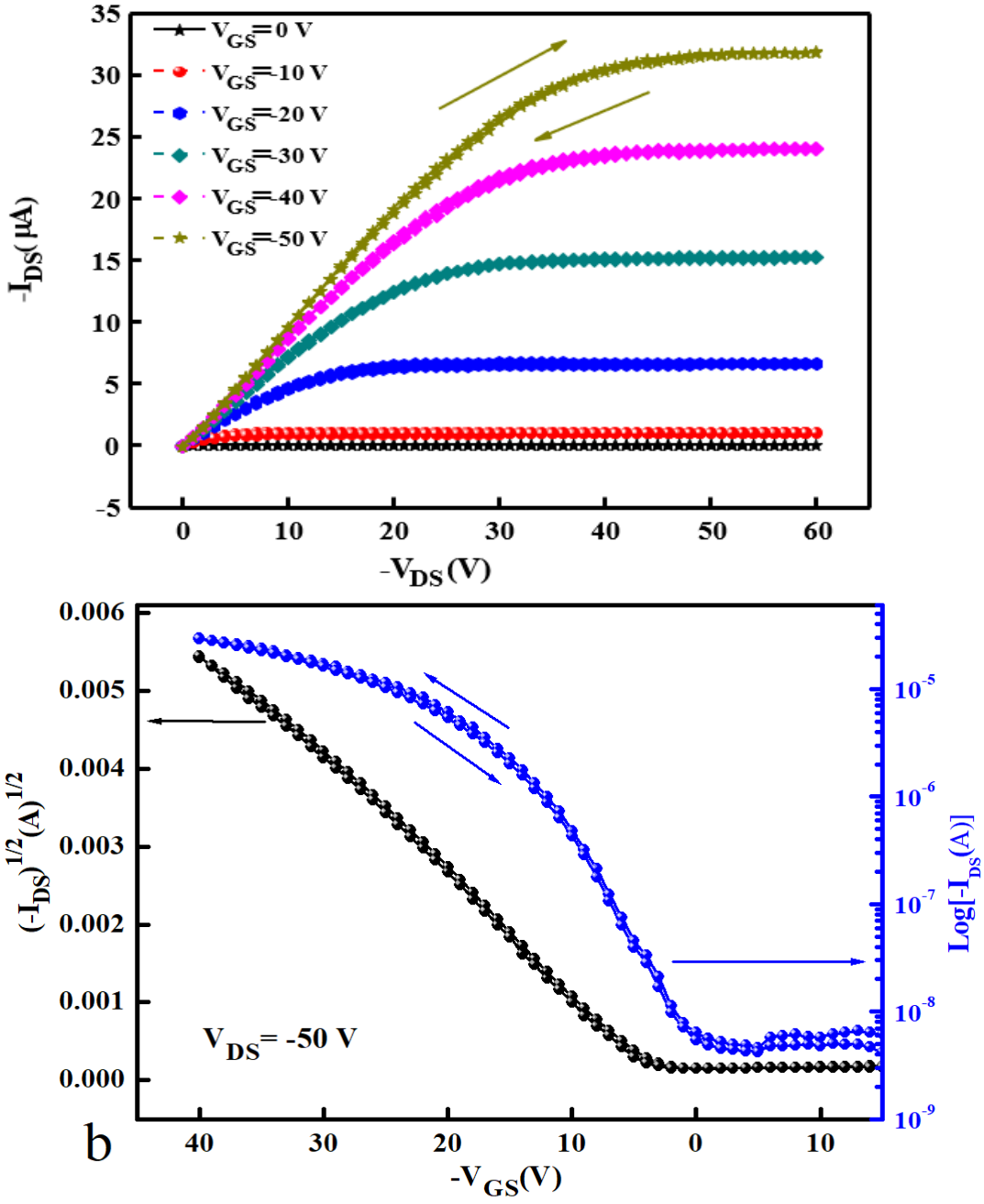

Figure 4. 6*: (a) Output and (b) Transfer characteristics of cPMMA- based OTFT immediately after fabrication.*

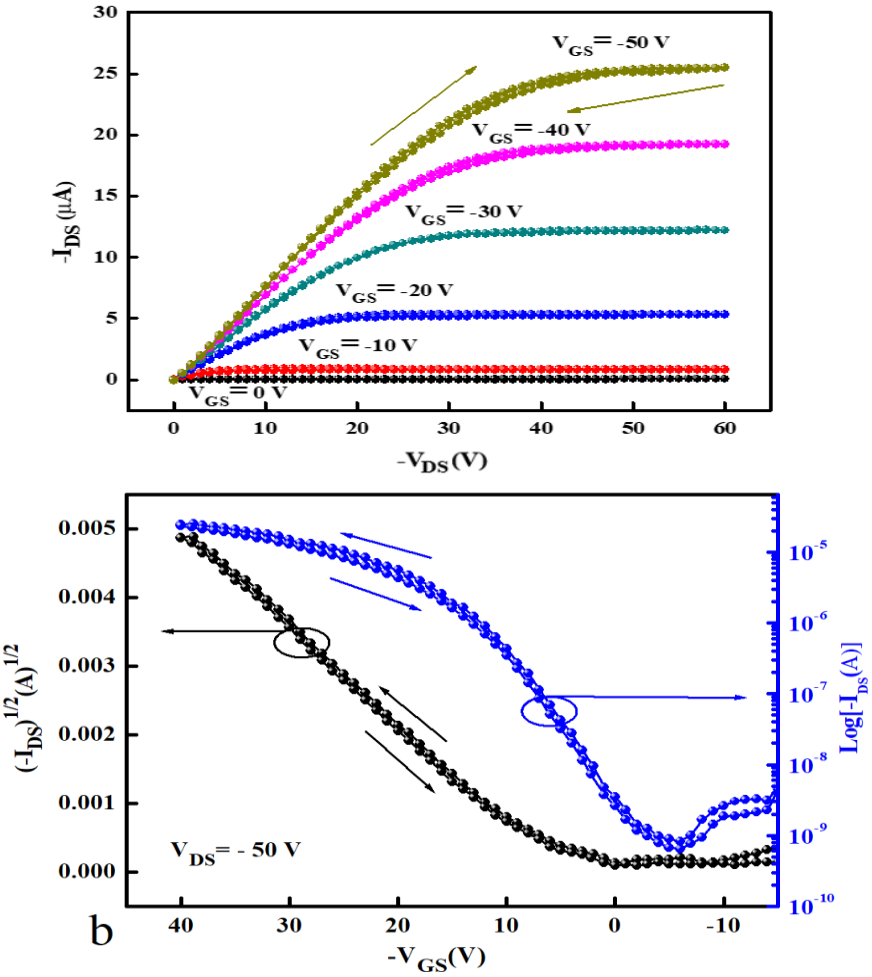

Figure 4. 7: *(a) Output and (b) Transfer characteristics of cPMMA- based OTFT 12 months under vacuum after fabrication (for device D_3).*

Table 4. 2: *Stability of devices after keeping under vacuum for a different storage time.*

Time of measurement	μ ($cm^2.V^{-1}\ s^{-1}$.)	On/off current ratio	$(V)_T$
Immediately after fabrication	1.36	1.6 x 10^5	-2
After 1 month	1.342	1.1 x 10^5	-4
After 3 months	1.31	1.6 x 10^5	-6
After 6 months	1.295	1.6 x 10^5	-7
After 12 months	1.281	2.5 x 10^4	-6

4.2.5 Bias stress effect on cPMMA-based OTFTs

In order to use OTFTs for practical applications, it is essential to study the effect of electrical stress. The degradation of devices over time is a barrier for extensive applications of OTFTs. In this section, three different electric bias stress were exploited to apply on TIPS-pentacene based OTFTs with cPMMA insulating layer. At first, we applied a fixed negative gate-source and drain-source voltage with different stress time to investigate the threshold voltage and the drain-source current behaviour after these conditions. Then, for the same device, a fixed time duration and drain-source potential were applied with different gate-source voltage stress. Finally, different drain-source stress voltages were applied with constant duration and fixed gate-source voltage. It was found that applying bias stress between the gate and source leads to a change in the charge transports properties such as decreasing of the channel current with dropping in charge carrier mobility resulting from the shift in the threshold voltage. In addition, hysteresis can be observed in the output and transfer characteristics. While the drain-source voltage bias stress affects the charge injection properties. Furthermore, the threshold voltage and drain-source current are more affected during the bias stress for most of OTFTs [17, 22, 23].

4.2.5.1 Initial test

To investigate the effect of bias stress on the OTFTs, the initial output and transfer characteristics were measured (immediately after fabrication) for a new device with the structure Al/cPMMA/TIPS-pentacene/Au. For this study, the output and transfer characteristics for device D_4 in Table 4.1 were measured, as shown in figure 4.8. From the device characteristics, the field-effect mobility, threshold voltage and on/off ratio for this device were found to be 1.40 $cm^2\ V^{-1}\ s^{-1}$, - 4 *V* and 7.5×10^5 respectively. Figure 4.8 (a) represents the output characteristics of device D_4 between drain-source voltage V_{DS} on the x-axis and the drain-source current I_{DS} on the Y-axis. The applied drain-source voltage range (V_{DS}) is from 0 V to - 60 V with a step of 1 V at a fixed gate-source voltage V_{GS} from 0 V to - 50 V with a step of -10 V. The transfers characteristics of the same device is shown in Figure 4.8 (b), which is the plot of the gate-source applied voltage V_{GS} in the range of 0 V to -60 V with a step of 1 V with respect to the square root of the associated drain-source

current $(I_{DS})^{1/2}$ at a constant drain-source voltage of -50 V. The channel length L and width W of the device under investigation are 145 µm and 1000 µm respectively. All the *I-V* characterisations were measured using a Keithley 2636 source meter at room temperature.

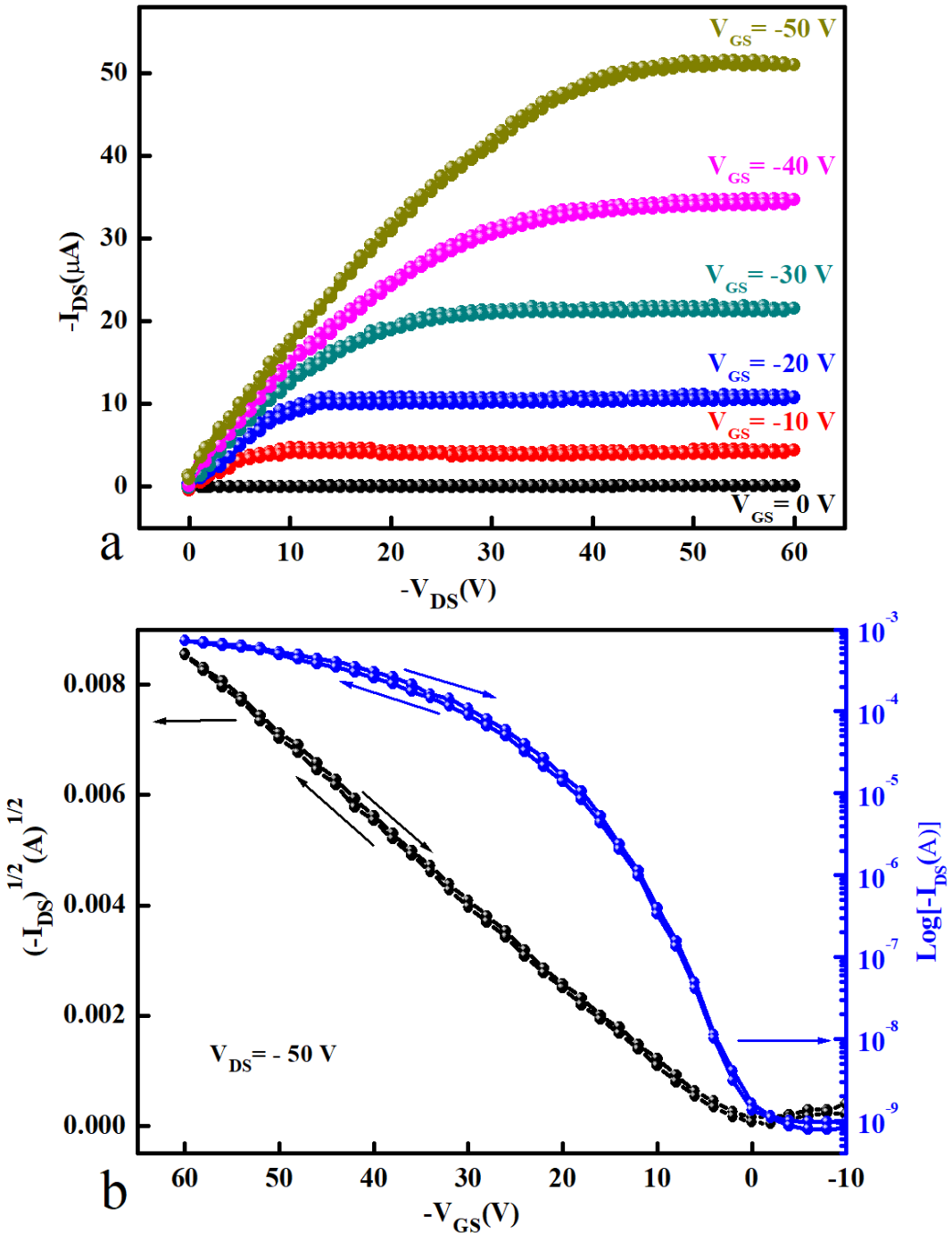

Figure 4. 8: *(a) Output and (b) Transfer of cPMMA- based OTFT Initial measurement of the device (D4)*

4.2.5.2 Gate bias-stress of -40 V at various stress time

It is common to use the change in threshold voltage ΔV_T to describe the effects of bias stress in OTFTs [24-26]. In this work, the same device D_4 as shown in Figure 4.8 was used to study the effect of applying a constant gate bias stress of -40 *V* on the *I-V* characteristics. This test was performed by applying different pulse durations of 0 s, 50 s, 100s, 1000 s, 5000 s and 10000 s. The applied gate-source voltage (base stress) of -40 *V* and drain-source of 0 *V* remained constant during each duration of bias stress. The transfer characteristics were measured after each stress time as per Figure 4.9 (a) and (d). Figure 4.9 (a) shows the transfer characteristics before and after bias stress for a different stress time. The gate voltage in x-axis ranging from 10 *V* to - 60 *V* against the square root of the drain-source current $(I_{DS})^{1/2}$ in the *Y*-axis under different stress time. It also shows the change in threshold voltage V_T for different stress time which is clearly moved to a higher voltage when a longer stress time is applied. The entire process was recorded under a fixed drain-source voltage of -50 V. It is also clear that no or negligible hysteresis was found even when applying bias stress for a longer time (10000 s). Figure 4.9 (b) is the enlarged version of data in Figure 4.9 (a) with a one direction sweep, where the gate voltage was shown from 0 V to -30 V. The logarithm scale Log ($-I_{DS}$) of Figure 4.9 (a) and 4.9 (b) has been shown in Figure 4.9 (c) and 4.9 (d), respectively. To analyses the effect of bias stress on threshold voltage shift [26-28], from the data reported in Figure 4.9 we can obtain a plot that represents the stress time vs threshold voltage change ΔV_T. Figure 4.10 represents the changes of threshold voltage and mobility as a function of stress time at a constant V_{GS}. With increasing the stress time, the threshold voltage increases to more negative values and the mobility decreases from 1.44 $cm^2\ V^{-1}\ s^{-1}$ as the initial value to 1.18 $cm^2\ V^{-1}\ s^{-1}$. The threshold voltage shift agrees with the stretched exponential function which define the threshold voltage shift dependence on time stress [29,30].

$$\Delta V_T = [V_T(\infty) - V_T(0)][1 - e^{-\left(\frac{t}{\tau}\right)\beta}] \qquad (4.2)$$

Where $V_T\ (0)$ is the initial state for the threshold voltage, $V_T(\infty)$ is the equilibrium state for the threshold voltage when ($t \rightarrow \infty$), β is the stretching parameter ($0 < \beta \leq 1$), and τ is the time constant. It is clear from Figure 4.10 that the exponential response for stress time beyond time constant τ (stress time > τ) is faster in comparing with that of lower stress time (stress time < τ). The effect of bias stress for a long time contributes to decreasing $I_{DS}(t)/I_{DS}(0)$ due to the carrier trapping located at or near the insulator /semiconductor interface,

which is resulting in a slower response. In this work, there is an agreement with other research [31,34] in the Threshold voltage shift depends on the bias stress as shown in figure 4.10 where the threshold voltage shift ΔV_T increased exponentially to 12 V in stress duration of 10^4 s.

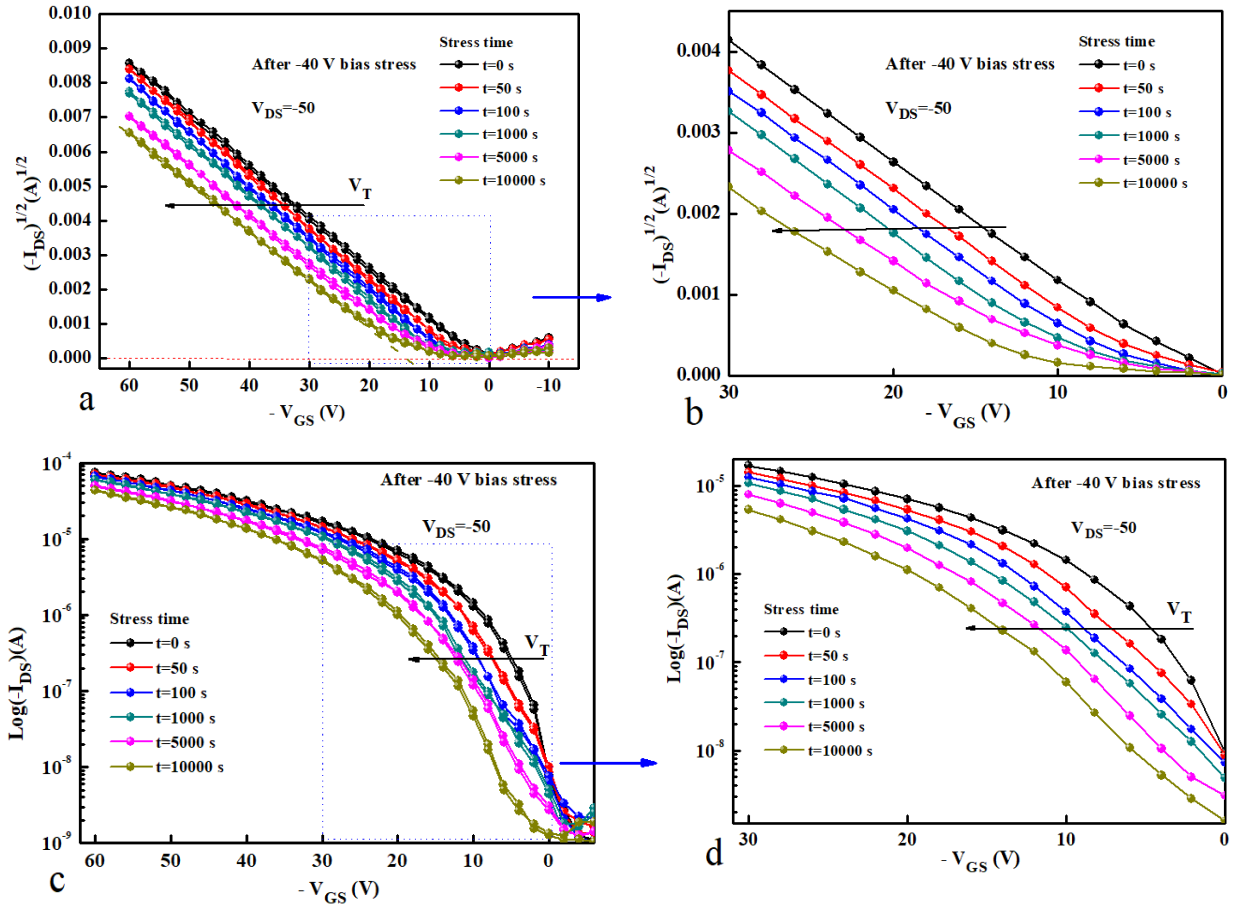

***Figure 4. 9**: (a) Transfer characteristics after bias stress at V_{GS} = -40 V at different stress time (t) (a) for $(I_{DS})^{1/2}$ versus V_{GS}. (b) the enlarged plot for (a) of the same data, (c) Log(-I_{DS}) versus V_{GS}. (d) the enlarged plot for (c) of the same data*

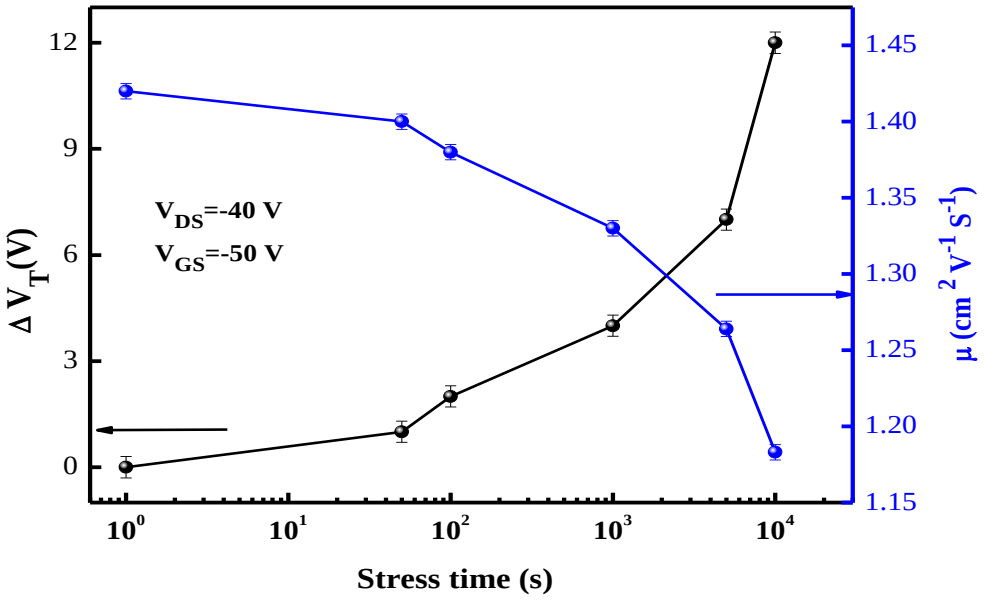

Figure 4.10: *The threshold voltage shift ΔV_T and saturation field-effect mobility μ versus stress time at V_{GS} = -50 V.*

4.2.5.3 Various gate bias-stress at 1000 s stress time

To investigate the dependence of V_T on gate bias stress V_{GS}, different V_{GS} stresses were applied (-20, -30, -40, -50, -60 V) to the device under test. A constant time stress of 1000 s was used in these measurements. The transfer characteristics were measured after applying each gate bias stress using a drain-source voltage of - 50 V. Figure 4.11 (a) shows a clear increase of the threshold voltage toward higher negative values when the gate bias stress increased. The V_T shift may be caused by the interface or near-interface charges, which are trapped electrons or holes near the dielectric/semiconductor interface [35,36]. Figure 4.11(a) shows clearly another evidence of device stability with no hysteresis in the transfer plot and the shape of the transfer characteristics did not change due to the stress voltage. The maximum threshold voltage obtained with bias stress of - 60 V is -18 V which producing ΔV_T = -14 V. *Figure* 4.11 (b) is the enlarged plot of figure 4.11 (a) with one direction sweep, from which we can see the apparent change in the threshold voltage during the gate bias-stress process.

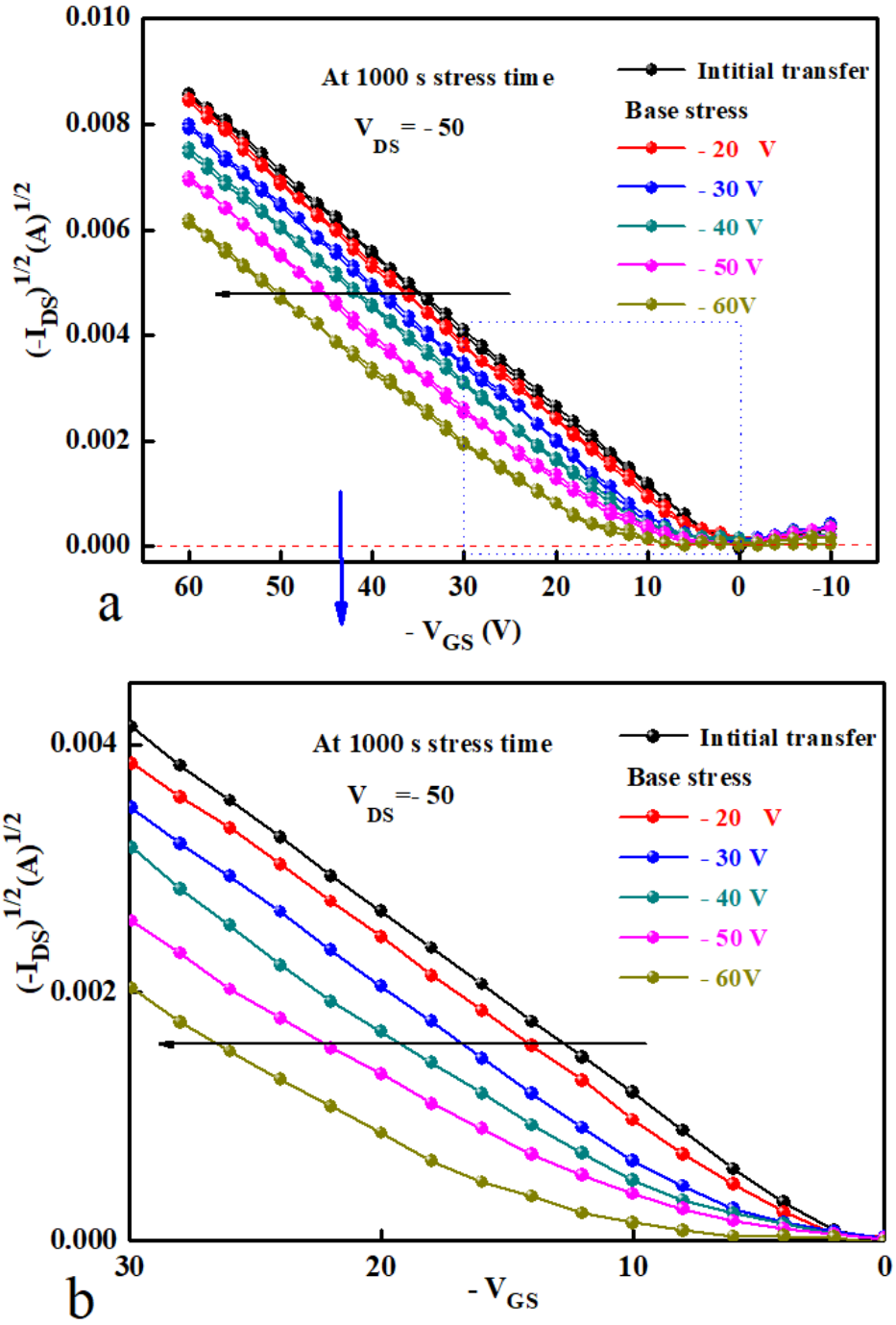

Figure 4. 11: *Transfer characteristics after different gate bias stress at stress time t = 10 0 s (a) for* $(I_{DS})^{1/2}$ *versus* V_{GS}*, (b) for the enlarged plot of the same data.*

These results agreed with previous works [2,37,38]. Figure 4.12 summarizes the gate bias stress-dependent of threshold voltage shift ΔV_T and saturation field-effect mobility μ of the OTFTs with a fixed stress time of 1000 s. It can be seen the decreasing in the mobility with a small amount (from 1.44 $cm^2\ V^{-1}\ s^{-1}$ to 1.15 $cm^2\ V^{-1}\ s^{-1}$) for a maximum gate bias stress of

-60 V. The bias-stress-induced deep charge trapping in the semiconductor/insulator interface [39,40] which participate in decreasing the field-effect mobility in OTFTs.

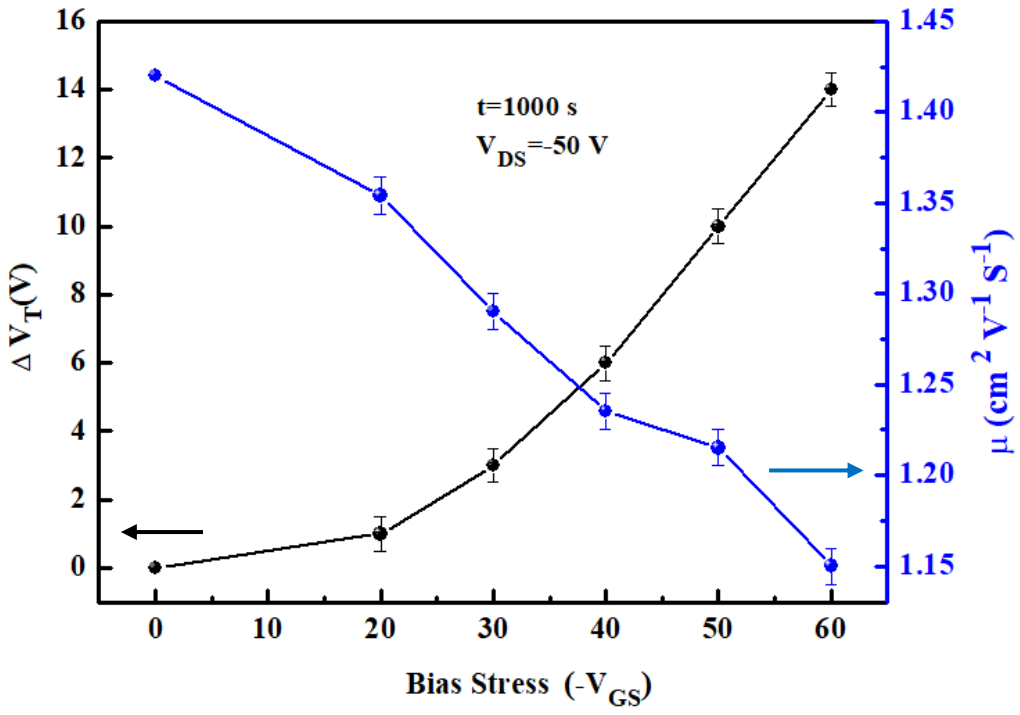

Figure 4. 12: *Saturation field-effect mobility and threshold voltage shift as a function of gate bias-stress at t=1000 s*

4.2.5.4 Various drain bias stress voltages at constants gate bias stress and stress time

In this section, various drain-source bias stress will apply (-10 V, -20 V, -30 V, - 40 V, -50 V) to study their effect on threshold voltage shift ΔV_T. A fixed stress time and gate voltage (and t = 1000 s V_{GS} = -50 V) were used to measure the transfer characteristics for each drain-source bias-stress. Figure 4.13 (a) represents these results with a double sweep of V_{GS} (from 10 V to - 60 V and then to 10 V). From this figure, it is clear that no hysteresis in the drain-source current even for high drain bias stress (-50 *V*), which is evidence for the high stability of the devices. Figure 4.13 (b) is the enlarged plot of the data (V_{GS} from 0 V to -30 V) in Figure 4.13 (a) which clearly shows the change in threshold voltage shift as a result of applying drain bias stress. Figure 4.14 illustrates the dependence of ΔV_T on the drain bias stress at a constant stress time of t = 1000 s and V_{GS} = - 50 V. The threshold voltage V_T increases when drain-sours bias stress increased. This result comes from the raising of trapped charges which are generated by the electric field across the channel as a result of

drain-source voltage. In the same time the constant gate bias -stress-induced deep charge trapping in the semiconductor/insulator interface, which participate with the drain stress in decreasing the field-effect mobility in OTFTs The larger V_{DS} produce a higher electric field between drain-source electrodes, which is counteract the main electric field produced by V_{GS}. As a result of this process, the trapped charge density around the drain contact will be reduced, which is decreased the ΔV_T [41,42].

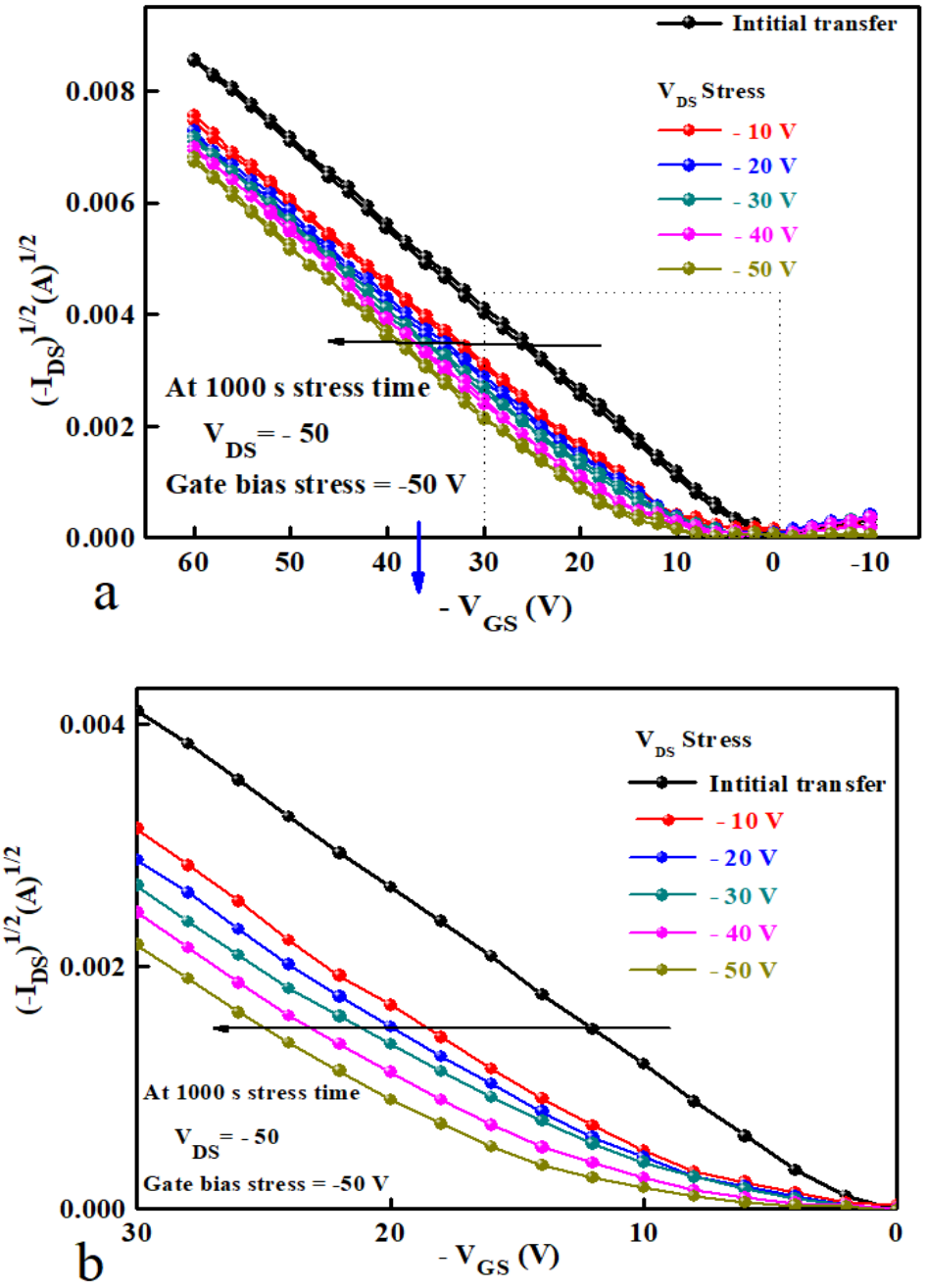

Figure 4. 13: *Transfer characteristics with applying varying drain-source voltages at V_{GS} = -50 V at stress time t=1000 s. (a) for $(I_{DS})^{1/2}$ versus V_{GS}, (b) for the enlarged plots of (a).*

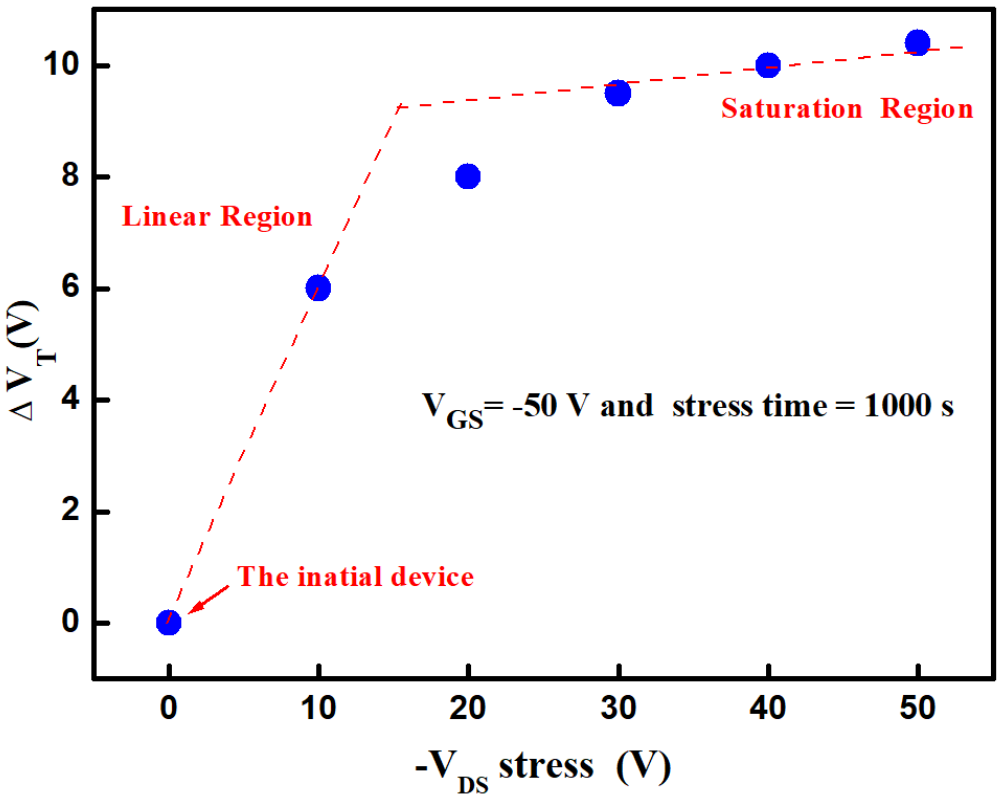

***Figure 4. 14**: Drain source-stress voltage versus threshold voltage shift ΔVT at t =1000 s and VGS = -50 V*

4.3 cPVA-based OTFT

4.3.1 Device fabrication

As in the previous work for cPMMA-based OTFTs, the same fabrication structure was used to fabricate cPVA-based OTFTs devices, as shown in Figure 4.15. For cross-linking polyvinyl alcohol, PVA 10 wt. % powder was dissolved in deionised water on a stirrer for 48 hours at 70 ^{o}C. Then, the PVA solution was filtered using a 0.45 µm syringe filter. Ammonium dichromate, 0.8 wt. % was added to the PVA solution as the cross-linking agent and was placed on a stirrer for 12 hours at a temperature of 65 ^{o}C. After that, the cPVA solution was filtered again using a 0.45 µm syringe filter to remove any accumulating particles. For the deposition of the insulating layer, the cPVA was spin-coated on the Al gate electrode with the same spin speed used for cPMMA insulating layer and annealed at 90 ^{o}C for 2 hours. The thickness of cPVA insulating layer was measured, and it was found

to be 400 ± 5 nm. Similar to cPMMA-based OTFTs, TIPS-pentacene (2% toluene solution) was drop-casted to provide a 60 nm active layer on the cPVA insulating layer. Then all devices were left under vacuum for 24 hours before thermally evaporated gold as drain-source contacts.

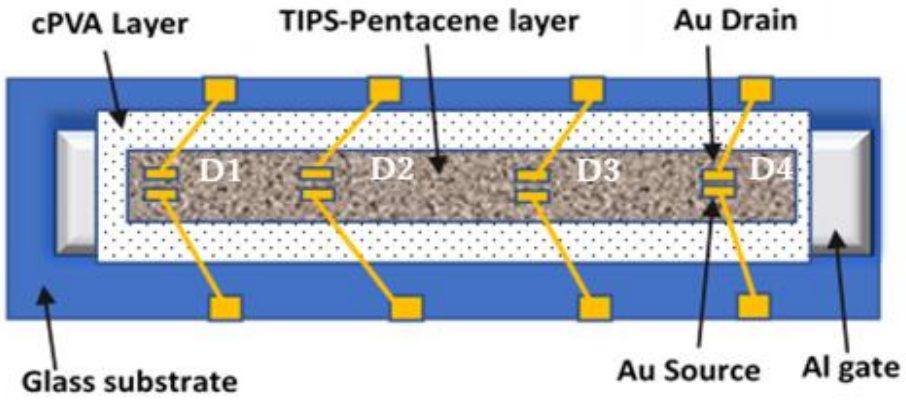

Figure 4. 15: *Schematic diagram of cPVA-based OTFTs structure*

4.3.2 Surface morphology and optimal parameters

Before starting the fabrication of cPVA-based OTFTs, a surface morphology study was performed for the cross-linking poly (vinyl alcohol) (cPVA) insulating layers and 6,13-Bis(triisopropyl-silylethynyl) pentacene (TIPS-pentacene) semiconductor layer using Atomic Force Microscopy as shown in Figures 4.16 and 4.17. Figure 4.16 (a) shows the AFM images (two and three dimensions) of cPVA layer which is deposited above an aluminium gate with a scan area of 5 µm. This layer was fabricated from 10 wt. % PVA using the on-centre spin-coating technique. The average roughness for this layer was found in the range of 4.9 nm. Figure 4.16 (b) shows AFM images (two and three dimensions) of the deposited cPVA layer using the off-centre spin-coating technique with an average roughness of 3.8 nm., It is clear that the surface roughness was decreased when the off-centre spin-coating technique has been used. Figure 4.17 (a) shows the AFM image of a 60 nm TIPS-pentacene semiconductor thin layer which is deposited using the drop-coasting method on 400 nm cPVA /50 nm Al layers (two and three dimensions). The average roughness of this layer was found around 18.8 nm. Figure 4.17 (b) displays the optical microscopic image for the same layer (with dimensions of 564 x 452 µm) which is showing the crystalline properties of the TIPS-pentacene layer.

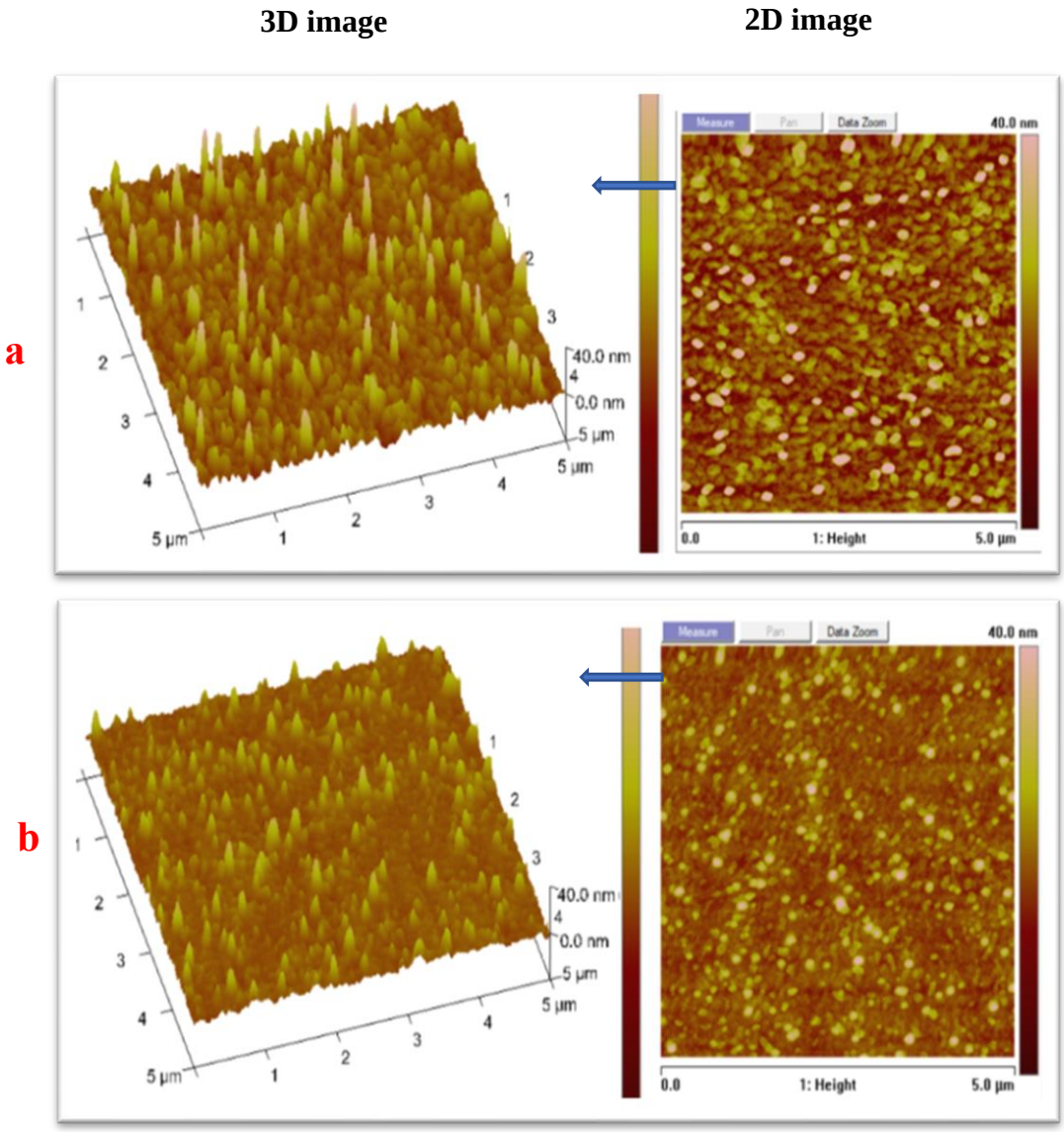

Figure 4. 16: *AFM of 400 nm cPVA layer spin-coated on 50 nm Al gate, (a) using on-centre spin-coating technique and (b) using off-centre spin-coating technique*

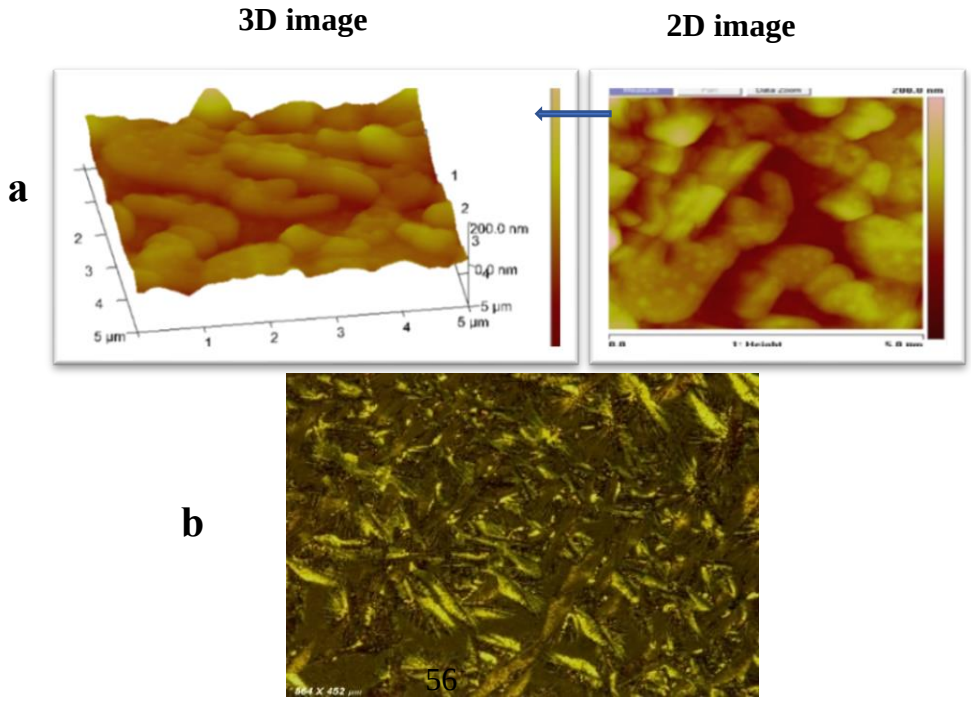

Figure 4. 17: *(a) AFM for 60 nm TIPS-pentacene drop coasted on cPVA/ Al, (b) the optical microscopic image for the same layer of TIPS-pentacene semiconductor (with dimensions of 564 × 452 µm)*

Different spin speeds were used to find the optimal thickness of the cross-linking poly (vinyl alcohol) (cPVA) insulator layer, as shown in Figure 4.18. Herein, it was found that 400 nm thickness of cPVA layer gives an effective behaver of OTFT. This thickness was achieved from a spin speed of 2000 rpm for 30 sec.

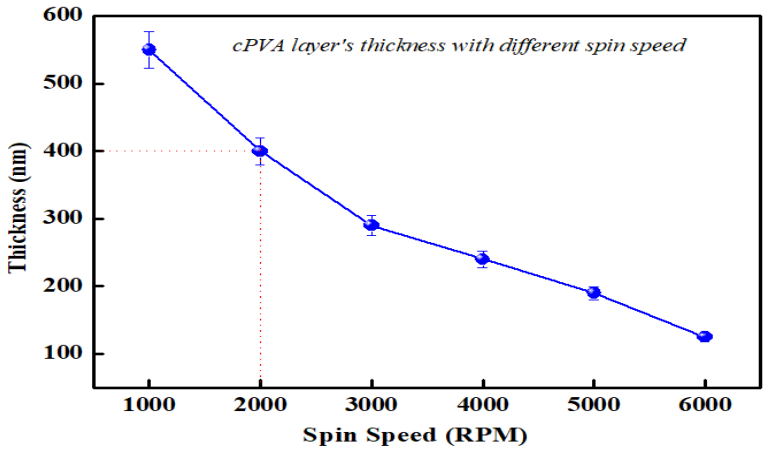

Figure 4. 18: *cPVA layer's thickness varies with the spin coating speed at a constant spin time of 30 s.*

In addition, the gold drain-source channels of the OTFTs were evaporated one day after the deposition of the active layer with a thickness of 50 nm. Drain-source voltage V_{DS} was applied with a double sweep (0 V to -40 V then to 0 V) to study the hysteresis effect on the output characteristics of the OTFT at different values of V_{GS} (0, -5, -10, -15, -20, -25, -30). From these measurements, it was found a low output current with clear hysteresis in the I_{DS} current as well as a large leakage current for PVA-based devices as shown in Figure 4.19. It is clear from Figure 4.19 that employing PVA as the insulating layer exhibited leakage current and no significant field effect mobility. To rectify this problem and produce hysteresis-free OTFTs, cross-linked PVA (cPVA) and off-centre spin-coating deposition technique were used to deposit the insulator layer. As shown in Figure 4.20 (a) and (b) where a clear output and transfer characteristics are observed. Therefore, in all our fabrications the cross-linked PVA insulating layer and the off-centre spin-coating technique will be used to produce OTFTs devices.

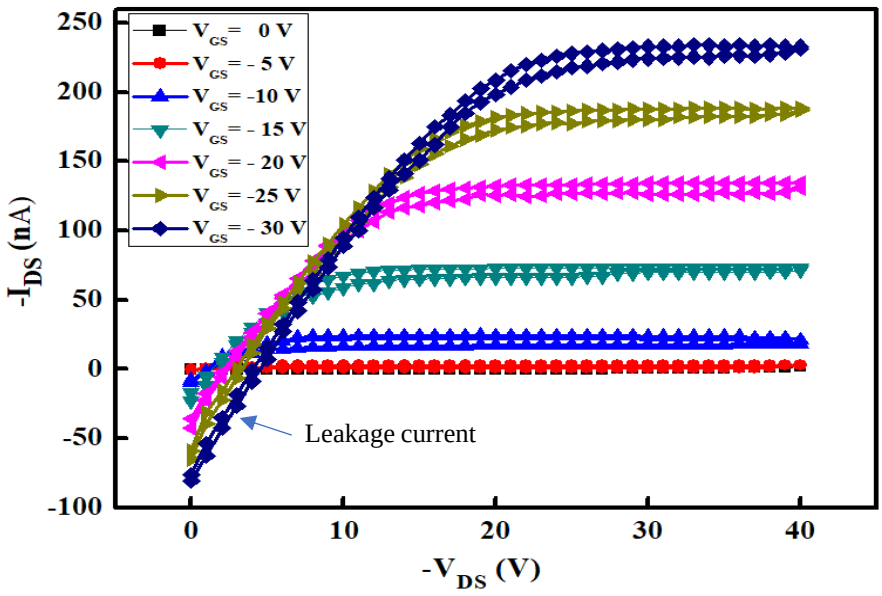

Figure 4. 19: Output characteristics of PVA-based OTFT

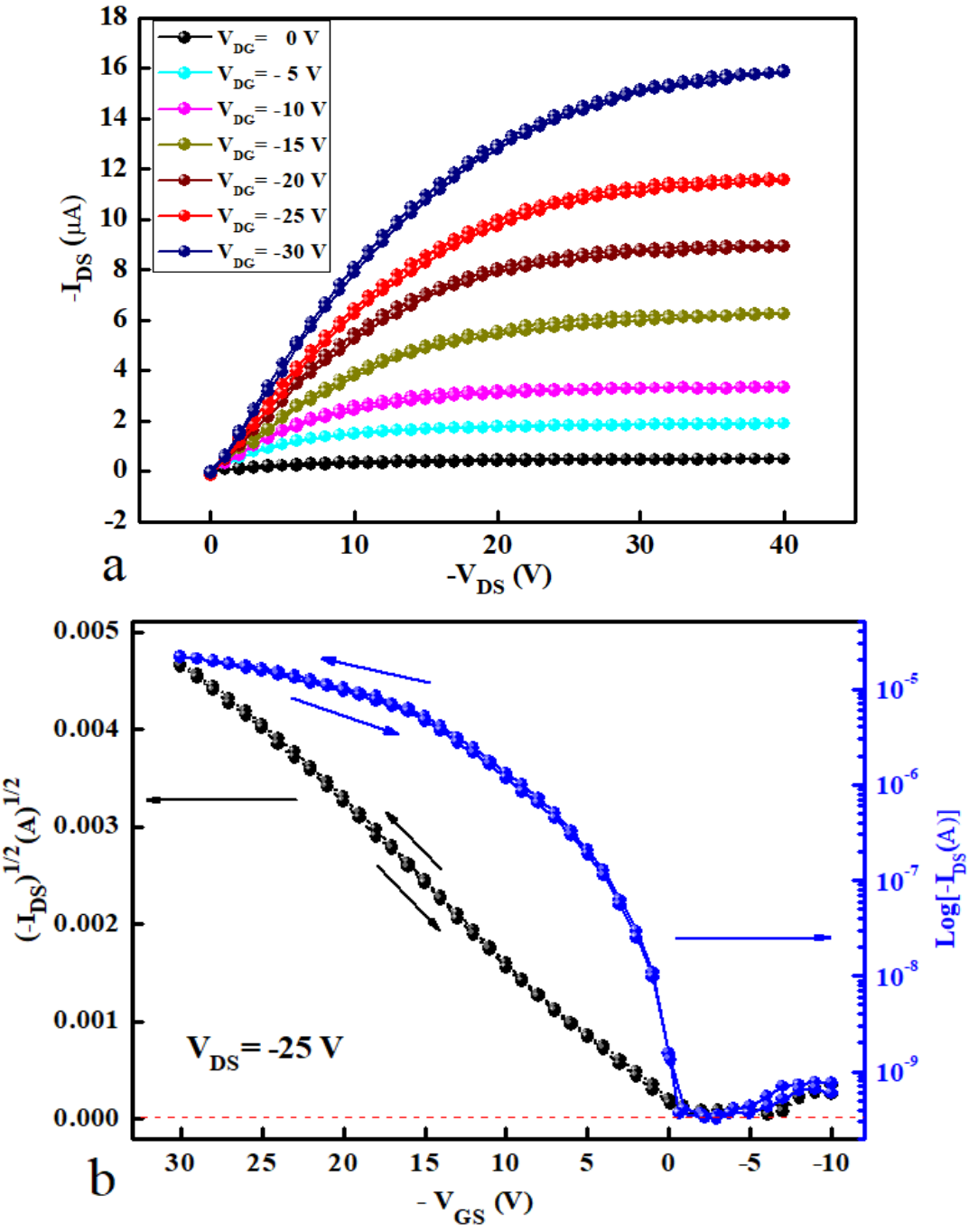

Figure 4. 20: *(a) Output characteristics and (b) transfer characteristics of OTFT using cross-linked PVA (cPVA)as an insulating layer.*

4.3.3 Electrical characterisation of OTFTs

To investigate the electrical characteristics of the cPVA-based OTFT's devices, it is essential to explain the structure of the glass slide at which devices were fabricated. As shown in Figure 4.15, there are four devices with different channel length for each sample. For the measurement purpose, the devices were given as (D_1, D_2, D_3 and D_4) as a reference. The channels length started from 50 µm for the device D_1 to 200 µm for D_4 with increasing of 50 µm respectively. While all the devices have the same channel width (W=1000 µm) and the area of the top Au electrodes was 5×10^{-3} cm^2. It was found that the actual channel length is different from the measurements above; this happened because of the evaporation alignment of the drain-source electrodes. To make the electrical characteristic measurement of the OTFTs devices more accurate, all the channel lengths were measured using optical microscopic images after the fabrication. In this work, all the devices were stored under vacuum and the measurements applied in air ambient using Keithley 3626B source meter. Figure 4.21 (a) shows the output characteristics of cPVA-based OTFT, a typical characteristic of p-type semiconductor-based transistor. The measurements were applied for the device D_2, which is representing the drain-source current (I_{DS}) variation with drain-source voltage (V_{DS}) in the range of (0 V to -60 V) with double sweep with applying different constant gate bias voltage from 0 V to -50 V. From the output characteristics in Figure 4.21 (a), the current increase linearly when the $V_{GS} > V_T$ for a small value of V_{DS}. Furthermore, the saturation region clearly obtained when $V_{DS} \geq V_{GS} - V_T$ and that can be observed from the pinch-off in the channel. Figure 4.21(b) illustrates the dependence of drain-source current (I_{DS}) on the gate-source voltage (V_{GS}) from (0 V to -50 V) with a fixed drain-source voltage (V_{DS}) of -40 V. The channel length and width of the devices under test are (150 µm and 1000 µm), respectively. The cPVA insulating layer thickness is 400 nm. From Figure 4.21 (b), The field effect mobility in the saturation region can be calculated using the mobility equation (4.1). Also, the threshold voltage V_T can be estimated from the intercept of V_{GS} plot versus $(I_{DS})^{1/2}$. In addition, On/Off current ratio was observed from the plot of V_{GS} versus log (I_{DS}). The obtained mobility, threshold voltage and on/off ratio for this device were estimated 1.13 $cm^2\ V^{-1}\ s^{-1}$, -6 V, and 4×10^4, respectively. Table 4.3 illustrates the four fabricated devices on one glass slide with their calculated parameters. The results in this investigation are very good in comparison with the other studies [5,43,44].

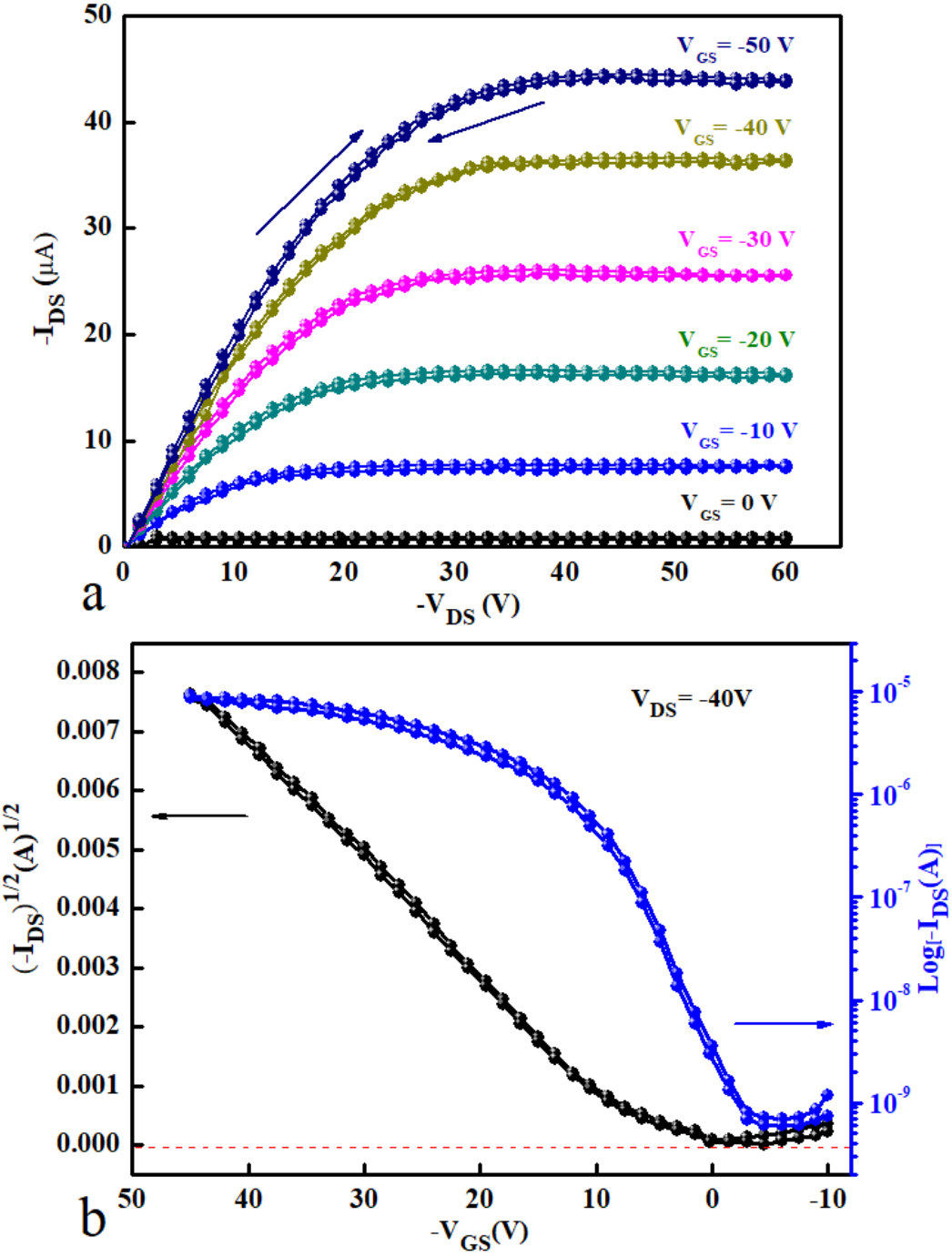

Figure 4. 21: *(a) Output and (b) Transfer of cPVA- based OTFT as a reference for the bias stress test. (D_2)*

4.3.4 Repeatability study of OTFTs fabrication

We made sure the electric behaviours of the OTFTs are similar under the same fabrication conditions and depend on the channel dimensions (*L* and *W*) and the applied voltages (V_{GS} and V_{DS}). The same fabrication method was used to fabricate a set of devices under the same environment. As shown in Table 4.3, under a fixed channel width (*W*= 1000 µm) and various channel length, the devices exhibit functional mobility, threshold voltage and on-off ratio. From table 4.3, it can be seen that the average mobility is 1.157 $cm^2 V^{-1} s^{-1}$ with a minimum and maximum of (1.06 and 1.22 $cm^2 V^{-1} s^{-1}$). Besides, the average threshold voltage and on /off ratio were found to be (4.25 *V* and 4.6 x 10^4) respectively. The minimum and maximum threshold voltage and on/off ratio were measured to be (-2 *V* and -6 *V*) and (1.32 x 10^4 and 8.6 x 10^4) respectively. This study produced a stable and high mobility cPVA-based OTFTs which is better than other studies, where Wei Huang *et al* [45] achieved current mobility of 0.024 $cm^2.V^{-1}s^{-1}$ and threshold voltage of 15.5 V with memory window of 9.1 V using PVA as insulator layer .And Zhuo-Ting Huang *et al* [46] achieved 0.33 $cm^2.V^{-1}s^{-1}$ and threshold voltage of 63 with on/off ratio of 10^2.

Table 4.3 : *The electrical parameters for a set of cPVA-based OTFTs measured directly after fabrication.*

Device	µ ($cm^2v^{-1} s^{-1}$)	On/off current ratio	V_T (V)	L (µm)
D_1	1.06	8.6×10^4	-2	198
D_2	1.13	4×10^4	-6	150
D_3	1.16	1.32×10^4	-4	148
D_4	1.22	4.5×10^4	-5	97

4.3.5 Bias stress effect in cPVA-based OTFTs devices

The stress response of OTFTs devices can be measured by study their behaviour with different bias stress. As for cPMMA-based OTFTs, three electrical stress condition were applied on the cPVA-based OTFTs to determine the threshold voltage and drain-source

current behaviour response after these conditions. First, a fixed negative gate-source and drain-source voltage with different time stress were applied. Then, a constant time stress duration and drain-source voltage with a different gate-source stress were used. Finally, applying a different drain-source voltages stress during a constant time and fixed gate-source voltage. Before these measurements, the initial test for a reference OTFT device was performed.

4.3.5.1 Initial test

As it was performed for the cPMMA-based OTFTs, the initial test of cPVA-based OTFTs must be measured before studying the response of these devices to bias stress. In this test, device (D_2) was used, and the transfer characteristics of the initial test are shown in figure 4.21 (b). The measurements were made in air ambient and room temperature (22 ± 1 ^{0}C) using a Keithley 2636 source meter.

4.3.5.2 Applying a gate bias-stress of -40 V at various stress time

In this test, a constant gate-source voltage (V_{GS}= -40 *V*) bias stress was applied to the OTFT device (D_2) for a different time duration (0, 50, 100, 500, 1000, 5000 and 10000 s). Drain-source voltage V_{DS} remained zero during the bias stress. After each period of stress, the transfers characteristics were measured by applying V_{GS} voltage from (10 *V* to -45 *V*) with a constant drain-source voltage of -40 *V* as shown in figure 4.22 (a). The behaver of the transfer curve still the same before and after applying the bias stress for a different period. It can be seen that the threshold voltage has increased and moved toward a high negative voltage after the bias stress was applied. Also, the stretched-exponential function Eq. 4.2 can be used to describe the threshold voltage depends on bias tress and stress time. Fuger 4.23 represents The saturation field effect mobility μ and threshold voltage as a function of versus stress time at a constant bias voltage V_{GS} = -40.

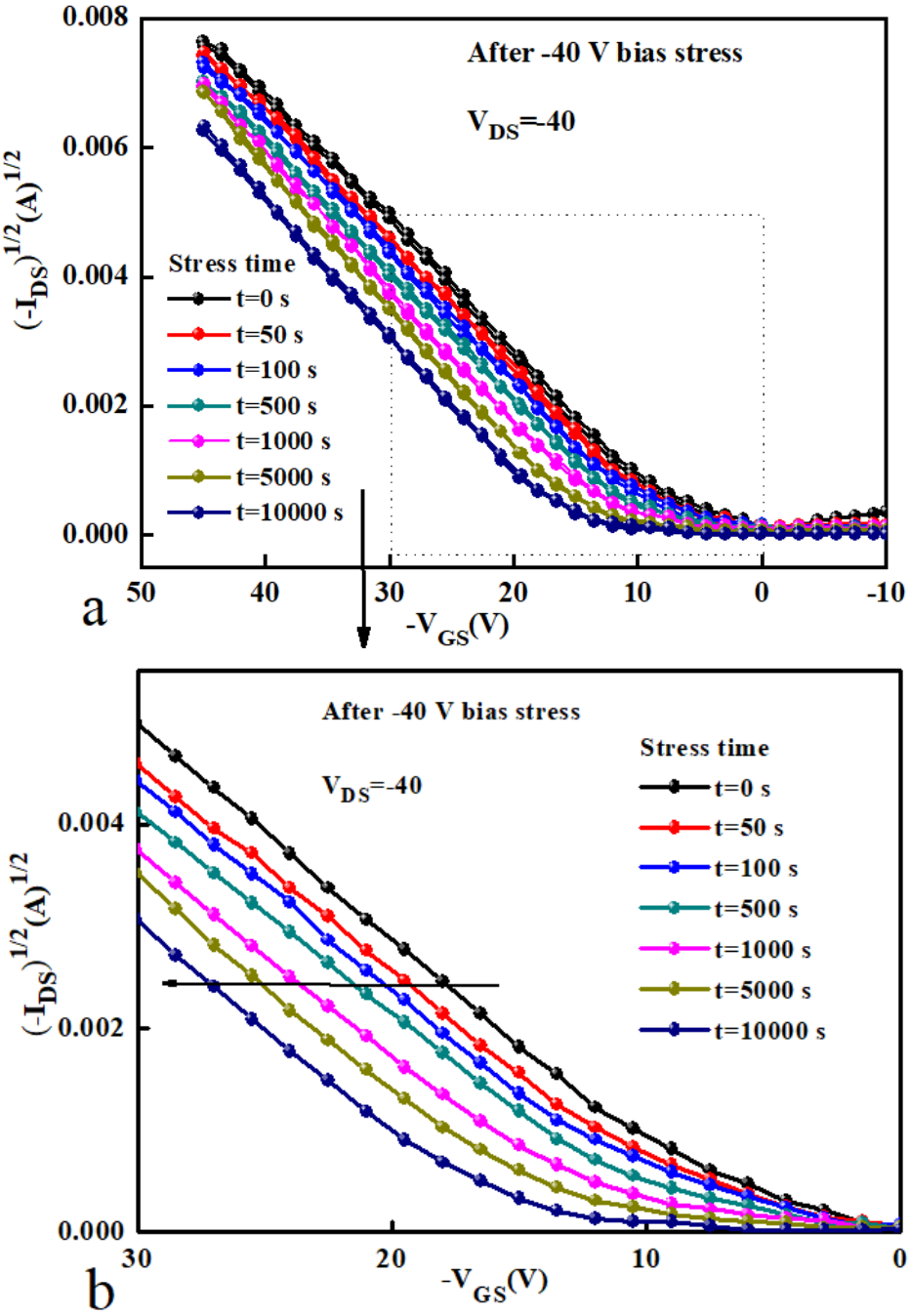

Figure 4. 22: *Transfer characteristics after bias stress at V_{GS} = -40 V at different stress time (t). (a) for $(I_{DS})^{1/2}$ versus V_{GS}, and (b) the enlarged plots of the same data in (a).*

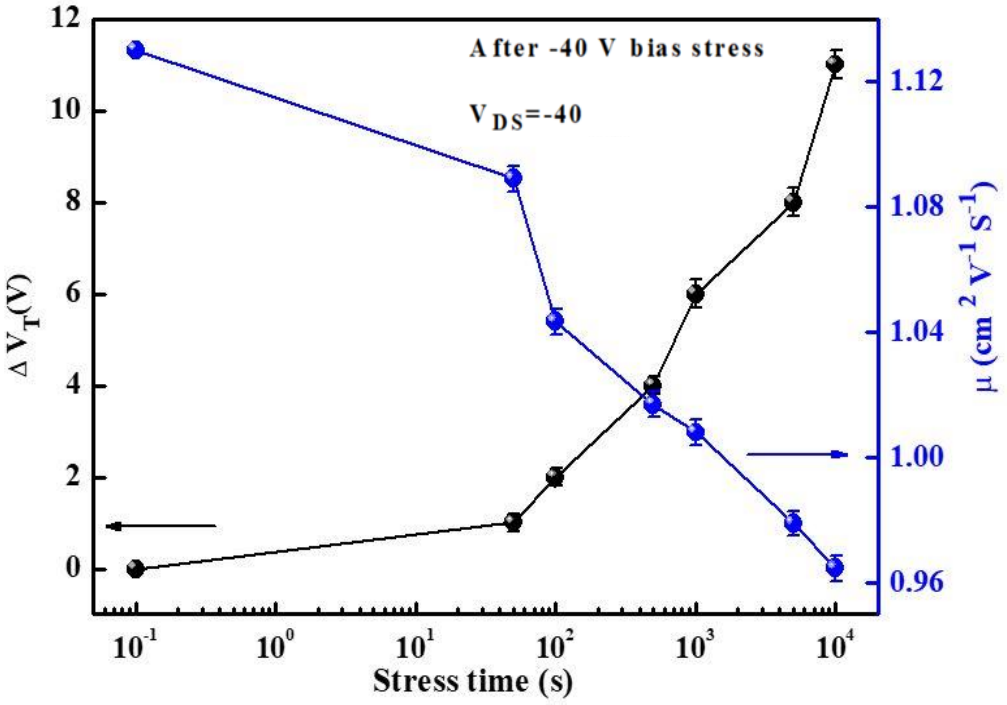

Figure 4. 23: *The saturation field effect mobility μ and threshold voltage as a function of versus stress time at* V_{GS} *= -40*

4.3.5.3 Applying various gate bias-stress at constant stress time and fixed drain-source voltage.

To study the effect of different bias stress V_{GS} on the threshold voltage shift, we obtained transfer curves at a fixed stress time and drain to source voltage of (1000 s and -40 *V*) respectively.

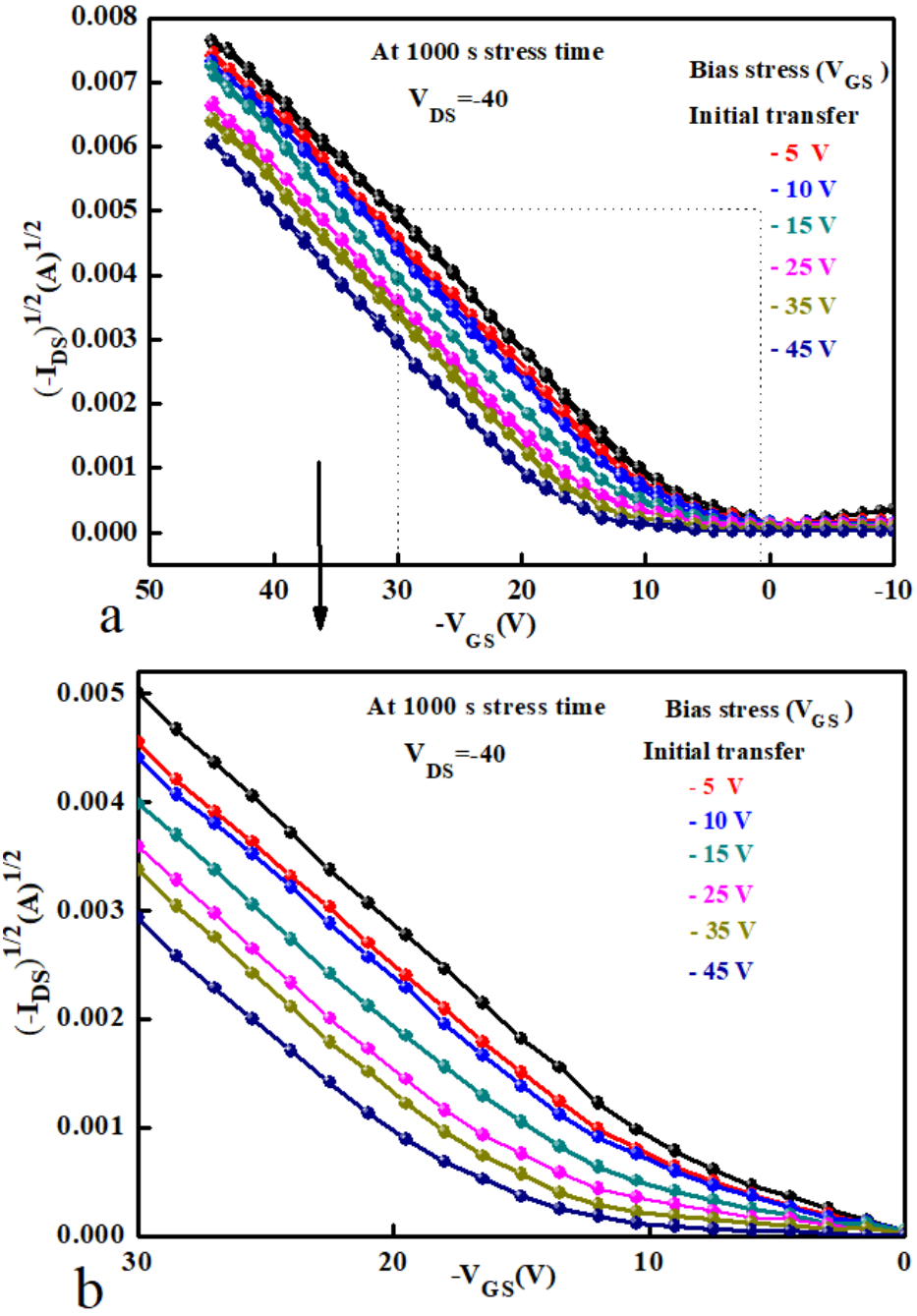

Figure 4. 24: *(a)Transfer characteristics before and after applying various gate bias stress at a constant stress time of 1000 s (b) enlarged data of (a).*

The gate to source voltage was modulated from -5 V to -45 V, as shown in Figure 4.24. Figure 4.24 (a) shows the transfer curves for the sample after each bias gate stress (-5, -10, -15, -25, -35, -45 *V*) and the enlarged data is represented in Figure 4.24 (b). Even after applying different bias stress, it can be seen that the shape of the transfer characteristic

curves still the same with a shift in the threshold voltages. The largest threshold voltage shift was obtained during this test is 10 V at bias stress -45 V. Figure 4.25 shows the threshold voltage shift and field-effect mobility dependence on the gate bias stress at a fixed stress time t=1000 s. Herein, the mobility slightly decreased (from 1.13 cm^2 V^{-1} s^{-1} to 0.935 cm^2 V^{-1} s^{-1}) due to the stress voltage. On the other hand, the threshold voltage shift was increased (from 0 *V* to 10 *V* at 45s stress time). It was found from several types of research, that a long time of discharging on OTFT leads to a change in the mobility and threshold voltage as well. This change comes from the effect of charge trapping in the interface between the active semiconductor layer and insulating layer [17,22,41].

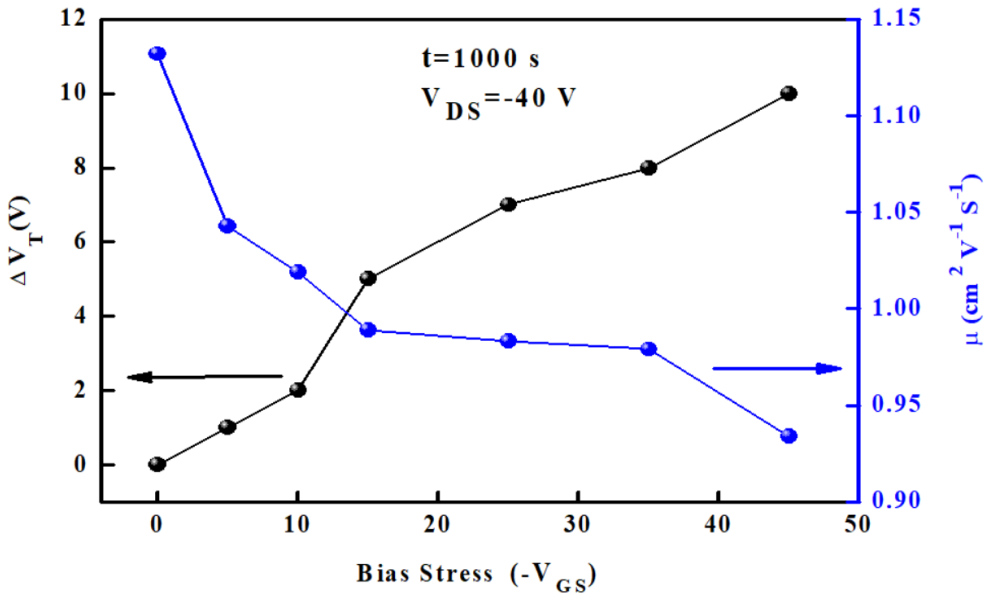

***Figure 4. 25**: (a) Threshold voltage shift ΔV_T and field-effect mobility μ as a function of gate bias stress at a constant stress time of 1000 s*

4. 3.5.4 Applying various drain bias stress voltage at a fixed stress time and gate bias stress.

In this test, the effect of V_{DS} bias stress on threshold voltage V_T has been studied. Figure 4.26 (a) shows the transfer curve before and after applying a different drain bias stress (0, 15, 25, 35, 45, 50 *V*) with a constant stress time of 1000 *s*. It is clear that the V_T increased when increasing the drain bias stress. Also, it has been observed that, no or negligible hysteresis and the same shape in double sweep transfer characteristics, which mean a good interface surface between the insulating layer and semiconductor. Figure 4.27 illustrates the

change in threshold voltage shift as a result of applying various drain-source bias stress. The threshold voltage shift started to change slowly and a linear-like at a small amount of drain-source voltage stress, comparing with the effect of gate bias stress, which is highly increased when the gate-source bias is increasing. This behaviour can happen from the charge trapping in the insulating-semiconductor interface. The low V_{DS} stress contributes to the release of the charge trapping, which decreases the charge transport through the insulating-semiconductor layers interface.

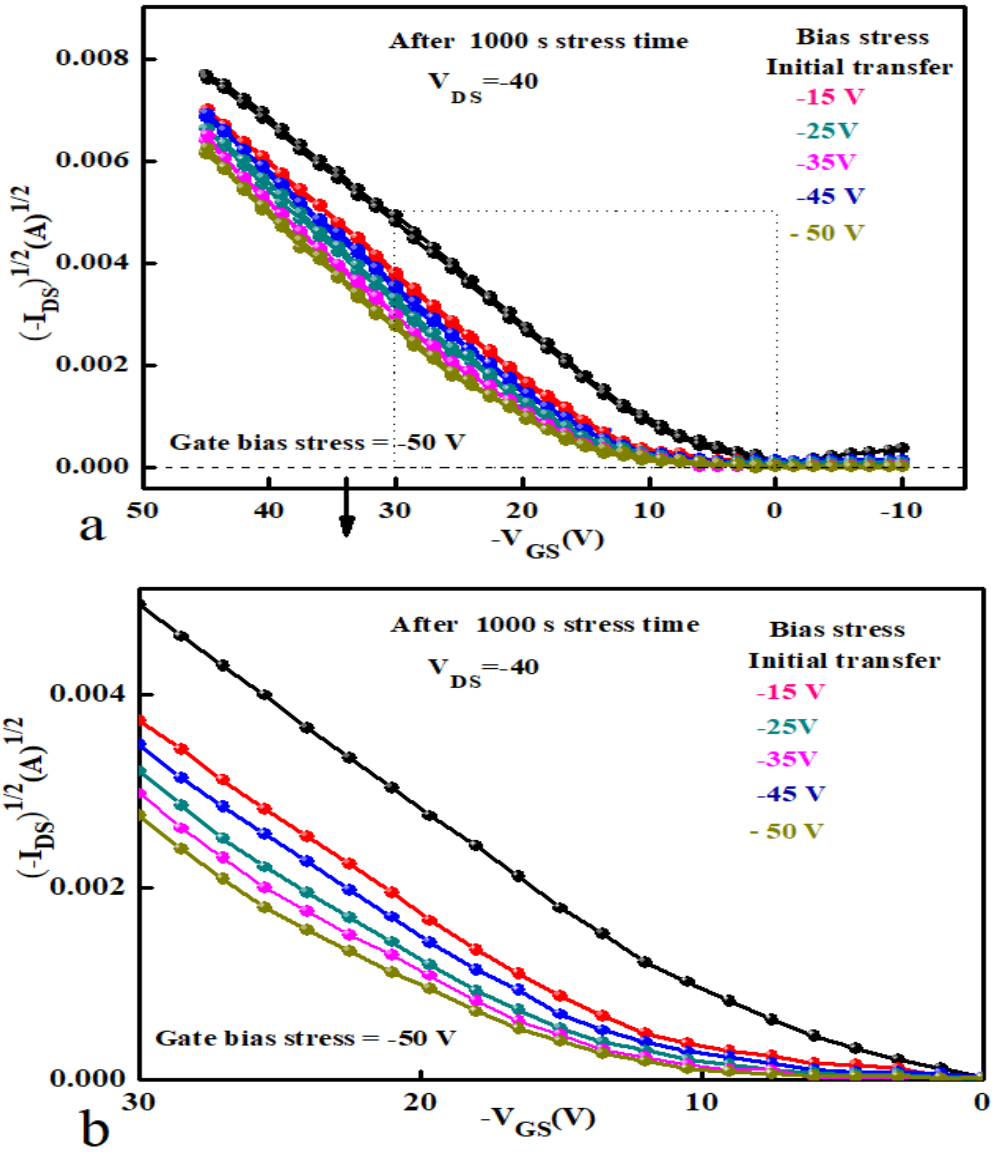

Figure 4. 26: *(a)Transfer characteristics before and after applying various drain-source voltage stress at a fixed stress time 1000 s and V_{GS}=-50 V. (b) represent the enlarged data in (a)*

For the higher V_{DS} bias stress, an electric field will be produced against the V_{GS} field and contribute to reducing the charge carrier in the OTFT channel leading to a small change in threshold voltage [47,48].

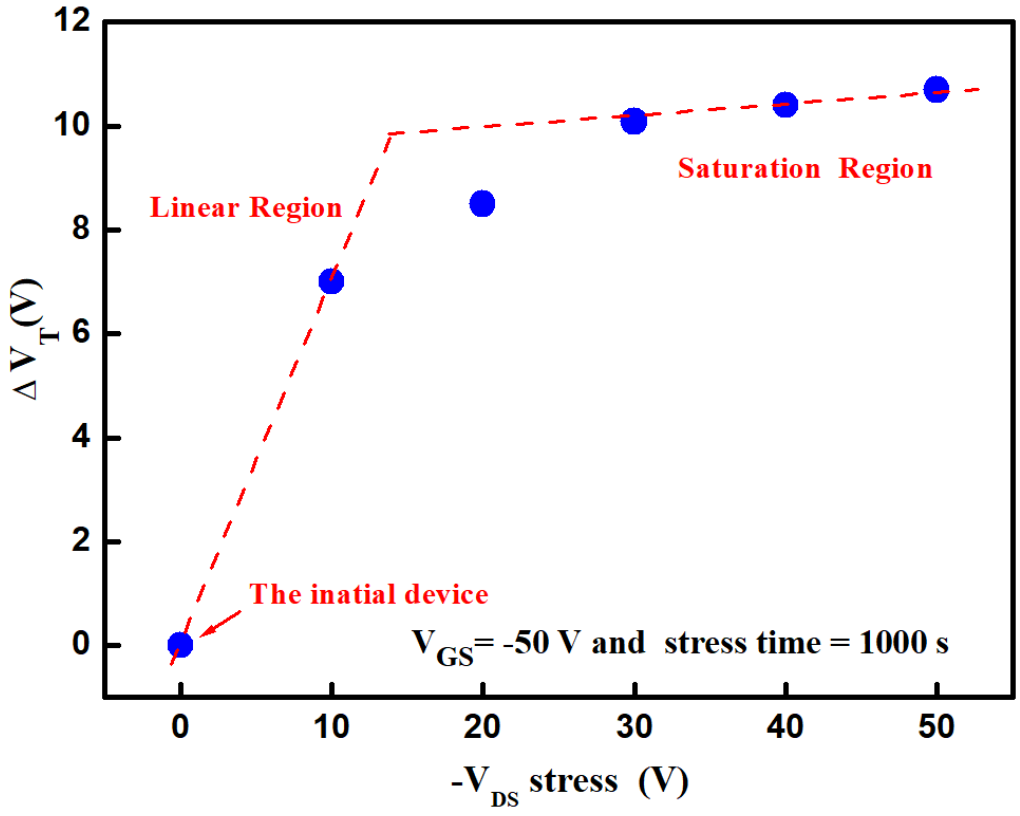

Figure 4. 27: *The effect of drain-source stress voltage on threshold voltage shift at VGS= -50 V and t= 1000 s.*

4.4 Summary

Two types of OTFTs were fabricated, PMMA-based and PVA-based OTFTs. Solution-based TIPS-pentacene was used as an active semiconductor layer. All devices were fabricated with a bottom-gate, top-contact (BG-TC) configuration. The investigation study of these devices showed low output current, high leakage current and clear hysteresis in the double sweep measurement. Further work was done to solve these problems. Cross-linking PMMA and PVA (cPMMA and cPVA) were used as an insulating layer instead of PMMA and PVA. Very good OTFTs behaviours without leakage current and hysteresis were a chivvied. The results showed high mobility, on/off ratio and with low threshold voltage for both types of OTFTs. For the cPMMA-base devices, the high mobility obtained was 1.42

$cm^2\ V^{-1}s^{-1}$ with threshold voltage and on/off ratio of (-8 V and 7.2×10^5) respectively. Otherwise, the cPVA-based devices attained a high mobility, threshold voltage and on/off ratio of ($1.22\ cm^2\ V^{-1}s^{-1}$, -5V and 4.5×10^4) respectively. By comparing the two types of OTFTs, cPMMA-based OTFTs are the highest mobility, and it can be good candidate for the TIPS-pentacene based OTFTs. Three different bias stresses were applied to study the endurance of these devices. The main thing in this fabrication is the solution-based semiconductor layer, which is made by the drop-coasting method instead of the thermal evaporation method.

All the devices in this study showed no hysteresis, which is a significant achievement. Also, all test measurements were done in the room temperature and lab environment, which gives evidence of the stability of devices. The stability of longer time storage for the devices was studied after one year of storage under vacuum, which is showed slightly degeneration the field-effect mobility and output saturation current with a very good operation for most of the devices. The repeatability of the devices was studied by fabrication more than one set of devices with the same fabrication procedure, and the results show very close parameters for all the devices under investigation.

4.5 References

[1] B. Jung, A. Lim, H. S. Lee, W. H. Lee, and K. Cho, "Control of the Morphology and Structural Development of Solution-Processed Functionalized Acenes for High-Performance Organic Transistors," pp. 1515–1525, 2009, doi: 10.1002/adfm.200801135.

[2] J. H. Kwon, X. Zhang, S. H. Piao, H. J. Choi, J. H. Bae, and J. Park, "Stability study of flexible 6,13-bis(triisopropylsilylethynyl)pentacene thin-film transistors with a cross-linked poly(4-vinylphenol)/yttrium oxide nanocomposite gate Insulator," *Polymers (Basel).*, vol. 8, no. 3, pp. 1–9, 2016, doi: 10.3390/polym8030088.

[3] T. N. Jackson, S. K. Park, T. N. Jackson, J. E. Anthony, and D. A. Mourey, "High mobility solution processed 6,13-bis(triisopropyl-silylethynyl) pentacene organic thin film transistors," *Appl. Phys. Lett.*, vol. 91, no. 6, pp. 6–9, 2007, doi: 10.1063/1.2768934.

[4] H. T. Page, J. H. J.-H. Kwon, X. X. Zhang, S. H. Piao, H. J. Choi, J. H. Bae, J. Park, J. M. Gohil, A. Bhattacharya, P. Ray, J. Veres, S. Ogier, G. Lloyd, D. M. De Leeuw, "A Facile Photo-cross-linking Method for Polymer Gate Dielectrics and Their Applications in Fully Solution Processed Low Voltage Organic Field-effect Transistors on Plastic Substrate," *Appl. Phys. Lett.*, vol. 19, no. 8, pp. 918–924, 2018, doi: 10.1007/s10118-018-2110-2.

[5] S. Il Shin, J. H. Kwon, H. Kang, and B. K. Ju, "Solution-processed 6,13-bis(triisopropylsilylethynyl) (TIPS) pentacene thin-film transistors with a polymer dielectric on a flexible substrate," *Semicond. Sci. Technol.*, vol. 23, no. 8, p. 085009, 2008, doi: 10.1088/0268-1242/23/8/085009.

[6] S. Ma, G. Zhang, F. Wang, Y. Dai, H. Lu, L. Qiu, Y. Ding, and K. Cho, "Tuning the Energy Levels of Aza-Heterocycle-Based Polymers for Long-Term n-Channel Bottom-Gate/Top-Contact Polymer Transistors," *Macromolecules*, vol. 51, no. 15, pp. 5704–5712, 2018.

[7] S. Ohmi, M. Hiroki, K. E. Park, and Y. Maeda, "Scaling of top-gate/bottom-contact pentacene-based organic field-effect transistors with amorphous rubrene gate insulator," *Jpn. J. Appl. Phys.*, vol. 58, no. SB, p. SBBG01, 2019.

[8] Y. Liu, J. Q. Zhao, W. J. Sun, Y. K. Huang, S. J. Chen, X. J. Guo, and Q. Zhang, "A Facile Photo-cross-linking Method for Polymer Gate Dielectrics and Their Applications in Fully Solution Processed Low Voltage Organic Field-effect Transistors on Plastic Substrate," *Chinese J. Polym. Sci. (English Ed.*, vol. 36, no. 8, pp. 918–924, 2018, doi: 10.1007/s10118-018-2110-2.

[9] A. You, M. A. Y. Be, and I. In, "Bias stress in organic thin-film transistors and logic gates," vol. 1124, no. August 2001, 2007, doi: 10.1063/1.1394718.

[10] Y. Yuan, G. Giri, A. L. Ayzner, A. P. Zoombelt, S. C. B. Mannsfeld, J. Chen, D. Nordlund, M. F. Toney, J. Huang, and Z. Bao, "Ultra-high mobility transparent organic thin film transistors grown by an off-centre spin- coating method Ultra-high mobility transparent organic thin film transistors grown by an off-centre spin-coating method," *Nat. Commun.*, vol. 5, no. January, pp. 1–9, 2014, doi: 10.1038/ncomms4005.

[11] W. Weber, "High-mobility polymer gate dielectric pentacene thin film transistors," vol. 5259, no. June 2002, pp. 1–6, 2007, doi: 10.1063/1.1511826.

[12] Y. H. Ting, C. C. Liu, S. M. Park, H. Jiang, P. F. Nealey, and A. E. Wendt, "Surface roughening of polystyrene and poly(methyl methacrylate) in Ar/O2 plasma etching," *Polymers (Basel).*, vol. 2, no. 4, pp. 649–663, 2010, doi: 10.3390/polym2040649.

[13] Y. Yun, C. Pearson, and M. C. Petty, "Pentacene thin film transistors with a poly(methyl methacrylate) gate dielectric: Optimization of device performance," *J. Appl. Phys.*, vol. 105, no. 3, 2009, doi: 10.1063/1.3075616.

[14] X. Jia, C. Fuentes-hernandez, C. Y. Wang, Y. Park, B. Kippelen, C. Reese, M. Roberts, M. Ling, Z. Bao, H. Klauk, G. H. Gelinck, E. Van Veenendaal, R. Coehoorn, and T. Zaki, "Organic thin-film transistors," *Mater. Today*, vol. 87, no. 7, pp. 20–27, 2004, doi: 10.1126/sciadv.aao1705.

[15] E. Orgiu, S. Locci, B. Fraboni, E. Scavetta, P. Lugli, and A. Bonfiglio, "Analysis of the hysteresis in organic thin-film transistors with polymeric gate dielectric," *Org. Electron. physics, Mater. Appl.*, vol. 12, no. 3, pp. 477–485, 2011, doi: 10.1016/j.orgel.2010.12.014.

[16] F. M. Li, A. Nathan, Y. Wu, and B. S. Ong, *Organic Thin Film Transistor Integration*. 2011.

[17] K. K. Ryu, I. Nausieda, D. Da He, A. I. Akinwande, V. Bulovic, C. G. Sodini, V. Bulović, and C. G. Sodini, "Bias-Stress Effect in Pentacene Organic Thin-Film Transistors," *IEEE Trans. Electron Devices*, vol. 57, no. 5, pp. 1003–1008, May 2010, doi: 10.1109/TED.2010.2044282. [18] D. Choi, B. Ahn, S. H. Kim, K. Hong, M. Ree, and C. E. Park, "High-performance triisopropylsilylethynyl pentacene transistors via spin coating with a crystallization-assisting layer," *ACS Appl. Mater. Interfaces*, vol. 4, no. 1, pp. 117–122, 2012, doi: 10.1021/am201074n.

[19] Y. Don Park, J. A. Lim, H. S. Lee, and K. Cho, "Interface engineering in organic transistors," *Mater. Today*, vol. 10, no. 3, pp. 46–54, 2007, doi: 10.1016/S1369-7021(07)70019-6.

[20] X. Zhu, X. Zhang, L. Huang, Z. Wang, and L. Chi, "Improving the performance of TIPS-pentacene thin film transistors via interface modification," *Chem. Res. Chinese Univ.*, vol. 34, no. 1, pp. 151–154, 2018, doi: 10.1007/s40242-017-7122-x.

[21] J. Kim, J. Kim, B. Ahn, T. Hassinen, Y. Jung, and S. Ko, "Optimization and improvement of TIPS-pentacene transistors (OTFT) with UV-ozone and chemical treatments using an all-step solution process," *Curr. Appl. Phys.*, vol. 15, no. 10, pp. 1238–1244, 2015, doi: 10.1016/j.cap.2015.07.012.

[22] W. H. Lee, H. H. Choi, D. H. Kim, and K. Cho, "25th anniversary article: Microstructure dependent bias stability of organic transistors," *Adv. Mater.*, vol. 26, no. 11, pp. 1660–1680, 2014, doi: 10.1002/adma.201304665.

[23] D. Kim, H. Lee, Y. Ham, J. Park, J. Bae, H. Lee, Y. Ham, and J. Park, "Bias stress effects in pentacene thin-film transistors with poly (methyl methacrylate) gate insulator," *Mol. Cryst. Liq. Cryst.*, vol. 645, no. 1, pp. 36–42, 2017, doi: 10.1080/15421406.2016.1277898.

.[24] S. G. J. Mathijssen, M. Cölle, H. Gomes, E. C. P. Smits, B. De Boer, I. McCulloch, P. A. Bobbert, and D. M. De Leeuw, "Dynamics of threshold voltage shifts in organic and amorphous silicon field-effect transistors," *Adv. Mater.*, vol. 19, no. 19, pp. 2785–2789, 2007, doi: 10.1002/adma.200602798.

[25] H. Zan and S. Kao, "The Effects of Drain-Bias on the Threshold Voltage Instability in Organic TFTs," vol. 29, no. 2, pp. 2007–2009, 2008.

[26] T. C. Union, C. Science, C. Science, C. G. Sodini, C. Science, T. Supervisor, T. Orlando, and C. Science, "The Bias-stress Effect in Pentacene Organic Thin-film Transistors Kevin Kyungbum Ryu," 2010.

[27] U. Zschieschang, R. T. Weitz, K. Kern, and H. Klauk, "Bias stress effect in low-voltage organic thin-film transistors," *Appl. Phys. A Mater. Sci. Process.*, vol. 95, no. 1, pp. 139–145, 2009, doi: 10.1007/s00339-008-5019-8.

[28] X. Jia, C. Fuentes-hernandez, C. Wang, Y. Park, and B. Kippelen, "Stable organic thin-film transistors," pp. 1–8, 2018.

[29] W. B. Jackson, J. M. Marshall, and M. D. Moyer, "Role of hydrogen in the formation of metastable defects in hydrogenated amorphous silicon," *Phys. Rev. B*, vol. 39, no. 2, pp. 1164–1179, 1989, doi: 10.1103/PhysRevB.39.1164.

[30] P. A. Bobbert, I. McCulloch, B. de Boer, H. Gomes, D. M. de Leeuw, E. C. P. P. Smits, S. G. J. J. Mathijssen, M. Cölle, H. Gomes, E. C. P. P. Smits, B. de Boer, I. McCulloch, P. A. Bobbert, and D. M. de Leeuw, "Dynamics of Threshold Voltage Shifts in Organic and Amorphous Silicon Field-Effect Transistors," *Adv. Mater.*, vol. 19, no. 19, pp. 2785–2789, 2007, doi: 10.1002/adma.200602798.

[31] U. Zschieschang, R. T. Weitz, K. Kern, and H. Klauk, "Bias stress effect in low-voltage organic thin-film transistors," *Appl. Phys. A Mater. Sci. Process.*, vol. 95, no. 1, pp. 139–145, 2009.

[32] C. L. Fan, T. H. Yang, and C. Y. Chiang, "Performance degradation of pentacene-based organic thin-film transistors under positive drain bias stress in the atmosphere," *IEEE Electron Device Lett.*, vol. 31, no. 8, pp. 887–889, 2010.

[33] J. H. Park, Y. T. Lee, H. S. Lee, J. Y. Lee, K. Lee, G. B. Lee, J. Han, T. W. Kim, and S. Im, "Origin of bias-stress induced instability in organic thin-film transistors with semiconducting small-molecule/insulating polymer blend channel," *ACS Appl. Mater. Interfaces*, vol. 5, no. 5, pp. 1625–1629, 2013, doi: 10.1021/am3022703.

[34] S. Singh and Y. N. Mohapatra, "Bias stress effect in solution-processed organic thin-film transistors: Evidence of field-induced emission from interfacial ions," *Org. Electron.*, vol. 51, pp. 128–136, 2017.

[35] H. Sirringhaus, "Reliability of organic field-effect transistors," *Adv. Mater.*, vol. 21, no. 38–39, pp. 3859–3873, 2009, doi: 10.1002/adma.200901136.

[36] K.-M. Han, J.-I. Park, J. Y. Kim, Z. Bao, H. M. Kang, B.-L. Lee, H. A. Becerril, B. W. Koo, E. J. Jeong, K. Cho, W. H. Lee, H. Moon, B. W. Yoo, D. H. Kim, "Liquid-Crystalline Semiconducting Copolymers with Intramolecular Donor−Acceptor Building Blocks for High-Stability Polymer Transistors," *J. Am. Chem. Soc.*, vol. 131, no. 17, pp. 6124–6132, 2009, doi: 10.1021/ja8095569.

[37] P. Tassini, M. G. Maglione, R. Rega, A. D. G. Del Mauro, T. Fasolino, G. Pandolfi, E. Calò, C. Minarini, and P. Maddalena, "Electrical stress effects on organic thin-film transistor with solution-processed TIPS-pentacene and poly-4-vinylphenol dielectric," *AIP Conf. Proc.*, vol. 1459, no. 1, pp. 262–264, 2012, doi: 10.1063/1.4738463.

[38] J. H. Park, Y. T. Lee, H. S. Lee, J. Y. Lee, K. Lee, G. B. Lee, J. Han, T. W. Kim, and S. Im, "Origin of bias-stress induced instability in organic thin-film transistors with semiconducting small-molecule/insulating polymer blend channel," *ACS Appl. Mater. Interfaces*, vol. 5, no. 5, pp. 1625–1629, 2013, doi: 10.1021/am3022703.

[39] H. L. Gomes, P. Stallinga, F. Dinelll, M. Murgia, F. Biscarini, D. M. De Leeuw, T. Muck, J. Geurts, L. W. Molenkamp, and V. Wagner, "Bias-induced threshold voltages shifts in thin-film organic transistors," *Appl. Phys. Lett.*, vol. 84, no. 16, pp. 3184–3186, 2004, doi: 10.1063/1.1713035.

[40] J. Park, J. H. Bae, W. H. Kim, M. H. Kim, C. M. Keum, S. D. Lee, and J. S. Choi, "Effects of interfacial charge depletion in organic thin-film transistors with polymeric dielectrics on electrical stability," *Materials (Basel).*, vol. 3, no. 6, pp. 3614–3624, 2010, doi: 10.3390/ma3063614.

[41] J. B. Chang and V. Subramanian, "Effect of active layer thickness on bias stress effect in pentacene thin-film transistors," *Appl. Phys. Lett.*, vol. 88, no. 23, pp. 2004–2007, 2006, doi: 10.1063/1.2210791.

[42] A. Shih and A. I. Akinwande, "Solution-Processed High-Voltage Organic Thin Film Transistor," *MRS Adv.*, vol. 2, no. 51, pp. 2961–2966, 2017, doi: 10.1557/adv.2017.359.

[43] B. Gunduz and F. Yakuphanoglu, “Effects of UV and white light illuminations on photosensing properties of the 6,13-bis(triisopropylsilylethynyl)pentacene thin film transistor,” *Sensors Actuators A. Phys.*, vol. 178, no. October 2017, pp. 141–153, 2012, doi: 10.1016/j.sna.2012.02.032.

[44] W. Tang, L. Feng, P. Yu, J. Zhao, and X. Guo, “Highly Efficient All-Solution-Processed Low-Voltage Organic Transistor with a Micrometer-Thick Low-k Polymer Gate Dielectric Layer,” *Adv. Electron. Mater.*, vol. 2, no. 5, pp. 1–7, 2016, doi: 10.1002/aelm.201500454.

[45] W. Huang, W. Shi, S. Han, and J. Yu, “Hysteresis mechanism and control in pentacene organic field-effect transistors with polymer dielectric,” *AIP Adv.*, vol. 3, no. 5, pp. 0–6, 2013, doi: 10.1063/1.4807660.

[46] Z. T. Huang, G. B. Xue, J. K. Wu, S. Liu, H. Y. H. B. H. Y. Li, Y. H. Yang, F. Yan, P. K. L. Chan, H. Z. Chen, and H. Y. H. B. H. Y. Li, “Electron transport in solution-grown TIPS-pentacene single crystals: Effects of gate dielectrics and polar impurities,” *Chinese Chem. Lett.*, vol. 27, no. 12, pp. 1781–1787, 2016, doi: 10.1016/j.cclet.2016.05.016.

[47] J. B. Chang and V. Subramanian, “Effect of active layer thickness on bias stress effect in pentacene thin-film transistors,” *Appl. Phys. Lett.*, vol. 88, no. 23, 2006, doi: 10.1063/1.2210791.

[48] S. Singh and Y. N. Mohapatra, “Bias stress effect in solution-processed organic thin-film transistors: Evidence of field-induced emission from interfacial ions,” *Org. Electron. physics, Mater. Appl.*, vol. 51, pp. 128–136, 2017, doi: 10.1016/j.orgel.2017.09.007.

Chapter 5

Organic Thin-Film Memory Transistors (OTFMTs)

5.1 Introduction

In this chapter, two types of organic non-volatile memory transistors (ONVMTs) were fabricated using graphene oxide (GO) as the floating gate. Cross-linked poly(methyl methacrylate) (cPMMA) and cross-linked poly(vinyl alcohol) (cPVA) were deposited with an off-centre spin-coating technique as the insulating layers for the OTFMTs. While p-type semiconductor, TIPS-pentacene, was used as the active layer. Different concentrations of GO with different solvents were used during this research to optimise the concentration of GO in solvents. Achieving a large hysteresis in both output and transfer characteristics (to represent the memory window) is a clear indication of the potential to use GO for high-density memory transistors. The reported memory transistors also produced high field-effect mobility for OTFMTs. The surface morphology and charge transfer mechanism were also investigated for these memory transistors. All transistors and memory transistors were fabricated on glass substrates which could provide the next stage for low cost flexible organic electronic circuits. Fabrication of the devices and the electrical characteristics were presented in this chapter.

5.2 cPMMA-based OTFMTs with GO as a floating gate.

In this section, the study is focused on the fabrication and characterization of ONVMTs - based on GO as a floating gate and cPMMA as the insulating layer. GO is a good candidate as a floating gate in memory transistors due to the high charge storage and producing large memory window [1-6]. The fabrication procedure of OTFMT is similar to the fabrication of OTFT with an added floating gate layer. The floating gate was made of spin-coating GO thin film inserted between two cPMMA insulating layers. As mentioned in (chapter 4) we have good OTFTs devices with high performance and negligible hysteresis in the transfer and output characteristics using cPMMM as the insulating layer. These results will be used as the bases for the fabrication of OTFMTs

5.2.1 cPMMA-based OTFMTs device fabrication

cPMMA-based organic non-volatile memory transistors (ONVMTs) were fabricated in class 1000 cleanroom. All the devices were fabricated with the geometry of bottom gate-top contacts (drain-source electrodes) configuration. Figure 5.1(a) shows a schematic configuration of cPMM-based organic memory transistor fabricated on a glass substrate using 50 nm thermally evaporated Al film as the gate electrode. Poly(methyl methacrylate) (PMMA) 5wt % butyl acetate (anhydrous ≥ 99% solution) was cross-linked using [1,6-bis(trichlorosilyl) hexane (C6-Si) (10µ/1ml)] as a cross-linking agent and filtered by 0.1µm syringe filter. The cross-linked PMMA (cPMMA) was spin-coated by a simple off-centre spin-coating (OCSC) method [7] with a spin speed of 2000 rpm for 40 sec and then annealed at 120°C for 60 minutes. The cPMMA insulating layer was then exposed to 0.8 SCCM O_2 ozone under a vacuum of (3 mbar) for 1 minute to reduce the moisture and improve the layer surface. The insulating layer thickness was measured using a profilometer, and it was found to be 330±5 nm. For the floating gate, a thin layer of graphene oxide (0.4 mg/ml water dispersion) [purchased from Sigma-Aldrich] was spin-coated using OCSC method over the cPMMA layer with a spin speed of 3500 rpm for 20 sec and then annealed at 80^{o}C for 20 minutes. In addition, the second cPMMA layer was spin-coated on the floating gate with the same deposition properties as of the first cPMMA layer. Finally, a drop-casting method was applied to produce a thin layer of TIPS-pentacene semiconductor (2wt % toluene solution). After preparing TIPS-pentacene solution in the glove box, it was drop-casted on the cPMMA with a small angle for the substrate as shown in Figure 3.9 (chap.3) and then annealed at 90^{o}C for 1h to produce a layer 60 nm thick. Finally, the drain and source have been made through a shadow mask by thermally evaporating 50 nm of gold (the channel width (W) and length (L) were 1000 µm and 150 µm respectively). The optical microscopic image of the device and its channel is shown in Figure 5.1(b) whereas, the morphological quality and coverage for the cPMMA, graphene oxide and TIPS-pentacene layers were examined using atomic force spectroscopy (AFM) and listed in Figure 5.1(c). The AFM image of GO shows a uniform deposition of the film. While the TIPS-pentacene shows a clear polycrystalline structure with large uniform and condenses grains. The large grains size of organic semiconductor is an important parameter for the fabrication of high-mobility thin-film transistors as it allows higher current when used as the active layer. The roughness of the cPMMA layer was estimated from the AFM images to be in the region of 4.65 nm.

Furthermore, the reference control transistors (without the floating gate) were also fabricated with the same fabrication conditions for comparison. The electrical characterization of cPMMA-based ONVMTs with double sweep current-voltage (*I-V*) was measured in air at room temperature (21±1) using Keithley B2636. All the details of the measurement setup are mentioned in chapter 3.

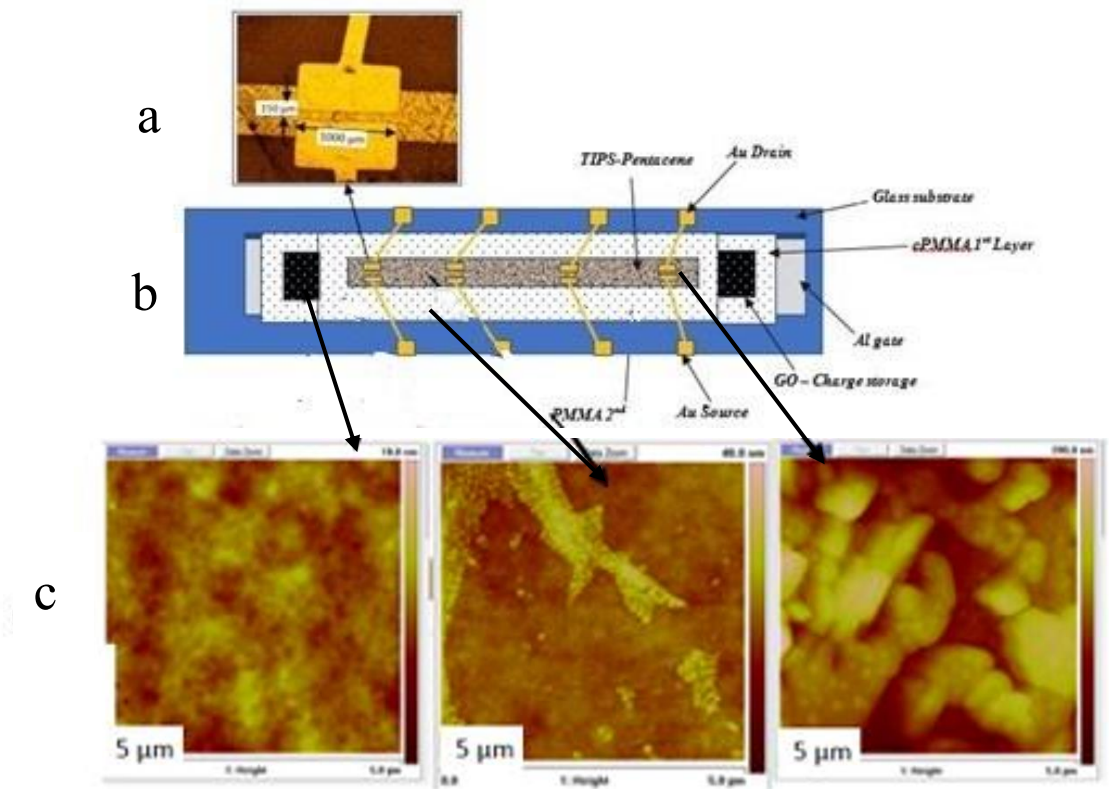

Figure 5. 1: *(a) Schematic configuration of graphene oxide-based organic memory transistor fabricated on a glass substrate (b) optical microscopic image of the device and its channel (c) the morphological quality and coverage for the cPMMA, graphene oxide and TIPS-pentacene layers.*

5.2.2 cPMMA-based OTFMTs device characterisations

The electrical characterisation of the control transistor is an important step to identify the effect of the floating gate in memory structures. Therefore, the first step in ensuring the memory behaviour is exclusively due to the presence of the floating gate, the control transistor should have no (or negligible) hysteresis in both output and transfer characteristics. Figures 5.2 (a) and (b) represent the output and transfer characteristics of the cPMMA-based OTFT respectively using the off-centre spin-coating technique. It is clear that the OTFT shows a high current and mobility as well as no (or negligible) gate leakage

current. It is also clear from Figures 5.2(a) and (b) the transistor behaviour showed no or negligible hysteresis for a double sweep of the current-voltage (*I-V*) measurements. As a result of the above characterisations, all the OTFTs and OTFMTs in this work were fabricated using the off-centre technique for the deposition of cPMMA.

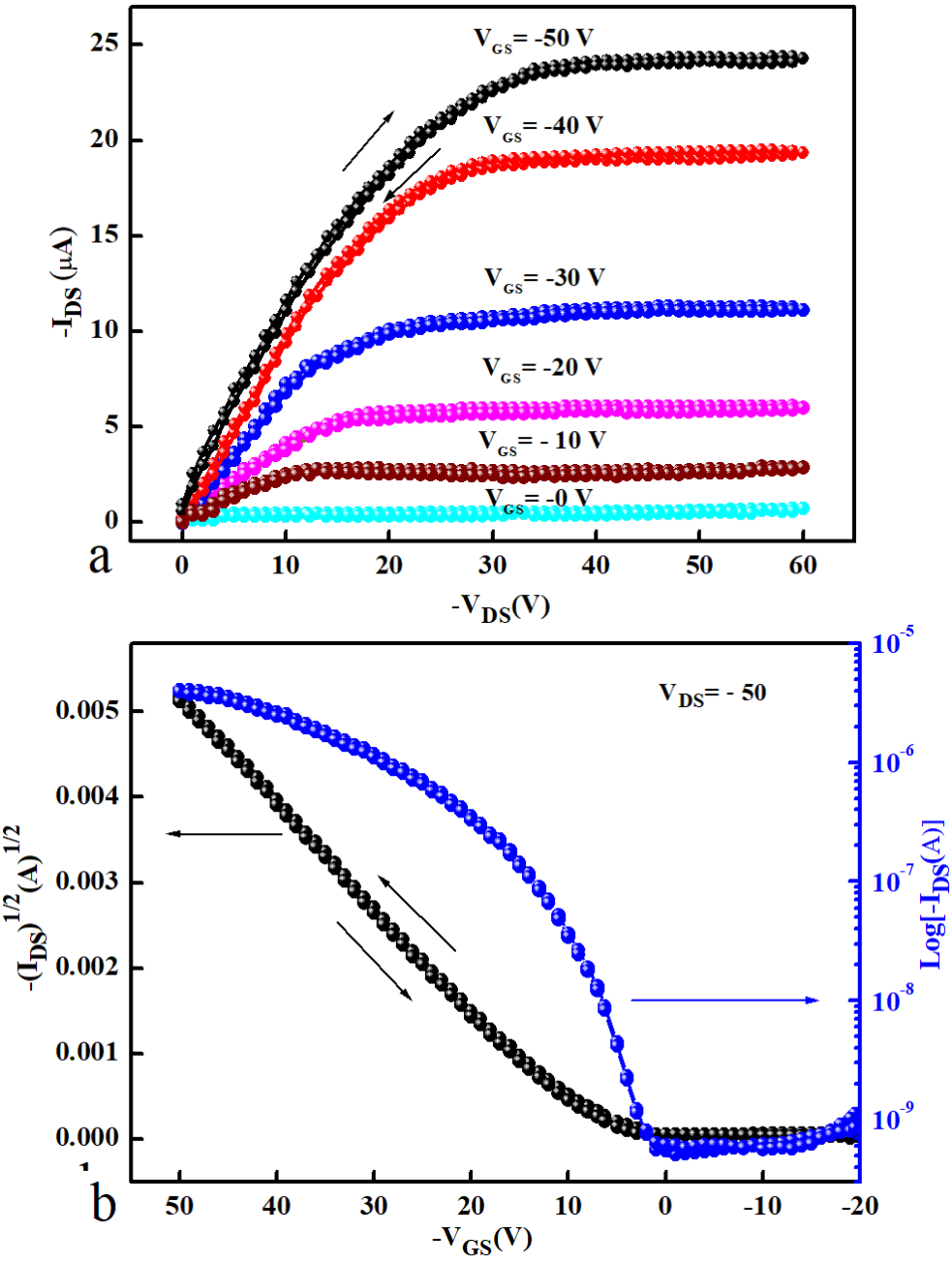

Figure 5.2: *(a) Output and (b) transfer characteristics of the cPMMA-based OTFTs as a reference for the OTFMT measurements.*

To investigate the role of GO as the charge trapping layer in organic memory transistors, an additional GO layer was inserted between the two cPMMA insulating layers of the transistor in form of Al/cPMMA/GO/cPMMA/TIPS-pentacene/Au as shown in Figure 5.1(a). The output and transfer characteristics of the organic memory transistor are illustrated in Figure 5.3(a) and (b), respectively. Figure 5.3(a) shows the output characteristics of the memory transistor at a gate voltage of -50 V as well as the output characteristics of the control device. The measurements were the same in the sweep range and scan rate of (1 $V.s^{-1}$) for the organic memory transistor and the control organic transistor in order to compare between them and represent the effect of GO as the floating gate in the memory transistor. It is clear from Figure 5.3(a) that the double sweep of the output characteristic gives a memory w(ΔV_T) of 38V for the memory device, while the control device exhibits a negligible hysteresis.

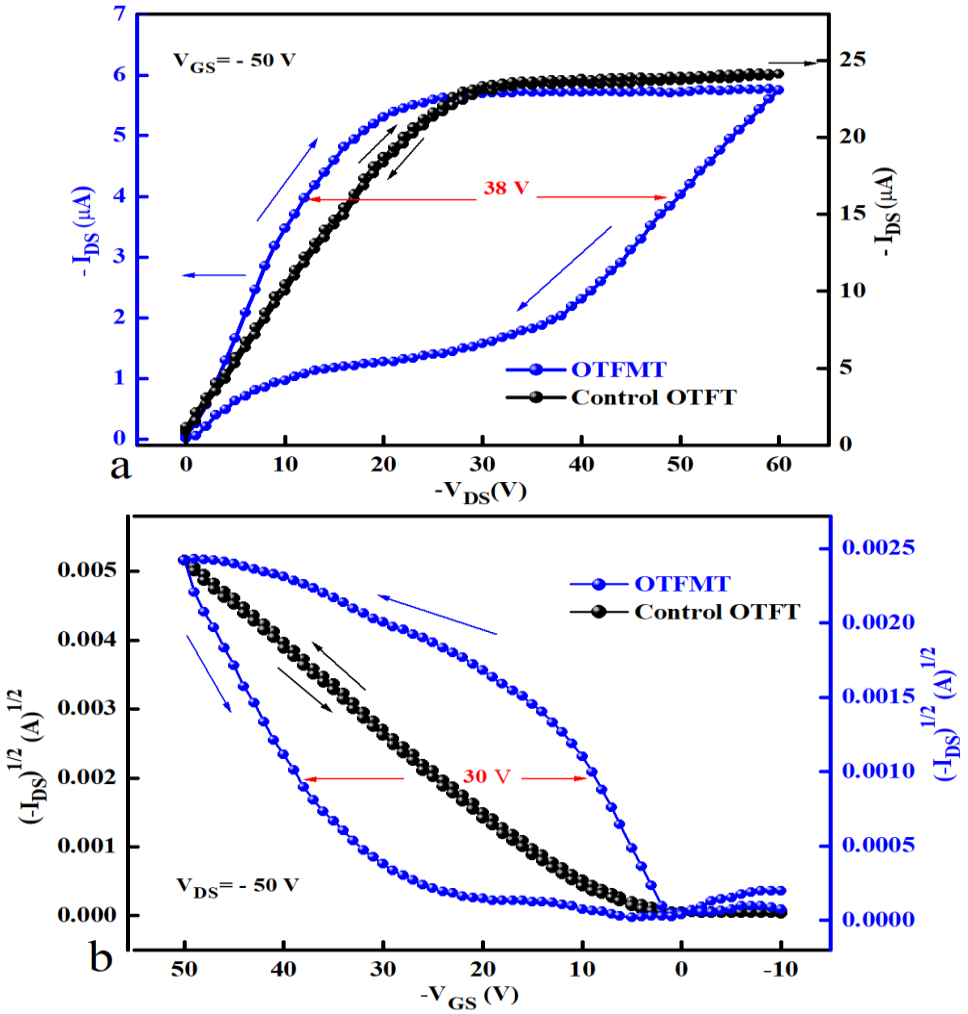

Figure 5. 3: *(a) Output and (b) transfer characteristics of the cPMMA-based OTFMT with and without the floating gate.*

The high hysteresis window in the output characteristics of the memory transistor is attributed to the charging and discharging of the GO trapping layer with the appropriate applied gate voltages. The counter-clockwise hysteresis in the transfer curves (I_{DS} –V_{GS}), Figure 5.3(b), indicates that charging and discharging of the memory transistor takes place through the semiconductor-insulator interface. When a high enough negative gate is applied, holes are injected from the p-type semiconductor (TIPS-pentacene) layer into the charge trapping floating gate (GO) layer (through the top insulating layer - cPMMA2), charging up the GO floating gate and programming the memory transistor. Whereas, when a positive gate voltage is applied ($V_{GS} > 0$), holes are removed from the charge trapping layer through the semiconductor layer to conduct the erase process of the memory devices [8-11]. In order to estimate the effect of the GO as the charge trapping layer, we determined the amount of charge stored (Q) in the GO floating gate using equation 5.1 [9,12-14].

$$Q = C_i \Delta V_T \ . \tag{5.1}$$

The insulator capacitance per unit area C_i was measured for TIPS-pentacene/cPMMA structure and estimated to be ~ 6.8×10^{-9} $F\ cm^{-2}$. For a memory window of 30V (from the transfer characteristics), the carrier charge stored was found to be approximately 9.15×10^{11} cm^{-2}. Whereas, the threshold voltage represents the value of the V_{GS} at which the transistor is turned on and can be determined from the intercept of the plot of $(I_{DS})^{1/2}$ versus V_{GS}, as shown in Figure 5.3(b). The field-effect mobility (μ) of the devices can be estimated using equation 2.12 (chap.2). The calculated value of the field-effect mobility μ for the control device was 1.36 $cm^{-2}\ V^{-1}\ s^{-1}$, with a threshold voltage of -6.5 V and an on/off current ratio of 8×10^3. With the large memory window exhibited in OTFMT devices, a good field-effect mobility of 0.85 $cm^{-2}\ V^{-1}\ s^{-1}$ has been observed. The threshold voltages were estimated to be about 2*V* and -28*V* for forward and reverse directions, respectively.

Successive positive and negative voltage pulses were applied on the gate electrode (with V_{DS} maintained at 0 *V*) in order to investigate the memory behaviour in terms of threshold voltage shift as a function of the applied voltage. The transfer characteristic of the memory transistor was measured after each application of the voltage pulse to calculate the shift in the threshold voltage compared to the unstressed device. Figure 5.4(a) represented the programming pulses of GO-based OTFMTs, herein negative and positive pulses were applied before measuring the transfer characteristics. These pulses result in a threshold voltage shift to produce the write and erase state. When applying a negative pulse to the

gate electrode (2 *s* pulses, -10*V*), the threshold voltage is shifted to a higher negative value. Whereas, applying a positive pulse to the gate electrode (2 s pulses +10*V*) leads to the threshold voltage to be shifted to a positive value from the unstressed device. Figure 5.4(b) shows the double transfer curve sweep for different maximum gate voltage sweeps. These curves illustrate increasing in the memory window when the maximum gate voltage (V_{GS} max) was increased. Preliminary tests on the reproducibility and stability of the OTFTs were made during this study. OTFTs fabricated on the same glass slide showed a maximum variation in the saturation value of I_{DS}, threshold voltage and μ of ±10%. Though, a greater variation of μ, of up to ± 30 %, was found for devices fabricated on different substrates.

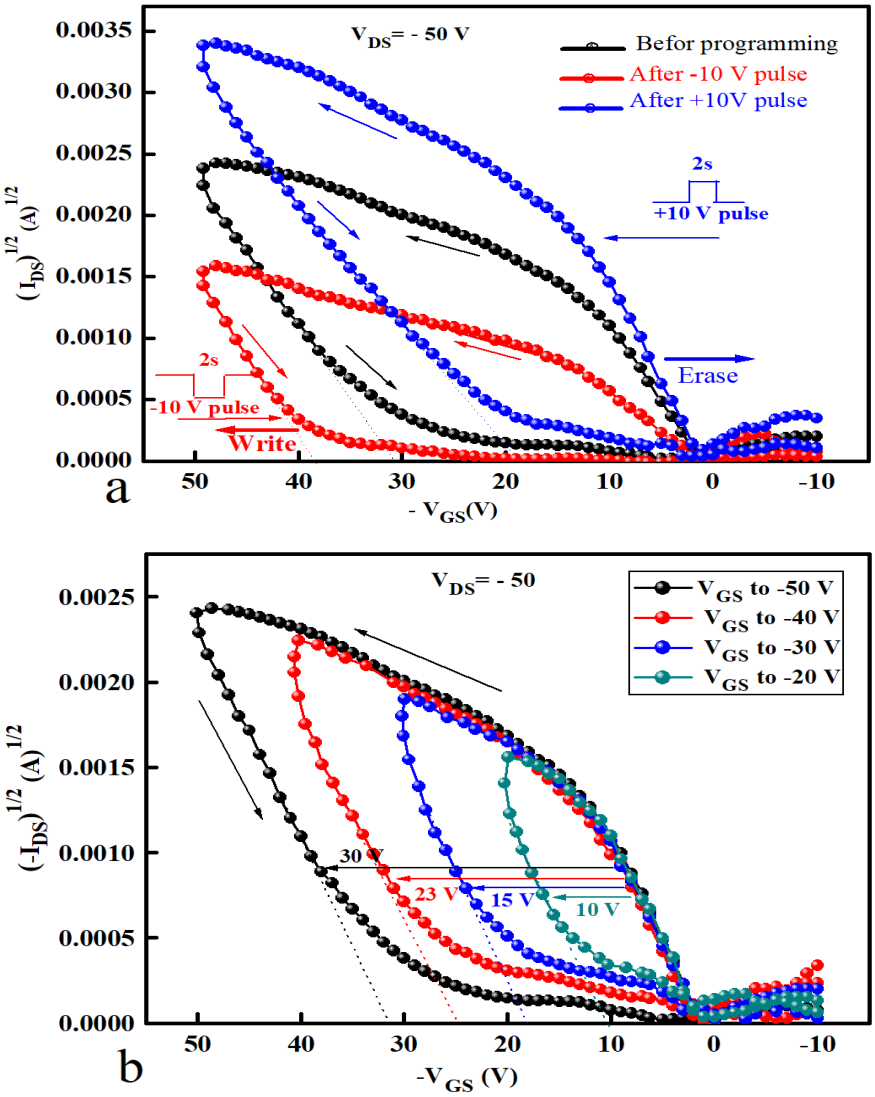

Figure 5. 4: *Transfer characteristics of the fabricated OTFMT after the application of positive and negative pulses of 10 V for 2 s. (b) A double sweep of transfer characteristics for different maximum gate voltage*

Overtime (devices stored under vacuum) showed good stability as the electronic parameters did not change significantly after regular testing for 24 months. The memory behaviour of the OTFMTs was also retained for more than 24 months for devices stored under vacuum. To further investigate the OTFMTs behaviours, positive and negative pulses (+2 to +10 *V* and -2 to -10 *V*) were applied on the gate electrode. Then immediately the transfer characteristics were measured to calculate the threshold voltage shift after applying stress on these voltages. It is clear from Figure 5.5(a) that the threshold voltage shifted to a higher negative V_{GS} voltage as the negative pulse (write state) increased. While, applying a positive pulse (erase state) to the gate electrode resulted in a clear positive shift of the threshold voltage, as shown in Figure 5.5(b). The shift in the threshold voltage leads to hysteresis and memory behaviour which are resulting from the charge storage and trapped in the floating gate [15-19].

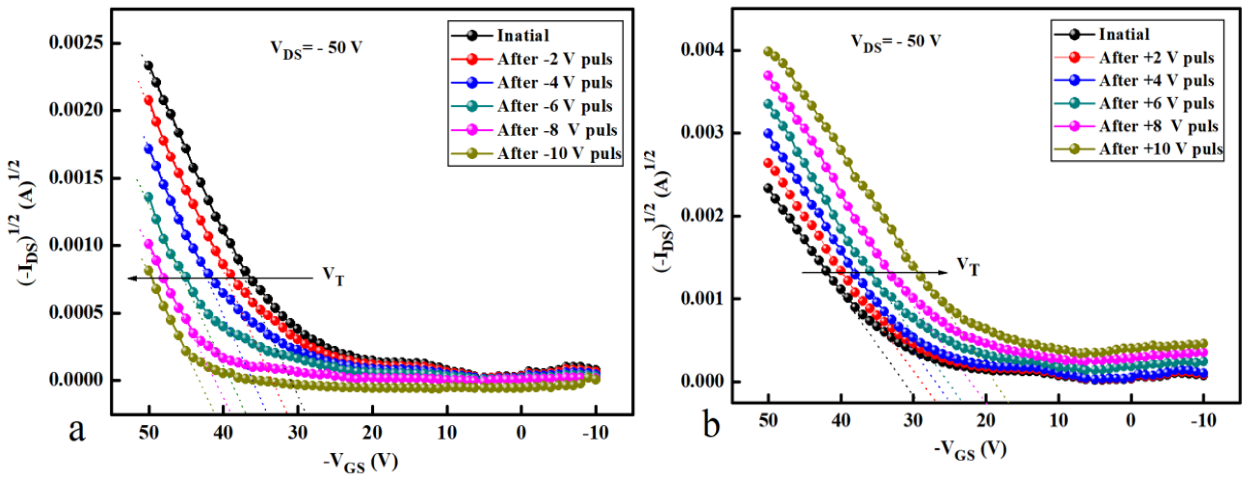

Figure 5. 5: *The effect of (a) negative and (b) positive pulses on transfer characteristics of OTFMT*

Figure 5.6 (a) shows the change in the threshold voltage shift depending on the applied voltage pulses to the gate of GO-based OTFMT. These pulses were applied to the gate electrode as shown and explained in figure 5.5. Increasing the applied voltage pulses leads to an increase in the shift in the threshold voltage. A clear memory window can be recognised with a programming voltage of less than 2*V*. Figure 5.6(b) shows the effect of programming pulses on the value of I_{DS} when applying a voltage to the gate electrode. The write state was realised by applying a voltage pulse of -20 *V* for 2 *s*. Whereas for the erase state, a voltage pulse of 20 *V* was applied. It is clear from Figure 5.6(b) that the I_{DS} value

did not change when a positive reading voltage is applied to the gate and it was possible to distinguish if the device is in the write or erase states.

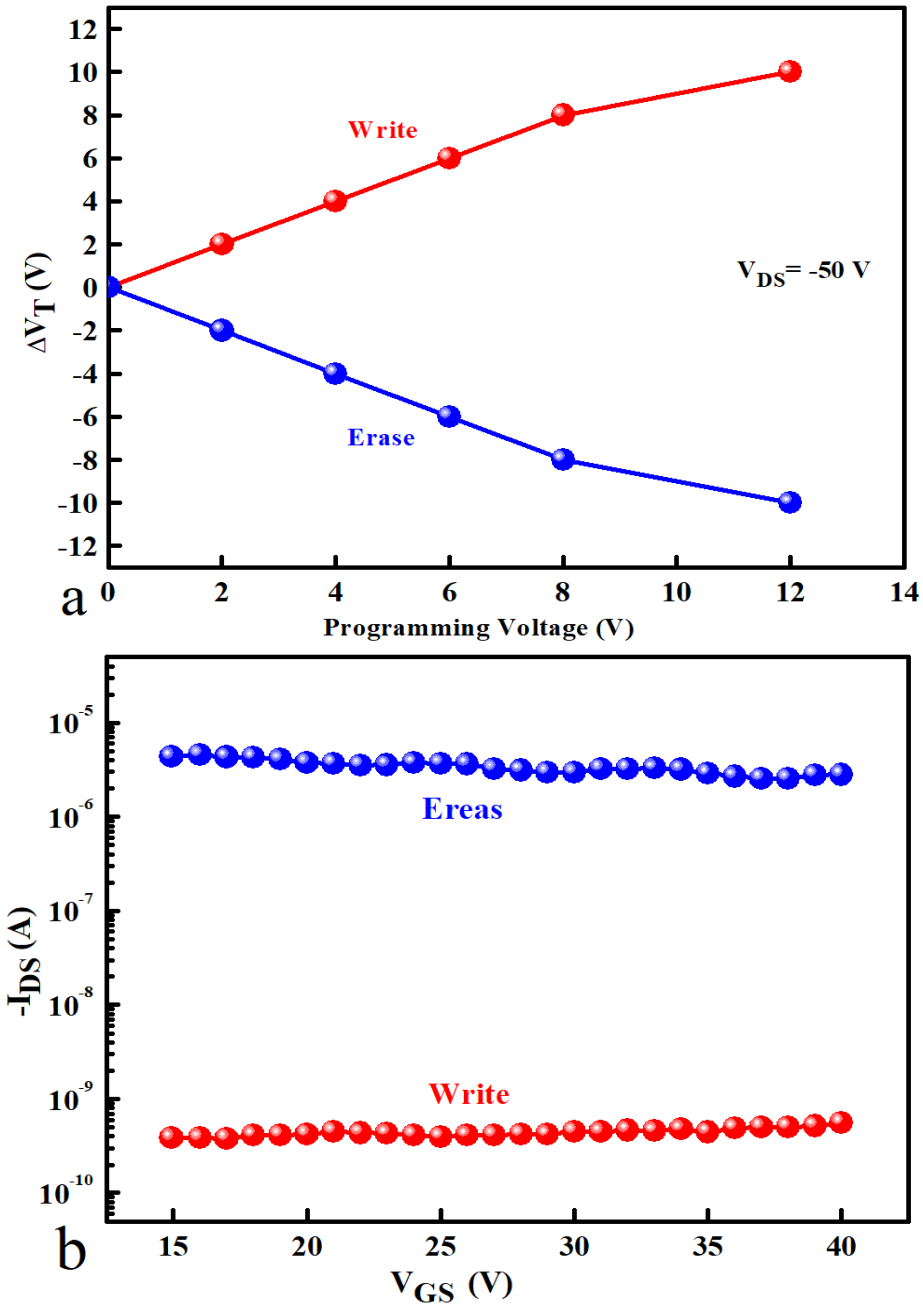

Figure 5. 6: *Programming characteristics of TIPS-pentacene based OTFMT. (a) The effect of the programming voltage (2 s pulses) on the threshold voltage shift(ΔV_T), (b) write and erase processes by applying a negative and positive pulse voltage, respectively, as a function of gate voltage.*

Using a reading voltage of 20*V*, the I_{DS} was periodically measured in order to study the retention behaviour of the memory transistors. Figure 5.7 shows the data retention capability as a function of time for GO-based OTFMT in the write/erase states under the ambient condition at room temperature. Appling negative pulses to the gate electrode (write state) leads to accumulating the positive charges (holes) in the floating gate (GO), these holes were transferred from the channel through the TIPS-pentacene semiconductor. As a result, the opposite internal electric field was generated between the gate electrode and the channel. Therefore, to turn on the transistor, a higher negative gate voltage is required which is resulting in a shift in the threshold voltage higher than of the unstressed device. On the other hand, applying positive pulses to the gate electrode (erase state), leads to move the holes from the floating gate to the transistor channel through the semiconductor.

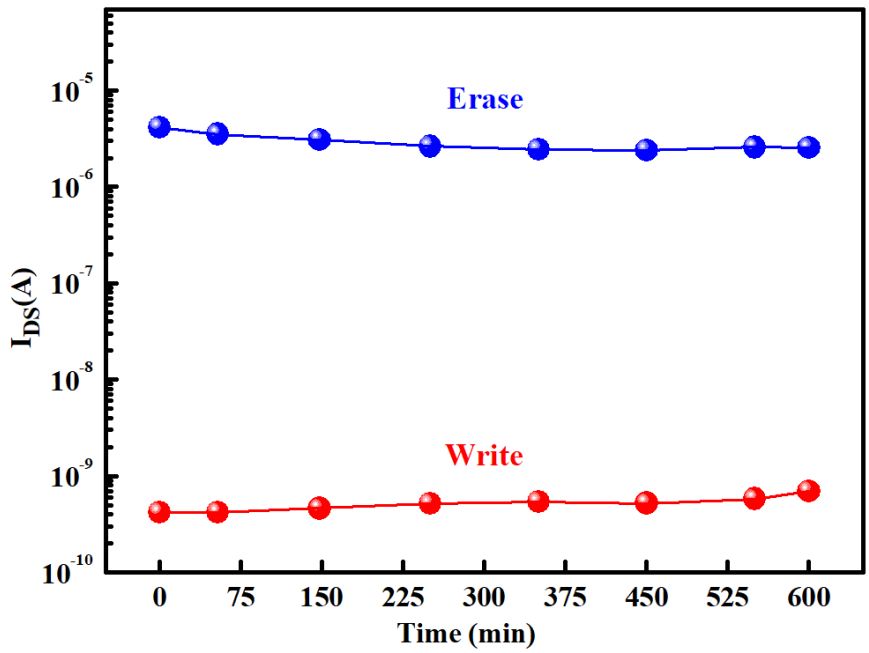

Figure 5. 7: *Charge retention characteristics of the OTFMT.*

In another approach to investigate the non-volatile behaviour of the memory transistors, voltage pulses for write and erase states (±20 *V* for 2 *s*) were applied to the gate and the I_{DS} values were monitored. The change in I_{DS} was recorded after a certain number of write/erase cycles, Figure 5.8 shows the measured values of the drain current as a function of a number of cycles. Figure 5.8 clearly shows that the current representing the write and erase states did not change after more than 200 cycles and after all these cycles it is still easy to

distinguish if the device is in write or erase state. The average current recorded for the write and erase states are 4×10^{-10}A and 3×10^{-6}A, respectively.

To understand the memory behaviour of the organic memory transistor, the energy band of the Au/TIPS-pentacene/cPMMA/GO/cPMMA/Al structure was considered for investigation. Figure 5.9 represents the relative energy diagrams for the materials used in the fabrication of the GO-based memory device.

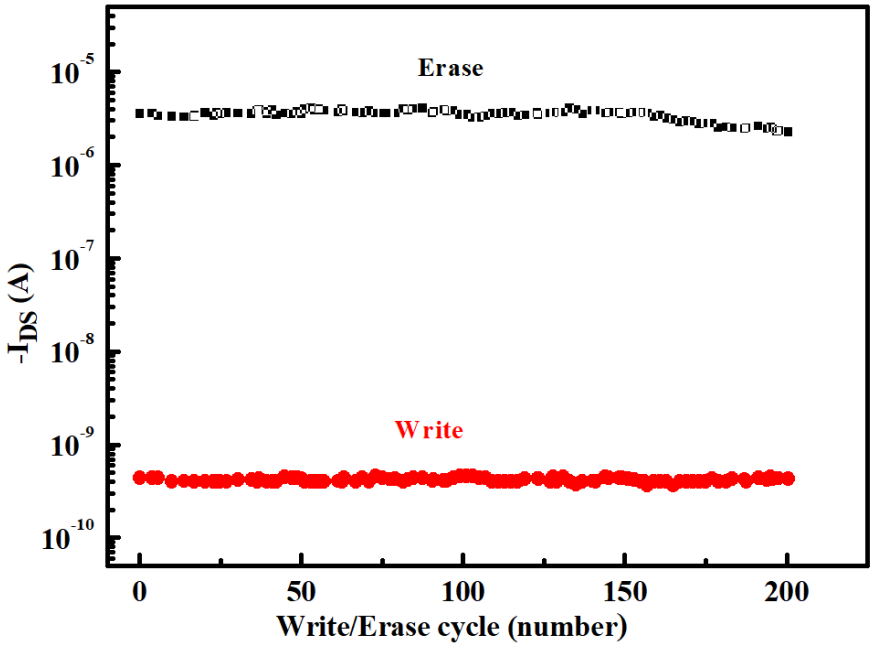

Figure 5. 8: *Endurance characteristic of the OTFMT device with GO as a charge-storage layer.*

The work function for Au and Al are 5.1 eV and 4.3 eV respectively [20]. While, the highest occupied molecular orbital (HOMO) and the lowest-unoccupied molecular orbital (LUMO) levels of TIPS-pentacene are -5.3 e*V* and -3.4 e*V*), respectively [21]. As discussed earlier, the counter-clockwise hysteresis direction of the transfer characteristics in Figure 5.3(b) indicates that charging and discharging of the memory transistor takes place through the semiconductor. When a high enough negative gate bias is applied, holes are injected from the semiconductor through cPMMA into the GO layer and program the memory device. In contrast, when a high enough positive gate voltage is applied, holes are ejected from the GO layer resulting in the erasing process. The charging and discharging of the GO layer lead to a clear shift in the memory transistor threshold voltage V_T; which in general represents the memory window of memory transistors. In The charging process (writing) shown in Figure

5.9 where under a negative bias is applied to the gate electrode, holes released from the HOMO level are injected through the cPMMA and stored by the GO floating gate. The presence of holes in the insulating layer leads to a higher negative threshold voltage. Based on the experimental results and the energy band diagram in Figure 5.9, the transfer of holes from the TIPS-pentacene to the GO floating gate occurs by tunnelling through the cPMMA. The charge carriers can cross the cPMMA energy barrier as the HOMO level of TIPS-pentacene and the work function of GO are very close. For all OTFMTs stored under vacuum, reproducible memory properties were observed as devices were tested on regular bases for 12 months. The results will help in the development of low-cost organic memory devices as part of all-organic flexible circuitries for future plastic technology.

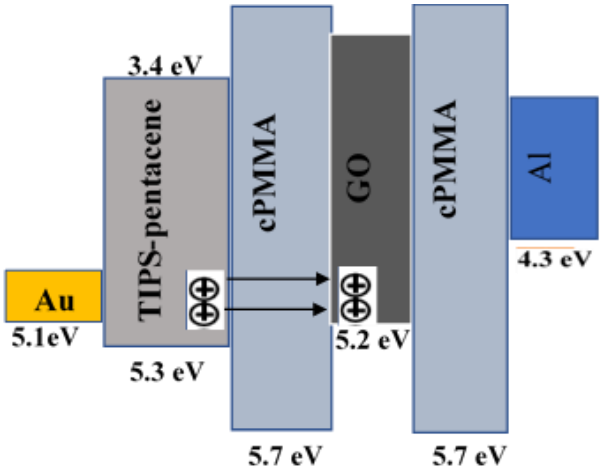

Figure 5. 9: *Schematic diagram of the energy band for the cPMMA-based OTFMT.*

5.3 cPVA-based OTFMTs with GO as a floating gate.

To investigate the memory transistors with cross-linked poly(vinyl alcohol) (cPVA) as an insulating layer, we fabricated several devices in the configuration of TIPS-pentacene /cPVA/GO/cPVA/Al. These devices were fabricated with the same procedure of the cPMMA-based OTFMTs, but cPVA insulating layer was used instead of cPMMA in this fabrication. For a comparison, cPVA-based OTFTs devices were fabricated as a reference with the same procedure described in chapter 4 to confirm that inserting GO as a floating gate in the cPVA-based OTFTs devices gives them the memory behaviour.

5.3.1 cPVA-based OTFMT device fabrication

In this section, cPVA-based ONVMTs using GO as a floating gate were fabricated with the geometry of bottom gate-top contacts (drain-source electrodes) as shown in Figure 5.1(a), with cPVA instead of CPMMA layers. These devices were fabricated on clean glass substrates in the cleanroom. After preparing the glass substrate, a 50 nm thin layer of Al was thermally evaporated as the gate electrode. Then, 10 wt % of the cross-linked PVA solution was prepared with the same procedure described in section (4.3). The cPVA water solution was spin-coated using off-centre spin-coating (OCSC) technique on the Al gate electrode with a spin speed of 2000 rpm then a annealed at 90^{o}C for 120 minutes to producea 400±5 nm insulating layer. Then, the cPVA layer was exposed to 0.8 SCCM O_2 ozone under vacuum (3 mbar) for 1 minute to reduce the moisture and improve the layer surface. Using the same graphene oxide (GO) (0.4 mg/ml water dispersion) used in the fabrication of cPMMA-based OTFMT and following the same spin-coating procedure with a spin speed of 3500 rpm for 20 sec and annealed at 80^{o}C for 20 minutes, a floating gate layer was produced over the cPVA layer. Furthermore, the second cPVA insulating layer was spin-coated on the GO floating gate with the same properties of the first cPVA insulating layer. Additionally, the TIPS-pentacene (2wt % toluene solution) semiconductor layer was drop-casted as the active layer on the second cPVA insulating layer with a small angle for the substrate as shown in Figure 4.2. All devices were annealed at 90^{o}C for 60 minutes to produce a 60 nm active layer. Thermal evaporation was used to evaporate gold as the drain and source through a shadow mask with a thickness of 50 nm (the channel width (W) and length (L) were 1000 µm and 150 µm respectively).

5.3.2 cPVA-based OTFMTs characterisations

To investigate (*I-V*) characteristics of cPVA-based OTFMTs, a reference OTFT device without a floating gate was fabricated as a control transistor. Figure 5.10 (a) shows the output characteristics of the control OTFT device with two direction sweep in the range of V_{DS} (0 *V* to -50 *V* then to 0 *V* and scan rate of 2 *V*) and V_{GS} (0 *V* to -40 *V* with a step of 10 *V)* which is showing no leakage current and no or negligible current hysteresis.

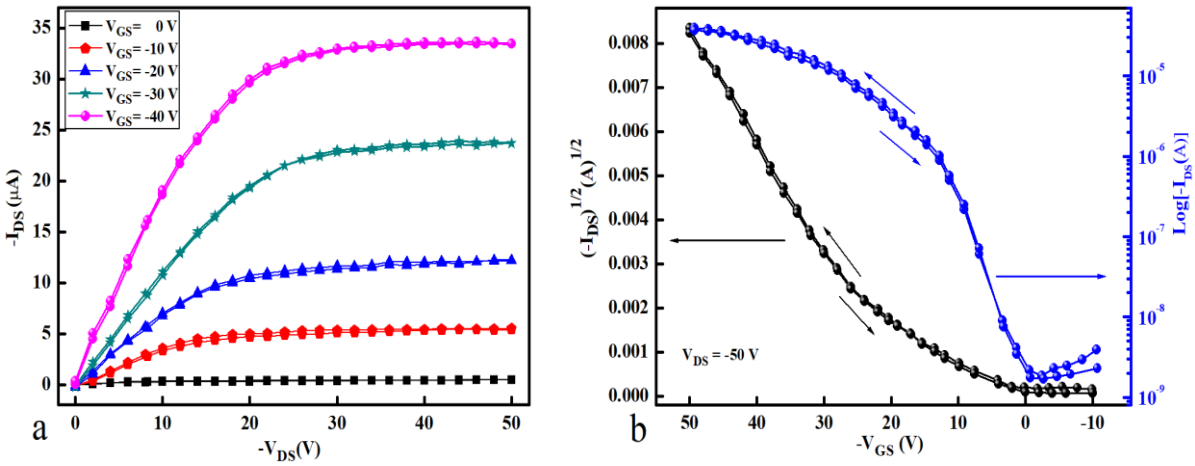

Figure 5. 10: *(a) Output and (b) transfer characteristics of the control cPVA-based OTFT.*

In addition, the transfer characteristic was measured by applying a fixed drain-source voltage (V_{DS}= -50 *V*) and a two direction sweep of V_{GS} (0 *V* to -50 *V* then to 0 *V*) were performed as shown in figure 5.10 (b). It is clear to notify that there is no leakage current and no or negligible hysteresis in the transfer characteristics.

Figure 5.11 illustrates the output and transfer characteristics of the cPVA-based OTFMT, where an additional layer of GO was inserted between the two cPVA insulating layers. Figure 5.11 (a) demonstrates the output characteristics of the control OTFT and the effect of the GO layer on the output behaviour of the memory transistor.

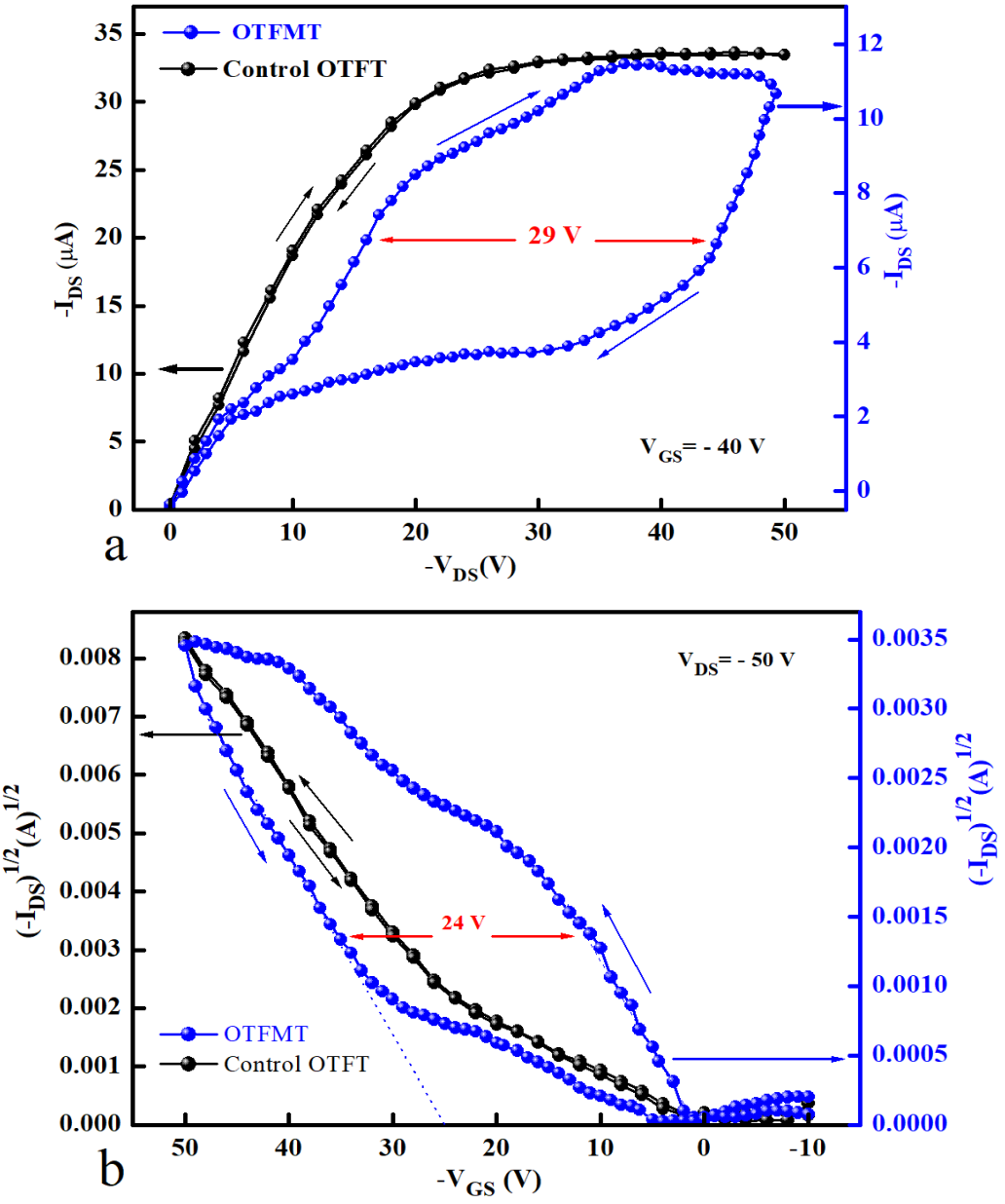

Figure 5. 11: *(a) Output and (b) transfer characteristics of the cPVA-based OTFT (without a floating gate) and OTFMT (with a GO floating gate).*

For the control device and the memory device, the gate voltage was fixed to -40 *V* and the drain-source voltages were swept from 0 to -50 *V*. The memory window (ΔV_T) in the output characteristics of OTFMT was 29*V*, which is obtained from the double sweep of V_{DS} voltage. Also, there is no, or negligible hysteresis can be found in the control device.

Furthermore, the memory window of the transfer characteristics was measured to be 23*V*, while the control device still has no or negligible hysteresis for the double sweep of V_{GS} in

the range of (0 *V* to -50 *V*) and V_{DS} was fixed to -50 *V* for both devices as shown in Figure 5.11 (b). Similar to the cPMMA-based memory transistor, counter-clockwise hysteresis in the transfer characteristics were obtained in these devices. When a high negative gate bias is applied to the cPVA-base OTFMT, holes can be injected from the TIPS-pentacene semiconductor layer into the GO floating gate passing the top cPVA layer. These holes will be charging up the GO floating gate and giving a programming state to the memory transistor. While applying a positive gate voltage ($V_{GS} > 0$), holes will be removed from the GO charge trapping to the semiconducting layer giving an erase state to the memory transistor. Equation 5.1 was applied to determine the charge stored (Q) in the GO floating gate, which was estimated to be 1.65×10^{12} cm^{-2} when C_i for the TIPS-pentacene/cPVA structure was found 1.15×10^{-9} F cm^{-2} and a memory window of 23*V*. This storage charge is about double of that for the cPMMA-based memory transistor. To find the field-effect mobility (μ) of the reference and the cPVA-based memory transistor, threshold voltages from the transfer characteristic in figure 5.10 (b) with equation 2.12 (chapter 2) can be applied and the motilities were estimated to be 1.15 $cm^{-2}\,V^{-1}\,s^{-1}$ and 0.68 $cm^{-2}\,V^{-1}\,s^{-1}$ for the reference transistor and the memory transistor respectively. In addition, threshold voltages of -1*V* and -25 *V* for the forward and reverse directions were estimated, respectively. Threshold voltage is an indicator to study the memory behaviour, for this investigation, consecutive positive and negative pulses of (+10 *V* and -10 *V*) were applied to the gate electrode when V_{DS} was kept at 0 *V*. The same procedure in cPMMA-based memory transistors was followed to measure the threshold voltage shift in the transfer characteristics. Figure 5.12 (a) represents the transfer characteristics of the cPVA-based memory transistor after applying negative and positive pulses (-10 *V* and +10 *V*) for 2s respectively to produce the write and erase state. When a negative pulse of (-10 *V*) is applied, a significant shift in the transfer curve can be observed to a higher negative direction, causing the writing process with a low drain-source current. In contrast, a positive shift of threshold voltages were detected when a positive pulse of (+10 *V*) is applied to produce the erase state. For more investigation, different gate voltages (-20*V*, -30*V*, -40*V* and -50*V*) were applied to measure the transfer characteristics as shown in Figure 5.12(b). The drain-source voltage is fixed to -50 *V* in both figures. From figure 5.12 (b), it is clear that the memory window of the transfer characteristics increased when the maximum applied gate voltage was increased and the obtained values were (8 *V*, 13 *V*,19 *V*,25 *V*) for the maximum gate voltages of (-20 *V*, -30 *V*, -40 *V*, -50 *V*), respectively.

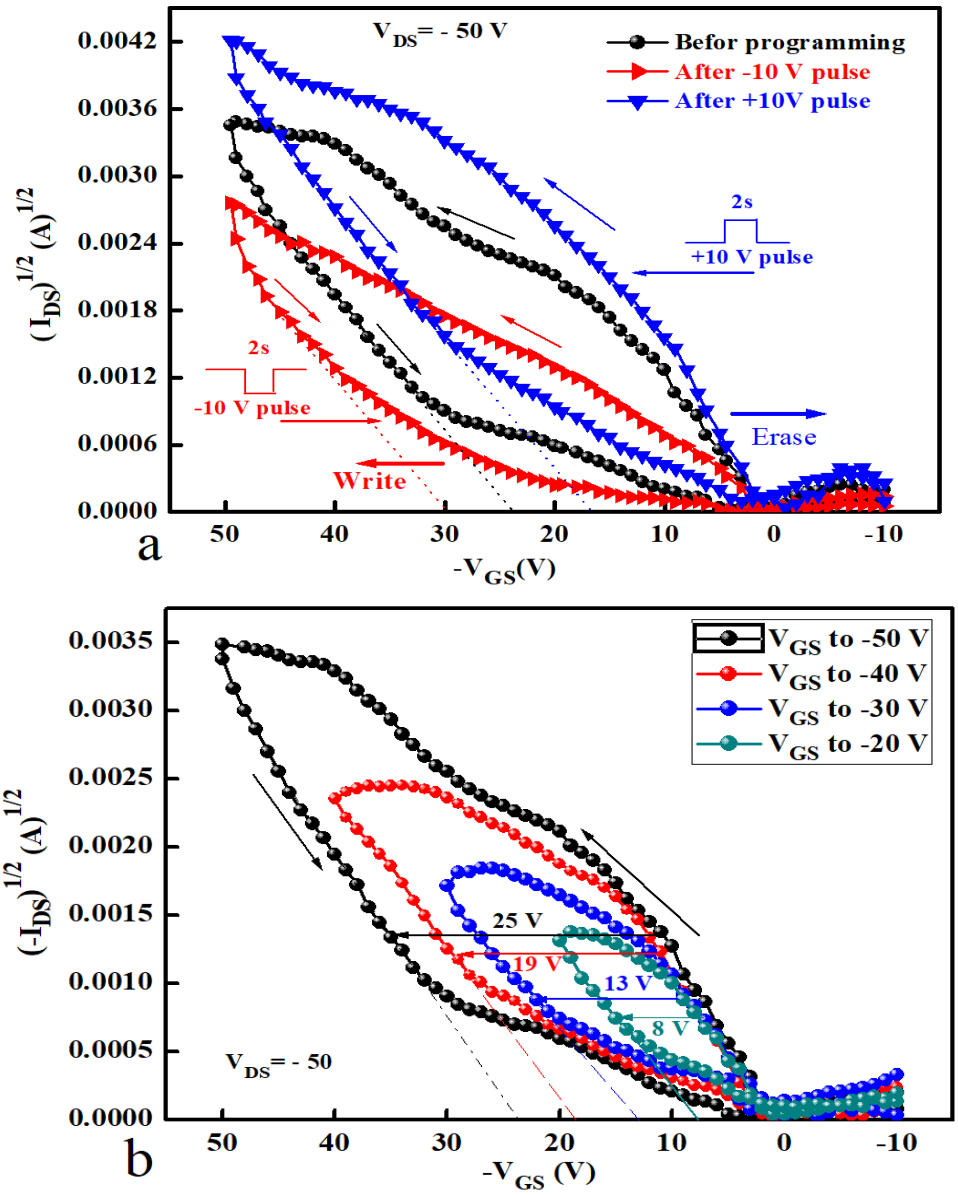

Figure 5. 12 *(a): Positive and negative pulses of 10 V for 2 sec were applied to the gate electrode to investigate the transfer characteristics of the fabricated cPVA-based OTFMT. (b) A double sweep of transfer characteristics of OTFMT with different maximin gate voltages (-20 V,-30 V,-40V and -50V).*

Figure 5.13 (a) demonstrates the effect on OTFMTs' behaviour when applying negative and positive voltage pulses to the gate electrode with (V_{DS} = 0*V*) and a fixed duration time of 2*s*. After each applied stress voltage, the transfer characteristics were measured to estimate the shift in the threshold voltage during applying a constant drain-source voltage (V_{DS} = -50) and V_{GS} was swept from +10 *V* to -50 *V* with a voltage step of 1*V*. Figure 5.13 (b) shows the effect of applying positive voltage pulses on the threshold shift.

It can be seen that increasing voltage pulses causes an increase in the threshold shift to a higher positive value (erase state). Whereas, a negative shift in the threshold voltages was obtained when negative voltage pulses are applied to the gate electrode (write state). This behaviour can be clearly seen in figure 5.12 (a).

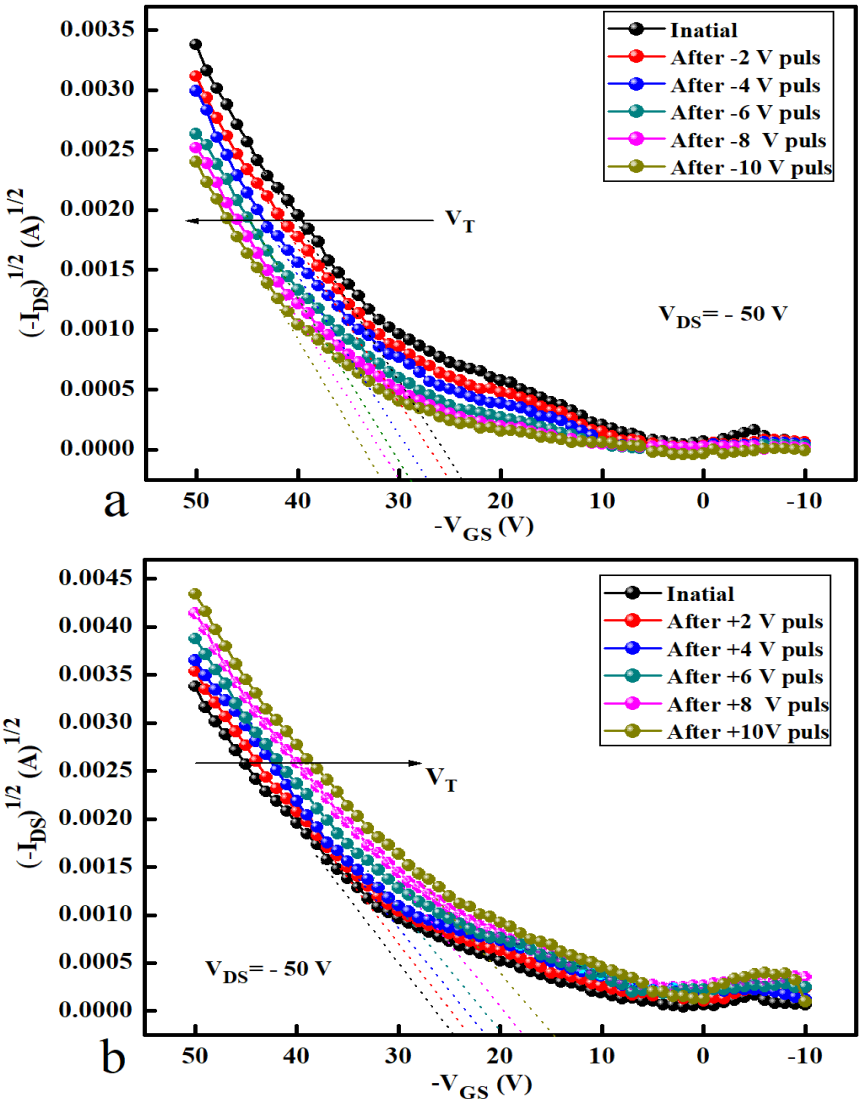

***Figure 5. 13**: The effect of applying different pulses on transfer characteristics of TFMT (a) negative pulses and (b) positive pulses.*

Figure 5.14 (a) illustrates the effect of applying negative and positive pulses to the gate electrode for 2*s* on the threshold voltage shift of the memory transistor. It is distinct that increasing the applied voltage pulses causes increasing of threshold voltages. The memory window can be clearly seen even with a programming voltage of 2 V or less.

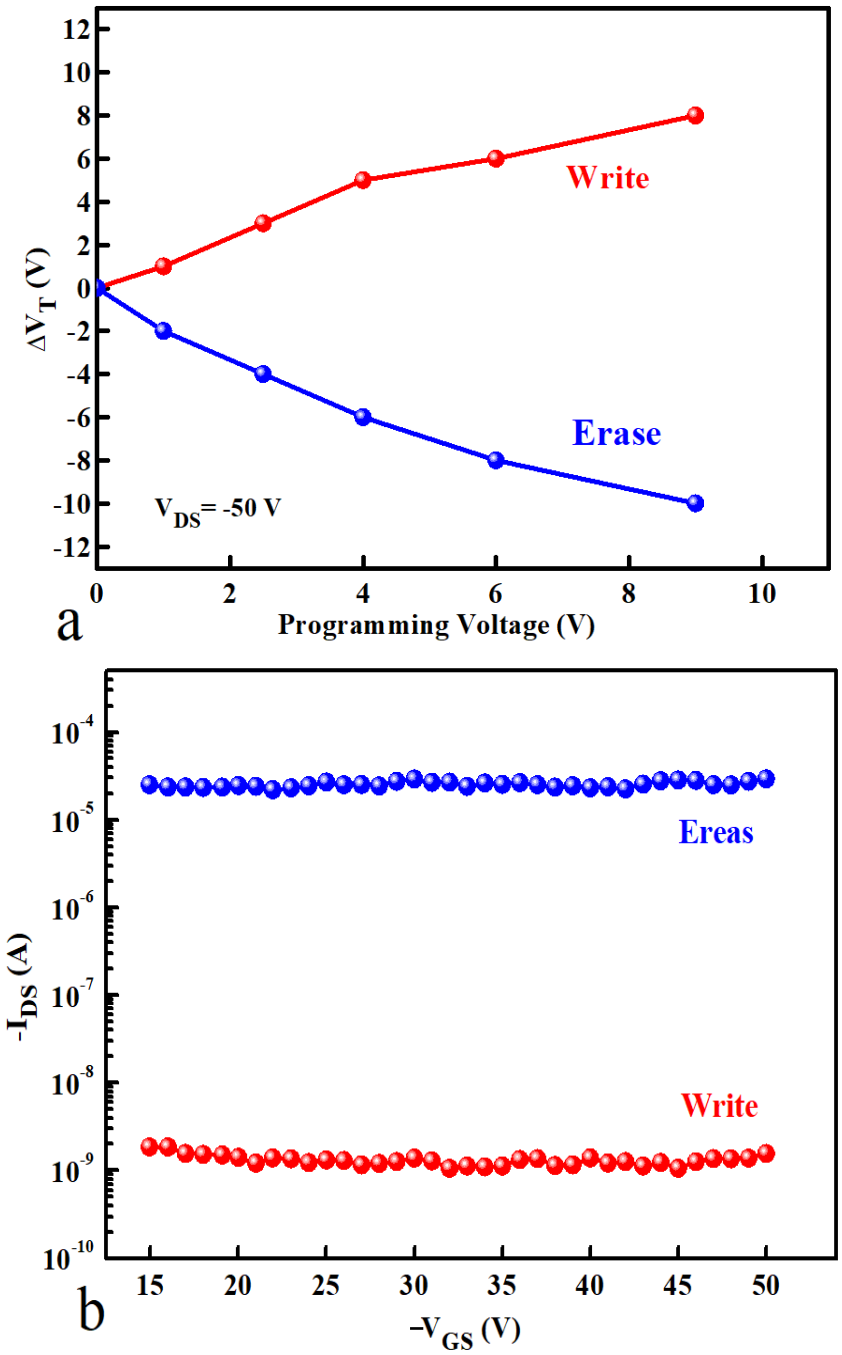

Figure 5. 14: *Programming characteristics of TIPS-pentacene based OTFMT. (a) the threshold voltage shift (ΔV_T) resulting from different applied voltage pulses, (b) applying a negative and positive pulses voltage to produce write and erase processes, respectively.*

From Figure 5.14 (b), the write and erase states can be recognised for a range of applied gate voltages (-15 *V* to -50 *V*) which are attained by the effect of programming pulses of -20 V and 20 V, respectively. As in the cPMMA-based memory transistor, applying a positive reading voltage did not affect the I_{DS} and still recognised the write and erase state of the device.

For more investigation, to study the retention capability as a function of time, Figure 5.15 shows the measurement of I_{DS} current after applying negative and positive pulses for the write and erase states. These measurements were made under the same ambient condition and temperature for measuring cPMMA-based OTFMT. Also, it can be seen that applying negative pulses to the gate electrode leads to the positive charge to be accumulated in the floating gate (GO). These positive charges came from the channel and transferred across the TIPS-pentacene semiconductor therefore, an internal electric field was produced in the opposite direction between the gate electrode and the channel. This opposite electric field leads to a higher negative gate voltage needed to turn on the transistor. As a result, the threshold voltage can be shifted more than in case of the unstressed device. On the contrary, the holes (positive charges) were released from the floating gate (GO) to the gate electrode through the TIPS-pentacene semiconductor when positive pulses were applied to the gate electrode. In addition, in this case, the shift in the threshold voltages was moved to a lower negative value leading to less gate voltage to be applied to turn on the transistor.

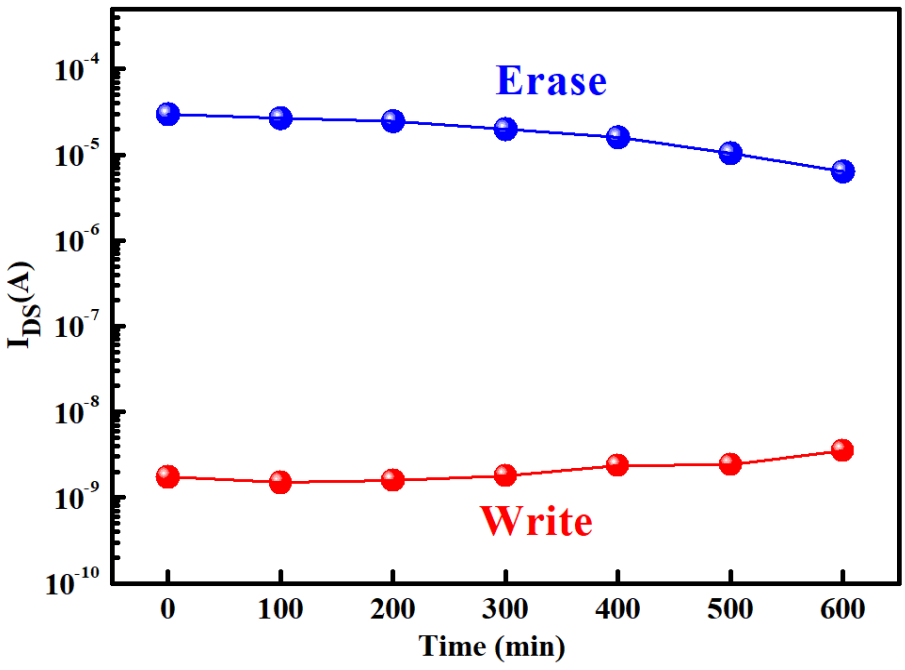

Figure 5. 15: *Characteristics of the charge retention for the OTFMT*

In order to test the endurance properties, a continuous bias pulses voltage of (±20 *V*) were applied for 2*s* to the gate for the write and erase states. After a certain number of write/erase cycles, the I_{DS} current was measured to identify any change in the current value after applying these numbers of pulses. Figure 5.16 clearly illustrates the write and erase current states values and it can be seen that the drain-source current in both cases does not change even after applying the bias pulses more than 200 cycles. the write and erase states produced an average current of 1 x 10^{-9}A and 3 x 10^{-5}A respectively.

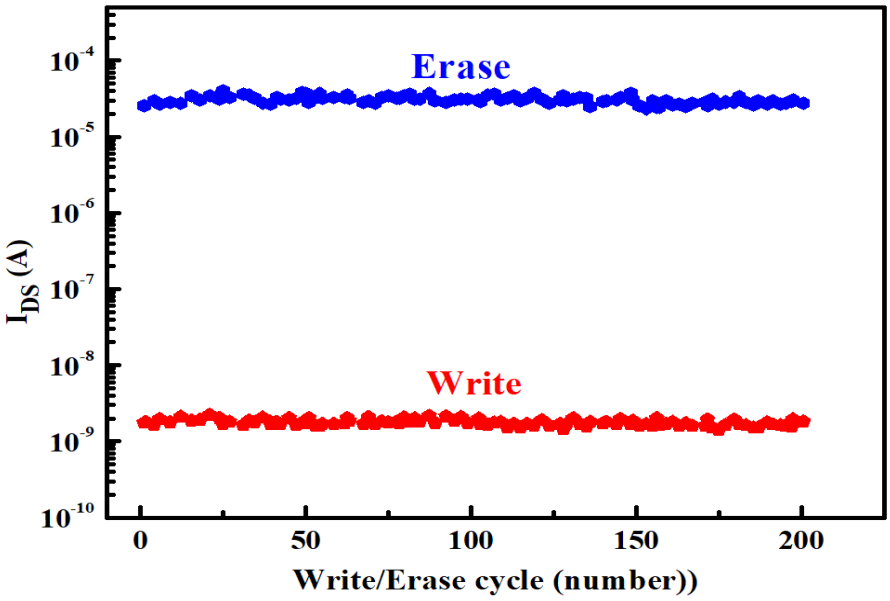

Figure 5.16: *Endurance characteristics of cPVA-based OTFMT with GO as a floating gate charge storage.*

5.4. Summary

Graphene oxide-based organic non-volatile memory transistors were fabricated using low-cost fabrication methods to fabricate two types of memory transistors depending on the blocking-tunnelling barrier layer. Cross-linked polymethyl methacrylate (cPMMA) and cross-linked polyvinyl alcohol (cPVA) were deposited using off-centre spin-coating technique followed by ozone treatment to produce the blocking-tunnelling barrier layers for these two types of memory transistors. Whereas, graphene oxide GO was spin-coated as the floating gate and TIPS-pentacene was drop-casted with an angle of 7^{o} to act as the active layer for both types of OTFMTs. The structure of the memory transistors was fabricated on a clean glass substrate, then thermally evaporated Al was used as a gate electrode for all

devices. Furthermore, gold was thermally evaporated as the source and drain ohmic contacts. All the used materials were examined using AFM plus optical microscopy and exhibited good morphology and crystallinity. In both types of transistors, output and transfer characteristics exhibited clear memory behaviour for the devices embedded with GO and no hysteresis associated with the control transistors. A clear shift in the threshold voltages was recognized when appropriate negative and positive voltage pulses are applied to the gate electrode. These shifts result from charging and discharging of the GO floating gate. Large memory windows of 30*V* and 24*V* with reliable memory operations were obtained for the cPMMA and cPVA-based memory transistors, respectively. The GO floating gate was used as a charge trapping layer where the carriers transferred from TIPS-pentacene through the top insulating layer. Good charge retention property was obtained for the two types of memory transistors. The erase and write states were easy to be recognised when applying pulses of ±2*V* for cPMMA-based OTFMTs and ±1*V* for the cPVA-based OTFMTs as shown in Figures 5.6 a and 5.14 a respectively. The average current recorded for the write and erase states for the cPMMA-based devices are 4 x 10^{-10}A and 3 x 10^{-6}A while for the cPVA-based were 1 x 10^{-9}A and 3 x 10^{-5}A. Of-centre spin-coating method was used to produce the insulating layer. Which provided a good interface surface morphology leading to improved devices. Table 5.1 shows the parameters determined for both types of memory transistors.

Table 5. 1*: The electrical parameters obtained from the two types of memory transistors*

Structure	**Mobility (cm^2v^{-1} s^{-1})**	**Threshold voltage (V)**		**Memory window (V)**	**Charge capacity Q(cm^{-2})**
		V_{TF}	V_{TR}		
cPMMA-based	0.85	2	-28	30	9.15×10^{11}
cPVA-based	0.68	-1	-25	24	1.65×10^{12}

All the devices were based on the solution-processed organic materials and dielectric layers which leads to low fabrication cost. Furthermore, using spin-coating and drop-casting methods could hypothetically be integrated with plastic electronic devices.

5.5 References

[1] Y. Park, D. Gupta, C. Lee, and Y. Hong, "Role of tunnelling layer in graphene-oxide based organic nonvolatile memory transistors," *Org. Electron. physics, Mater. Appl.*, vol. 13, no. 12, pp. 2887–2892, 2012.

[2] S. H. Bae, O. Kahya, B. K. Sharma, J. Kwon, H. J. Cho, B. Özyilmaz, and J. H. Ahn, "Graphene-P(VDF-TrFE) multilayer film for flexible applications," *ACS Nano*, vol. 7, no. 4, pp. 3130–3138, 2013, doi: 10.1021/nn400848j.

[3] T. W. Kim, N. Cernetic, Y. Gao, S. Bae, S. Lee, H. Ma, H. Chen, and A. K. Y. Jen, "Low operational voltage and high performance organic field effect memory transistor with solution processed graphene oxide charge storage media," *Org. Electron. physics, Mater. Appl.*, vol. 15, no. 11, pp. 2775–2782, 2014.

[4] A. Sleiman, P. Sayers, M. F. Mabrook, and H. S. Alaabdlqader, "Graphene oxide-based non-volatile organic field effect memory transistors," *IET Circuits, Devices Syst.*, vol. 9, no. 1, pp. 67–71, 2015.

[5] Y. Che, Y. Zhang, X. Cao, X. Song, M. Cao, H. Dai, J. Yang, G. Zhang, and J. Yao, "Low operating voltage ambipolar graphene oxide-floating-gate memory devices based on quantum dots," *J. Mater. Chem. C*, vol. 4, no. 7, pp. 1420–1424, 2016.

[6] K. J. Sarkar, B. Pal, and P. Banerji, "Graphene oxide as a dielectric and charge trap element in pentacene-based organic thin-film transistors for nonvolatile memory," *ACS Omega*, vol. 4, no. 2, pp. 4312–4319, 2019.

[7] Y. Yuan, G. Giri, A. L. Ayzner, A. P. Zoombelt, S. C. B. Mannsfeld, J. Chen, D. Nordlund, M. F. Toney, J. Huang, and Z. Bao, "Ultra-high mobility transparent organic thin film transistors grown by an off-centre spin- coating method Ultra-high mobility transparent organic thin film transistors grown by an off-centre spin-coating method," *Nat. Commun.*, vol. 5, no. January, pp. 1–9, 2014.

[8] H. Wang, Y. Q. Peng, Z. Y. Ji, M. Liu, L. W. Shang, and X. H. Liu, "Nonvolatile memory devices based on organic field-effect transistors," *Chinese Sci. Bull.*, vol. 56, no. 13, pp. 1325–1332, 2011.

[9] M. F. Mabrook, Y. Yun, C. Pearson, D. A. Zeze, and M. C. Petty, "Charge storage in pentacene/polymethyimethacrylate memory devices," *IEEE Electron Device Lett.*, vol. 30, no. 6, pp. 632–634, 2009.

[10] D. S. Chung, S. M. Lee, J. Y. Back, S. Kwon, Y. Kim, and S. T. Chang, "High Performance Organic Nonvolatile Flash Memory Transistors with High-Resolution Reduced Graphene Oxide Patterns as a Floating Gate," vol. 4, 2014.

[11] Y. Park, K. J. Baeg, and C. Kim, "Solution-Processed Nonvolatile Organic Transistor Memory Based on Semiconductor Blends," *ACS Appl. Mater. Interfaces*, vol. 11, no. 8, pp. 8327–8336, 2019.

[12] S. J. Kim and J. S. Lee, "Flexible organic transistor memory devices," *Nano Lett.*, vol. 10, no. 8, pp. 2884–2890, 2010.

[13] M. F. Mabrook, Y. Yun, C. Pearson, D. A. Zeze, and M. C. Petty, "A pentacene-based organic thin film memory transistor," *Appl. Phys. Lett.*, vol. 94, no. 17, pp. 1–4, 2009.

[14] S. Fakher, A. Sleiman, A. Ayesh, M. C. Petty, D. Zeze, and M. Mabrook, ' *Organic Floating Gate Memory Structures. In: Dimitrakis P. (eds) Charge-Trapping Non-Volatile Memories. Springer, Cham. https://doi.org/10.1007/978-3-319-48705-2_4'*. 2017.

[15] K. J. Baeg, Y. Y. Noh, J. Ghim, S. J. Kang, H. Lee, and D. Y. Kim, "Organic non-volatile memory based on pentacene field-effect transistors using a polymeric gate electret," *Adv. Mater.*, vol. 18, no. 23, pp. 3179–3183, 2006.

[16] T. B. Singh, N. Marjanović, G. J. Matt, N. S. Sariciftci, R. Schwödiauer, and S. Bauer, "Nonvolatile organic field-effect transistor memory element with a polymeric gate electret," *Appl. Phys. Lett.*, vol. 85, no. 22, pp. 5409–5411, 2004.

[17] T. W. Kim, N. Cernetic, Y. Gao, S. Bae, S. Lee, H. Ma, H. Chen, and A. K. Y. Jen, "Low operational voltage and high performance organic field effect memory transistor with solution processed graphene oxide charge storage media," *Org. Electron.*, vol. 15, no. 11, pp. 2775–2782, 2014.

[18] S. Fakher, R. Nejm, A. Ayesh, A. Al-Ghaferi, D. Zeze, and M. Mabrook, "Single-walled carbon-nanotubes-based organic memory structures," *Molecules*, vol. 21, no. 9, pp. 1–11, 2016.

[19] D. Hu, G. Zhang, H. Yang, J. Zhang, C. Chen, S. Lan, H. Chen, and T. Guo, "High-Performance Nonvolatile Organic Transistor Memory Using Quantum Dots-Based Floating Gate," *IEEE Trans. Electron Devices*, vol. 64, no. 9, pp. 3816–3821, 2017.

[20] D. Hu, G. Zhang, H. Yang, J. Zhang, C. Chen, S. Lan, H. Chen, and T. Guo, "High-Performance Nonvolatile Organic Transistor Memory Using Quantum Dots-Based Floating Gate," *IEEE Trans. Electron Devices*, vol. 64, no. 9, pp. 3816–3821, 2017.

[21] J. P. Hong, A. Y. Park, S. Lee, J. Kang, N. Shin, and D. Y. Yoon, "Tuning of Ag work functions by self-assembled monolayers of aromatic thiols for an efficient hole injection for solution processed triisopropylsilylethynyl pentacene organic thin film transistors," *Appl. Phys. Lett.*, vol. 92, no. 14, 2008.

Chapter 6

Organic Thin Film Transistor-Based Sensor

6.1 Introduction

Organic thin film transistor based-sensing technology has been widely investigated in the last few years [1-6]. The low fabrication cost, high sensitivity, short response and recovery time allowed this type of sensors to dominate the research activities in academia and industry [7]. In this chapter,, we tried to investigate and applying the two types of solution-processed organic thin film transistors (OTFTs) based on cross-linking Poly(methyl methacrylate) cPMMA and cross-linking Poly(vinyl alcohol) cPVA as insulating layers which were deposited using off-centre deposition technique in chapter 4.Where the (TIPS) pentacene semiconductor has been used as an active layer for alcohol sensors. The fabrication and characterisation of the OTFTs were explained in detail in chapter 4. These two types of transistors were exposed to alcohol vapours (ethanol and methanol) with parts per million (ppm) concentrations for both gasses (1 ppm to 8 ppm). While exposing the devices to different concentration of vapours, the current-voltage characteristics of the OTFTs were investigated. The output characteristics (V_{DS}-I_{DS}) at different gate voltage (V_{GS}) and different gas concentrations were investigated. Furthermore, the threshold voltage and device mobility with different gas concentrations were calculated using the transfer characteristics. Alcohol vapour was produced with nitrogen as the gas carrier with a flow rate F_1 of 100 ml.min^{-1} passing over a permeation vial containing a quantity of alcohol solvent at room temperature (23 ^{0}C ±1 ^{0}C) and under atmospheric pressure. Then the concentration of alcohol vapour C_1 was be calculated using equation (6.1) [8,9].

$$C_1 = \frac{P\,\rho}{F_1} \tag{6.1}$$

where P is the permeation rate, ρ is the reciprocal vapour density of alcohol and F_1 is the nitrogen gas flow rate. To produce different concentrations of alcohol vapour (methanol or ethanol), another nitrogen diluting stream of a flow rate F_2 was be mixed with alcohol vapour to produce alcohol concentrations (1, 2, 4, 6, 7 and 8 ppm) using equation (6.2) [8,9].

$$C = C_1 \frac{F_1}{F_1 + F_2} \tag{6.2}$$

Where C is the alcohol vapour concentration under the test, F_2 is the flow rate of dilution nitrogen stream. All measurements were made in atmospheric pressure and room temperature using in-house Bangor gas sensing system and Keithley 2636 source meter. More detail about the gas sensing system is described in detail in chapter 3 section 3.5.4 (experimental technique).

6.2 cPMMA-based OTFTs as gas sensors.

To investigate cPMMA-based OTFTs as gas sensors, the devices were exposed to alcohol (ethanol and methanol) vapours with different concentrations 0 to 8 ppm (section 3.5.4 explained in detail how to get these concentrations) during the *I-V* measurements. The response and recovery time and the sensitivity of these devices were estimated from the change in the field-effect mobility, the current on-off ratio, output saturation current and the shift in the threshold voltages during the gas exposure [10-14].

6.2.1 Measurements and electrical properties

6.2.1.1 Ethanol sensing

First, the cPMMA-based OTFTs were tested as ethanol gas detector. In this investigation, the output and transfer of the reference device were measured at room temperature, as shown in Figure 6.1. Figure 6.1 (a) represents the output characteristics of the reference device, were obtained by applying drain-source voltages (V_{DS} = 0 to -60 V*)* with different gate bias voltages (V_{GS} = 0 , -10, -20, -30, -40, -50 V). Figure 6.1 (b) shows the transfer characteristics for the same device when the V_{GS} is swept from 20 *V* to -50 V versus $(I_{DS})^{1/2}$ (with a step of 1V) with a fixed V_{DS} = -50 V. Figure 6.1 (a) and (b), exhibited a clear output and transfer behaviour of OTFT. The maximum saturation current (I_{sat}) from the output characteristics for the reference device was estimated to be 26.7 µA when -50 V of V_{GS} is applied. While the threshold voltage (V_T), on-off ratio and the field-effect mobility for the same device are -8V, 1×10^{-4} and 1.34 $cm^2V^{-1}s^{-1}$, respectively. In order to test the OTFT as a gas sensor, ethanol vapour was prepared from nitrogen gas stream with a flow rate of 100 ml. min^{-1} passing over ethanol solvent. From equation 6.1, ethanol vapour with a concentration of 8

ppm was generated from the main flow F_1 ($P = 0.630$ mg. min^{-1} and $\rho = 1.267 \times 10^{-3}$ ml. mg^{-1}).

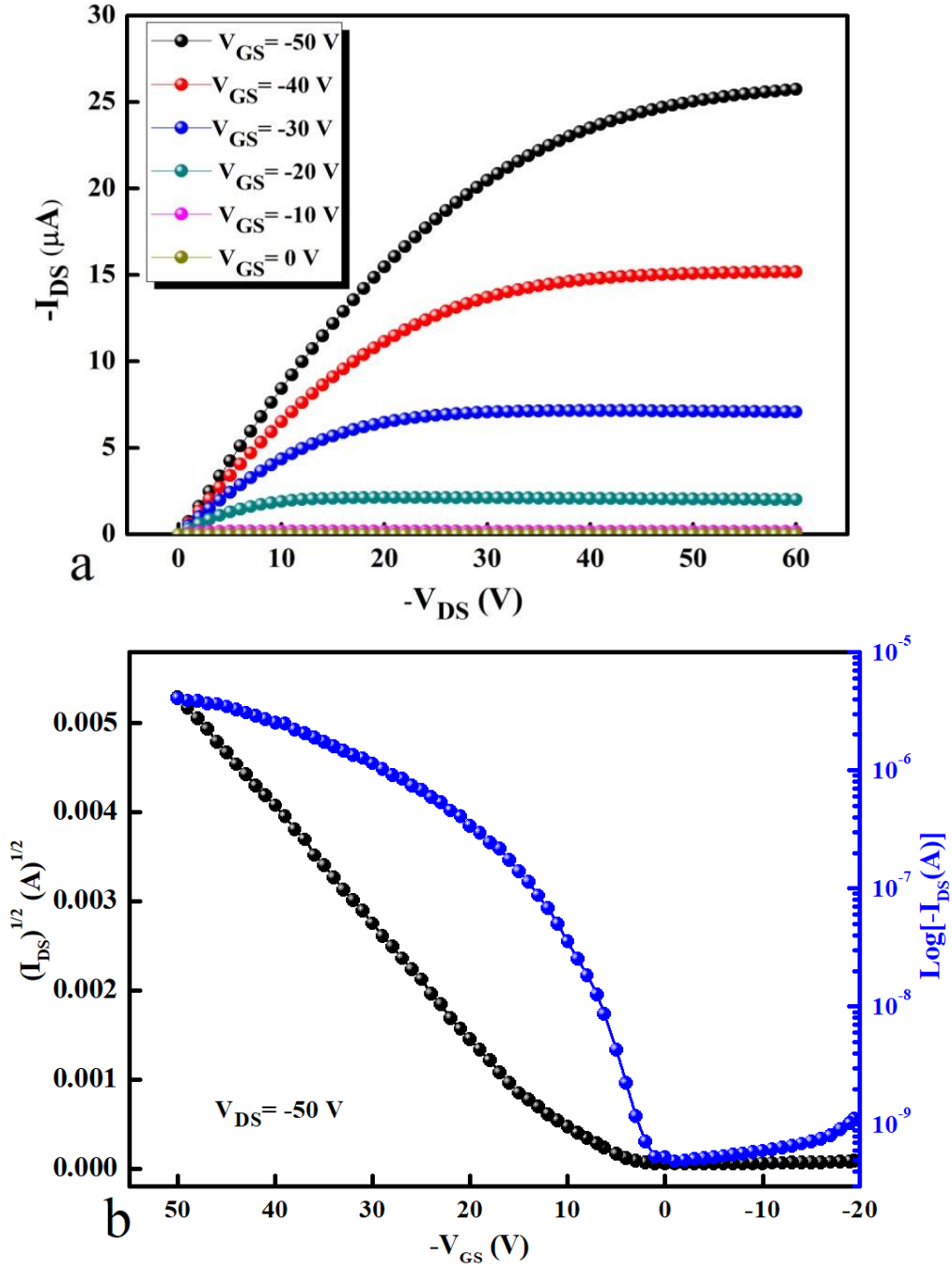

Figure 6.1: *(a) Output characteristics and (b) transfer characteristics of OTFT as a reference for gas sensing measurements.*

To produce different ethanol concentrations, various nitrogen flow rates were used in the flowmeter (F_2 =100, 200, 300, 400 and 500 ml/min) for the ethanol vapour to be diluted, and the final ethanol concentrations can be calculated from the equating 6.2. This method

produced (1, 2, 4, 6,7 and 8 ppm) of ethanol vapour concentrations to be used in this test. Figure 6.2 represents the effect of ethanol vapour exposure with a concentration of 8 ppm on the output characteristics of the cPMMA-based OTFT. In this measurement, the output curves of the reference device were measured under nitrogen gas only with applying a gate voltage of (V_{GS} = -20 V, -30 V, -40 V, -50 V) and the drain-source voltage was swept from 0 to -60 V (The blue curves in figure 6.2). On the other hand, for the same parameters of V_{GS} and V_{DS}, the output characteristics of the device were measured during exposure of ethanol vapour in a concentration of 8 ppm. The ethanol exposure affected the device as clearly decreased the output saturation current. In an OTFT-based sensor, the parameters such as field-effect mobility, threshold voltage and on-off current ration can also be affected by the exposed gas molecular and through chemical interaction with the semiconductor and (or) insulator layers. Herein, the gas will be absorbed or adsorbed to contribute as dopants to trap and reduce the charge transport or assist in increasing charge transports between semiconductor and insulator layers [3,15-20]. In this test, the exposed ethanol vapour was permeated into the organic semiconductor to the accumulation region through the grain boundaries and the analyst will hamper the charge carriers to cross the boundaries (making charges traps at the grain boundaries) which leads to reducing the output current [21-23]. For the applied gate voltage of -50 V, the saturation current was dropped from 26.7 µA to 12.5 µA during the investigation under N_2 and 8 ppm ethanol, respectively.

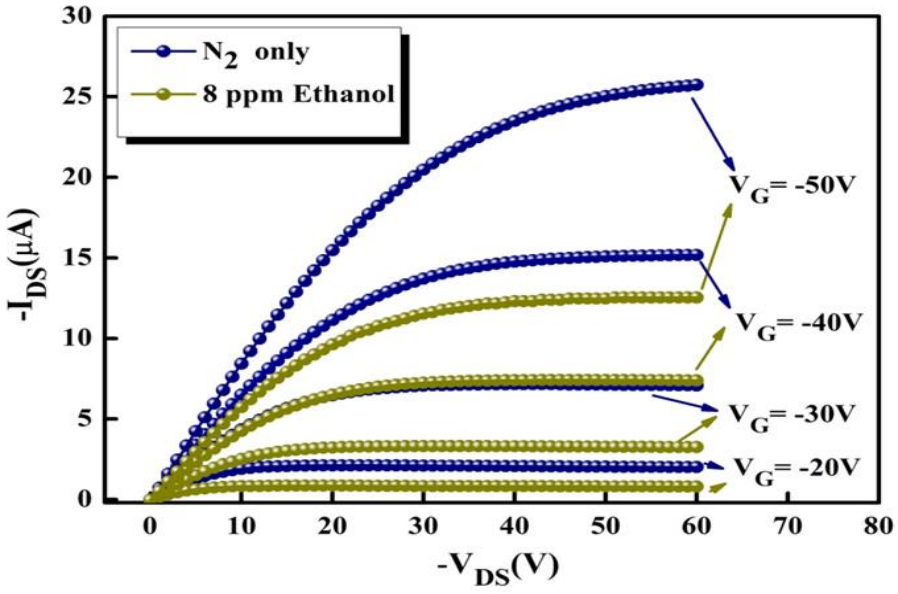

Figure 6.2: *Output characteristics of cPMMA-based OTFT when exposed to N_2 only and 8ppm ethanol vapour for a different V_{GS}.*

Figure 6.3 shows the change in the saturation current of the output characteristics during exposure of different ethanol vapour concentrations (1, 2, 4, 6, 7 and 8 ppm) with an applied V_{GS} = -50 *V* and V_{DS} is swept from 0 to -60 *V*. It is clear from Figure 6.3 that there is a decline in the saturation current with increasing ethanol concentration. Therefore, the change in the output characteristics of the cPMMA-based OTFT can be used as a sensing parameter to detect the presence of ethanol vapour in the environment. This behaviour in the output curves agrees with previous work for using OTFT to detect ammonia gas [24,25]. Figure 6.4 (a) represents the change in the drain-source current I_{DS} as a function of different exposed ethanol concentrations (0 to 8 ppm) at a fixed V_{GS} = -50 V and V_{DS} = -60 V.

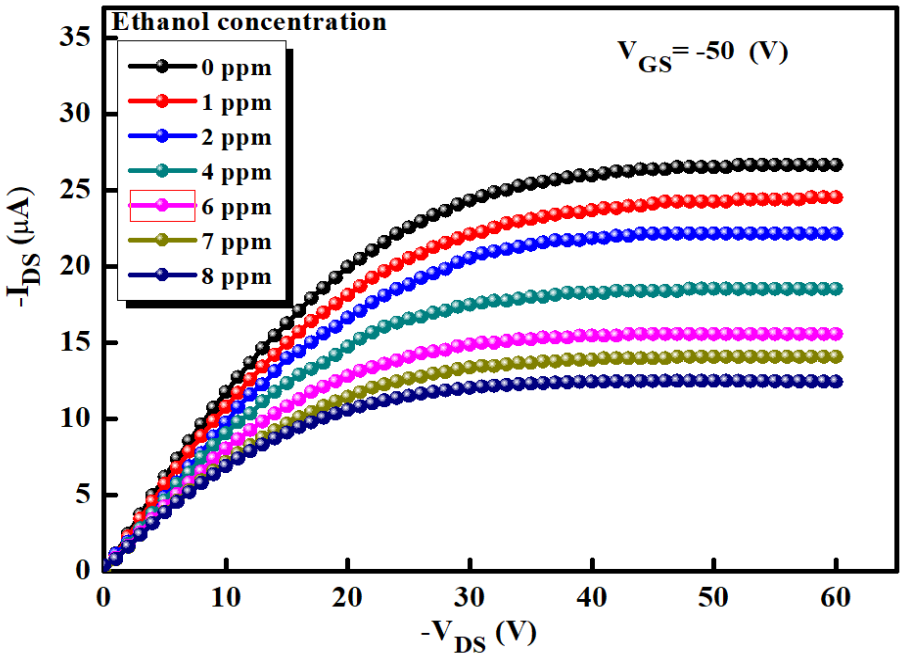

Figure 6. 3: *Output characteristics of cPMMA-based OTFT sensor during exposure to different concentrations of ethanol vapour (0 to 8 ppm), for a fixed gate voltage (V_{GS}=-50 V).*

From Figure 6.4 (a), it can be seen that the response of the cPMMA-based OTFT sensor have a linear relationship over the change of the exposed ethanol concentration as I_{DS} decreased with increasing the exposed ethanol vapour concentration. The sensitivity of this device for the applied parameters (V_{GS} and V_{DS}) was found approximately = -1.708 x 10^{-6} A. ppm^{-1}. Figure 6.4 (b) shows the percentage of relative variation of the drain-source current ($\Delta I/I \times 100$ %) as a function of the ethanol vapour concentration;

$$\text{Where} \qquad \Delta I/I \times 100(\%) = \frac{(I - I_o)}{I_o} \times 100\ \%, \tag{6.3}$$

I is the I_{DS} current when the device is exposed to a known ethanol vapour concentration, and I_o is the I_{DS} current when the device is exposed to N_2 gas only. The sensitivity of the sensor with respect to the change in saturation current S_{IDS} was calculated from the slope of the curve in Figure 6.4 (b) which is - 6.6% ppm^{-1}.

For more investigation, the transfer characteristics of the cPMMA-based OTFT were measured during exposing the sample to the same ethanol vapour concentrations (1 to 8ppm). In these measurements, V_{DS} was fixed to -50 V, while V_{GS} was swept from 20 V to -50 V, as shown in Figure 6.5.

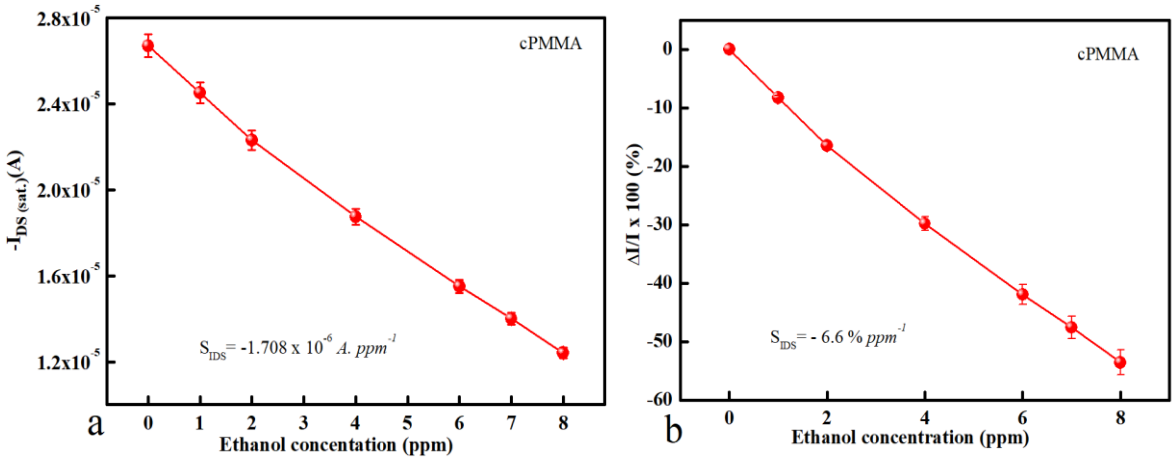

***Figure 6.4**: (a) The change in saturation current of the output characteristics for cPMMA-based OTFT sensor as a result of the exposure of different ethanol vapour concentrations, (b) The relative variation of I_{DS} as function to expose ethanol vapour concentration. V_{GS}= V_{DS} = - 50 V*

A clear shift to a higher negative threshold voltage and decrease in the drain-source current can be observed in the transfer characteristics as a result of increasing the exposed ethanol concentration. In this test, the threshold voltage shift was increased from -8 V to -20 V as a result of exposure 8ppm ethanol vapour to the device. Therefore, for the apparent change in the threshold voltage of the OTFT-based sensor, it can be considered as an indicator to detect ethanol vapour at low concentration. Figure 6.5 (c) illustrates the logarithm of the drain-source-current $log(I_{DS})$ as a function of V_{GS} to estimate the change in the on-off current ratio of the device due to the exposure of different ethanol concentration. It can be seen clearly from Figure 6.5 (c) the on-off ratio decreases with increasing the exposed ethanol vapour concentration. These results are in agreement with previous work using OTFT as a gas sensor [3,25,26]. It was found that exposure ethanol vapour of 8 ppm contributes to

decreasing the on-current from 2.79×10^{-5} A to 1.07×10^{-5} A. This change in the on-current when the device exposed to different concentrations of ethanol vapour can be employed as a gas sensing parameter. Figures 6.5 (b) and (d) are the enlarged data in Figure 6.5 (a) and (c) respectively.

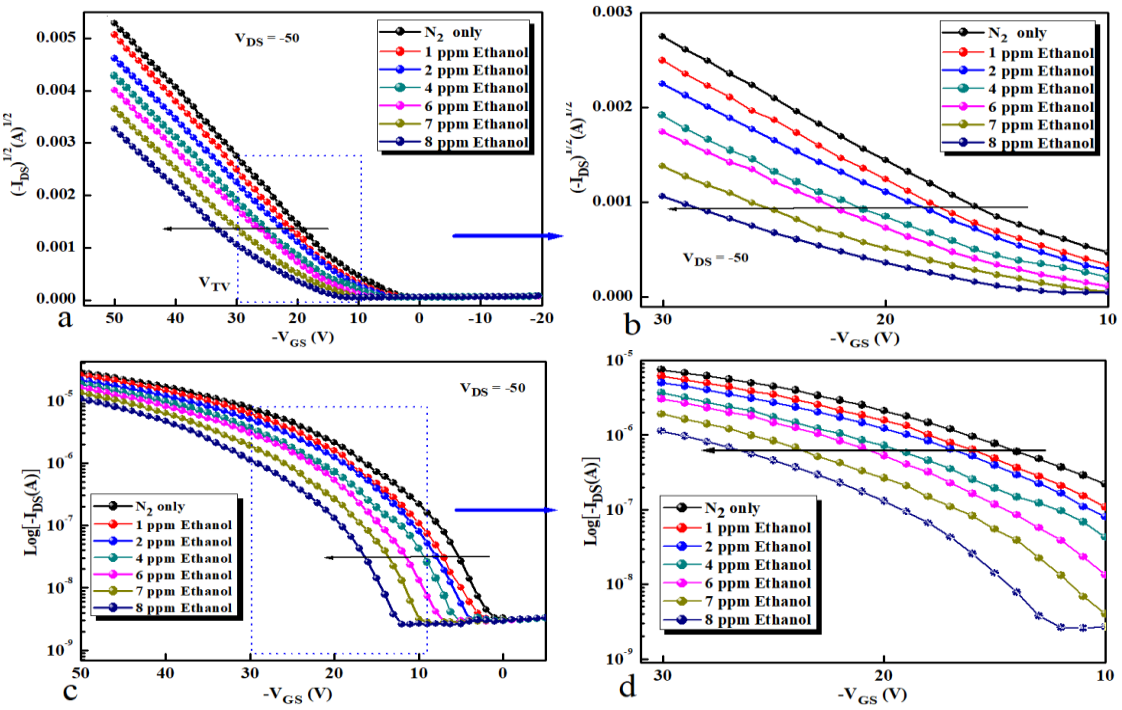

Figure 6.5: *Transfer characteristics of cPMMA-OTFT-based sensor when exposed to different ethanol vapour concentrations (0 to 8ppm) at a fixed V_{DS} = -50. (a) for $(I_{DS})^{1/2}$ versus V_{GS} (c) for Log(I_{DS}) versus V_{GS}. (b) and (d) are the enlarged data in (a) and (c) respectively.*

The percentage sensitivity of the sensor depends on the change in threshold voltage S_{VT} can be estimated from the slope in Figure 6.6(b), which is found to be in the region of 17.2% ppm^{-1}. There is a noticeably increase in threshold voltage value to a higher negative voltage with increasing of the exposed ethanol concentration. Therefore, the change in the threshold voltage of cPMMA-based OTFT sensor can be used as an indicator to detect ethanol vapour concentration in an environment. Figure 6.7 shows the effect of exposure to ethanol vapour concentration on the field-effect mobility of the cPMMA-based OTFT sensor. The mobility of each exposed ethanol concentration was estimated using the threshold voltage data from Figure 6.5(a) and equation (4.1). The field-effect mobility of the device under investigation was dropped from 1.34 $cm^2 V^{-1}s^{-1}$ (exposed to N_2 only) to 0.85 $cm^2 V^{-1}s^{-1}$ when the device was exposed to a maximum ethanol concentration (8ppm).

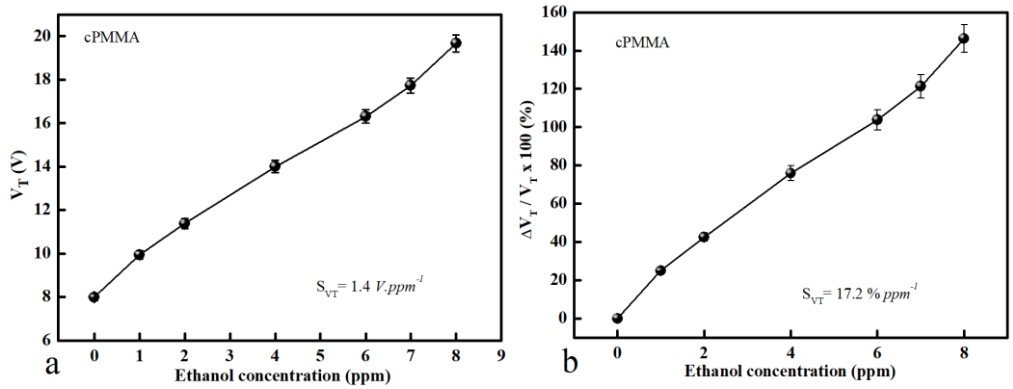

Figure 6.6: *(a) Threshold voltage shift of the cPMMA-based OTFT device versus the exposed ethanol vapour concentration. (b)The percentage relative variation of the threshold voltage shift as a function of the exposed ethanol concentration.* $V_{DS} = V_{GS} = -50$ *V.*

From this result, it is clear to recognise that mobility is decreasing when the exposed gas concentration is increased. The device sensitivity as a change in the mobility S_μ for the applied voltages (V_{GS} and V_{DS}) to the ethanol concentration can be measure from the slope in Figure 6.7(a), which is estimated to -0.0574 ($cm^2\ V^{-1}s^{-1}$).ppm^{-1}. Figure 6.7(b) shows the relative variation of the mobility as a function of exposed ethanol concentration, and from the slope, it was found - 4.2% ppm^{-1}. Accordingly, the change in mobility can be used as a parameter to indicate ethanol gas concentration in an environment.

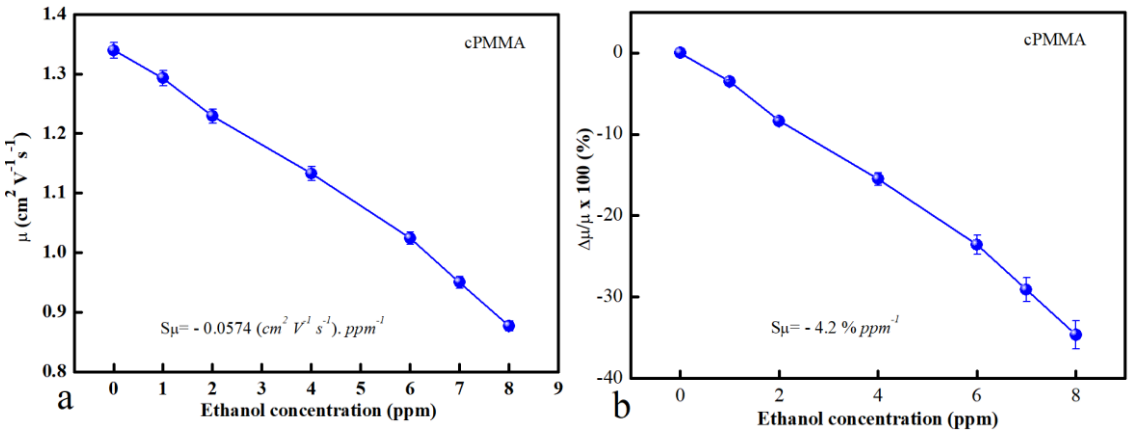

Figure 6.7: *(a)The change in the field-effect mobility values of the cPMMA-based OTFT sensing device versus the exposed ethanol vapour concentrations. (b) The relative variation of the field-effect mobility as a function of the exposed ethanol concentration,* $V_{DS} = V_{GS} = -50$ *V.*

Figure 6.8 represents the change in drain-source current I_{DS} as a function of time when the cPMMA-based OTFT sensor was exposed to different ethanol gas concentration. The test was made by applying gate and drain voltage (V_{GS}= V_{DS} = -50 V). First, the drain-source

current I_{DS} was measured for a period during which the sensor is exposed to N_2 only until reaching the saturation point. Then, different concentrations of ethanol vapour were.

For each concentration, the I_{DS} current measurement must reach the saturation state before exposing a pure N_2 for purifying and getting the recovery state. It is clear that I_{DS} current decreased as a function of increasing the exposed ethanol concentration. In this test, the response time ($R_{es.time}$) (which is measured as the response changed from 10% to 90%) was estimated to be 54 s when the device was exposed to 8 ppm ethanol vapour concentration. Also, the recovery time was found very short as the I_{DS} was recovered in 36 s when the device was flushed with N_2 gas to be purified. It can clearly recognise that the device response was started from the first few seconds of exposure, which can be set as an alarm, and we do not need to reach the saturation region for detecting. The inset figure in Figure 6.8 is the enlarged data for the device responses when it was exposed to 8 ppm of ethanol vapour concentration, which is showing the current saturation region as a function of the exposure time. The test was repeated after 3, 6, 12 and 24 months, and excellent stability was observed for devices stored under vacuum.

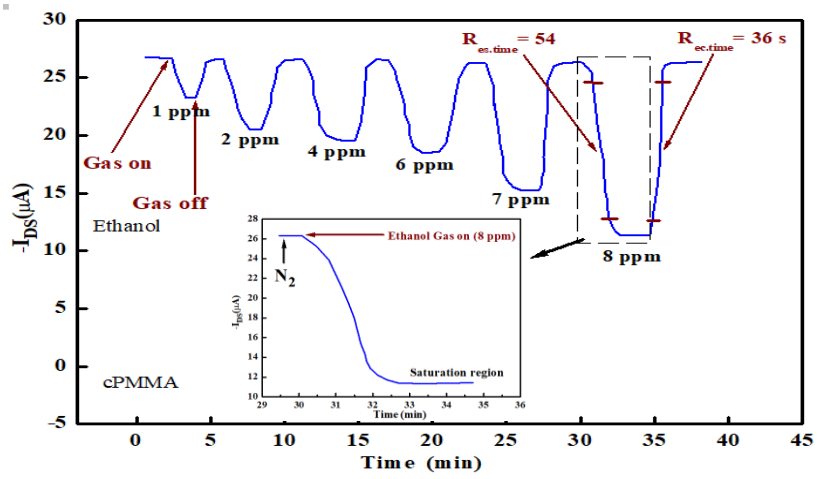

Figure 6. 8: The drain-source current as a function of time when cPMMA-based OTFT sensor is exposed to various ethanol vapour concentration (0 to 8 ppm). The inset figure is the enlarged part of the current when the device was exposed to 8ppm ethanol vapour concentration. $V_{GS} = V_{DS} = -50$ *V*

Figure 6.9 illustrates the device response (relative variation of the I_{DS} current) of cPMMA-based OTFT sensor as a function of time during exposure to different concentrations of ethanol vapour. The I_{DS} current percentage change $\Delta I/I\%$ can be found from equation 6.3. For these measurements, a fixed ($V_{GS} = V_{DS} = -50$ V) is used to estimate the drain-source current during different exposure of ethanol vapour concentrations. From Figure 6.9 the

device response increased due to increasing of exposed ethanol concentration. A response of ~57 % was obtained for exposing the device to 8 ppm of ethanol vapour. Whereas ~13% was attained from exposing 1ppm of ethanol concentration.

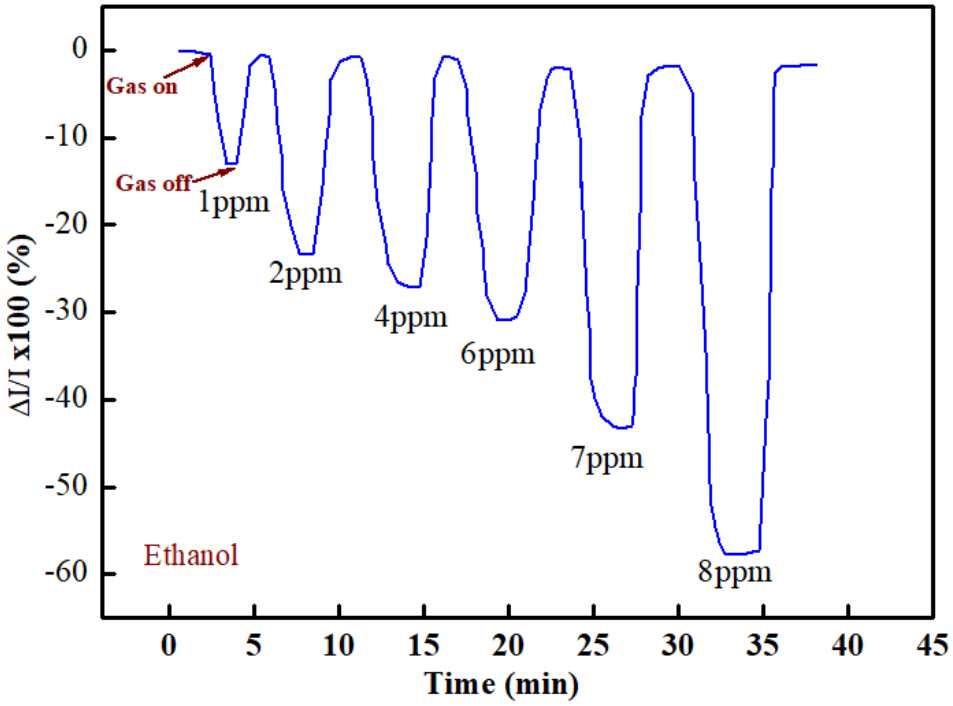

Figure 6.9: *The output current relative variation of the cPMMA-based OTFT sensor as a function of time during exposure to various concentrations of ethanol vapour,* V_{GS} = V_{DS} = - 50 *V.*

6.2.1.2 Methanol sensing

In this section, cPMMA-based OTFTs were tested as a methanol vapour detector. The same device which is used in detecting ethanol vapour (section 6.2.1.1), was used in this sensing evaluation after being kept under vacuum for seven days for purifying. The sensing test was made during exposure to methanol vapour with different concentrations (1 ppm to 8 ppm). Therefore, the same procedure in case of ethanol sensing test was followed to calculate the permeation rate P and reciprocal vapour density ρ of methanol, they were found 0.693 mg. min^{-1} and 1.264 $x10^{-3}$ ml. mg^{-1}, respectively. To find out a reference data of the output characteristics, the device was investigated under a nitrogen environment and normal atmospheric pressure at room temperature. For this test, various gate voltages were applied (V_{GS} = -20, -30, -40, -50 V) and the drain-source voltage was swept from 0 V to -60 V as shown in Figure 6.10 (the blue curves). Furthermore, the output characteristics for the same sensing device with applying the same voltages range were measured during exposing the

sensor to methanol vapour with a concentration of 8 ppm as in Figure 6.10 (the magenta curves). From figure 6.10, it can be seen that the drain-source current curves in the output characteristics during exposure to methanol concentration of 8 ppm have lower values than those of the reference curves for the same drain-gate voltages V_{GS}. It was found that the output current in the saturation region was decreased from 26.7 µA (with exposing of 0 ppm methanol vapour) to 16.3 µA (with exposing of 8 ppm of methanol vapour).

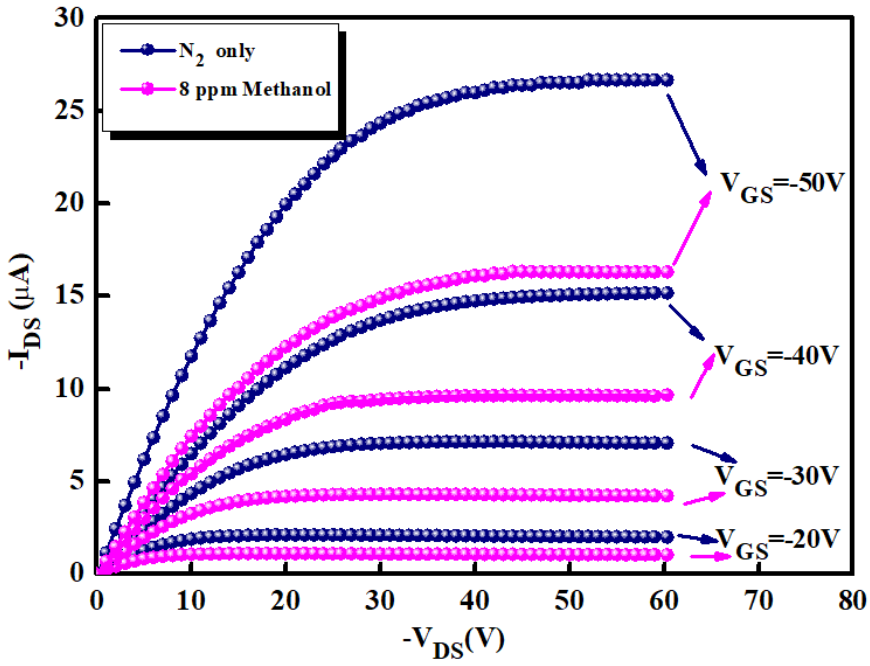

Figure 6.10: *Output characteristics of the cPMMA-based OTFT sensor device during exposing N_2 gas (blue curves) and 8 ppm methanol vapour(magenta curves) for different gate voltages.*

Figure 6.11 illustrates the effect of exposing different methanol vapour concentrations (1 to 8 ppm) on the output characteristics of cPMMA-based OTFT sensor. Herein, the gate voltage was fixed to -50V, and the drain-source voltage V_{DS} was swept from 0 to -60 V for each exposed methanol concentration. It can be recognised that increasing the exposed methanol concentration leads to a drop in the output saturation current curves (this effect was explained in section 6.2.1.1). Figure 6.12 (a) shows the device sensitivity to different exposed methanol concentrations in term of change in I_{DS} saturation current value (extracted from the data in Figure 6.11). The sensitivity of the device under investigation was estimated to be in the region of -1.21×10^{-6} A. ppm^{-1}. Figure 6.12(b) represents the relative variation of the drain-source current ($\Delta I/I \times 100\ \%$) as a function of the methanol vapour

concentration. The device sensitivity (S_{IDS}) to the methanol vapour was found less than the sensitivity to the ethanol vapour which is estimated from the slope of the curve in Figure 6.12(b) to be -4.51% ppm^{-1}.

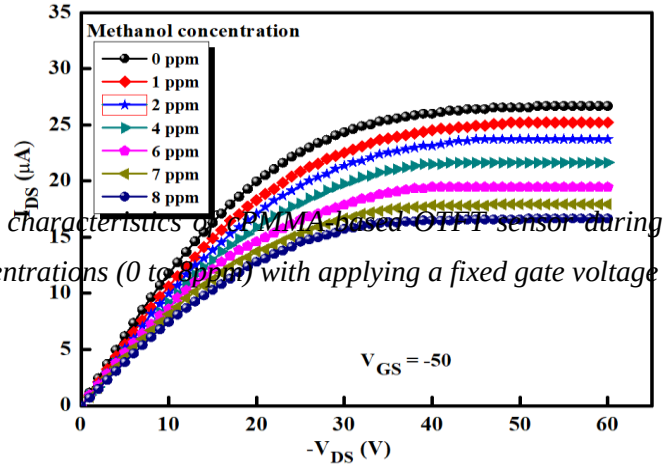

Figure 6.11: *Output characteristics of cPMMA-based OTFT sensor during exposure to various ethanol vapour concentrations (0 to 8 ppm) with applying a fixed gate voltage of V_{GS} = -50 V.*

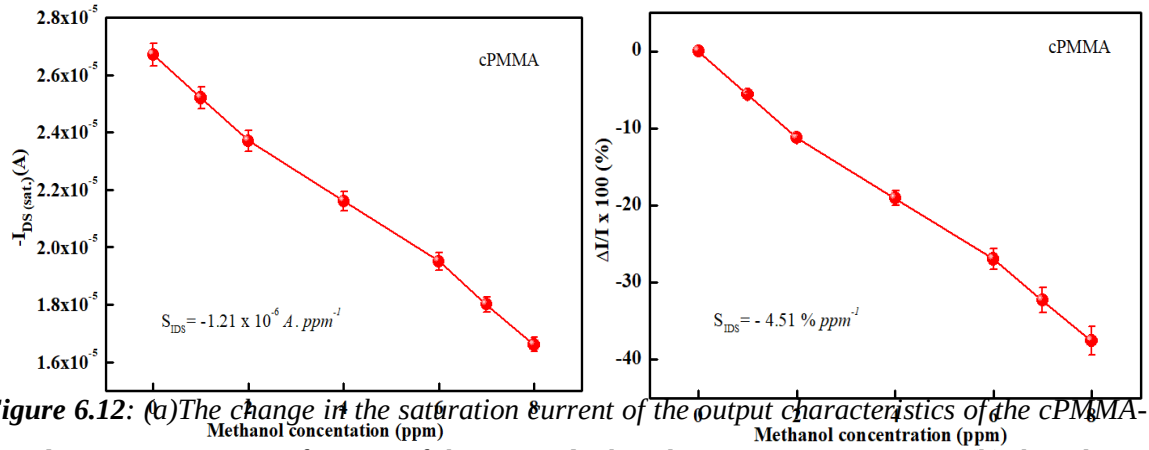

Figure 6.12*: (a)The change in the saturation current of the output characteristics of the cPMMA-based OTFT sensor as a function of the exposed ethanol vapour concentrations. (b) the relative variation of the drain-source current versus different exposed methanol vapour concentrations (0 to 8 ppm),V_{GS} = V_{DS} = - 50 V.*

Figure 6.13(a) shows the transfer characteristics of the device during exposure of different methanol vapour concentration. Herein, the square root of the drain-source current $(-I_{DS})^{1/2}$ is plotted versus the swept gate-source voltage ($-V_{GS}$) from 20 V to -50 V with a fixed drain-source voltage of -50 V. From the transfer curves in Figure 6.13 (a), it can be found that the threshold voltage (V_T) was shifted to a higher negative voltage with increasing the exposed methanol concentration. The maximum shift in the threshold voltage was obtained with

exposure of 8 ppm methanol vapour which is equal to -11 V. In Figure 6.13 (c), the gate voltage was plotted versus log($-I_{DS}$) which is showing the change in the on-current of the transfer carves as a result of the exposed methanol concentration. Here, the on-current was decreased from 2.79 × 10^{-5} A (exposure N_2 only) to 1.17 × 10^{-5} A (exposure 8 ppm of methanol). Figure 6.13 (b) and (d) are the enlarged data in Figure 6.13 (a) and (c) respectively which clearly show the shift in threshold voltages and the decreasing in the on-current when the exposed methanol vapour is increasing.

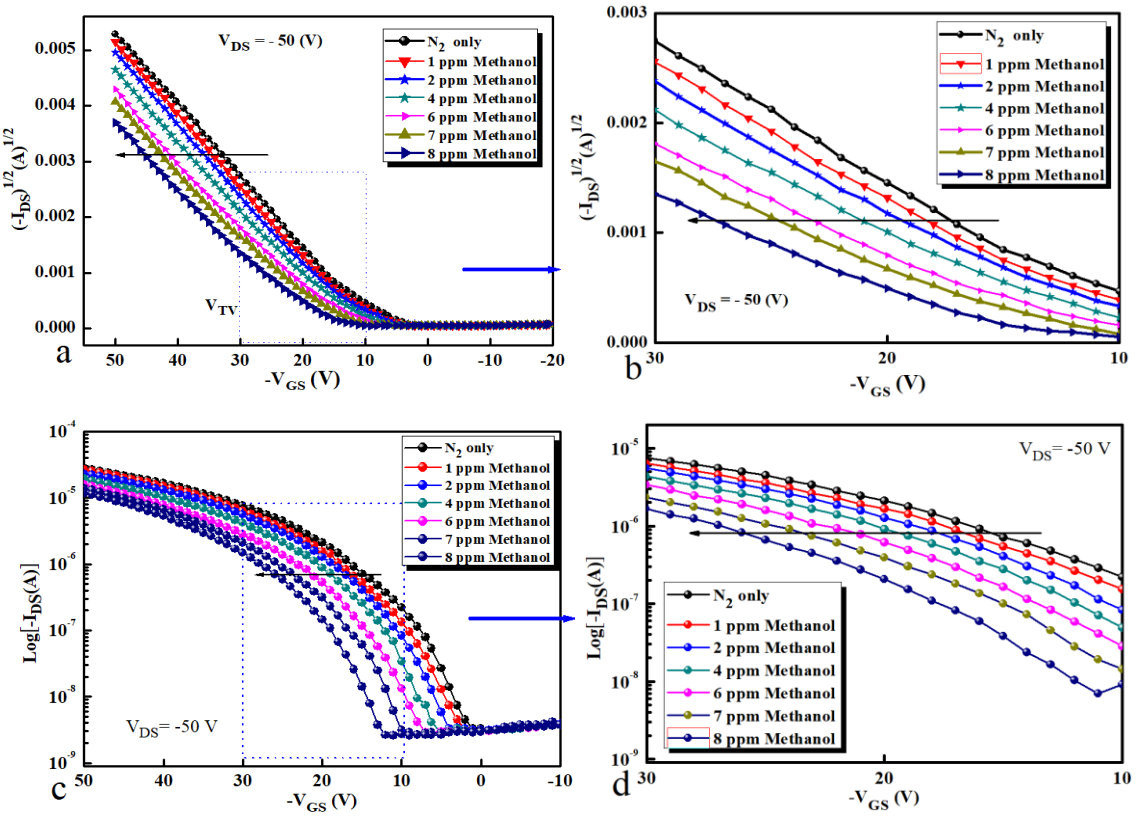

Figure 6.13: *Transfer characteristics of the cPMMA-based OTFT sensor during exposure to various methanol vapour concentration (0 to 8ppm)at a fixed V_{DS}=-50 V. (a) for $(I_{DS})^{1/2}$ versus V_{GS} (c) for Log(I_{DS}) versus V_{GS} (b) and (d) are the enlarged data in (a) and (c) respectively.*

Figure 6.14(a) represents the shift in the threshold voltage ΔV_T as a function of various exposed methanol concentration. The threshold voltages shift values resulting from exposing different methanol concentrations, were obtained from transfer characteristics in Figure 6.13 (a). There is a conspicuously increasing in the threshold voltage shift to a higher negative voltage with increasing of the exposed methanol vapour concentration. The sensitivity of the device under investigation as a change in the threshold voltage shift was

found to be 1.3 V. ppm^{-1}. Figure 6.14(b) illustrates the threshold voltage relative variation ($\Delta V_T/V_T$ %) of the sensor as a result of exposing different methanol concentrations. Therefore, the device percentage sensitivity can be estimated from the slope of the curve in Figure 6.14(b), which it was found 16.1% ppm$^{-1,}$ and it is 1% ppm^{-1} less than of the ethanol vapour detection. To determine the effect of exposure methanol vapour on the mobility of the cPMMA-based OTFT sensor, different concentrations were exposed to the device under investigation. Threshold voltages shift data from Figure 6.13 (a) and equation 4.1 were used to calculate field-effect mobility values of the device during exposing methanol vapour.

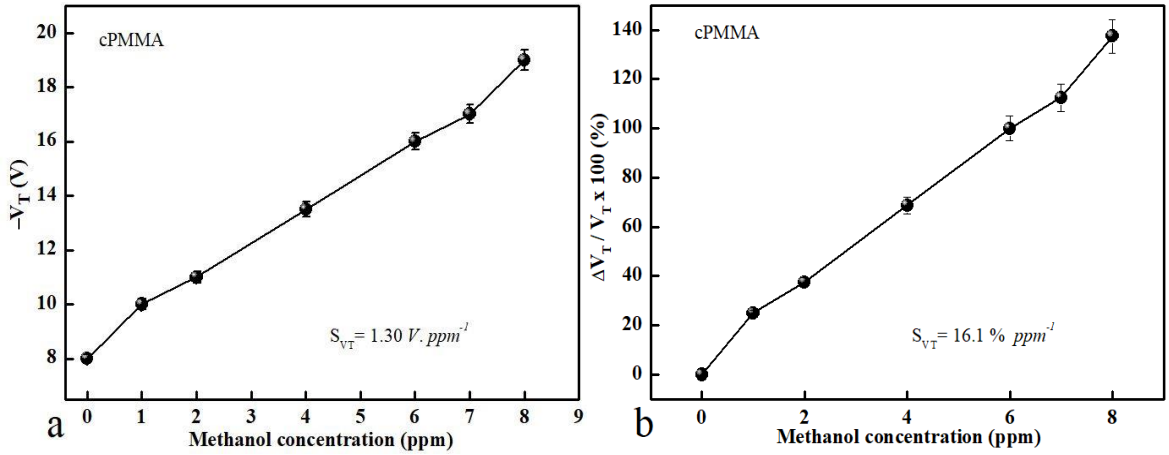

Figure 6.14: *The effect of exposed different concentration of methanol vapour on the threshold voltage shift of the OTFT-based sensor device, V_{DS} = -50 V and V_{GS} = 0 to -50 V.*

Figure 6.15(a) shows the change of the mobility values for the OTFT-based sensor device during exposing various methanol concentration. It can be seen that increasing the exposed methanol vapour concentration leads to decreasing of the device mobility value. The slope of the curve in Figure 6.15(a) represents the device sensitivity depends on mobility changes $S\mu$ to detect methanol vapour, and it was found 0.031 cm^2 V^{-1} s^{-1}. ppm^{-1}. Figure 6.15(b) represents the mobility relative variation of the device as a function of the exposed methanol concentration. The slope of the curve in Figure 6.15(b) represents the device sensitivity which was found -2.2 % ppm^{-1} and still less than of the ethanol detection.

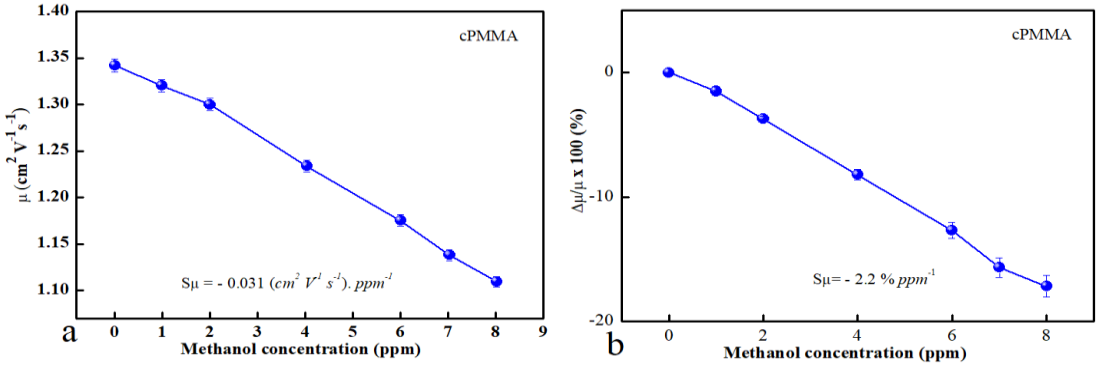

Figure 6.15: *The effect of different of exposed methanol concentration on mobility value of the OTFT-based sensor device, V_{DS} = -50 V and V_{GS} = 0 to -50 V.*

Figure 6.16 illustrates the response of I_{DS} current to a different exposed methanol concentration (0 to 8 ppm) with a continuous-time of measurement at (V_{GS} = V_{DS} = - 50 V). This investigation was started by exposing the cPMMA-based OTFT sensor with N_2 gas only (methanol gas off) until the I_{DS} getting in saturation status, then 1ppm of methanol (methanol Gas on) was exposed to the device. Slightly decreasing in the I_{DS} current was recognised until it reaches saturation value again. After this point, N_2 gas was flashed again (methanol Gas off) to purify the device and recover I_{DS} value. These steps were continually and quickly repeated with increasing of the exposed methanol concentration (0, 1, 2, 4, 6, 7 and 8 ppm) in each step. From the response plot in Figure 6.16, the response time (Res. time) and recovery time (Rec. time) were calculated for the exposed methanol concentration of 8 ppm. These times have been taken between 10% and 90% of the response and recovery curves. The response and recovery time of the cPMMA-based OTFT sensor to methanol vapour were found 66 s and 48 s, respectively. The inset figure in figure 6.16 shows the enlarged response curve of exposing 8 ppm methanol concentration. Herein, the saturation current can be clearly recognised. Figure 6.17 illustrates the relative variation of the drain-source current $\Delta I/I$ % of the sensor during exposure to different methanol concentration as a function of exposing time. The gate and drain-source voltage were taken to a fixed value (V_{GS} = V_{DS} = -50 V). From the test, the maximum relative variation of I_{DS} current was found ~39 % for the exposed methanol concentration of 8 ppm while ~6 % was obtained for exposing 1 ppm concentration. Organic thin film transistor-based sensors have so much attention due to the valuable sensing mechanisms towards alcohol such as; (1) alcohol molecular volume having an effect on the sensing response of the OTFT-based sensor which

affects the analyte diffusion into the semiconductor/insulator interface [27]. (2) sensitivity towards polar alcohols, due to polar-type interactions being dominant in polar-polymer sensors. While, in non-polar-polymer sensors where sensitivity is more towards long alkyl chain-bearing alcohols, dispersion-type interaction was found [28,29]. (3) The hydroxyl group (- OH) has a lone electronic pair. So because of that, hole charge carriers can be trapped in the channel region by alcohol which decreases the drain-source current [30-32]. The hydroxyl group in the alcohol produced a deep trap state making a negative shift of threshold voltage. The weak interaction between the semiconductor and gas analytes generated a low trap density which is decreased the mobility of the OTFT-based sensor [3]. Furthermore, the sensing behaviour can be affected by the grain boundary of the semiconductor active layer, which affects OTFT charge transport [33].

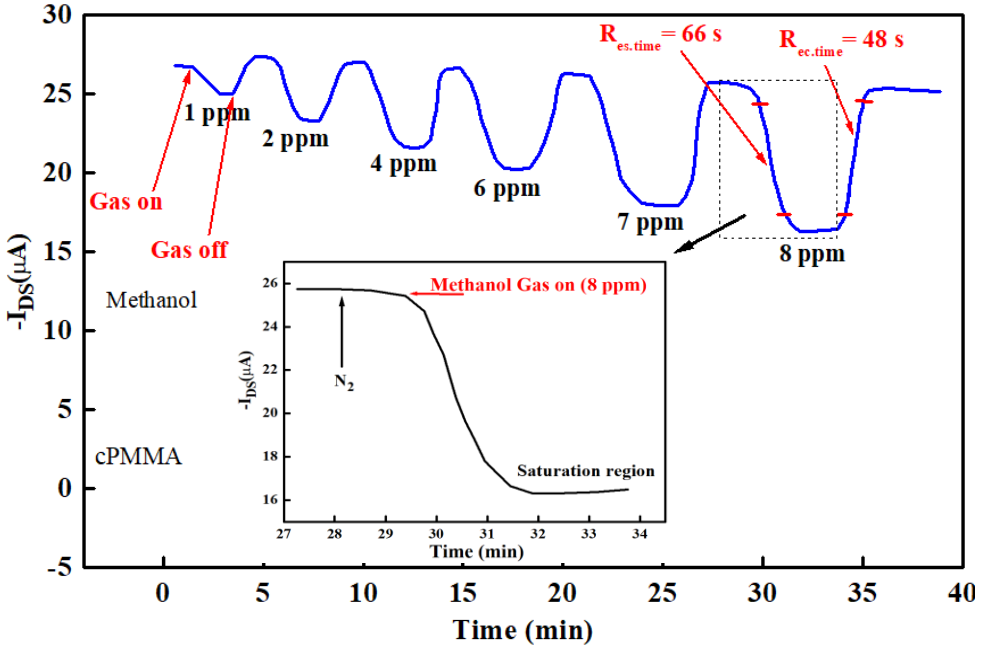

Figure 6.16: *The response of drain-source current to exposed various concentration of methanol vapour (0 ppm to 8ppm). The inset figure is the enlarged part of the current change with 8ppm gas concentration.* V_{GS}= V_{DS} = - 50 V

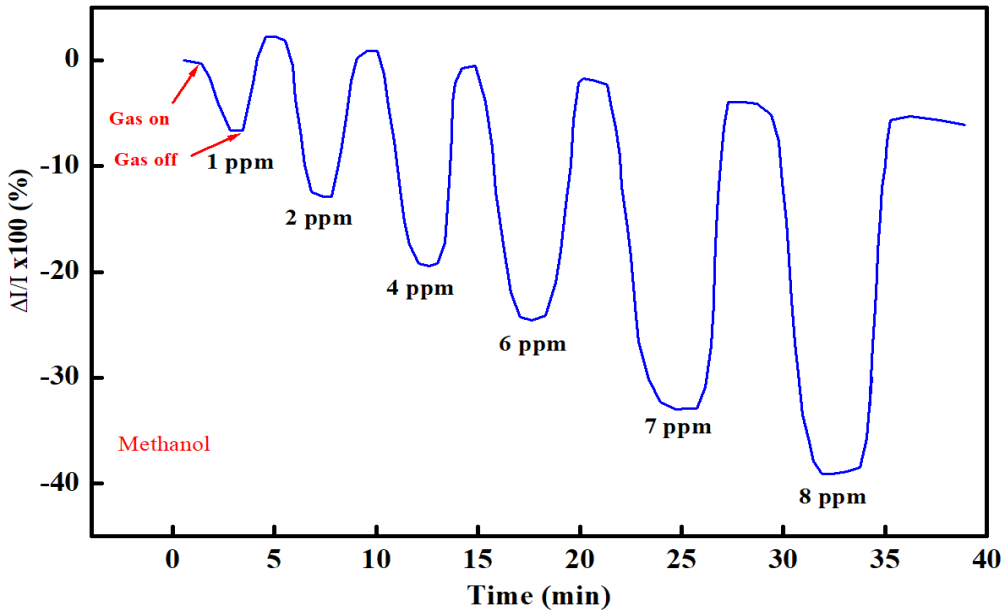

Figure 6.17: *The variation rate of the drain-source current ΔI/I ×100% of the cPMMA-based sensor when exposed different methanol vapour concentration as a function of time,* $V_{GS} = V_{DS} = -50$ *V.*

6.3 cPVA-based OTFTs as a gas sensor.

In this section, cPVA-based OTFTs were fabricated and tested as gas sensor. The same procedure in chapter 4.3.1 was followed for the device fabrication. Furthermore, the same method used in the cPMMA-based OTFT was applied for gas sensing test by exposing the device to the same range of alcohol vapours (ethanol and methanol) concentrations (0 to 8 ppm). The electrical characterisations of the devices under investigation were measured to study their capability to be used as gas sensors.

6.3.1 Measurement and electric characterisations

6.3.1.1 Ethanol sensing

In order to test the cPVA-based OTFTs as gas detectors, the output and transfer characteristics were measured for a reference device (exposed to N_2 only) under atmospheric pressure at room temperature. Figure 6.18(a) and (b) illustrate the output and transfer characteristics of the reference device. The output characteristic was performed by applying different gate voltages (0 V, -10 V, -20 V, -30 V and -40 V) and the drain-source voltage was swept from 0 V to -30 V as shown in Figure 6.18(a). A maximum output saturation

current (I_{sat}) of -22.5 µA was obtained by applying V_{GS} = -40 V. Whereas Figure 6.18 (b) shows the transfer characteristics of the reference device. Herein, V_{DS} was fixed to -40 V and the gate-source voltage V_{GS} was swept from 12V to -30V. The field-effect mobility μ and threshold voltage (V_T) of the reference device were estimated from the transfer characteristic, which found to be 1.21 cm^2 V^{-1} s^{-1} and -3 V, respectively. Figure 6.18 displays a clear output and transfer of OTFT behaviours which can be used as a comparison data to calculate the electrical characteristic of the cPVA-based OTFT gas sensor. The same gas system and testing gases in case of the cPMMA-based sensor test were used to examine the capability of cPVA-based OTFT as a gas detector. Ethanol and methanol gases were prepared and used with concentrations of (1, 2, 4,6,7 and 8 ppm) as explained in sections 6.2.1.1 and 6.2.1.2. Figure 6.19 demonstrated the output characteristic of the cPVA-based OTFT device when it was exposed to N_2 only and 8 ppm of ethanol vapour concentration by applying different gate voltages V_{GS}.

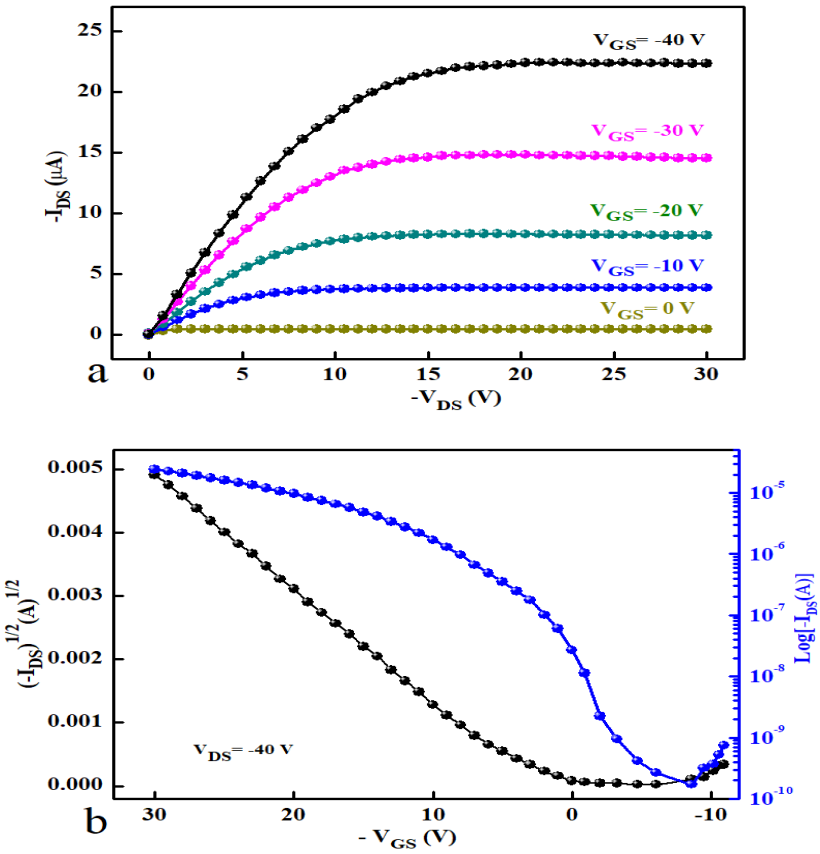

Figure 6. 18: *(a) Output characteristics and (b) transfer characteristics of OTFT device as a reference for cPVA-based OTFT gas sensing testing.*

It is clear from Figure 6.19 that the I_{DS} current was dropped from 22.5 µA to 13 µA when the device was exposed 8 ppm of ethanol, for the gate voltage of -40 V. Which is a good indicator in the OTFT-based sensor can be used to detect ethanol vapour in an environment.

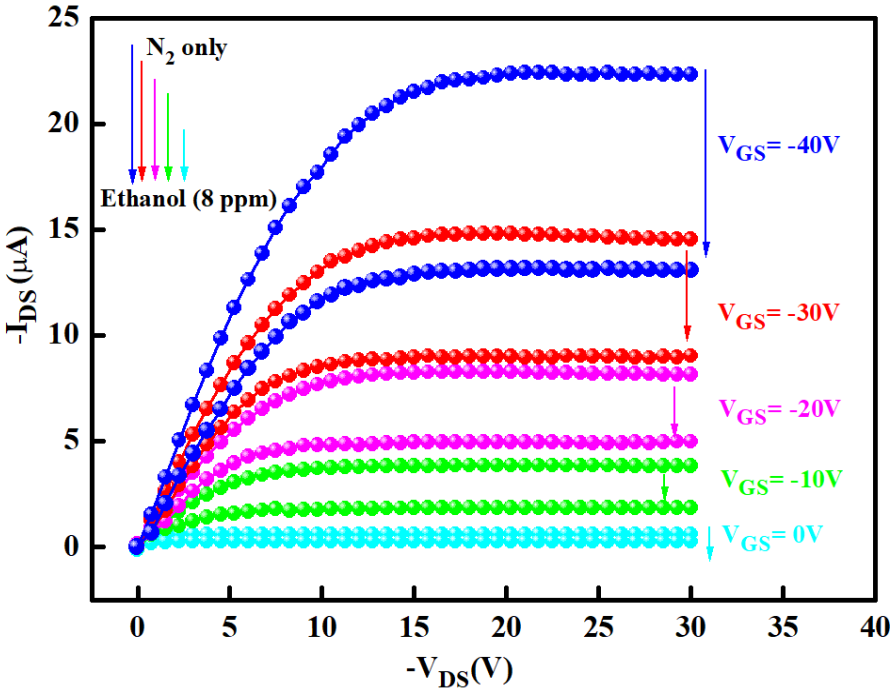

Figure 6.19: *Output characteristics of cPVA-based OTFT sensor during exposing the device to N_2 only and 8 ppm ethanol vapour for different applied gate voltages.*

Figure 6.20 shows the effect of exposing different ethanol vapour concentrations on the output characteristics of the cPVA-based OFTT sensor. A fixed gate-source voltage V_{GS} of -40 V was applied during this test, while the drain-source voltage V_{DS} was swept from 0 to -30 V. It is clear from Figure 6.20, increasing the exposed ethanol concentration from 0 to 8 ppm leads to a decrease in the saturation current of the output characteristic.

The data from Figure 6.20 can be illustrated in Figure 6.21(a), where the ethanol vapour concentration is plotted as a function of the drain-source saturation current. The sensing response based on the drain-source saturation current of the device to detect ethanol vapour was estimated to be 1.20×10^{-6} A ppm^{-1}. Moreover, Figure 6.21(b) represents the relative variation of the drain-source current ($\Delta I/I \times 100(\%)$) of the tested sensor as a function of the exposed ethanol concentration. The device sensitivity depends on the I_{DS} change (S_{IDS}) can be estimated from the curve slope in Figure 6.21 (b), which was found 5.1% ppm^{-1}. Even though the sensitivity of the cPVA-based sensor to detect ethanol vapour less than of

cPMMA-based sensor (6.6% ppm^{-1}), it is still a remarkable result to concede the cPVA-based OTFTs can be used as ethanol sensors.

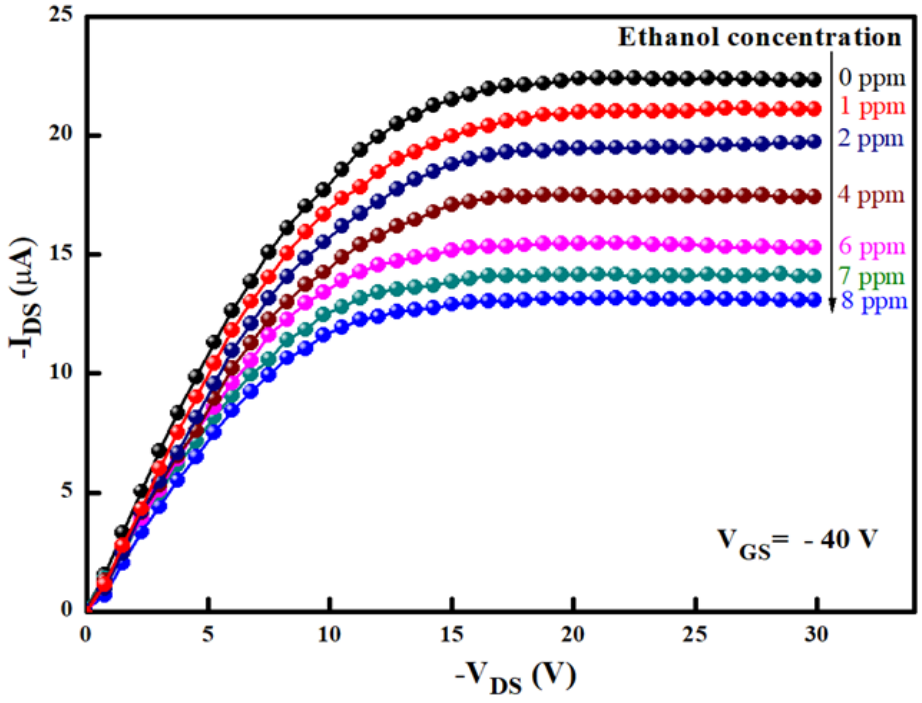

Figure 6.20: *Output characteristics of OTFT device exposed to (0 to 8 ppm) concentration of ethanol vapour for gate voltage V_{GS} = -40 V.*

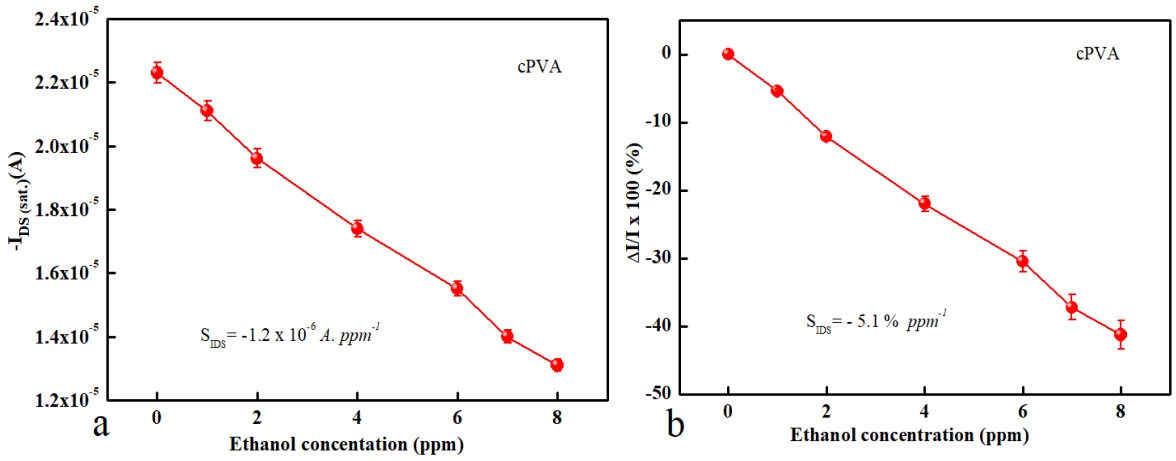

Figure 6.21: *(a) The saturation current values of the output characteristics for the cPVA-based OTFT device versus the exposed ethanol vapour concentration, V_{GS} = -40 V and V_{DS} = -30 V. (b)The relative variation of I_{DS} as a function of different exposed ethanol vapour concentration. At V_{GS}=40 V and V_{DS} = - 30 V.*

Figure 6.22 shows the effect of exposing different ethanol vapour concentrations on the transfer characteristic of cPVA-based OTFTs. Figure 6.22 (a) and (c) illustrate $-(I_{DS})^{1/2}$ and $-\text{Log}[I_{DS}]$ versus $-V_{DS}$, respectively, during exposing various concentrations of ethanol vapour. It was evident that the threshold voltage V_T was shifted to a higher negative voltage, and the device on-current was decreased during increasing the exposure of ethanol vapour concentration. After exposure of 8 ppm ethanol vapour, the threshold voltage and the device on-current were changed from -3 V to -12.5 V and 2.4×10^{-5} to 1.69×10^{-5}, respectively. While Figures 6.22 (b) and (d) represent the enlarge data of Figures 6.22(a) and (c) respectively. These changes in threshold voltage and the device on-current can be considered as ethanol sensing indicators.

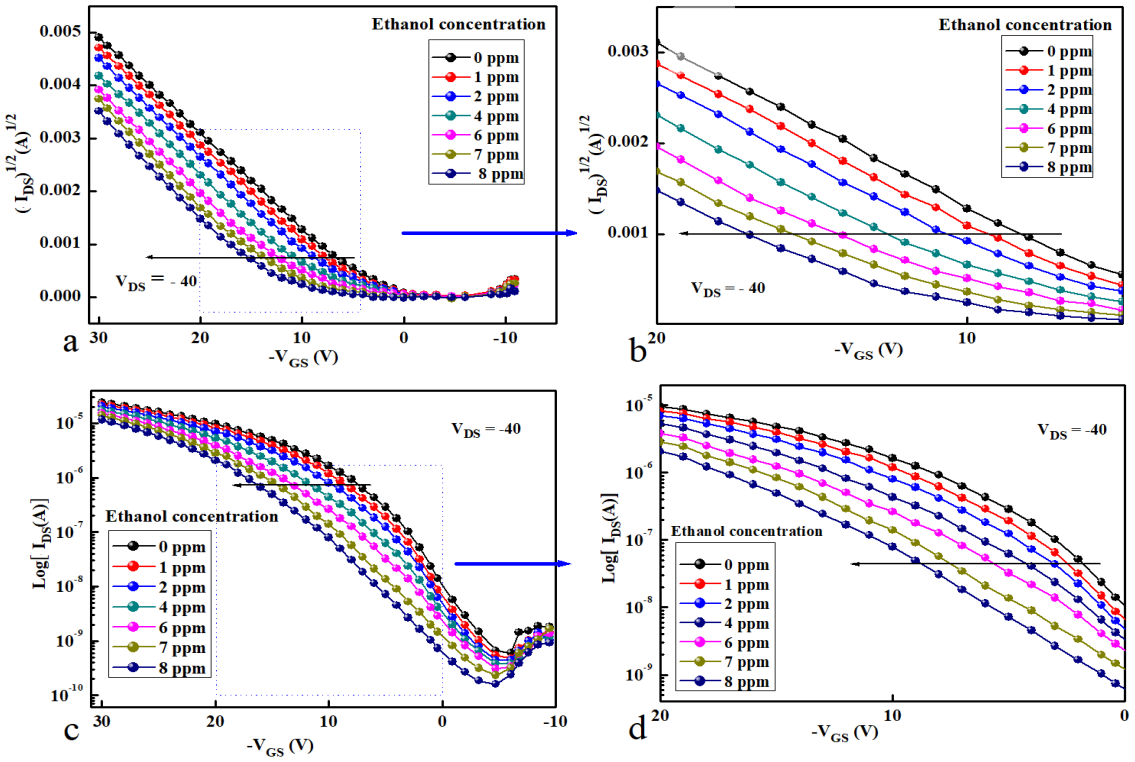

Figure 6.22: *Transfer characteristics of the cPVA-based OTFT sensor during exposing to different ethanol vapour concentrations (0 to 8ppm). (a) for $(I_{DS})^{1/2}$ versus V_{GS} (c) for Log(I_{DS}) versus V_{GS}. (b) and (d) The enlarged data in (a) and (c) respectively.*

The device's response to different exposed ethanol concentration based on the change in threshold voltage S_{VT} can be found when the threshold voltage data from Figure 6.22 (a) are plotted versus the exposed ethanol concentration as shown in Figure 6.23(a). Form the curve slope in Figure 6.23(a), the device's response was estimated to be 1.2 V. ppm^{-1} for a fixed drain-source voltage of -40 V. Figure 6.23(b) shows the relative variation of threshold voltage $\Delta V_T/V_T$ as a function of exposed different ethanol concentration. The sensitivity of the device can be estimated from the curve response, which is about 38% ppm^{-1}.The change in mobility is a significant parameter of the cPVA-based OTFT sensor. Therefore, the device mobility for each exposed ethanol concentration (1, 2, 4, 6, 7, and 8 ppm) was calculated using threshold voltages data from Figure 6.22(a) and equation (4.1). Then, the mobility values were plotted against these concentrations in Figure 6.24(a). The device sensitivity based on the change in mobility S_μ was estimated from the slope of the curve, which is 0.038 $cm^2\ V^{-1}\ s^{-1}.ppm^{-1}$. Figure 6.24 (b) displays the relative variation of the field-effect mobility ($\Delta\mu/\mu$%) as a function of various exposure of ethanol vapour concentration. The device percentage sensitivity was estimated from the slope, and it was found 3.3% ppm^{-1}.

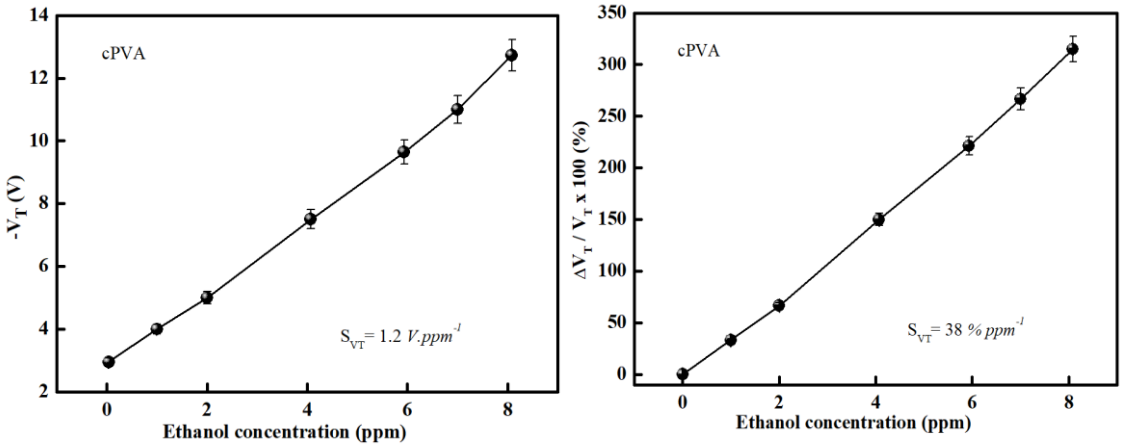

***Figure 6.23**: (a) Threshold voltage shift of the cPVA-based OTFT sensor versus the exposed ethanol vapour concentration. (b) Relative variation of the threshold voltage shift $\Delta V_T/V_T$ as a function of exposed ethanol vapour concentration. V_{DS} = -40 V.*

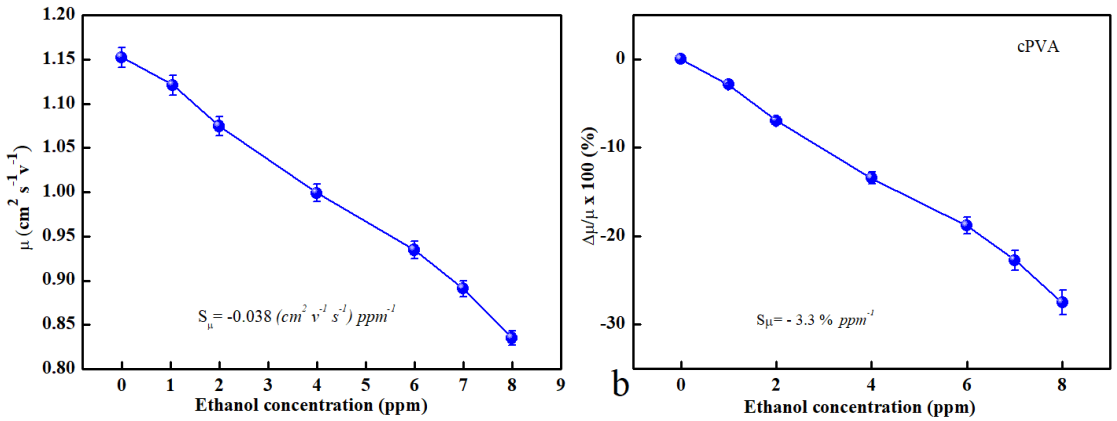

Figure 6.24: *The change in the mobility value of the OTFT-based sensor device versus the exposed ethanol vapour concentrations,* V_{DS} *= -50 V and* V_{GS} *= 0 to -50 V.*

Figure 6.25 displays the change in the drain-source current I_{DS} as a function of the time when cPVA-based OTFT device sensor is exposed to various ethanol vapour concentrations. All the measurement were done under atmospheric pressure at room temperature with applied voltages (V_{GS} =-40 V and V_{DS} =-30 V). The test was started when the device exposed to N_2 only with a measured I_{DS} current of 22.33 µA in the saturation region, and then ethanol vapour with a concentration of 1 ppm is exposure for 10 minutes, (gas on in Figure 6.25) until the I_{DS} current reaches the saturation region, which is increased to 20.8 µA. After that, the device was exposed to N_2 gas again for purifying. To continue in this test, the same procedure of exposing 1 ppm ethanol concentration was followed and applied for exposing different ethanol concentrations (2, 4, 6, 7 and 8 ppm) for 10 minutes for each concentration. Figure 6.25 shows decreasing in the I_{DS} saturation current to 19.66 , 17.32, 15.2 *µA*, 14.0 and 12.9 µA, respectively. The response and recovery time to ethanol vapour for this device were measured for exposing 8ppm ethanol concentration, and they were found *(Res. time= 60 s)* and *(Rec. time= 42 s)* respectively.

The inter graph in Figure 6.25 is the enlarged data of exposing 8 ppm of ethanol vapour.

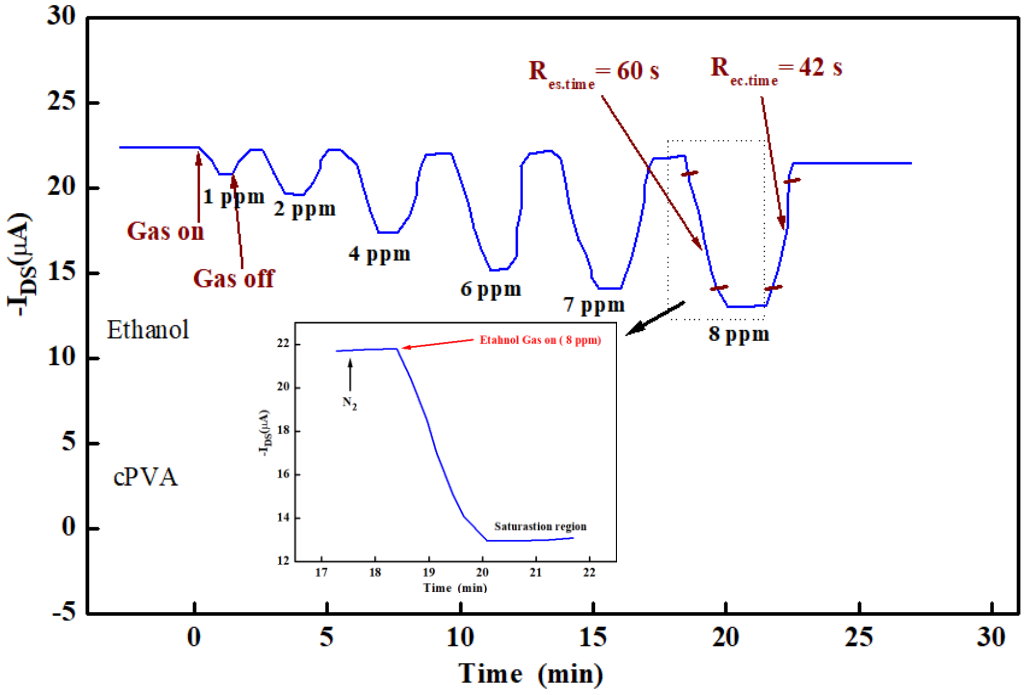

Figure 6.25: *The drain-source current of cPVA-based OTFT sensor as a function of time during exposing various ethanol concentrations (1 ppm to 8ppm). The interior figure is the enlarged part of the* I_{DS} *current during eposure of 8ppm ethanol concentration.* V_{GS}*=-40 Vand* V_{DS} *= - 30 V*

Figure 6.26 shows the relative variation of the drain-source current $\Delta I/I$ % when the device was exposed to deferent concentrations of ethanol vapour.

This test was made with applying a fixed V_{DS} and V_{GS} voltages of -30 V and -40 V, respectively. The exposed ethanol concentration of 8 ppm produced a drain-source current percentage change of 42 %. It can be seen that the relative variation of the I_{DS} current was increased with increasing the exposed ethanol concentration.

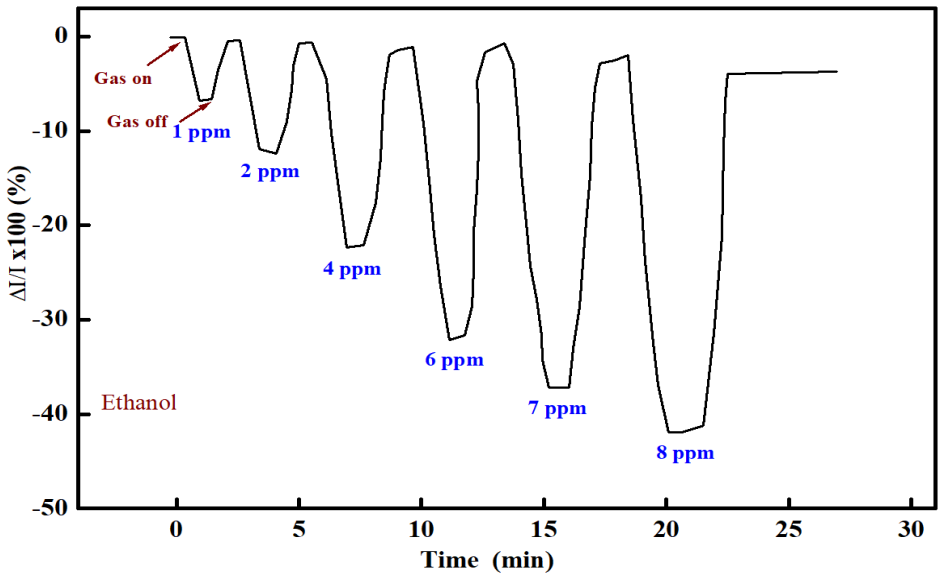

Figure 6.26: *The relative variation of the drain-source current for cPVA-based OTFT sensor during exposing different concentrations of ethanol vapour.* V_{GS}*=-40 V and* V_{DS} *= - 30 V*

6.3.1.2 Methanol sensing

In order to test the cPVA-based OTFTs devices as a methanol detector, the same method for testing ethanol vapour was followed and applied. Therefore, for comparison, the same cPVA-based OTFT device was used after being kept for 7 days under vacuum to be purified. The same exposed methanol concentrations (1 ppm to 8 ppm) in case of testing cPMMA-based OTFT as a gas detector (6.2.1.2) were used in this test. Figure 6.27 represents the output characteristics of the reference (when the device was exposed to expose N_2 only) and when exposing of 8 ppm methanol vapour for cPVA-based OTFT. Herein the applied gate-source voltage V_{GS} was varied from 0 V to -40 V with a step of 10 V and the drain-source V_{DS} was swept from 0 V to – 30 V. Figure 6.27 indicates a dropping in the drain-source saturation current when the exposed methanol concentration is increased for different applied gate voltages. The maximum shift in the drain-source saturation current was found 7.2 µA when exposing 8 ppm of ethanol vapour for the applied gate voltage of -40 V.

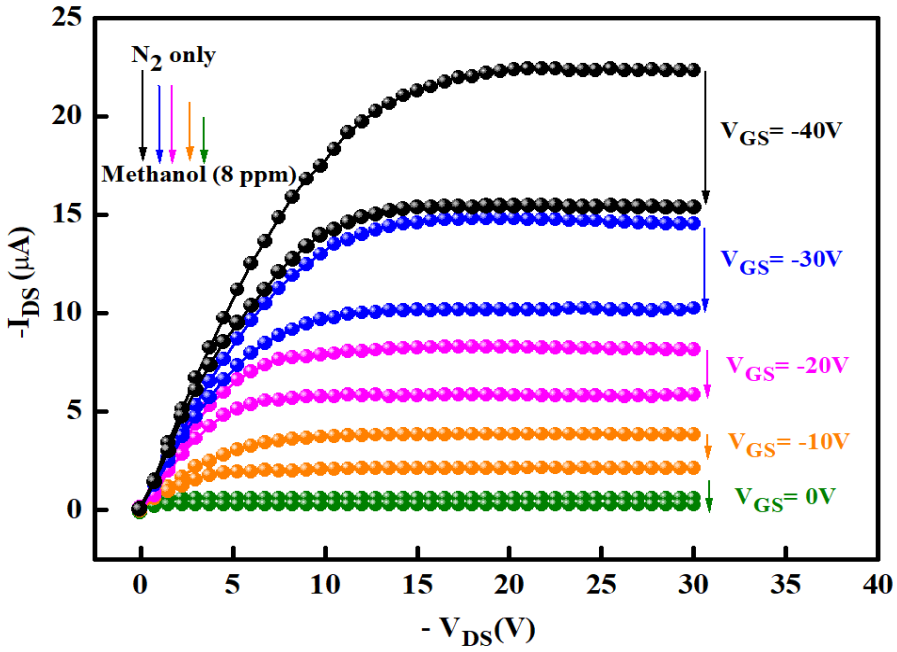

Figure 6.27: *Output characteristics of cPVA-based OTFT device when exposing of N_2 gas only (reference) and 8 ppm of methanol vapour for different gate voltages (V_{GS}= 0 to -40 V)*

Figure 6.28 displays the effect of exposure deferent methanol concentrations (1 to 8 ppm) on the device's output characteristics for a fixed gate voltage of -40 V. this test demonstrates that increasing of the exposed methanol vapour resulting in decreasing of drain-source current. For example, the I_{DS} saturation current was dropped from 22.33 to 15.4 µA when the device was exposed to N_2 and 8 ppm, respectively. This fact of changing the saturation current allowed to cPVA-based OTFT devices to be employed as a gas sensor.

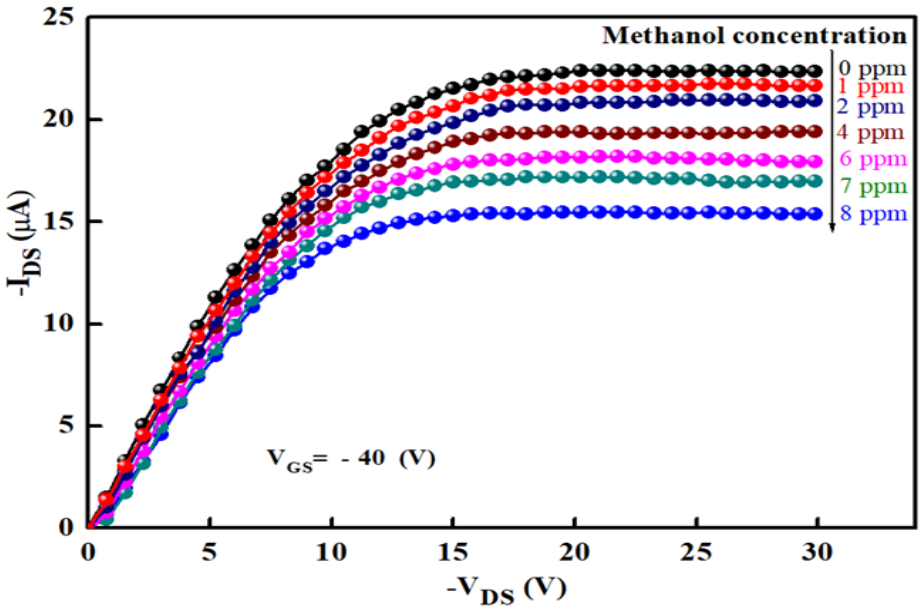

Figure 6.28: *Output characteristics of cPVA-based OTFT device exposed to a various concentration of methanol vapour (0 to 8 ppm) for the applied gate voltage (V_{GS} = -40 V).*

To estimate the sensitivity of the sensor depends on the change in the I_{DS} saturation current, the resulting saturation current values for exposing different methanol concentration from Figure 6.28 were plotted in Figure 6.29.

Figure 6.29(a) shows the dependent of I_{DS} saturating current of cPVA-based OTFT sensor on the exposed methanol concentration. From the slope of this plot, it was found that the device sensitivity to methanol vapour S_{IDS} is -0.84 $\times 10^{-6}$ A. ppm^{-1}. While Figure 6.29 (b) illustrate the relative variation of the I_{DS} saturation current as a function of the exposed methanol concentration. From the slope of the linear curve in Figure 6.29 (b), the relative device sensitivity was estimated to 3.7 % ppm^{-1}, which is less than the device sensitivity to ethanol. Figure 6.30 represents the effect of exposing different methanol vapour concentration on the transfer characteristics of cPVA-based OTFT sensor. Figure 6.30 (a) and (c) show the plot of $-(I_{DS})^{1/2}$ and $-\text{Log}[I_{DS}]$ versus $-V_{DS}$ respectively during exposing various concentrations of methanol vapour (0 to 8 ppm). Whereas, Figure 6.30(b) and (d) represent the enlarged data in Figure (a) and (c) respectively. In this test, the drain-source voltage V_{DS} was fixed to -40 V while the gate-source voltage V_{GS} was swept from 10 V to -30 V. It is clear that increasing the exposed methanol concentration to the sensor resulting

in increasing the magnitude of threshold voltage shift to a higher negative value as clearly shown in Figure 6.30 (b). Threshold voltage and the device on-current were changed from -3 V to -10 V and 2.4 × 10^{-5} to 1.4× 10^{-5} respectively, which are still less that of ethanol sensing.

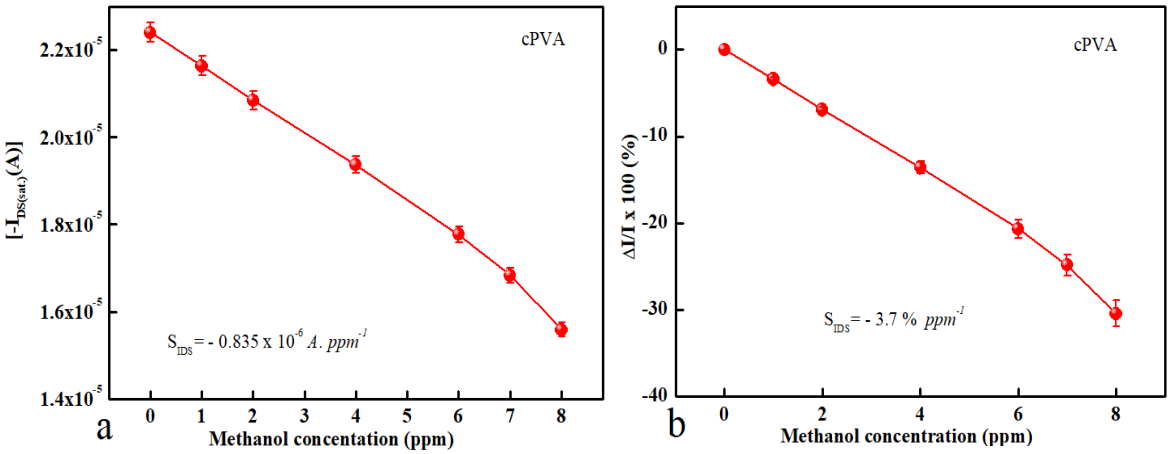

Figure 6.29: *Saturation current of the output characteristics for the cPVA-base OTFT as a function of the exposed methanol vapour concentration, V_{GS} = -40 V and V_{DS} = -30 V b) The response of cPVA-based OTFT sensor for a different exposed methanol vapour concentration.V_{DS}=-30 Vand V_{GS}=-40 V*

Figure 6.31(a) shows the change in the threshold voltage shift ΔV_T of the cPVA-based OTFT as a function of the exposed methanol concentration from 0 to 8 ppm. The data of the threshold voltage shift was extracted from the transfer characteristics in figure 6.30 (a). It is an apparent linear curve can be seen as increasing of the exposed ethanol concentration leads to an increase in the threshold voltage shift of the OTFT-based sensor.

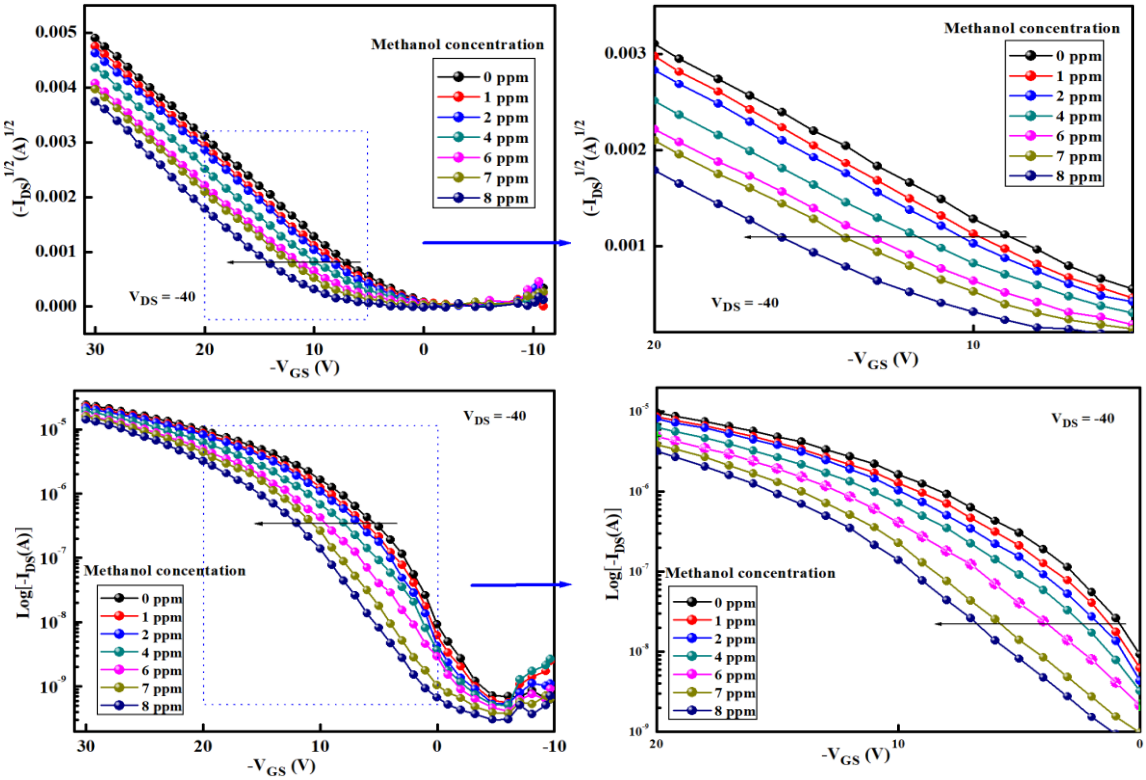

Figure 6. 30: *Transfer characteristics of the cPVA-based OTFT sensor device at a fixed V_{DS} = -40 when exposed to a different methanol vapour concentration (0 to 8ppm). (a) for $(I_{DS})^{1/2}$ versus V_{GS} (c) for Log(I_{DS}) versus V_{GS}. (b) and (d) are the enlarged data in (a) and (c) respectively.*

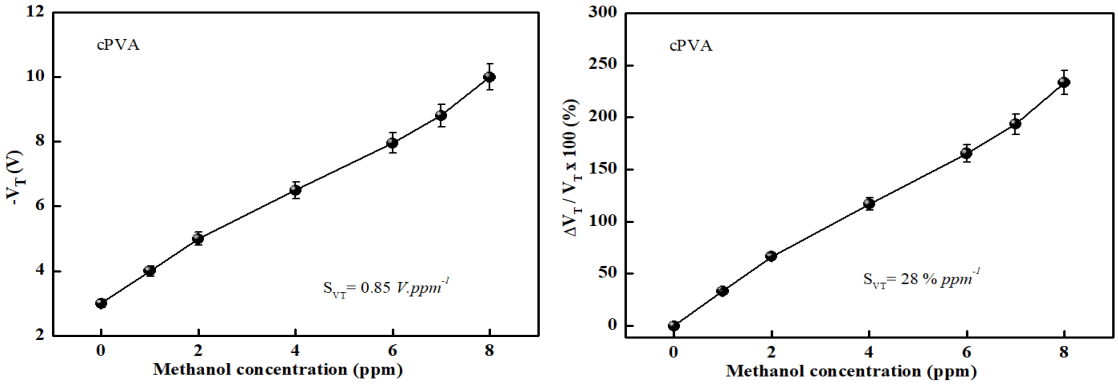

Figure 6.31: *Threshold voltage shift of the cPVA-based OTFT sensor as a function of The exposed of methanol vapour with a different concentration, V_{DS} = -30 V and V_{GS} = 0 to -40 V.*

For more investigation, the effect of various exposed methanol concentration (1 to 8 ppm) on the field-effect mobility of cPVA-based OTFT sensor was determined, as shown in Figure 6.32(a) where equation (4.1) was used to estimate the mobility values of the device as a result of exposed different methanol concentration.

The device's sensitivity to methanol vapour as a change in its mobility (S_μ) was calculated from the slope in Figure 6.32(a) which is found 0.028 $cm^2\ V^{-1}\ s^{-1}$. ppm^{-1}. The relation variation of the device mobility $\Delta\mu/\mu\%$ as a function of exposure different methanol concentration is shown in Figure 6.32(b). Herein, the percentage change of the device sensitivity to different methanol concentration was estimated from the slope in Figure 6.32, which is 2.45% ppm^{-1}.

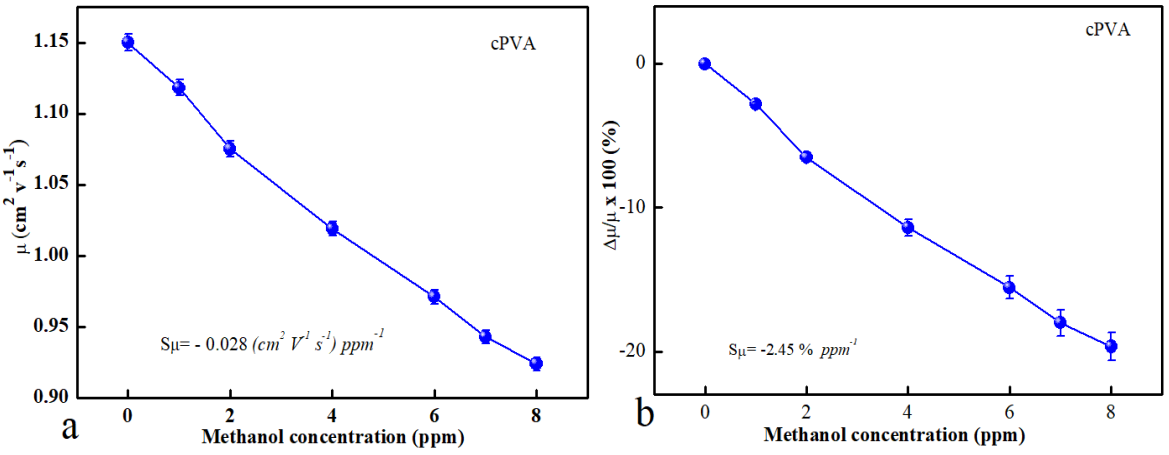

Figure 6. 32: *The mobility value of cPVA-based OTFT sensor device changed as a function of exposed different methanol vapour concentrations,* V_{DS} *= -30 V and* V_{GS} *= 0 to -40 V*

To estimate the device response and recovery time, the change in drain-source current I_{DS} of the cPVA-based OTFT sensor was studied as a function of exposure to different methanol concentration (0 to 8 ppm). In this test, the applied drain-source and drain-gate voltage were fixed to -30 V *and* -40 V, respectively. Then the test was started to measure the drain-source current at the room temperature as a result of exposure N_2 only to get the saturation region, as shown in figure 6.33. After that, the device was exposed to 1 ppm methanol vapours for 10 minutes until the I_{DS} reached the saturation state. Then, immediately the device was exposed to N_2 gas only for purifying and recovery. By following the same procedure, the

device was exposed to (2, 4, 6, 7, and 8 ppm) of methanol vapour with continues measurement time. It can be seen that increasing methanol concentration resulting in a drop of the I_{DS} saturation value. For the exposed concentration of 8 ppm , the response and recovery time of this device were found *(Res. time= 72 s)* and *(Rec. time= 64 s)* respectively. The inter graph represents the enlarged part of the plot during exposing 8 ppm of methanol which is clearly show the saturation current region.

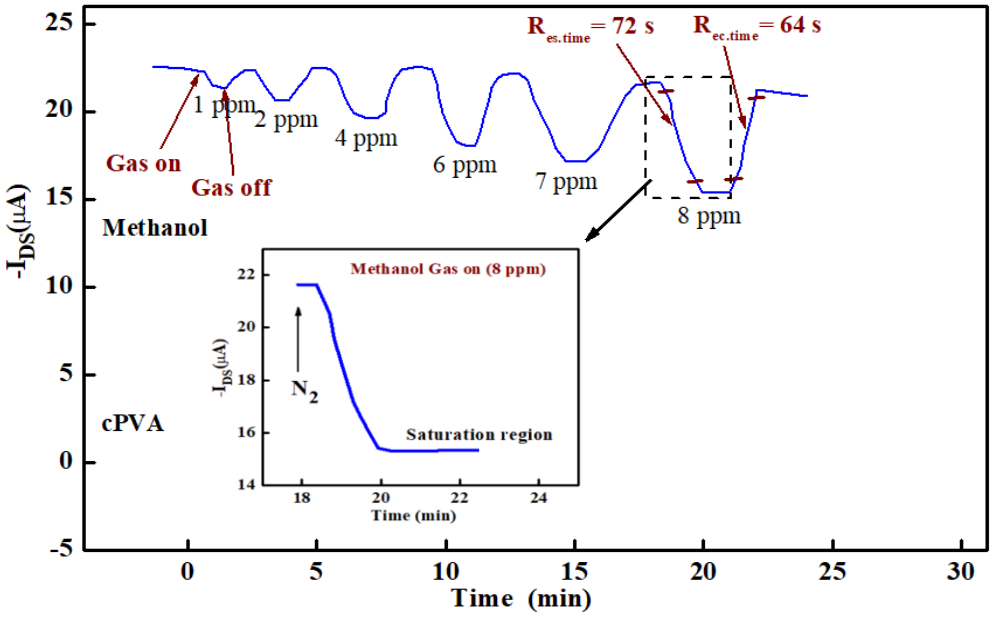

Figure 6. 33: *The depends on the drain-source current of cPVA-based OTFT sensor on the various exposed concentration of methanol vapour (0 ppm to 8ppm). The interior figure is the enlarged part of the I_{DS} current changed with exposed 8ppm methanol concentration. V_{GS}=-40 V and V_{DS} = - 30 V*

Figure 6.34 represents the percentage change of the I_{DS} current $\Delta I/I$ % as a function of exposure a different methanol vapour concentration to the cPVA-based OTFT sensor. The applied V_{DS} and V_{GS} were fixed to -30 V and -40 V, respectively in this test. The maximum response was 32 % when the methanol vapour was exposed with 8 ppm. Also, it is easy to distinguish the device response even with exposure 1 ppm of the methanol vapour.

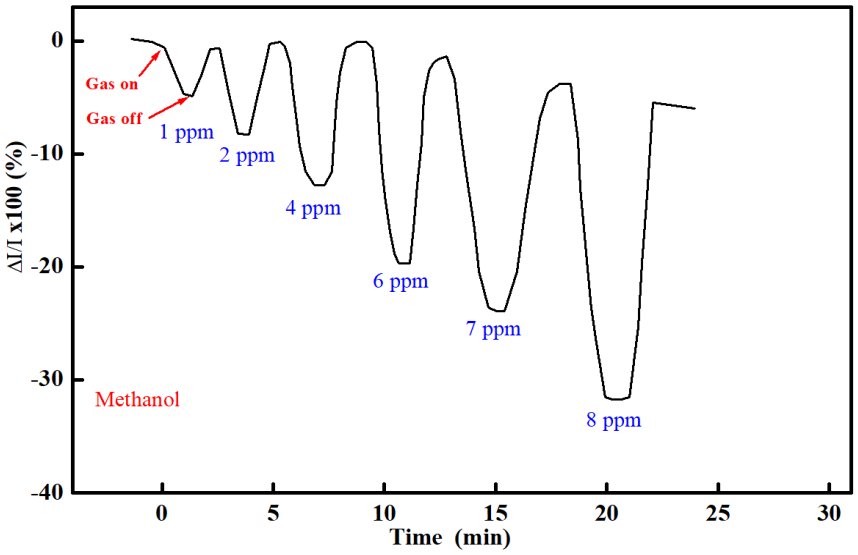

Figure 6. 34: *The variation rate of the drain-source current ΔI/I ×100 % of the cPMMA-based sensor when exposed different methanol vapour concentration as a function of time,* V_{GS}= V_{DS} = -50 *V.*

6.4 Summery

In this chapter, the two types of transistors were fabricated in chapter 4 (cPMMA-based and cPVA-based OTFTs) are tested as gas sensors to detect two types of alcohol (Ethanol and Methanol). The test was performed at room temperature under atmospheric pressure using a gas test system and Keithley 2636 source meter. Alcohol vapours (ethanol and methanol) were prepared with concentrations (1, 2, 4, 6, 7 and 8 ppm) for this test. The electric characteristics of both OTFT-based sensors were measured during exposure to N_2 gas as a reference and when exposing deferent concentration of ethanol and methanol. The main parameters of the OTFT-based sensor, which affected by exposing different alcohol concentration are the output drain-source current, threshold voltage shift and field-effect mobility. Therefore, for each device, these parameters were measured during exposing different alcohol concentration.

Table 6.1 illustrates all the results of the sensing test. It is clear that cPMMA-based OTFT sensors are more sensitive to alcohol than cPVA-based OTFT sensors. Also, cPMMA-based devices showed less response-recovery time and a higher relative sensitivity to detect

ethanol vapour than detecting methanol vapour for the parameters; saturation current S_{IDS}, threshold-voltage S_{VT} and field-effect mobility S_{μ} which are -6.6 %, 17.2 % and 4.2 % for ethanol and 4.51 %,16.1 % and 2.2 % for methanol respectively. The response and recovery time for the cPMMA-based OTFT sensors to detect ethanol vapour were found 18% and 25% less than for detecting methanol vapour which are estimated 54 sec,36 sec for ethanol and 66 sec, 48 sec for methanol respectively.

The same procedure was followed to test cPVA-based OTFTs as ethanol and methanol detectors. The result in table 6.1 showed that cPVA-based OTFTs sensors are less sensitivity than cPMMA-based OTFTs for both types of alcohol(ethanol and methanol). However, the sensitivity of cPVA-based OTFT sensor to detect ethanol vapour still better than that for detecting methanol vapour. Where the three parameters were estimated (S_{IDS} =5.1 % , S_{VT} =38 % and S_{μ} =3.3 %) for ethanol and (S_{IDS} =3.7 % , S_{VT} =28 % and S_{μ} =2.45 %) for methanol. Also, the device response and recovery time to detect ethanol vapour were found 17% and 34% less than of detecting methanol.

***Table 6.1**: Illustrates the sensitivity and response data for testing cPMMA-based and cPVA-based OTFTs as an alcohol sensor.*

Parameter	cPMMA-based OTFT sensor		cPVA-based OTFT sensor	
	Ethanol	Methanol	Ethanol	Methanol
$S_{IDS.}$(A. ppm^{-1})	1.708×10^{-6}	1.21 × 10^{-6}	1.20 × 10^{-6}	0.84 ×10^{-6}
$S_{IDS.}$% (ppm^{-1})	-6.6 %	4.51 %	5.1 %	3.7 %
S_{VT} (V. ppm^{-1})	1.4	1.3	1.2	0.85
S_{VT} % (ppm^{-1})	17.2 %	16.1 %	38 %	28 %
S_{μ} (cm^2 V^{-1}s^{-1}. ppm^{-1})	0.0571	0.031	0.038	0.028
S_{μ}% (ppm^{-1})	4.2 %	2.2 %	3.3 %	2.45 %
$R_{es.time}$ (s)	54	66	60	72
$R_{ec.time}$ (s)	36	48	42	64

6.5 References

[1] D. Elkington, N. Cooling, W. Belcher, P. C. Dastoor, and X. Zhou, "Organic Thin-Film Transistor (OTFT)-Based Sensors," *Electronics*, vol. 3, no. 2, pp. 234–254, 2014.

[2] I. Engineering, "Review : Use of Organic Semiconductor in GasSensing," *Int. J. Adv. Res. Electr. Electron. Instrum. Eng.*, vol. 3, no. 5, pp. 9351–9360, 2014.

[3] K. H. Cheon, J. Cho, Y. H. Kim, and D. S. Chung, "Thin Film Transistor Gas Sensors Incorporating High-Mobility Diketopyrrolopyrole-Based Polymeric Semiconductor Doped with Graphene Oxide," *ACS Appl. Mater. Interfaces*, vol. 7, no. 25, pp. 14004–14010, 2015.

[4] C. Zhang, P. Chen, and W. Hu, "Organic field-effect transistor-based gas sensors," *Chem. Soc. Rev.*, vol. 44, no. 8, pp. 2087–2107, 2015.

[5] Y. H. Lee, M. Jang, M. Y. Lee, O. Y. Kweon, and J. H. Oh, "Flexible Field-Effect Transistor-Type Sensors Based on Conjugated Molecules," *Chem*, vol. 3, no. 5, pp. 724–763, 2017.

[6] X. Zhuang, S. Han, B. Huai, W. Shi, and Y. Junsheng, "Sub-ppm and high response organic thin-film transistor NO2 sensor based on nanofibrillar structured TIPS-pentacene," *Sensors Actuators, B Chem.*, vol. 279, no. 2, pp. 238–244, 2019.

[7] X. Yu, N. Zhou, S. Han, H. Lin, D. B. Buchholz, J. Yu, R. P. H. Chang, T. J. Marks, and A. Facchetti, "Flexible spray-coated TIPS-pentacene organic thin-film transistors as ammonia gas sensors," *J. Mater. Chem. C*, vol. 1, no. 40, pp. 6532–6535, 2013.

[8] J. Namieśnik, "Generation of standard gaseous mixtures," *J. Chromatogr. A*, vol. 300, no. C, pp. 79–108, 1984.

[9] M. Mabrook and P. Hawkins, "A rapidly-responding sensor for benzene , methanol and ethanol vapours based on ® lms of titanium dioxide dispersed in a polymer operating at room temperature," vol. 75, pp. 197–202, 2001.

[10] W. Huang, J. Sinha, M. L. Yeh, J. F. M. Hardigree, R. LeCover, K. Besar, A. M. Rule, P. N. Breysse, and H. E. Katz, "Diverse organic field-effect transistor sensor responses from two functionalized naphthalenetetracarboxylic diimides and copper phthalocyanine semiconductors distinguishable over a wide analyte range," *Adv.*

Funct. Mater., vol. 23, no. 33, pp. 4094–4104, 2013.

[11] M. R. Cavallari, J. E. E. Izquierdo, G. S. Braga, E. A. T. Dirani, M. A. Pereira-da-Silva, E. F. G. Rodríguez, and F. J. Fonseca, "Enhanced sensitivity of gas sensor based on poly(3-hexylthiophene) thin-film transistors for disease diagnosis and environment monitoring," *Sensors (Switzerland)*, vol. 15, no. 4, pp. 9592–9609, 2015.

[12] G. S. Ryu, B. Nketia-Yawson, E. Y. Choi, and Y. Y. Noh, "Diketopyrrolopyrrole-based polymer transistors for hazardous volatile organic compound detection," *Org. Electron.*, vol. 51, pp. 264–268, 2017.

[13] X. Yu, N. Zhou, S. Han, H. Lin, D. B. Buchholz, J. Yu, R. P. H. Chang, T. J. Marks, and A. Facchetti, "Flexible spray-coated TIPS-pentacene organic thin-film transistors as ammonia gas sensors," *J. Mater. Chem. C*, vol. 1, no. 40, pp. 6532–6535, 2013.

[14] A. Dodabalapur, L. Torsi, and H. E. Katz, "Organic transistors: Two-dimensional transport and improved electrical characteristics," *Science (80-.).*, vol. 268, no. 5208, pp. 270–271, 1995.

[15] J. Yu, X. Yu, L. Zhang, and H. Zeng, "Ammonia gas sensor based on pentacene organic field-effect transistor," *Sensors Actuators, B Chem.*, vol. 173, pp. 133–138, 2012.

[16] J. Zhang, X. Liu, G. Neri, and N. Pinna, "Nanostructured Materials for Room-Temperature Gas Sensors," *Adv. Mater.*, vol. 28, no. 5, pp. 795–831, 2016.

[17] L. Wang, D. Fine, and A. Dodabalapur, "Nanoscale chemical sensor based on organic thin-film transistors," *Appl. Phys. Lett.*, vol. 85, no. 26, pp. 6386–6388, 2004.

[18] C. D. Dimitrakopoulos and D. J. Mascaro, "by C. D. Dimitrakopoulos D. J. Mascaro," vol. 45, no. 1, pp. 11–27, 2001.

[19] P. Lin and F. Yan, "Organic thin-film transistors for chemical and biological sensing," *Adv. Mater.*, vol. 24, no. 1, pp. 34–51, 2012.

[20] W. Huang, J. Yu, X. Yu, and W. Shi, "Polymer dielectric layer functionality in organic field-effect transistor based ammonia gas sensor," *Org. Electron.*, vol. 14, no. 12, pp. 3453–3459, 2013.

[21] T. Someya, H. E. Katz, A. Gelperin, A. J. Lovinger, and A. Dodabalapur, "Vapor sensing with α,ω-dihexylquarterthiophene field-effect transistors: The role of grain boundaries," *Appl. Phys. Lett.*, vol. 81, no. 16, pp. 3079–3081, 2002.

[22] L. Torsi, A. J. Lovinger, B. Crone, T. Someya, A. Dodabalapur, H. E. Katz, and A. Gelperin, "Correlation between oligothiophene thin film transistor morphology and vapor responses," *J. Phys. Chem. B*, vol. 106, no. 48, pp. 12563–12568, 2002.

[23] H. W. Zan, M. Z. Dai, T. Y. Hsu, H. C. Lin, H. F. Meng, and Y. S. Yang, "Porous organic TFTs for the applications on real-time and sensitive gas sensors," *IEEE Electron Device Lett.*, vol. 32, no. 8, pp. 1143–1145, 2011.

[24] S. Tiwari, A. K. Singh, L. Joshi, P. Chakrabarti, W. Takashima, K. Kaneto, and R. Prakash, "Poly-3-hexylthiophene based organic field-effect transistor: Detection of low concentration of ammonia," *Sensors Actuators, B Chem.*, vol. 171–172, pp. 962–968, 2012.

[25] S. Han, X. Zhuang, Y. Jiang, X. Yang, L. Li, and J. Yu, "Sensors and Actuators B : Chemical Poly (vinyl alcohol) as a gas accumulation layer for an organic field-effect transistor ammonia sensor," vol. 243, pp. 1248–1254, 2017.

[26] J. W. Jeong, Y. D. Lee, Y. M. Kim, Y. W. Park, J. H. Choi, T. H. Park, C. D. Soo, S. M. Won, I. K. Han, and B. K. Ju, "The response characteristics of a gas sensor based on poly-3-hexylithiophene thin-film transistors," *Sensors Actuators, B Chem.*, vol. 146, no. 1, pp. 40–45, 2010.

[27] J. B. Chang, V. Liu, V. Subramanian, K. Sivula, C. Luscombe, A. Murphy, J. Liu, and J. M. J. Fréchet, "Printable polythiophene gas sensor array for low-cost electronic noses," *J. Appl. Phys.*, vol. 100, no. 1, 2006.

[28] L. Torsi, M. C. Tanese, N. Cioffi, M. C. Gallazzi, L. Sabbatini, P. G. Zambonin, G. Raos, S. V. Meille, and M. M. Giangregorio, "Side-chain role in chemically sensing conducting polymer field-effect transistors," *J. Phys. Chem. B*, vol. 107, no. 31, pp. 7589–7594, 2003.

[29] L. Torsi, A. Tafuri, N. Cioffi, M. C. Gallazzi, A. Sassella, L. Sabbatini, and P. G. Zambonin, "Regioregular polythiophene field-effect transistors employed as chemical sensors," *Sensors Actuators, B Chem.*, vol. 93, no. 1–3, pp. 257–262, 2003.

[30] P. Lienerth, S. Fall, P. Lévêque, U. Soysal, and T. Heiser, "Improving the selectivity to polar vapors of OFET-based sensors by using the transfer characteristics hysteresis response," *Sensors Actuators, B Chem.*, vol. 225, pp. 90–95, 2016.

[31] Y. Kim, T. K. An, J. Kim, J. Hwang, S. Park, S. Nam, H. Cha, W. J. Park, J. M. Baik, and C. E. Park, "A composite of a graphene oxide derivative as a novel sensing layer in an organic field-effect transistor," *J. Mater. Chem. C*, vol. 2, no. 23, pp. 4539–4544, 2014.

[32] A. Das, R. Dost, T. H. Richardson, M. Grell, D. C. Wedge, D. B. Kell, J. J. Morrison, and M. L. Turner, "Low cost, portable, fast multiparameter data acquisition system for organic transistor odour sensors," *Sensors Actuators, B Chem.*, vol. 137, no. 2, pp. 586–591, 2009.

[33] B. Li and D. N. Lambeth, "Chemical sensing using nanostructured polythiophene transistors," *Nano Lett.*, vol. 8, no. 11, pp. 3564–3567, 2008.

Chapter 7

Conclusions and Further Work

7.1 Conclusion

In this study TIPS-pentacene- based organic thin film transistors (OTFTs) were fabricated with a B-G, T-C construction using two types of insulators, polymethyl methacrylate (PMMA) and poly (vinyl alcohol (PVA). High performance and relativity high mobility were achieved using the off-centre spin coating method to deposit the organic insulator layers. This method enhanced the semiconductor/insulator interface. Therefore, the charge transport through this interface becomes easier leading to high current conductivity. In addition, negligible hysterics and leakage current were realised for these devices. Before getting these results, a study of the insulators and their cross-linking technique was carried out to realise the optimum parameters using cross-linked PMMA (cPMMA) and PVA (cPVA). Various spin-coating speed and spin time, as well as different insulator solution concentrations, have been applied. Also, surface morphology has been investigated for these insulating layers and the organic semiconductor. The best spin speed and time to deposit the insulators were found at 2000 rpm, 40 sec for cPMMA and 3500 rpm, 20 sec for cPVA, respectively. It was found that exposing the deposited insulating layers to 0.8 scum O_2 ozone under vacuum (3 mbar) for 1 min reduced the moisture and improve the layer surface. This procedure gave a smooth surface with strong insulating layers without leakage current. Also, using the drop-casting method to deposit TIP-pentacene semiconductor produced large crystalline and connected grains. Storing devices under vacuum for 24 hours before depositing the gold contacts (drain-source) produced crack-free and pinhole-free contact layers. All these devices were fabricated and characterised under normal environments at room temperate. OTFTs devices displayed a typical p-type based transistor behaviour when the output and transfer characteristics have been measured. The study shows that depositing TIPS-pentacene on the cPMMA insulating layer gives much better OTFTs characteristics than cPVA, where the average mobility was achieved (1.35 $cm^2.v^{-1}\ s^{-1}$) for cPMMA-based OTFTs and 1.22 for cPVA-based OTFTs. Moreover, measurements applied for these

devices after been stored under vacuum for 12 months showed high stability with minimal degradation in the mobility changing from 1.35 to 1.281 $cm^2\ V^{-1}\ s^{-1}$.

To study the endurance properties of the organic transistors, three types of stress voltages were applied: a constant gate bias at different stress time, different gate bias stress at constant stress time and constant gate bias at a constant stress time. These tests showed a clear stability of the OTFTs with negligible hysteresis in the transfer characteristics between the forward and reverse direction as well as transfer characteristics shape fixed without any change during applying the three types of stress. This is an important parameter to prove that the OTFTs are free of trap and applying a bias voltage in the accumulation region did not affect devices behaviour. These tests proved that cPMMA-based OTFTs are appropriate for the fabrication of high-performance OTFMTs devices.

Organic thin film memory transistors (OTFMTs) based on TIPS-pentacene semiconductor as active layer were also fabricated with the same materials, parameters and methods of the transistors using an additional layer of graphene oxide as the floating gate, inserted between two insulating layers. These memory devices produced high performance with a large memory window of 38 V and 29 V for devices based on cPMMA and cPVA as insulating layer, respectively, while the control devices (without floating gate) exhibited negligible hysteresis. The high hysteresis window achieved in the output characteristics of memory transistors is attributed to the charging and discharging of the GO floating gate layer (trapping layer) when an appropriate gate voltage is applied. The hysteresis in the transfer curves with a counter-clockwise direction for the two types of the memory transistors (cPMMA and cPVA based) indicates that the charging and discharging in these devices occur through the interface between the semiconductor and floating gate. Therefore, when applying a high enough negative gate voltage, holes were injected from TIPS-pentacene (p-type semiconductor) layer into GO trapping layer (through the top insulating layer-$cPMMA_2$ or $cPVA_2$) which is charging up the floating gate and producing the programming state of the memory transistor. While when applying a positive gate voltage ($V_{GS} > 0$), holes are moved from the trapping layer (GO) to the semiconductor layer and producing the erase state of the memory transistor. Also, these memory devices demonstrated good field-effect mobility and threshold voltage for the forward and reverse directions of ($0.85\ cm^{-2}\ V^{-1}\ s^{-1}$, 2 V and -28) and $0.68\ cm^{-2}\ V^{-1}\ s^{-1}$ (-1 and -25) for cPMMA-based and cPVA-based memory devices, respectively. The carrier charge stored in the memory devices were found to be approximately $9.15\times 10^{11}\ cm^{-2}$ and $1.65 \times 10^{12}\ cm^{-2}$ for cPMMA and cPVA-based memory

transistors, respectively. From the experimental study of data retention and endurance in chapter 5, it was found that TIPS-pentacene-based organic memory transistors have good electrical reliability and mechanical stability. Also, these measurements showed that all the fabricated OTFT-based memory devices have a non-volatile behaviour and properties. Therefore OTFT-based memory devices can be fabricated with TIPS-pentacene as an active layer and GO as a floating gate with high performance and good stability and reliability.

From the results in chapters 4 and 5, it is clear that using cPMMA as an insulating layer to fabricate OTFTs and OTFMT has more enhanced performance than using cPVA for this purpose. Maybe the cPVA insulator needs more modification to improve its performance.

In chapter 6, a wide study was applied to test the fabricated OTFTs as gas sensors. In this study, alcohol (ethanol and methanol) have been chosen as the candidate gas. The experimental work was in two parts, the first part is for testing cPMMA-based OTFTs as ethanol and methanol detector, while the second part was focusing on cPVA-based OTFTs for this test.

A gas sensing system was designed for this study. Because alcohol (ethanol and methanol) is a liquid, therefore vapour form was used in this study with a known concentration in nitrogen gas. Low alcohol concentrations were applied in this study (0 to 8 ppm), and OTFTs devices demonstrate high performance and very good sensing characteristics at these low concentrations. OTFT-based sensor devices have three parameters that can be used to indicate the presence of gases in the environment: output drain-source current, field-effect mobility and threshold voltage shift. These parameters were measured during exposing the devices under the test to a fixed concentration of ethanol or methanol. Sensitivity and response-recovery times were also recorded for each sensor (cPMMA and cPVA-based sensor). All the tests were performed at room temperature (21±1 ^{o}C) under atmospheric pressure using a gas test system and Keithley 2636 source meter. From table 6.1 in chapter 6, it is clear that the sensitivity of cPMMA-based OTFTs sensors to alcohol (ethanol and methanol) showed a better sensitivity than cPVA-based OTFTs sensors. Also, cPMMA-based devices sensors have a shorter response-recovery time and higher relative sensitivity to detect ethanol vapour. The results showed that the relative sensitivity with respect to saturation current S_{IDS}, threshold voltage S_{VT} and field-effect mobility S_{μ} are -6.6 %, 17.2 % and 4.2 % for ethanol and 4.51 %,16.1 % and 2.2 % for methanol, respectively. While the response and recovery time for cPMMA-based sensors to detect ethanol vapour were found 18% and 25% less than for detecting methanol respectively.

Also from the results, it can be seen that the cPVA-based OTFTs sensors are more sensitive to ethanol vapour as the parameters were estimated (S_{IDS} =5.1 % , S_{VT} =38 % and S_{μ} =3.3 %) for ethanol and (S_{IDS} =3.7 % , S_{VT} =28 % and S_{μ} =2.45 %) for methanol. While the response and recovery time to detect ethanol are 17% and 34% less than of detecting methanol respectively.

7.2 Further work

Further work can be carried out to get more efficiency of the devices to be used for more applications such as;

1. Testing organic thin film transistors (OTFTs) devices in a different environment; humidity and temperature.
2. More study of insulator cross-linking using a different cross-linking agent with further capacitor testing to improve the insulator proprieties which is leading to enhance charge transport.
3. Graphene can be used as a connector (drain-source).
4. To improve OTFTs-based memory devices, it can be different floating gated, such as gold nanoparticles.
5. Extend gas sensing candidates using ammonia (NH_3), carbon monoxide (CO) and (CO2), for their importance in the environment.

Publications

1. **A. Al-Shawi**, M. Alias, P. Sayers, and M. F. Mabrook, “Improved memory properties of graphene oxide-based organic memory transistors,” *Micromachines*, vol. 10, no. 10, 2019, doi: 10.3390/mi10100643.

Conferences

1. Scientific Program ,Advanced Nanoscience and Nanotechnology 21st International Conference "Graphene oxide-based organic memory transistors"
   June 21-22, 2018 | London, UK

2. Biomaterials and Nanomaterials & Materials Physics and Materials Science 2nd International Conference on Journal of Materials Science and Nanotechnology | **Volume 3** "Highly sensitive gas sensor utilising tips pentacene based organic thin film transistor".
   May 20-21, 2019 | Vienna, Austria